DIELECTRIC PROPERTIES OF PEROVSKITES WITH POLAR DISORDER ($K_{1-x}Li_x TaO_3$ and $Pb[Mg_{1/3}Nb_{2/3}]O_3$) and of $SrTiO_3$ films

THÈSE N^{O} 1235 (1994)

PRÉSENTÉE AU DÉPARTEMENT DE PHYSIQUE

ÉCOLE POLYTECHNIQUE FÉDÉRALE DE LAUSANNE

POUR L'OBTENTION DU GRADE DE DOCTEUR ÈS SCIENCES

PAR

HANS-MARTIN CHRISTEN
Ingénieur physicien diplômé EPF
originaire d'Affoltern (BE)

acceptée sur proposition du jury:

Prof. A. Châtelain, rapporteur
Dr L. A. Boatner, corapporteur
Dr U. T. Höchli, corapporteur
Dr J. Mannhart, corapporteur
Dr D. Pavuna, corapporteur

Lausanne, EPFL
1994

Abstract

Dielectric properties of perovskites are studied both to gain insight into fundamental aspects of the freezing of polar disorder, and to investigate their technological potential.

The dynamics of freezing of polar disorder is investigated in single crystals of Li-doped potassium tantalate ($K_{1-x}Li_xTaO_3$) and lead magnesium niobate ($Pb[Mg_{1/3}Nb_{2/3}]O_3$).

For the mixed crystal $K_{1-x}Li_xTaO_3$, the dielectric permittivity $\varepsilon(\omega)$ is measured at various temperatures and for frequencies $\omega/2\pi$ ranging from 2×10^{-4} to 10^9 Hz. These results are complemented by measurements of field-induced pyroelectric currents and polarization vs field loops. Further information is gained from microscopic model calculations of the Li-Li interaction energy. The present study reveals that this material can neither be described by a spin-glass model nor as a ferroelectric. In particular, the polarization of previously reported nanometer-sized clusters cannot be switched by an applied electric field. The analysis of the numerical results of the Li-Li interaction energy reveals the importance of elastic interactions. Nearest-neighbor effects are observed in the shape of the $\varepsilon(\omega)$ curves. Finally, the freezing of disorder is interpreted as a consequence of hierarchical constraints.

For the "prototype" relaxor $Pb(Mg_{1/3}Nb_{2/3})O_3$, a comparison between new dielectric results and published data provides evidence of two relaxation branches. Phenomenologically, they bear strong similarities to those of glass-forming polymers and are thus labelled α- and β-type relaxations. The α branch is responsible for the characteristic peak in the temperature dependence of the permittivity. The parameters describing this relaxation show no anomalies or extrema in the investigated temperature range, and the peak is seen to be of purely dynamic origin, rather than being related to a structural phase transition. This confirms earlier claims that $Pb(Mg_{1/3}Nb_{2/3})O_3$ is nontransforming in the absence of an applied electric field.

Motivated by a technological interest in highly polarizable dielectric layers, epitaxial $SrTiO_3$ films with thicknesses between 50 and 330 nm are studied using Mg/$SrTiO_3$/-$SrTiO_3$:Nb heterostructures. Their low-temperature dielectric properties differ from those of single-crystal $SrTiO_3$ samples, but can be understood in the framework of a simple model built for this purpose. This approach takes into consideration the nonlinear polarization vs field dependence of $SrTiO_3$ and assumes strong charge trapping at the film/substrate interface.

The present films are characterized by a high permittivity: $\varepsilon \approx 100$ is reproducibly obtained at 4.2 K, corresponding to capacitances of the order of 10 nF/mm^2. Large charge densities (80 mC/m^2) can be induced by applied voltages as low as ±5 V.

Résumé

Dans cette thèse, les propriétés diélectriques des perovskites sont étudiées pour apporter un éclairage nouveau sur les aspects fondamentaux du gel du désordre polaire, ainsi que pour examiner les potentiels technologiques de ces matériaux.

La dynamique du gel du désordre polaire est étudiée en détail dans des monocristaux de $K_{1-x}Li_xTaO_3$ et de $Pb(Mg_{1/3}Nb_{2/3})O_3$.

Pour les cristaux mixtes $K_{1-x}Li_xTaO_3$, la permittivité diélectrique $\varepsilon(\omega)$ est mesurée à différentes températures dans la gamme de fréquences $\omega/2\pi$ de 2×10^{-4} à 10^9 Hz. Ces résultats sont complétés par des mesures du courant pyroélectrique induit par un champ électrique, ainsi que par des mesures des cycles polarisation-champ. Des renseignements supplémentaires sont obtenus par un calcul numérique basé sur un modèle microscopique décrivant l'interaction Li-Li. Notre étude montre que ce matériau ne peut pas être décrit par un modèle de verres de spin, ni être considéré comme un ferroélectrique. En particulier, les microdomaines qui sont mentionés dans la littérature possèdent une polarisation qui ne peut pas être inversée par l'application d'un champ électrique. L'importance des intéractions élastiques est conclue de l'analyse des résultats numériques de l'énergie d'interaction Li-Li. La forme particulière des spectres $\varepsilon(\omega)$ permet de mettre en évidence l'influence des plus proches voisins. Le gel du désordre polaire est interprété comme le résultat des contraintes hiérarchiques sur la relaxation des dipôles.

Pour le "relaxeur" type, $Pb(Mg_{1/3}Nb_{2/3})O_3$, une comparaison des nouvelles mesures diélectriques avec les résultats publiés met en évidence deux branches de relaxation. Phénoménologiquement, elles ressemblent à celles des polymères vitreux et de ce fait sont appelées branches α et β. De ces deux branches, α est la branche dominante et est responsable pour le pic caractéristique dans la dépendence en température de la permittivité ε. Les paramètres décrivant cette relaxation ne présentent aucune anomalie ni extremum dans l'intervalle de température étudié, et le pic est donc d'origine purement dynamique plutôt qu'associé à une transition de phase. Ceci confirme les affirmations précédentes que le $Pb(Mg_{1/3}Nb_{2/3})O_3$ ne subit aucune transition structurale en l'absence de champ appliqué.

Motivé par l'intérêt technologique des couches diélectriques de haute polarisabilité, des films de $SrTiO_3$ avec une épaisseur variant entre 50 et 330 nm ont été étudiés en utilisant des hétérostructures $Mg/SrTiO_3/SrTiO_3$:Nb. Leurs propriétés diélectriques à basse température diffèrent de celles des monocristaux de $SrTiO_3$, mais peuvent être comprises à l'aide d'un modèle simple établi dans ce but. Ce modèle considère en particulier la relation non-linéaire entre la polarisation et le champ électrique, et la présence de charges piégées à l'interface entre la couche et le substrat.

Les films obtenus ici sont caractérisés par une permittivité élevée: des valeurs de $\varepsilon \approx 100$ sont observées régulièrement à 4.2 K. Ceci correspond à une capacitance de l'ordre de 10 nF/mm^2. De fortes densités de charge (80 nC/mm^2) peuvent ainsi être induites en applicant des tensions aussi faibles que ±5 V.

Preface

This thesis is based on the results of research performed by the author at the IBM Research Division, Zurich Research Laboratory, Rüschlikon, and at the Institute of Experimental Physics, Swiss Federal Institute of Technology, Lausanne, from the beginning of 1991 to the spring of 1994.

The reader interested in the dynamics of freezing in $K_{1-x}Li_xTaO_3$ and $Pb(Mg_{1/3}Nb_{2/3})O_3$ will find that information in Chapters 1–5 and 7, whereas a complete treatment of the dielectric properties of $SrTiO_3$ films can be found in Chapters 1–3, 6, and 7.

Appendix A summarizes the phenomenology of dielectric relaxation. It contains information that can be found in the literature and may thus be ignored by the reader familiar with dielectric relaxation. The remaining appendixes contain mathematical and computational details (Appendixes B– E) as well as complementary experimental results (Appendixes F and G). Their essential results are summarized in the corresponding chapters.

Part of this work has been published in the following articles:

1. "Random-Barrier and Hierarchical Relaxation in $K_{1-x}Li_xTaO_3$"
   H.-M. Christen, U. T. Höchli, A. Châtelain, and S. Ziolkievicz.
   J. Phys.: Condens. Matter, **3**, 8387 (1991).
2. "Dipole-Dipole Interactions in $K_{1-x}Li_xTaO_3$"
   M. Stachiotti, R. Migoni, H.-M. Christen, J. Kohanoff, and U. T. Höchli.
   J. Phys.: Condens. Matter (in press).
3. "Small-Signal Dielectric Relaxation in the Disordered Perovskite $Pb(Mg_{1/3}Nb_{2/3})O_3$"
   H.-M. Christen, R. Sommer, N. K. Yushin, and J. J. van der Klink.
   J. Phys.: Condens. Matter, **6**, 2631 (1994).
4. "Dielectric Properties of Sputtered $SrTiO_3$ Films"
   H.-M. Christen, J. Mannhart, E. J. Williams, and Ch. Gerber.
   Phys. Rev. B (in press).

Contents

1. Introduction

1.1 Overview

Perovskite-structure compounds (perovskites for short) have received continuing attention in recent decades due to their technological potential and their fundamentally interesting properties.

Apart from research on superconductivity, interest is focused on the structural instabilities of the relatively simple perovskite lattice. At high temperatures, the lattice of most perovskites exhibits cubic symmetry, as shown in Fig. 1.1. Structural instabilities, which may appear at lower temperatures, typically manifest themselves in a series of phase transitions. Some of these transitions are purely structural, such as the 105 K antiferrodistortive transition in $SrTiO_3$, whereas others are linked to additional phenomena such as the occurrence of ferroelectricity. Incipient ferroelectrics,

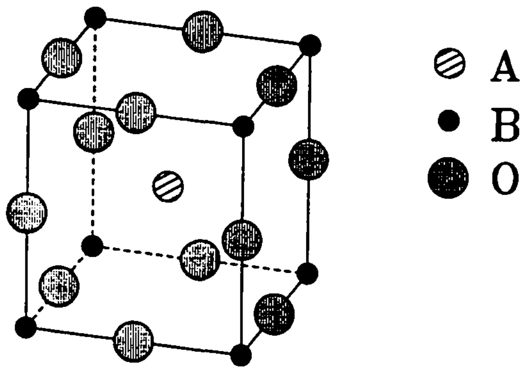

Figure 1.1 Crystal structure of a simple cubic oxide perovskite (ABO_3). This representation shows the A cation in the center of the cube. Each B cation is surrounded by an oxygen octahedron.

such as $SrTiO_3$ and $KTaO_3$, are compounds in which the ferroelectric phase transition is inhibited by quantum fluctuations;[1] polar characteristics can, however, be induced by defects. A prominent example thereof is $KTa_{1-x}Nb_xO_3$ (KTN) which is ferroelectric for $x \geq 0.008$.[2] Doping of $KTaO_3$ with lithium instead of niobium results in quite different behavior: Li concentrations larger than a few percent lead to ferroelectricity, but low doping rates result in the electric analogue of spin glasses (these terms are defined in section 1.2). The properties of $K_{1-x}Li_xTaO_3$ in the intermediate concentration range, where the system is not described by either of these concepts, offer insight to the competition between mechanisms leading to short-range order and to long-range disorder. A detailed investigation thereof is presented in Chapter 4.

Complex polar behavior is also observed in stoichiometric mixed systems, such as in the "relaxor" $Pb(Mg_{1/3}Nb_{2/3})O_3$ (PMN). The microscopic origin of the relaxor-type dielectric properties is a subject of current controversy. Similarities with dipole glasses — and thus with $K_{1-x}Li_xTaO_3$ — have recently been suggested.[3] In order to shed light on this subject, Chapter 5 investigates the phenomenological properties of relaxation in $Pb(Mg_{1/3}Nb_{2/3})O_3$.

In addition to serving as model systems for the study of dielectric relaxation in complex materials, both paraelectric and ferroelectric perovskites are of great technological interest: their high dielectric polarizability renders them suitable for volatile (paraelectric) or non-volatile (ferroelectric) charge storage applications. Recently, additional interest has been generated by the fact that a number of oxide perovskites are the parent materials of high-T_c superconductors. Their structural similarity to high-T_c materials predestines insulating $SrTiO_3$ and semiconductive Nb-doped $SrTiO_3$ to be used as constituents of devices based on superconductors; possible applications of $SrTiO_3$ and $SrTiO_3$:Nb are described in section 1.3, motivating the detailed study of structural and dielectric properties of metal/$SrTiO_3$/$SrTiO_3$:Nb thin film capacitors. In particular, the aim of Chapter 6 is to propose a model that correctly describes the electric field dependence of the polarization in such perovskite heterostructures.

1.2 Polar characteristics: concepts, notations and definitions

A **dielectric** is a material in which an electric polarization or dipole moment can be induced by an applied electric field. If the polarization can be induced by an applied mechanical stress, the material is called **piezoelectric**. Ten of the 20 piezoelectric crystal classes have a polar axis and thus acquire a spontaneous polarization which generally depends on temperature. These materials are called **pyroelectrics**.

A **ferroelectric** is defined as a pyroelectric in which the polarization "has two or more orientational states in the absence of an electric field and can be shifted from one to another of these states by an electric field. Any two of the orientation states

[...] differ only in electric polarization at null electric field."[4] For a material being cooled from the paraelectric to the ferroelectric state in the absence of applied fields, at least two equivalent directions exist along which the spontaneous polarization may occur; thus, different regions of the sample polarize in each of these directions. Each volume of uniform polarization is referred to as a domain, and the resulting domain structure can lead to very small pyroelectric and piezoelectric effects.

Dipole glasses are dielectric systems in which the interaction between electric dipoles are "in conflict" with each other, due to some frozen-in structural disorder. **Quadrupole glasses** are defined in the same way except that electric or elastic quadrupoles are considered. Typically, such systems are solids consisting of a regular lattice, some of whose sites are occupied by constituents containing a dipole or quadrupole moment possessing orientational degrees of freedom. Pure quadrupoles are realized experimentally, for example, in argon-nitrogen mixed crystals, but the moments in typical dipolar systems, such as $K_{1-x}Li_xTaO_3$ and $(KBr)_{0.5}(KCN)_{0.5}$, carry both a dipolar as well as a quadrupolar component. These systems are called **orientational glasses.**[a] Dipole and quadrupole glasses are thus viewed as special cases of this more general class.

Orientational glasses share straight-forward phenomenological and conceptual similarities with spin glasses, as outlined in the review articles by Höchli, Knorr and Loidl[8] as well as by Binder and Reger.[5] In **spin glasses**, the interaction between the magnetic moments depends on distance r according to $\cos(k_F r)/r^3$. The most successful model Hamiltonians disregard the influence of distance and Fermi wave number k_F, and, in the presence of an applied magnetic field H, are expressed as

$$\mathcal{H} = -\frac{1}{2}\sum_{i,j} J_{ij} S_i S_j - H \sum_i S_i^z. \tag{1.1}$$

Here, J_{ij} is the interaction between spins S_i and S_j at sites i and j respectively, and S^z is the component of the spins in the direction of H. The interaction is written in terms of a distribution $g(J_{ij})$ with average J and variance Var$J$. For large J and small Var$J$, (1.1) describes a ferromagnet; in the opposite case, the spin-glass behavior is obtained. By replacing the spins by electric dipoles or elastic quadrupoles, and H by an electric or a strain field, the electric and elastic analogues to spin glasses are found. In the case of $J \gg \mathrm{Var}J$, Eq. (1.1) then describes a ferroelectric or ferroelastic, and an orientational glass is obtained for $J \lesssim \mathrm{Var}J$.

A parameter K is introduced[8] to denote the coupling of the moments to the host lattice. Spin glasses are characterized by a small value of K, justifying the use of the above Hamiltonian, which neglects all interaction with the lattice. At the other extreme, **glassy crystals** are found if disorder arises mainly from the coupling of

---

[a] The term "orientational glass" is sometimes used to denote quadrupole glasses,[5] and originally the term "polar glass"[6] was used for what is here called orientational glass. To avoid confusion with the "polar glasses" in the sense of materials consisting of oriented crystallites in a glass matrix (see Ref. 7, page 27), this term is not used here.

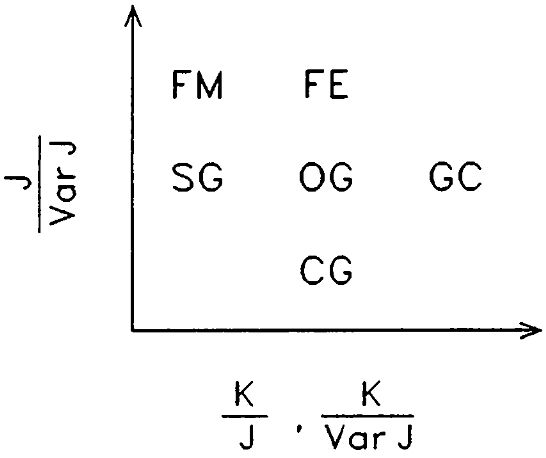

Figure 1.2 Classification of different polar states according to the ratio of mean moment-moment interaction J to its variance Var$J$, and according to the ratio of the moment-lattice coupling K to J or Var$J$. Ferromagnets (FM) and spin glasses (SG) are cases of weak moment-lattice coupling, and in ferroelectrics and ferroelastics (FE) and in orientational glasses (OG), K is of the same order as J or Var$J$, respectively. For canonical glasses (CG), K is not defined, but Var$J$ is large. Glassy crystals (GC) arise when K dominates over moment-moment interactions.

the moments to the lattice. In a typical orientational glass, the coupling K is of the same order of magnitude as J or Var$J$.

In the framework of this Hamiltonian, **canonical glasses** (such as fused silica, SiO_2) are viewed as the limit at which every lattice site carries a moment and where the moments cannot arrange themselves in an ordered structure owing to the way in which the sample was prepared. Conceptually, this corresponds to an enhancement of Var$J$.[8]

Orientational glasses are thus seen as systems lying in between spin glasses, ferroelectrics, glassy crystals, and canonical glasses, as summarized in Fig. 1.2.

The word **relaxor** (or "relaxator") refers to a group of dielectrics that exhibit a characteristic dielectric response: in particular, a temperature-dependent frequency dispersion of the complex permittivity ε, and a "diffuse" peak in $\varepsilon(T)$. Other names, such as "relaxor ferroelectrics," "ferroelectrics with a **diffuse phase transition**," or "diffuse phase transition materials" (implying that different portions of the sample undergo a ferroelectric phase transition at different temperatures) are misleading since no proof of any phase transition has been given for the prototype relaxors, such as $Pb(Mg_{1/3}Nb_{2/3})O_3$ and lanthanum-doped $Pb(Zr_{0.5}Ti_{0.5})O_3$ ceramics, in the absence of applied fields. These materials are characterized by disorder resulting from the spatial distribution of the different B cations in the ABO_3 lattice, but the above definition of relaxors does not imply a particular physical mechanism leading to the observed relaxation behavior. Understanding the underlying microscopic mechanisms is currently a subject of controversy. Similarities with orientational glasses and with martensitic-type behavior have recently been pointed out (see section 5.2).

$K_{1-x}Li_xTaO_3$ and $Pb(Mg_{1/3}Nb_{2/3})O_3$ are studied in this work as model systems of materials whose complex dielectric behavior is related to their compositional inhomogeneities. $K_{1-x}Li_xTaO_3$ is investigated at concentrations slightly higher than those for which a dipole-glass state has been proposed. In particular, the properties of the polarized microdomains and the origin of glassy freezing are analyzed. For $Pb(Mg_{1/3}Nb_{2/3})O_3$, a phenomenological description of the relaxation is presented.

1.3 An application of simple perovskites: epitaxial $SrTiO_3$ films in $SrTiO_3$/$SrTiO_3$:Nb heterostructures

Thin films of perovskites have found widespread applications in a number of fields. Their dielectric polarizability makes them suitable for memory applications and thin film capacitors. Piezoelectric perovskites, such as $Pb(Zr_{0.5}Ti_{0.5})O_3$ and $Pb(Mg_{1/3}Nb_{2/3})O_3$, are used in surface acoustic wave devices and microactuators, and the optoelectric effects found in $KNbO_3$ and $LiNbO_3$, for example, are utilized for optical wave-guides. Light modulators may take advantage of the photo-refractive effects found, for example, in $(Pb,La)(Zr,Ti)O_3$, whereas frequency doublers bring into play the second harmonic generation of compounds such as $LiNbO_3$ and $KNbO_3$. Infrared detectors rely on the pyroelectric effects in materials such as $PbTiO_3$ and $KTa_{1-x}Nb_xO_3$(see Ref. 9 for a review). Recently, $SrTiO_3$ and $KTaO_3$ have been used as substrates and buffer layers for high-T_c superconductors.

Strontium titanate lends itself to the study of basic dielectric properties of oxide thin films: the bulk properties of this paraelectric are well known (including its low-temperature behavior), and high quality epitaxial films of this substance can be grown. A detailed study of the influence of electric fields, trapped charges, surface roughness, etc. on the dielectric properties of $SrTiO_3$ films will yield a description of the phenomena that are expected to be observed in the behavior of perovskite layers in general. The results are thus relevant not only to technological applications of $SrTiO_3$ films, but also to the understanding of the characteristics of more complicated oxide layers.

Particular interest in $SrTiO_3$ films arises from the fact that they can be grown on platinum as well as on Pt-covered silicon wafers.[10,11,12] This allows $SrTiO_3$ to be integrated with semiconductors, and opens perspectives for memory applications and for including high-T_c superconducting materials in semiconductor devices.

The combination of $SrTiO_3$ and high-T_c superconductors has been successfully used in SQUID's,[13] microwave applications,[14] and electric field effect devices.[15]

In electric field devices, the carrier density in a high-T_c-superconductor is modulated by an applied voltage, resulting in particular in a change of the superconducting transition temperature. In addition to the prospective technological applications, such experiments offer insight into fundamental properties of high-T_c superconductivity. The devices can be built as heterostructures similar to semiconductor MISFET's: a thin superconducting film is deposited as a channel on an insulating substrate, and a gate insulator is grown on top of this channel. The disadvantage of this standard MISFET layout, used by a number of researchers,[16,17,18] is the requirement that an insulator be grown on a very thin superconducting film, a process that may deteriorate the film's superconductive properties. This disadvantage can be circumvented[15,19] by using an "inverted MISFET" structure, in which an insulator layer is deposited on an electrically conducting substrate serving as gate electrode, with the superconducting channel grown last. For the substrate, a material has to be chosen whose transport properties do not deteriorate in the oxidizing environment required for the growth of oxide insulating films such as $SrTiO_3$. Epitaxy thereof is a prerequisite for growing an epitaxial superconducting channel.

A possible realization of such an inverted MISFET is shown in Fig. 1.3, using a niobium-doped $SrTiO_3$ single crystal as a substrate. The amount by which the superconducting transition temperature can be shifted by an applied voltage V_G then depends on the maximum of the polarization P that can be induced in the $SrTiO_3$ film. For device optimization and for interpretation of experiments to study the induced changes in the superconductor's properties, the $P(V_G)$ relation must be known.

The study of such $SrTiO_3/SrTiO_3$:Nb structures, shown in Fig. 1.4, is further motivated by the fact that semiconducting $SrTiO_3$:Nb is now commercially available and widely used in the study of superconductor/semiconductor junctions, including $YBa_2Cu_3O_{7-x}$,[20] Er-Ba-Cu-O,[21] or $Ba_{1-x}K_xBiO_3$[22]. In addition, other insulators such as the low-permittivity material $NdGaO_3$ (Ref. 23) can be grown on $SrTiO_3$:Nb.

The sample in Fig. 1.4 has the geometry of a parallel-plate capacitor. Therefore, the capacity C_{film} can be related to the geometric dimensions d (thickness) and S (top electrode surface area) via the definition of an **effective permittivity** ε_{eff} by

$$C_{\text{film}} = \frac{\varepsilon_{\text{eff}}\, \varepsilon_O\, S}{d} \qquad \text{with } \varepsilon_O = 8.85 \text{ pF/m}. \tag{1.2}$$

Typical experiments show that ε_{eff} differs both qualitatively and quantitatively from the permittivity of $SrTiO_3$ bulk samples, as illustrated in Fig. 1.5.

Chapter 6 studies to what extent this different behavior can be understood through the field dependence $\varepsilon(E)$ of the permittivity, the presence of trapped

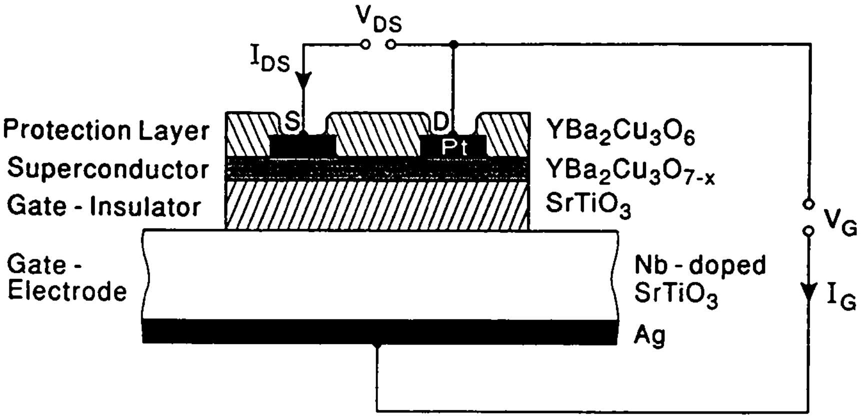

Figure 1.3 Inverted MISFET structure studied in our laboratory (Mannhart *et al.*[15]).

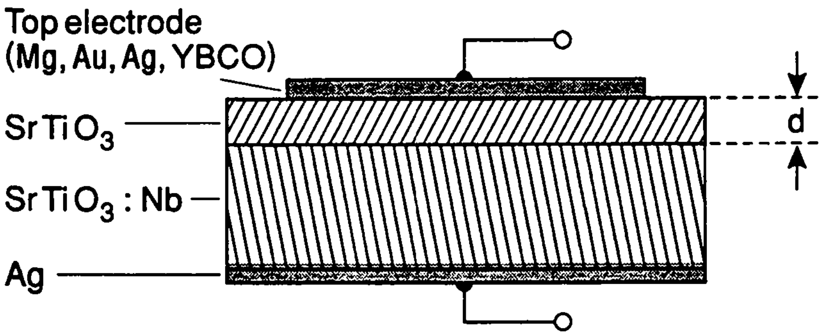

Figure 1.4 Typical sample structure as studied in Chapter 6. Film thicknesses *d* varying from 50 nm to 330 nm have been used.

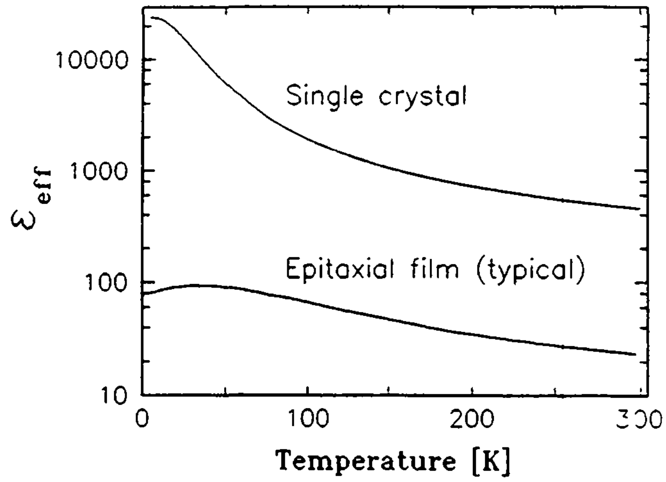

Figure 1.5 Temperature dependence of the dielectric permittivity $\varepsilon(T)$ of bulk $SrTiO_3$ compared to the effective permittivity ε_{eff} defined in Eq. (1.2) of a thin film capacitor with the structure shown in Fig. 1.4.

charges, and structural imperfections of the films. This requires quantitative knowledge of the $\varepsilon(E)$ dependence, as obtained in Chapter 3.

1.4 Dielectric properties: definitions and notations

By definition, the **permittivity** ε (or *dielectric constant*) of a material is given by the derivative of the polarization P with respect to the electric field E:

$$\varepsilon(E) = 1 + \frac{1}{\varepsilon_o}\frac{\partial P}{\partial E}\,. \tag{1.3}$$

Throughout this thesis, P and E can be treated as scalar quantities for symmetry reasons, and $\varepsilon(E)$ is thus also a scalar. The **linear** permittivity is defined as

$$\varepsilon_l = \lim_{E\to 0}\varepsilon(E) = \lim_{E\to 0}\ 1 + \frac{1}{\varepsilon_o}\frac{P}{E}\,. \tag{1.4}$$

The macroscopic polarization is due to the orientation of microscopic dipoles, and P does not follow E instantaneously. The time dependence of $P(t)$ for a given $E(t)$

can be studied in order to shed light on the properties of these microscopic moments. This is done in Chapters 4 and 5. For sufficiently weak electric fields (i.e. in the linear regime), a sinusoidal stimulation $E(t) = \hat{E}e^{j\omega t}$ of frequency $f = \omega/2\pi$ results in a phase-shifted sinusoidal time dependence of the polarization $P(t) = \hat{P}e^{j[\omega t+\phi(\omega)]}$. Thus, a frequency-dependent permittivity can be defined as

$$\varepsilon_l^*(\omega) = \lim_{\hat{E}\to 0} 1 + \frac{1}{\varepsilon_O} \frac{\hat{P}}{\hat{E}} e^{j\phi(\omega)} \tag{1.5}$$

with $\varepsilon_l^*(\omega) = \varepsilon_l'(\omega) - j\varepsilon_l''(\omega)$.

In general, the permittivity $\varepsilon^*(E,\omega)$ thus depends both on the applied field E and on the frequency $f = \omega/2\pi$. Throughout this thesis, the following notations are used:

$$\begin{aligned} \varepsilon(\omega) = \varepsilon'(\omega) - j\varepsilon''(\omega) &= \lim_{E\to 0} \varepsilon^*(E,\omega) && (1.6)\\ \varepsilon(E) &= \lim_{\omega\to 0} \varepsilon^*(E,\omega) = \lim_{\omega\to 0} \varepsilon'(E,\omega). && (1.7) \end{aligned}$$

Typically, $\varepsilon(E,\omega)$ is obtained from a measurement of the capacity $C(V,\omega)$ and the conductivity $G(V,\omega)$ of a parallel-plate capacitor of thickness d and electrode surface S:

$$\varepsilon'(E,\omega) = \frac{C(V,\omega)}{C_O} \qquad \varepsilon''(E,\omega) = \frac{G(V,\omega)}{\omega C_O}, \tag{1.8}$$

where $C_O = (\varepsilon_O S)/d$ and $E = V/d$, with V denoting a static (dc) voltage bias. C and G are measured with a small oscillating test signal superimposed on V.

As an alternative to measuring the response to a sinusoidal test signal, the **depolarization currents** i induced by a step function excitation can be measured as a function of time t. In the linear regime, the quantities $i(t)$ and $\varepsilon(\omega)$ are related by Fourier transforms (listed in Appendix A). Thus, a measurement of $i(t)$ corresponds to a measurement of $\varepsilon(\omega)$ at $\omega \approx 1/t$, i.e. at $f \approx (2\pi\omega)^{-1}$.

Experimental results will be represented throughout this thesis as a function of f rather than of ω. Nevertheless, ω arises as a more natural quantity in most models and generally leads to simpler mathematical expressions. Therefore, physical properties are discussed in terms of $\varepsilon(\omega)$.

2. Experimental methods

This chapter gives a brief overview of the applied experimental techniques. Cryostats and sample holders, the measurement/data acquisition equipment and the sample preparation techniques (including crystal growth and surface treatment) are described. Growth of the $SrTiO_3$ films will be discussed in Chapter 6.

2.1 Sample holders and cryogenic environment

For measurements at 4.2 K and for short-time (< 1 hour) experiments at temperatures between 4.2 and 300 K, a sample holder was built that allows measurements to be performed directly in a helium dewar (figure 2.1). In this setup, the sample is glued to a copper plate with silver paint, and electrical connections are made to the pins of an integrated-circuit socket. This unit (sample, copper plate, and socket) is then easily mounted onto the main body of the sample holder, allowing fast sample exchange. The main body of the sample holder is cut from a single copper block, and contains two heating resistors and a silicon diode as temperature sensor[a] (specified tolerance: ± 0.5 K below 100 K, and 1% of the reading at higher temperatures). A closed-end pierced brass tube serves as a protective case and heat shield, and is slid over the inner part from below. Temperature stability better than ± 0.5 K is obtained for time intervals exceeding 1 hour for $15\ \mathrm{K} \leq T \leq 300\ \mathrm{K}$. This is largely sufficient for the presented measurements on $SrTiO_3$ films. More time-consuming experiments on such samples were performed directly in liquid helium.

For other types of experiments, in particular for the depolarization current measurements, the temperature must be kept constant to within less than 0.1 K for several hours. A home-made combined helium flux and bath cryostat was used for these experiments. The sample holder, as described by M. Maglione,[24] consists of two concentric copper cylinders, of which the inner one is heated by a winding of constantan wire. The sample itself hangs freely in a small copper cavity, the temperature of which is measured by a Pt-100 resistor. From measurements of temperature-

---

[a] Lake Shore DT-470-SD-12A

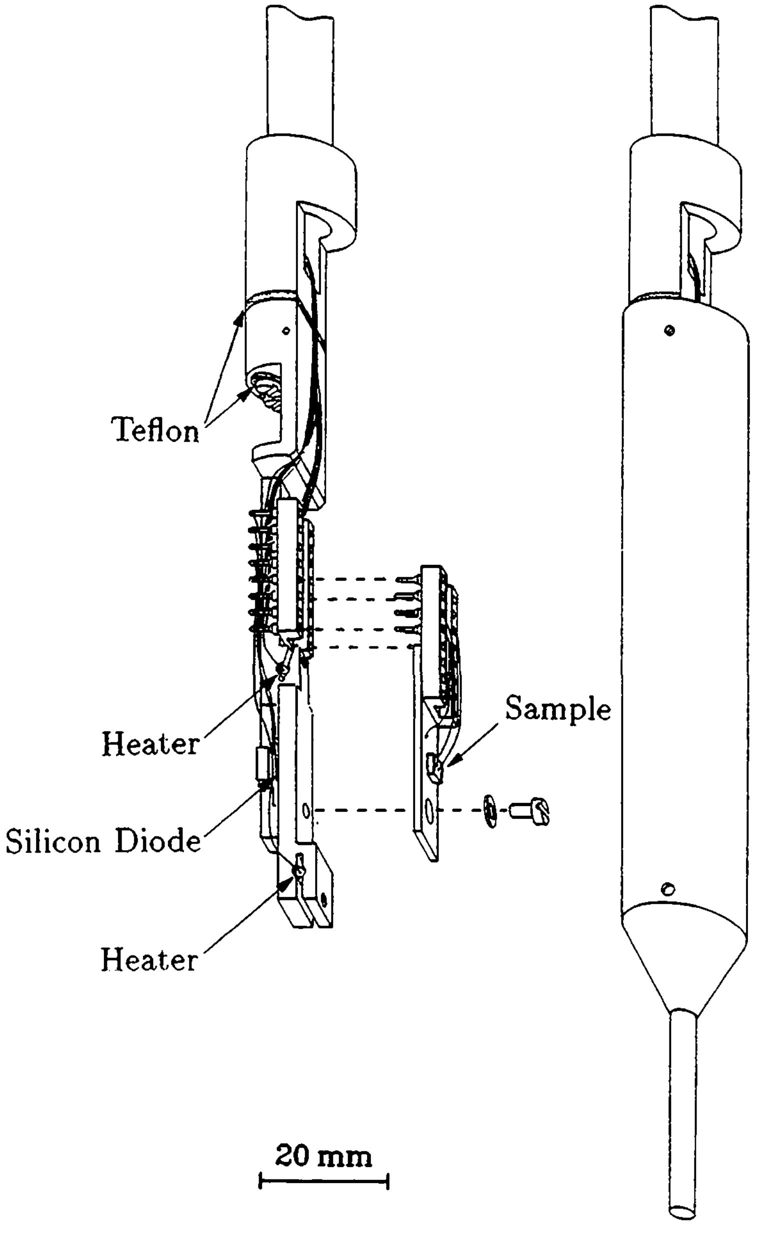

Figure 2.1 Sample holder for dielectric measurements, shown open (left) and closed (right).

dependent properties of $K_{1-x}Li_xTaO_3$ crystals (section 4.3.2a), the absolute temperature determination was seen to agree with the temperature measurements at the University of Mainz to within 0.5 K (tested at $T = 35$ and 50 K).

Pyroelectric measurements were also performed in this cryostat. Here, the sample was first cooled by a strong helium flux. After interruption of this flux, temperature rates of 0.01–0.1 K/s were achieved through the use of the heater winding. Therefore, no movable parts were required in this setup, and connections to the electrometer were made by rigid coaxial lines to reduce noise.

For measurements at high frequencies (10^6 Hz $\leq f \leq 10^9$ Hz), a sample holder built by M. Maglione[24] was used. Its fully coaxial design is based on the HP16091A test fixture and connected to the HP4191A impedance analyzer via rigid air lines.

2.2 Measurement equipment

2.2.1 The frequency dependence of the permittivity

The present study requires measurements of the complex permittivity at frequencies 1 mHz $\leq f \leq$ 1 GHz, using the following combination of experimental techniques:

- 10^6 Hz $\leq f \leq 10^9$ Hz: determination of the sample's vector reflection coefficient for a sinusoidal measurement signal, using a **HP4191A Impedance Analyzer**. Directivity errors, undesired reflections, and electrical length errors are corrected by the error vectors measured at all test frequencies on standard terminations with 0 Ω, 0 S, and 50 Ω impedance.

- 10^5 Hz $\leq f \leq 10^6$ Hz: conventional bridge technique, using a **Marconi TF2002AS Signal Generator** and a **Boonton 75A** bridge to yield the capacity and conductivity of the sample. With the three-terminal connection, the series capacitance of the coaxial cables does not need to be known. Manual balancing of the bridge, however, is time-consuming and tedious.

- 10 Hz $\leq f \leq 10^5$ Hz: two alternative setups have been used.
  - The **HP4192A Impedance Analyzer** determines the sample's complex impedance from a measurement of the vector ratio between the applied test signal (5 Hz $\leq f \leq 1.3\times10^6$ Hz) and the current flowing through the specimen. Calibration measurements to determine the residual impedance and stray admittance of the test fixture were taken at 10 Hz, 30 Hz, and 100 kHz. For the sample holders used in this work, the cable length exceeded 2 m, making sufficient adjustment impossible for frequencies $f >$ 100 kHz.
  - A **General Radio GR1616 Precision Capacitance Bridge** was used for experiments where its high conductivity resolution (1 fS) was required.

The same considerations regarding conventional bridge techniques apply as to the Boonton 75A.

- 10^{-2} Hz $\leq f \leq 10^4$ Hz: measurements in this range were performed at the Department of Physics (KOMA) of the University of Mainz, Germany, using a **Solartron Instruments/Schlumberger Frequency Response Analyzer FRA1255**. The essential difference between the FRA1255 and the HP4192A is that the former synthesizes and analyzes the test signal numerically. Its low input resistance (10^7 Ω) requires the use of a high-impedance interface,[b] such as the **Chelsea Dielectric Interface** (J. Pugh, Dielectric Instrumentation, Worcestershire).

- 1.6×10^{-4} Hz $\leq f \leq 1.6\times10^{-1}$ Hz: **depolarization currents** were measured as the time-domain equivalent of the frequency-dependent permittivity. Using a HP6634A power supply (fall time: 40 μs), the sample was first charged for at least three times the measurement time of the decay. A Keithley 642 electrometer with remote head was used to record the current. The connections between the remote head and the cryogenic sample holder being made of rigid coaxial lines, the noise level was kept below 0.1 pA.

2.2.2 The field dependence of the permittivity

With an HP4192A impedance analyzer, the field dependence of the permittivity can be studied using the instrument's built-in voltage bias. However, it became clear in the process of this work that the experiments on the $SrTiO_3$ thin films require sample current and capacity to be measured simultaneously. Therefore, the circuit shown in Fig. 2.2 was used. Its design is based on information from the HP instruction manual and consists of blocking capacitors and protection Zener diodes. The R_1C_1-element imposes a lower frequency limit. For $R_1 = 1$ kΩ and $C_1 = 8.2$ μF, the typical test signal frequency of 10 kHz lies well above this value. The bias was applied by a Hewlett-Packard HP6634A power supply. Voltage and sample current were measured with a HP3474A and a Keithley 195A Digital Multimeter, respectively. A current resolution of better than 2 nA was achieved.

2.2.3 Pyroelectric currents

Pyroelectric currents were measured with the Keithley 642 remote head electrometer while the sample temperature was increased linearly with time. The HP6634A power supply was used for field-cooling.

---

[b] With an input resistance of 10^7 Ω, low-frequency measurements (10^{-2} Hz) of ε'' on a typical sample with electrode surface of 10 mm^2 and 1 mm thickness are possible only for materials with $\varepsilon'' > (10^7\Omega \cdot C_0 2\pi f)^{-1} \sim 10^7$, which is well above the typical values ($< 10^3$) observed in this study.

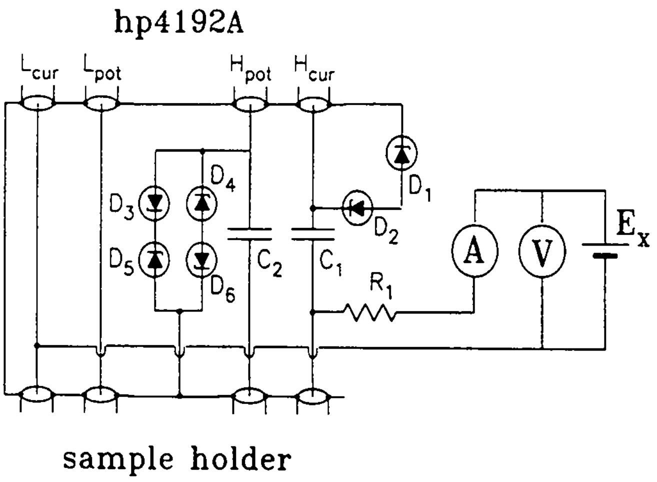

Figure 2.2 Circuit used to connect an external power supply to the HP4192A impedance analyzer, allowing for the dc sample current, the capacitance, and the ac conductance, to be measured simultaneously. E_x stands for the HP6634A power supply, V for the HP3474A multimeter, and A for the Keithley 194A multimeter. The values for the resistor, capacitors, and Zener diodes are: $R_1 = 1\ k\Omega$, $C_1 = 8.2\ \mu F$, $C_2 = 1\ \mu F$, $D_1, D_2 = 47$ V, $D_3, D_4 = 33$ V, $D_5, D_6 = 3.3$ V.

2.2.4 Polarization vs field loops

$P(E)$ loops were obtained by sweeping the voltage using a Tektronix FG504 Function Generator, allowing frequencies as low as 0.1 mHz to be studied. The sample current was measured with the Keithley 642 electrometer and integrated numerically. The electrometer's integration time (40 ms) imposes an upper frequency limit near 1 Hz.

2.2.5 Data acquisition and computer control

All instruments were connected to an IBM PS/2 Model 80 computer via an IEEE 488 bus, using the National Instruments MC-GPIB interface board and DOS Handler. Ad hoc programs were written to read data from the instruments and to set parameters such as the dc bias in capacitance-voltage measurements or the temperature set-point in pyroelectric experiments.

2.3 Sample preparation

The measurements presented in this thesis have been performed either on single crystals (Chapters 3, 4, and 5) or on epitaxial films (Chapter 6). Preparation of the latter by J. Mannhart is described in the chapter mentioned, but the treatment of the substrate surfaces is discussed here. Some of the $K_{1-x}Li_xTaO_3$ crystals were grown as part of this work, as explained below, whereas the $SrTiO_3$, $SrTiO_3$:Nb, and $Sr_{1-x}Ca_xTiO_3$ samples, grown by a zone-melting method,[25] were made available by J. G. Bednorz.

2.3.1 Growth of $K_{1-x}Li_xTaO_3$ crystals

Single crystals of $K_{1-x}Li_xTaO_3$ were grown in collaboration with M. Fazan and S. Rod at the Institut de Physique Expérimentale of the EPF Lausanne. The spontaneous nucleation technique was employed[26,27] in which the crystal grows in a K_2CO_3 flux according to the formula

$$Ta_2O_5 + (1 - x_i + 0.2)K_2CO_3 + x_iLi_2CO_3 \longrightarrow 2K_{1-x_f}Li_{x_f}TaO_3 + CO_2 + \ldots,$$

where the final concentration x_f is smaller than the ingot concentration x_i.[27]

Typically, the melt is first heated to ≈ 1350 °C in a platinum crucible, and then cooled slowly (≈ 0.5 °C/hour) to a temperature just below the melting point of $K_{1-x}Li_xTaO_3$ (depending on concentration, see Ref. 26), typically ≈ 1300 °C.

After removal of the remaining melt, the crystal is cooled to room temperature at a rate of typically 10–15 °C/hour.

For comparison, samples were obtained from other laboratories where they were grown from the same type of a melt but either by the Czochralski top-seeded solution growth or the accelerated crucible rotation technique (ACRT).[26]

The dielectric properties of $K_{1-x}Li_xTaO_3$ were found not to depend on the growth method to within experimental error.[28] Therefore, no distinction between samples of different growth methods will be made.[c]

The **Li concentration** of the samples is obtained by comparing their dielectric properties (in particular the $\varepsilon(T)$ curves measured at 1 kHz or 10 kHz) to those of standard samples, of which the Li-concentration has been determined by nuclear magnetic resonance (NMR).[27] It is estimated that the obtained values are correct to within $\Delta x = 0.002$.

---

[c] The following samples were grown by spontaneous nucleation at the EPF Lausanne: 0%, 3.3%, 5%, and 7%. The crystals with x = 1%, 2.5%, 4%, and 7% were grown by the Czochralski method, whereas the ACRT was used for the x =1.5%, 2.4%, 2.6%, and 3.4% samples.

2.3.2 Parallel-plate capacitor samples

For the measurement of the dielectric constant, parallel-plate capacitor samples were prepared as described here. [The $Pb(Mg_{1/3}Nb_{2/3})O_3$ sample studied in Chapter 5 was made available by R. Sommer (IPE-EPFL).]

Rectangular blocks are cut from the raw crystals, with the orientation determined to within $< 1°$ either by natural faces or by Laue diffraction. Polishing with diamond paste (1 μm grain size) on a soft plastic film (3M IR1940) yields optically smooth surfaces. The crystals are then cleaned by ultrasound in acetone, rinsed with isopropyl alcohol, and dried in a jet of nitrogen gas. Metal electrodes are deposited by evaporation from a heated tungsten filament. Typically, a 50-nm-thick gold layer was deposited on top of a 5-nm-thick film of chromium. Electrodes consisting only of gold show poor mechanical properties and yield irreproducible results in high-frequency ($f \geq 10^6$ Hz) measurements.

The size of the samples to be used in dielectric measurements is determined by the following two considerations: first, large sample capacitance yields a better signal-to-noise ratio; second, the doped samples have to be kept sufficiently small to ensure compositional homogeneity. Furthermore, Maglione[24] has shown that resonances can occur in these materials of large refractive index due to standing electromagnetic waves. To avoid resonances in the accessible frequency range, sample dimensions of the order of 1 mm × 1 mm × 1 mm are used from 1 MHz to 1 GHz, whereas samples of approximately 1 mm × 3 mm × 3 mm are employed at lower frequencies. In view of the high dielectric constant of the material, stray fields are not a problem, even with this apparently unfavorable geometry. Thinner samples ($d < 100\ \mu$m) are used in $\varepsilon(E)$ (section 3.2) and $P(E)$ (section 4.6) experiments to allow higher fields to be applied.

2.3.3 Surface etching

Chapter 3.2 will show that thin ($d < 100\ \mu$m) samples of $SrTiO_3$ exhibit degraded dielectric properties if prepared as described above. It is found that the bulk properties can be restored in these specimens by H_3PO_4-etching of the surfaces prior to electrode deposition. The procedure described here was applied to all samples with thicknesses below 100 μm, as well as to the $SrTiO_3$:Nb substrates used for $SrTiO_3$ film growth. The polished and cleaned crystals are mounted in a basket made of platinum wire and immersed in 85% H_3PO_4 at 100 °C for 10 minutes. Temperatures above 150 °C result in opaque surfaces, whereas etching at less than 70 °C results in no measurable change of the crystal's dielectric properties. To remove phosphates, the sample is then transferred to concentrated HCl (25 °C, 10 minutes), and cleaned in boiling deionized water (10–20 minutes). After rinsing in running deionized water for approximately 1 hour, the crystal is dried in a jet of nitrogen gas.

Before and after etching, some of the surfaces were analyzed with a commercially available atomic force microscope (AFM) using optical beam deflection to monitor

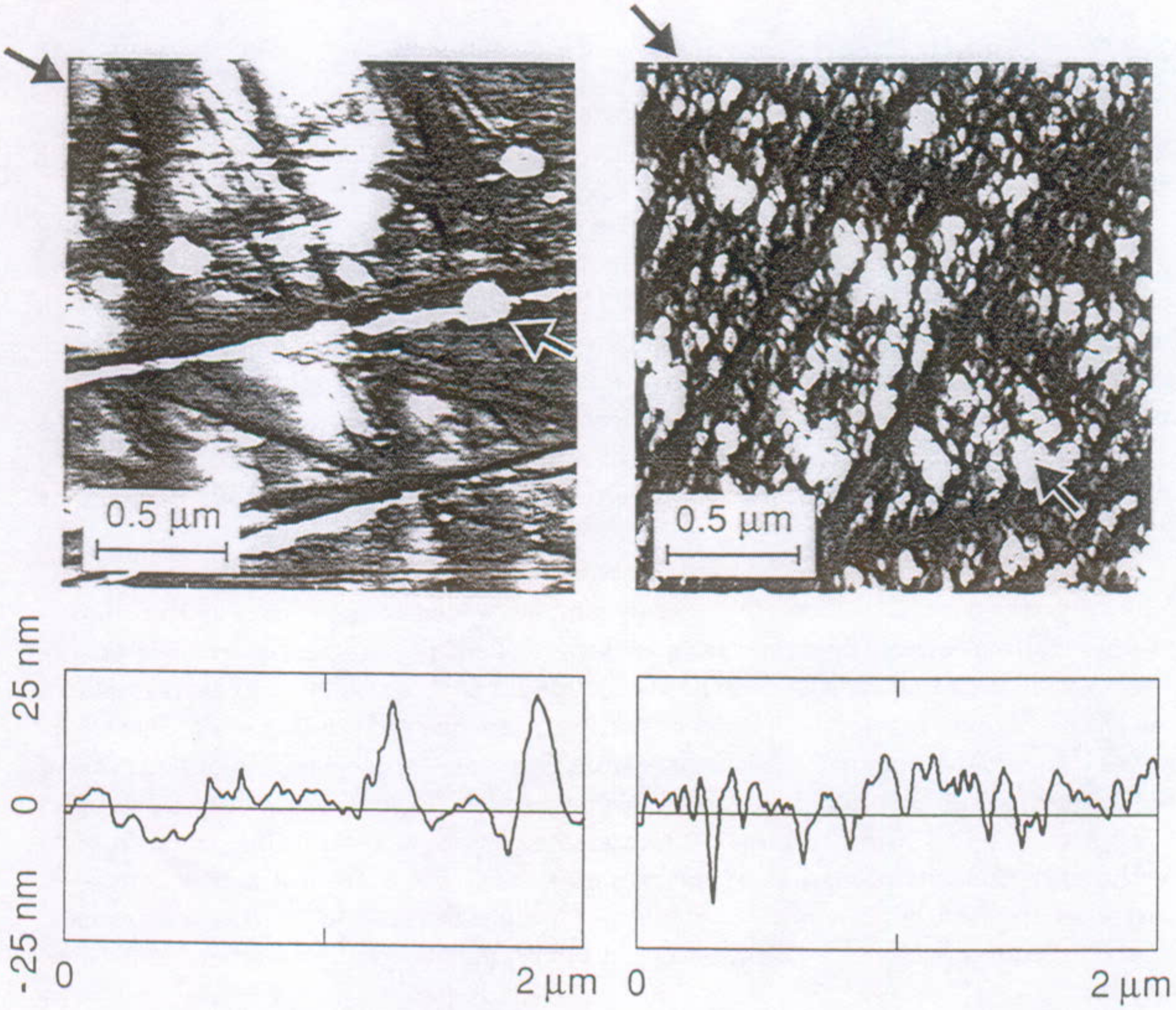

Figure 2.3 Atomic force microscope image and height profile of (left) a polished and (right) a polished and etched ⟨100⟩-oriented surface of SrTiO$_3$:Nb. Arrows in the micrographs indicate the position of the cuts represented as height profiles beneath the images. Microscopy performed by Ch. Gerber.

the displacement of a microfabricated Si$_3$N$_4$-type cantilever. As an example, these images are shown in Fig. 2.3 for SrTiO$_3$:Nb. Scratches with a typical depth of ≈ 10 nm were incurred through polishing and are visible as dark traces across the images both before and after etching. This indicates that less than 1 μm of the material is removed by the acid. The roughness of the etched surface was 5.5 nm (rms) compared to the 3.9 nm (rms) of the unetched crystal. However, the latter shows individual hillocks with heights exceeding 20 nm, which are removed by etching.

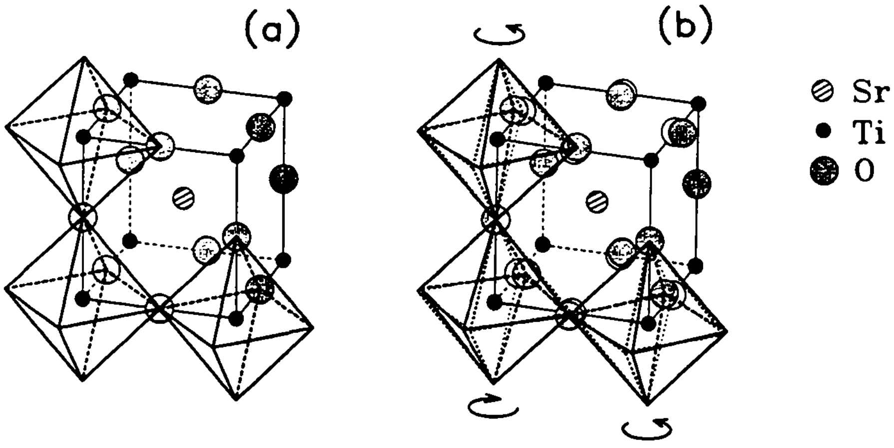

Figure 3.1 Crystal structure of $SrTiO_3$ (a) above and (b) below the antiferrodistortive phase transition. Arrows indicate the sense of rotation of the oxygen octahedra. The rotation angle reaches 2 degrees at the lowest temperatures.[30]

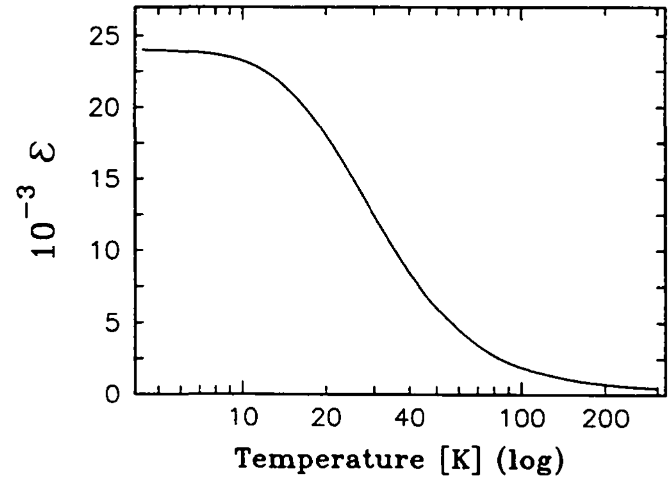

Figure 3.2 Dielectric constant of a ⟨100⟩-oriented $SrTiO_3$ single crystal, strontium titanate as a function of the logarithm of temperature. Test signal: 50 mV, 10 kHz.

3. Dielectric properties of $SrTiO_3$ and $KTaO_3$

Section 3.1 reviews literature regarding dielectric properties of $SrTiO_3$ and $KTaO_3$. Section 3.2 describes experiments performed on single-crystal samples. The resulting quantitative description of the field and temperature dependence of the dielectric constant will be used in Chapter 4 to understand the properties of impurity-impurity interactions in a $KTaO_3$ host lattice, as well as in Chapter 6 to model the behavior of $SrTiO_3$ films.

3.1 General description

$SrTiO_3$ and $KTaO_3$ are well-studied perovskites. $KTaO_3$ has the cubic structure, as shown in the introduction, Fig. 1.1, at all temperatures investigated.[29] $SrTiO_3$ undergoes an antiferrodistortive transition at 105±5 K from a cubic (above) to a tetragonal state (below). This transition consists of a rotation of the oxygen octahedra surrounding the Ti ions around the c-axis, as shown in Fig. 3.1.[30] In our measurements of $\varepsilon(T)$ however, this transition is not observable. (See Fig. 3.2.) Instead, the dielectric constants of both $SrTiO_3$ and $KTaO_3$ follow Curie laws $\varepsilon \propto (T - T_c)^{-1}$ for temperatures $\gtrsim 60$ K, with Curie temperatures T_c lying in the range of 30–36 K[1,31] for $SrTiO_3$ and 5–13 K[4,32] for $KTaO_3$.

In the low-temperature quantum paraelectric state, the dielectric constant of $SrTiO_3$ saturates at a value of $\sim$ 24 000 (Fig. 3.2). Its temperature dependence approximately follows the Barret[33] expression, with a more precise description being obtained in an approach taking into consideration the coupling of the ferroelectric soft mode to the acoustic modes.[1]

The frequency dependence of the dielectric constant is determined by the Lyddane-Sachs-Teller mechanism, thus ε is frequency-independent up to the gigahertz range.

3.2 Measurement of $\varepsilon(E)$

Modelling the dielectric behavior of $SrTiO_3$ thin films (Chapter 6) requires a quantitative description of the field dependence of the dielectric constant. While qualitative results can be found in the literature, the required numerical values are not available. Thus, experiments were performed on ⟨100⟩-oriented single-crystal samples of $SrTiO_3$ and $KTaO_3$. (The results regarding the latter will be used in Chapter 4.) In the course of these experiments, it became clear that the effects need to be separated into extrinsic phenomena (such as surface layers and charge injection) and intrinsic phenomena (due to the anharmonic behavior of the ions in the crystal lattice).

3.2.1 Extrinsic field dependence

a) Formation of a space charge layer

The dielectric constant of $SrTiO_3$ and $KTaO_3$ was determined on parallel-plate capacitor samples from measurements of the capacitance as a function of an applied voltage bias. In these experiments, the dielectric constant is seen to fall off sharply as the voltage was swept to higher values (see Fig. 3.3). When the applied bias is then removed, the sample capacitance does not return to its original value, but remains reduced by a factor of almost four. A similar behavior was previously observed on $KTaO_3$ (Ref. 32) and $SrTiO_3$.[34] Analoguous to earlier work on $KTaO_3$,[35]

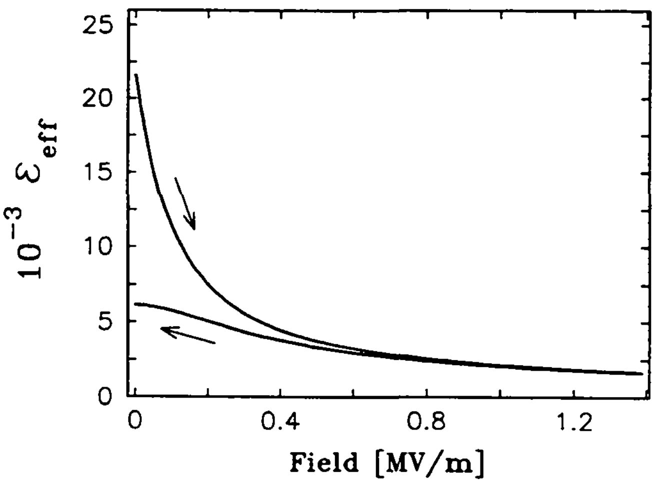

Figure 3.3 Dielectric constant of a $SrTiO_3$ single crystal, (thickness 70 μm), as the field is swept up to 1.4 MV/m and back to zero.

this phenomenon is interpreted as electron tunneling into the sample region near the electrodes, leading to the formation of a space charge layer. This layer then acts as a series capacitor with a reduced dielectric constant.

In the following, only results from first "up" sweeps are considered.

b) Surface preparation and sample thickness

In order to gain further insight into the above observations, crystals of different thickness and surface treatment are studied. Several samples were etched in phosphoric acid (as described in Chapter 2). Figure 3.4 compares the results of a measurement of the field dependence of the dielectric constant for etched and nonetched samples. Etched specimens exhibit a behavior that cannot (within experimental error) be distinguished from that of thicker crystals. On the other hand, the nonetched samples show a clear thickness dependence of the dielectric constant, similar to what is reported for $KTa_{1-x}Nb_xO_3$.[36]

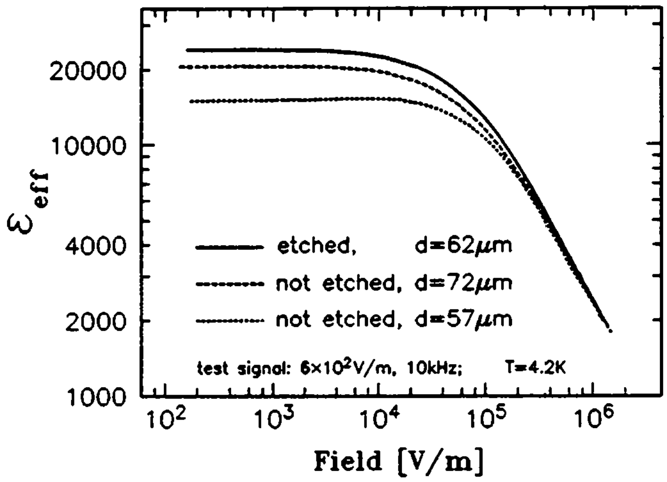

Figure 3.4 Field dependence of the dielectric constant of three $SrTiO_3$ single crystals as a function of thickness and surface treatment.

This reduction of the dielectric constant with decreasing sample thickness is interpreted as a consequence of a surface layer with decreased polarizability. Additionally, surface contaminants and individual hillocks are likely to lead to degraded metal/crystal contacts. These poor contacts and the assumed surface layer act as series capacitors, and their influence is strongest on the thinnest samples (i.e. on those with the highest capacitance). Therefore, thin ($d < 100$ μm) samples were only studied with etched surfaces.

3.2.2 Intrinsic field dependence

a) Measurement of $\varepsilon(E)$ at different temperatures

The above considerations have shown which precautions to take when studying the field dependence of the dielectric constant of $SrTiO_3$. Owing to the similarity of the two perovskites, $SrTiO_3$ and $KTaO_3$, the phenomena observed on $SrTiO_3$ are assumed also to influence the data for $KTaO_3$. However, since only qualitative results thereof will be used below, $KTaO_3$ has not been analyzed as extensively, but the same etching procedure is applied. Figure 3.5 shows the results of $\varepsilon(E)$ measurements at different temperatures for both materials.

b) $\varepsilon(E)$ in the Devonshire theory

In this section, results are recalled which have been published previously by a number of researchers. It is shown that the intrinsic field dependence of the dielectric constant of $SrTiO_3$ and $KTaO_3$ can be well described by the expressions resulting from the Devonshire theory.

Following the notation of Refs. 37 and 38, the Gibbs free energy is expanded into powers of the electrical polarization P in analogy to what was proposed by Devonshire[39] for barium titanate:

$$G = \frac{1}{2}\alpha(T)\,P^2 + \frac{1}{4}\beta(T)\,P^4 + \ldots - E\,P\,. \tag{3.1}$$

At thermodynamical equilibrium ($\partial G/\partial P = 0$), it follows that

$$E = \alpha(T)\,P + \beta(T)\,P^3 + \ldots\,. \tag{3.2}$$

In the following, all terms of the fifth and higher orders in P are neglected. The dielectric constant

$$\varepsilon(E) = 1 + \frac{1}{\varepsilon_o}\frac{\partial P}{\partial E} \tag{3.3}$$

can be approximated for low and high electric fields by the expressions

$$\varepsilon(E) - 1 = \begin{cases} \dfrac{1}{\varepsilon_o\,\alpha(T)} & \text{if} \quad E \approx \alpha(T)\cdot P \\ \\ \dfrac{1}{3\varepsilon_o\beta^{1/3}(T)}\,E^{-2/3} & \text{if} \quad E \approx \beta(T)\cdot P^3\,. \end{cases} \tag{3.4}$$

Thus $\varepsilon(E)$ tends to the value $\varepsilon_l = \lim_{E\to 0}\varepsilon(E) = 1 + (\varepsilon_o\alpha(T))^{-1}$ for low fields, and falls off at higher fields as $E^{-2/3}$. An exact expression for $\varepsilon(E)$ can be found [neglecting fifth and higher order terms in (3.2)] and is given in Appendix E.

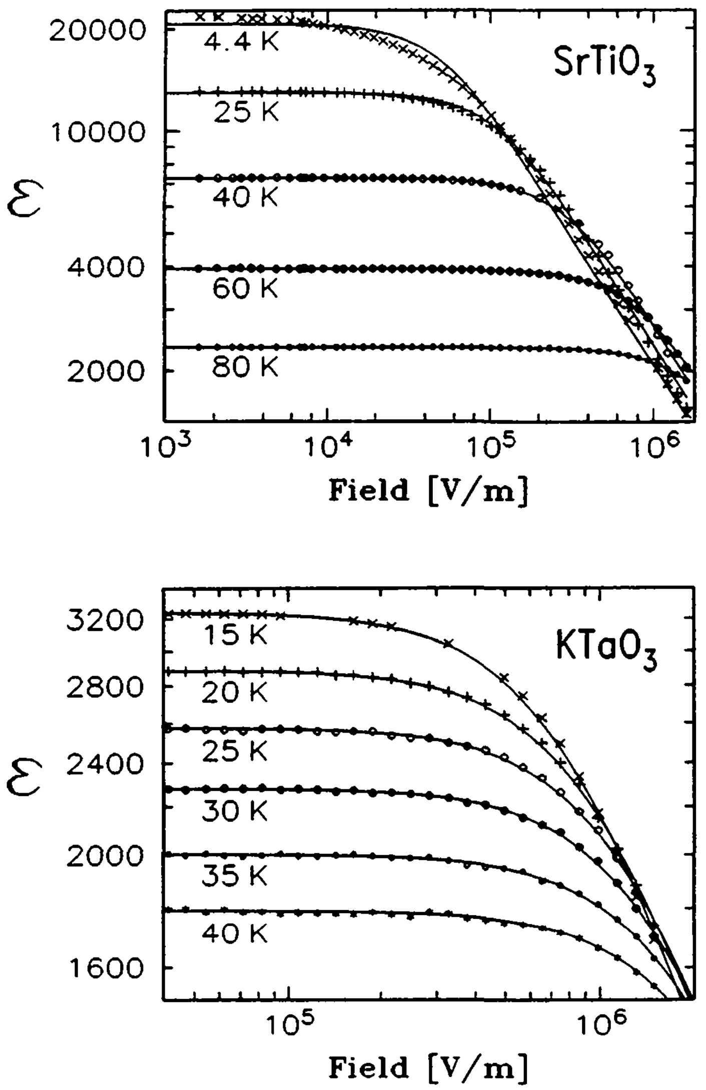

Figure 3.5 Dielectric constant of ⟨100⟩-oriented $SrTiO_3$ (top) and $KTaO_3$ (bottom) as a function of the applied electric field. Test signal: 50 mV, 10 kHz. Symbols are measurements, curves are fits using Eqs. (3.2) and (3.3).

c) Fit to data

The data in Fig. 3.5 are fitted using expressions (3.2) and (3.3). The agreement between the measurements (symbols) and the fit (solid lines) shows that in the investigated electric field range, fifth and higher order terms in (3.2) can safely be disregarded. The resulting fit parameters are shown in Fig. 3.6, indicating that the nonlinearity is most important at the lowest temperatures.

Using the parameters of Fig. 3.6, the complete dependence $\varepsilon(E,T)$ can be interpolated for all values of E and T lying in the experimentally studied range. For $SrTiO_3$, this is done in Fig. 3.7. It is clearly visible in this figure that the $\varepsilon(T)$ cuts [i.e. the curves $\varepsilon(T)$ obtained for a given applied field E] show a maximum at a temperature $T_{(\mathrm{max}\ \varepsilon(T))}$ which shifts to higher values for higher fields. The field dependence of this temperature is depicted in Fig. 3.8, providing a quantitative description of what has previously been qualitatively observed.[34,37,38]

d) Maximum attainable polarization in $SrTiO_3$

The maximum attainable polarization P_{max} in an insulating material is of technological interest as it determines the maximum of the electric charge storable in a device. In this section, P_{max} is determined using published data for the breakdown field.

Using the parameters $\alpha(T)$ and $\beta(T)$ from Fig. 3.6, a three-dimensional representation of $P(E,T)$ according to Eq. (3.2) can be given (Fig. 3.9). Similar to what has been observed above for the $\varepsilon(E,T)$ curves, the maximum polarization for a given field is not obtained at 4.2 K, but at a temperature which again depends on the value of the applied field. This temperature lies below $T_{(\mathrm{max}\ \varepsilon(T))}$, but exhibits a similar field dependence. The $P(E)$ curves at low temperatures show the expected curvature of the inverse of a cubic polynomial. At temperatures higher than ≈ 100 K they appear to be nearly linear, as predicted by the $\varepsilon(E)$ curves (Fig. 3.5).

Barret[40] has studied the dielectric breakdown on $SrTiO_3$ single-crystal samples with thicknesses ranging from 0.3 to 1 mm. Within experimental error, the breakdown field was seen to be temperature-independent, $E_{\mathrm{BD}} = (4 \pm 1)\times 10^7$ V/m. If this value is introduced into Eq. (3.2), a maximum polarization of $P_{\mathrm{max}} = 200 \pm 50$ mC/m^2 at 4.2 K and $P_{\mathrm{max}} = 100 \pm 30$ mC/m^2 at 300 K results. These values compare very favorably to other paraelectric insulators, including Si_3N_4 ($P_{\mathrm{max}} \approx 7$ μC/m^2),[41] and Ta_2O_5 thin films ($P_{\mathrm{max}} \approx 20$ mC/m^2),[42] but lie below the values of the spontaneous polarization in perovskite ferroelectrics such as $BaTiO_3$ ($P_S = 260$ mC/m^2) or $LiNbO_3$ ($P_S = 710$ mC/m^2).[43]

3.3 Summary

The dielectric properties of $SrTiO_3$ and $KTaO_3$ have been reviewed and complemented with new measurements. A quantitative description of the dependence

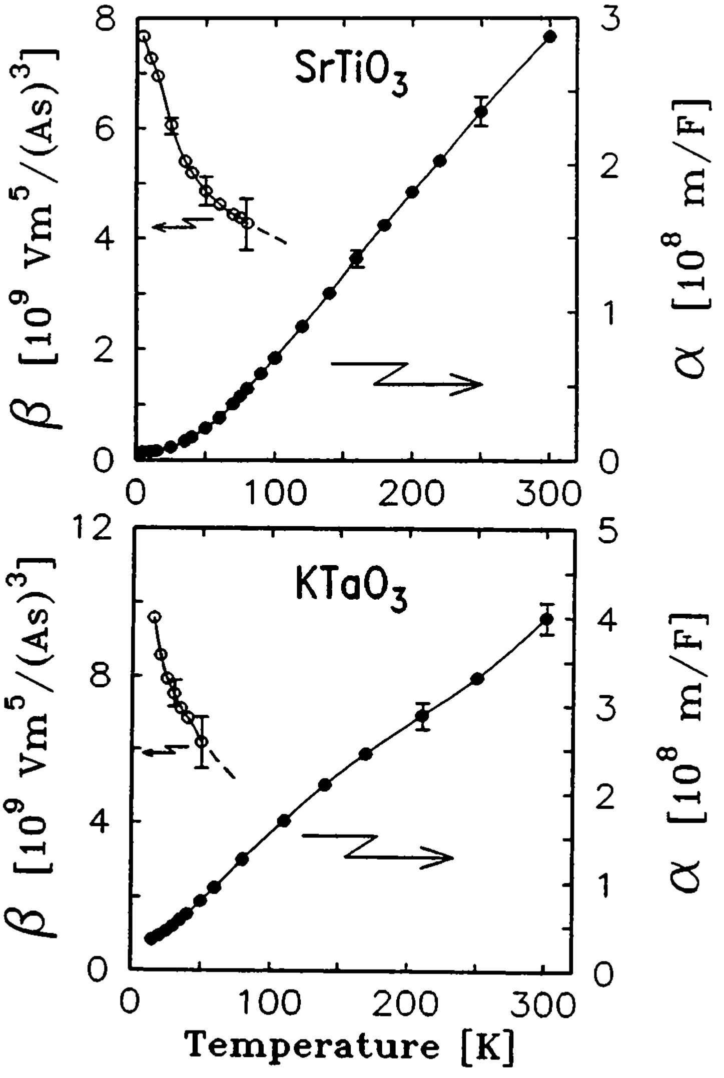

Figure 3.6 Parameters $\alpha(T)$ and $\beta(T)$ describing the field dependence of the dielectric constant of $SrTiO_3$ (top) and $KTaO_3$ (bottom) obtained from least squares fits for the data in Fig. 3.5. Note that the low-field dielectric constant, ε_l, is related to α by $\varepsilon_l = (\varepsilon_0\alpha)^{-1}$. As seen in Fig. 3.5, reasonable precision for the nonlinearity parameter can be obtained only at lower temperatures.

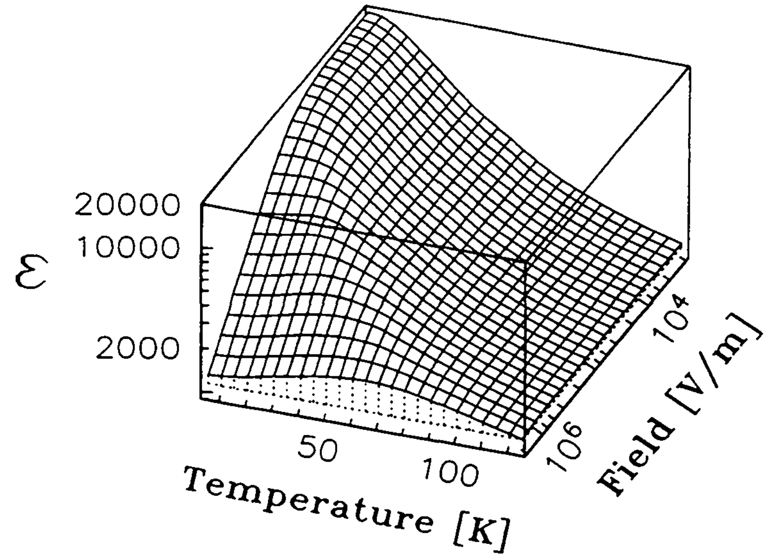

Figure 3.7 The dielectric constant $\varepsilon(E, T)$ of $\langle 100\rangle$-oriented $SrTiO_3$ as a function of the electric field E and the temperature T, calculated with Eqs. (3.2) and (3.3) and using the parameters in Fig. 3.6.

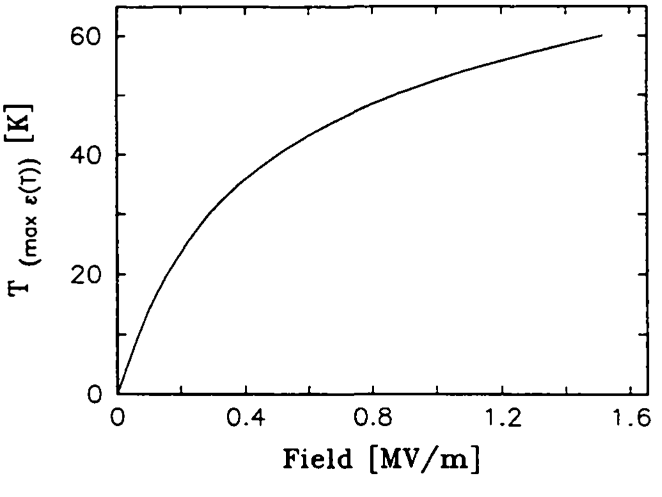

Figure 3.8 Field dependence of the temperature $T_{(\max\,\varepsilon(T))}$ at which the curve $\varepsilon(T)$ goes through a maximum.

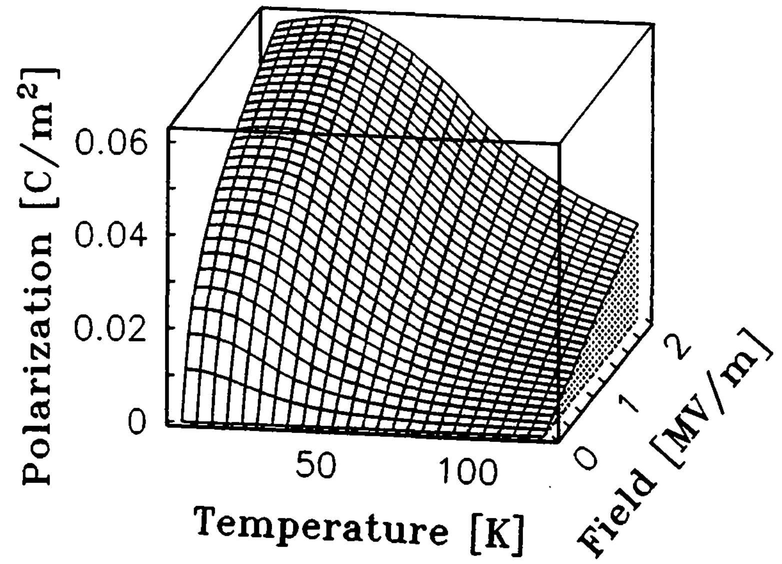

Figure 3.9 Polarization of $SrTiO_3$ as a function of temperature T and electric field E, calculated with Eq. (3.2) and the same parameters as used for Fig. 3.7. The maximum polarization for a given field is not obtained at 4.2 K, but at a temperature depending on the value of this field.

of the polarization $P(E,T)$ and the dielectric constant ε on an applied electric field $E(E,T)$ and on the temperature T was given. A high dielectric polarization $P_{\max} \approx 200\ \mathrm{mC/m^2}$ is expected to be obtained in $SrTiO_3$, rendering this material a promising candidate for applications in devices where a high charge density must be obtained.

4. Li-doped potassium tantalate

The mixed crystal system $K_{1-x}Li_xTaO_3$ is studied in the Li concentration range of $2.5\% \leq x \leq 4\%$.
Results of dielectric measurements (section 4.3) and a comparison thereof to various models (section 4.4), an analysis of field-induced pyroelectric currents (section 4.5), a comparison to some properties of $Sr_{1-x}Ca_xTiO_3$ (section 4.6), and a numerical study of the effective Li-Li-interaction energy (section 4.7) shed light on the relaxation mechanisms and ground state properties.
It is shown that the nanometer-sized dipolar-ordered microdomains have fundamentally different properties than ferroelectric domains.

4.1 Introduction

As mentioned in Chapter 1, the cubic lattice of the incipient ferroelectric $KTaO_3$ has little stability against polar distortions. A ferroelectric phase transition can be induced by mechanical stress,[44] and ferroelectric microregions with spatial dimensions reaching about 4 a (where $a = 3.99$ Å is the lattice constant) at 4.2 K were observed in nominally pure $KTaO_3$ (probably induced by unidentified defects).[45]

Different types of polar behavior are obtained by doping with isovalent impurities. As mentioned above, replacing tantalum with niobium leads to ferroelectricity, whereas doping with lithium or sodium results in a low-temperature state devoid of long-range polar order.

Lithium dopants replace potassium, and thus are surrounded by twelve oxygen ions (Fig. 4.1). As the ionic radius of lithium ($r_{\mathrm{Li}} = 0.68$ Å), Ref. 46, is considerably smaller than that of potassium ($r_{\mathrm{K}} = 1.33$ Å) the equilibrium position of this impurity is moved away from the centrosymmetric site by 1.3 Å along a $\langle 100 \rangle$ direction.[47] The situation is sketched in Fig. 4.2, where a cut through a $\{100\}$ plane containing one Li impurity is drawn. Of the six equivalent positions of the Li, the four that fall into this plane are shown (only one of these off-center sites is occupied by the Li). The large Li displacement leads to a strong local polarization of the region

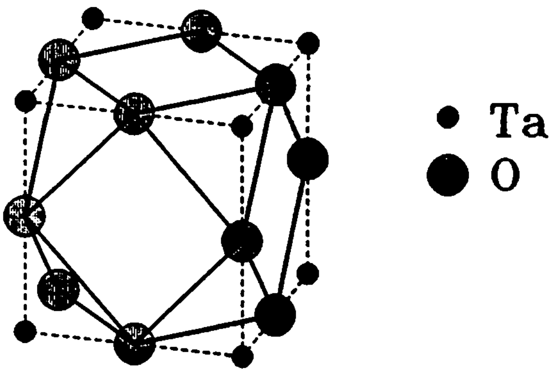

Figure 4.1 Crystal structure of $KTaO_3$. The solid lines connect the sites of the twelve oxygen ions surrounding the lithium (for clarity, the ions which are hidden by this polyhedron are not shown).

surrounding the impurity. Thus, the interaction between the impurities differs from that of classical dipoles, resulting in a polar character which has been investigated by numerous groups using various experimental techniques. Important results of these studies are reviewed in the following section.

In the high-temperature paraelectric state, the impurities move freely between the six off-center positions. A head-to-tail reorientation of a dipole, such as a change from a displacement along a [100] axis to one along a $[\bar{1}00]$, is called a π-flip, and a 90° change is referred to as a $^{\pi}/_{2}$-flip.

It is generally accepted that for concentrations below $x_c = 2.2\%$, the low-temperature state is disordered and can be described as an orientational glass. Above $x \approx 7\%$, ferroelectricity has been proposed, although clear evidence is lacking.[48,49,50]

In the concentration range of $x_c \leq x \leq 7\%$, a transition is observed at a concentration-dependent temperature T_f into a state resembling ferroelectrics in some respects and glasses in others.

Unfortunately, the ground state of these systems is experimentally inaccessible as the relaxation times of dipole motion exceeds laboratory time scales at low temperatures. Information about the mechanisms leading to the frozen state must be obtained from the system's behavior as it approaches the freezing temperature.

Therefore, dielectric measurements have been performed on $\langle 100 \rangle$-oriented samples in the concentration range of $2.5\% \leq x \leq 4\%$, where both relaxation branches,

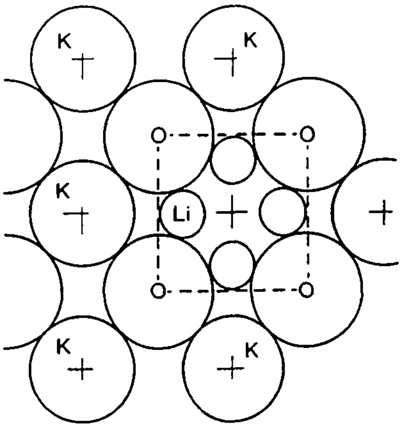

Figure 4.2 Cut along a {100} plane of $K_{1-x}Li_xTaO_3$. Drawing of ionic radii and crystal structure to scale. Only one of the Li sites shown is occupied.

corresponding to $\pi/2$- and to π-flips, are clearly observed. For comparison, several samples with higher concentrations were studied in much less detail.

Additional information is gained from numerical calculations of the Li-Li interaction energy (obtained in collaboration with R. Migoni and M. Stachiotti, University of Rosario, Argentina, and J. Kohanoff, University of Lyon, France).

4.2 Review of published experimental results

In this section, published experimental results are summarized for $K_{1-x}Li_xTaO_3$ samples in the concentration range of $x \lesssim 7\%$.

In view of the experimental difficulties related to the studies of static properties, we first focus our attention on the dynamics of relaxation associated with dipole reorientations. The largest amount of the respective experimental data comes from dielectric investigations[28,51,52] and is consistent with NMR,[53,54] ultrasound[55] and low-frequency shear modulus[56] results. The main characteristics can be summarized as follows:

The qualitative behavior of the dynamics is essentially independent of the Li concentration x for $x \lesssim 7\%$, and no signs of criticality are observed at any temperature, neither in the relaxation time nor in the relaxation step. This is an argument against the occurrence of a ferroelectric phase transition in these samples. Relaxation can occur via $\pi/2$- or by π-flips between two of the six equivalent Li-positions. The relaxation time of the latter is several orders of magnitude larger than that of the former. However, the faster $\pi/2$-flips are associated with an important elastic contribution and become inhibited below a temperature called T_f. Below T_f, the still detectable, faster $\pi/2$ branch contributes only insignificantly to the relaxation, because the number of impurities for which the $\pi/2$-flips are not hindered by elastic interactions becomes negligible. Therefore, the dynamics seems to exhibit a jump-like slow-down at T_f, as motion is now restricted to the much slower π-flips.

The temperature T_f is related to the Li concentration by $T_f = 535 \cdot x^{2/3}$K,[57] but the energy barriers governing the relaxation times are essentially concentration-independent. These barriers are distributed and lead to strongly polydispersive relaxation.[6]

Attempts to measure the magnitude of the electrical polarization have revealed the absence of spontaneous polarization in zero-field-cooled samples[57] and nonergodicity[58] in much the same manner as in spin glasses.[59] Thus, the terms "polar glass" [6] and "orientational glass" have been used to describe $K_{1-x}Li_xTaO_3$.[a]

The study of correlations is complicated by the existence of two correlation functions with different spatial extent; namely a dipolar correlation length ξ_d, defined as the size of the region in which dipoles are parallel to one another, and a quadrupolar correlation length ξ_q defined in the corresponding way for quadrupoles. Thus, ξ_d defines the size of dipolar-ordered, and ξ_q that of quadrupolar-ordered microdomains. It is seen that a quadrupolar-ordered microdomain, which can reach macroscopic dimensions at higher concentrations as determined from birefringence[60,61] and neutron scattering[62] results, consists of a number of dipolar-ordered microdomains. The size

---

[a] A distinction between "dipolar" and "quadrupolar" glass has been made[8] based on the observation that in typical relaxation experiments, the $\pi/2$ (π) branch is mainly visible in samples with concentrations lower (larger) than 3–4%. However, this distinction is seen as a consequence of the experimental frequency window rather than of a fundamental physical difference.

of the latter is concentration-dependent: it grows from 6 nm at 1.6% to 23 nm at 6% as found by second-harmonic generation[63] and microwave-induced Brillouin scattering results[64], and remains temperature-independent below T_f. Long-range order is thus absent in zero-field-cooled samples with $x \lesssim 7\%$.

Experiments on field-cooled samples have lead to the definition of a "critical" concentration $x_c \approx 2.2\%$ based on dielectric,[65,66] ultrasonic[67] and second harmonic generation[68] data. Field-cooled samples with $x_c \leq x$ show anomalies in the respective properties' temperature dependences, but exhibit no long-range order. Terms such as "domain-state-like"[65] or "disordered ferroelectric"[67] are sometimes used to describe the low-temperature state of samples with $x_c \leq x \leq 7\%$, where true long-range order is still absent.

Zero-field cooled $K_{1-x}Li_xTaO_3$ samples are never in thermal equilibrium because reorientation of impurities below T_f exceeds a typical experimental time scale of 1 hour, for example, on samples with concentrations $\lesssim 4\%$ (1 year for $x \approx 3\%$). This means that a domain or the polarization within a domain will not have time to grow upon cooling. Therefore, experiments are always performed in the quenched state, particularly on lower-concentration samples. It has been proposed[69] that this is the only — but essential — difference in the macroscopic behavior of $K_{1-x}Li_xTaO_3$ and ordinary ferroelectrics. However, no ferroelectric hysteresis cycles have been revealed for $K_{1-x}Li_xTaO_3$ at any concentration. In addition, fundamentally different characteristics on a microscopic scale are suggested by the fact that the relaxation time in $K_{1-x}Li_xTaO_3$ is about 10^8 times that of $KTa_{1-x}Nb_xO_3$,[70] a ferroelectric with a similar transition temperature.

4.3 Dipole relaxation: Experiments

The dynamics of dipole relaxation is investigated over a 12-decade frequency interval (10^{-3} Hz $\leq f \leq 10^9$ Hz) for temperatures 20 K $\leq T \leq$ 200 K using depolarization current (section 4.3.1) and capacitance/conductance measurements (section 4.3.2). The data are parametrized by least squares fits using the Debye-Wagner (Gaussian) or a double Gaussian distribution of relaxation times $G(\ln \tau)$, or the Kohlrausch-Williams-Watts (stretched exponential) decay function. The temperature dependence of the fit parameters is obtained.
Comparison to various models of dielectric relaxation will be made later (section 4.4).
Part of the results presented in this section are published in "Random-Barrier and Hierarchical Relaxation in $K_{1-x}Li_xTaO_3$," H.-M. Christen, U. T. Höchli, A. Châtelain, and S. Ziolkievicz, *J. Phys.: Condens. Matter*, **3**, 8387 (1991).

The dynamics of dipole relaxation is studied by the use of dielectric measurements both in the time (depolarization currents) and in the frequency domains [frequency dependence of the dielectric constant $\varepsilon(\omega)$]. From a mathematical point of view, the two techniques are identical for a linear system, and their results are related by Fourier transforms. (Appendix A lists the corresponding equations and states the necessary conditions for the equivalence, and section 4.3.2 gives the experimental verification thereof.)

The experimental setup used to obtain the results presented here was described in Chapter 2 (page 13).

As outlined above, various aspects of dielectric relaxation in $K_{1-x}Li_xTaO_3$ have been studied over the past 10–15 years by a number of groups. In the present work, the largest presently available frequency window (12 decades) is used to obtain a more complete characterization of the observed phenomena. In particular, the high resolution achieved with the GR1616 bridge (see section 2.2) for the imaginary part of the $\varepsilon(\omega)$ allows previously unnoticed features to be detected and studied in detail. These measurements lead to a new and consistent interpretation of present and earlier results.

The present analysis of the $i(t)$ and $\varepsilon(\omega)$ data in terms of various empirical relaxation functions goes well beyond the published parametrization of such data. For clarity, the physical significance of the expressions used is explained in a later section. At this point, they are introduced merely as a mathematical tool for data parametrization.

4.3.1 Observations in the time domain

In this section, the results of depolarization current measurements are presented. It is recalled (see section 2.2) that these currents are recorded after removal of a dc bias which had been applied to a zero-field-cooled sample. Typical charging time are chosen between 3 and 10 times the measurement time (see Appendix A for a discussion of the effect of the charging time). Between any two measurements, the sample is heated to well above the measurement temperature in order to release residual charges on the sample.

To begin the presentation of experimental results, data obtained on a $K_{0.967}Li_{0.033}TaO_3$ sample are considered. Results for this concentration will be shown wherever possible, because they allow both relaxation branches to be observed in the time domain as well as in the frequency domain.

The results are displayed in Fig. 4.3 for temperatures between 25 and 70 K, obtained with a charging field of $E_O = 10^4$ V/m. The shape of the currents shows that they do not correspond to a simple exponential decay of the polarization, which would be characterized by a zero slope of the $\log i(\log t)$ curves for the lowest values of t. For the sake of argument, it can be assumed that the current is described (or approximated) by a distribution of relaxation times $G(\ln\tau)$ so that, for $t > 0$,

$$i(t) = \varepsilon_O E_O \Delta\varepsilon \int_{-\infty}^{\infty} G(\ln\tau) \frac{e^{(-t/\tau)}}{\tau} d\ln\tau, \tag{4.1}$$

where the relaxation step $\Delta\varepsilon$ measures the strength of the relaxation branch, i.e. the polarizability resulting from the mechanism under investigation [see Eqs. (A.22)–(A.25) and (A.38) of Appendix A]. It is recalled that Eq. (4.1) is introduced merely as a mathematical tool. As shown on page A-18, a distribution $G(\ln\tau)$ can be approximated by

$$G(\ln\tau) \propto t \cdot i(t)$$

for wide relaxation time distributions. A plot of $\log\{t \cdot i(t)\}$ vs $\log(t)$ is displayed in Fig. 4.4 (showing the same data as presented in Fig. 4.3). The two relaxation branches are clearly distinguishable. They are labelled "LF" (low frequency) and "HF" (high frequency), where the LF (HF) branch can be observed at longer (shorter) times in the $i(t)$ curves at a given temperature, thus at lower (higher) frequencies in the $\varepsilon(\omega)$ experiments. By comparison to acoustic measurements[b] (see section 4.2 above), the HF branch can be attributed to the $\pi/2$-flips, and the LF branch to the π-flips.

In order to quantitatively as well as qualitatively compare various sets of data such as those presented in Fig. 4.3, a parametrization of the curve is required, yielding parameters for which the temperature dependence can be studied.

---

[b] The comparison with the ultrasound experiments (which probe the change of a quadrupolar moment and are thus insensitive to π-flips) is made on the basis of the position of the relaxation peaks in the frequency-temperature plane.

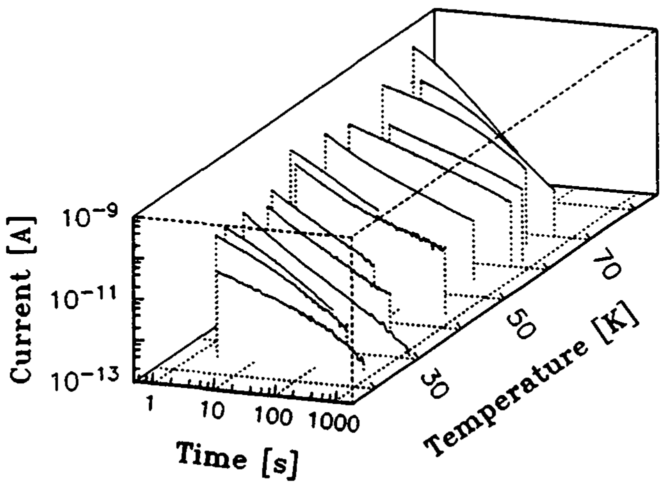

Figure 4.3 Depolarization current measurement at various temperatures for a $K_{0.967}Li_{0.033}TaO_3$ sample in a log(current) vs log(time) representation.

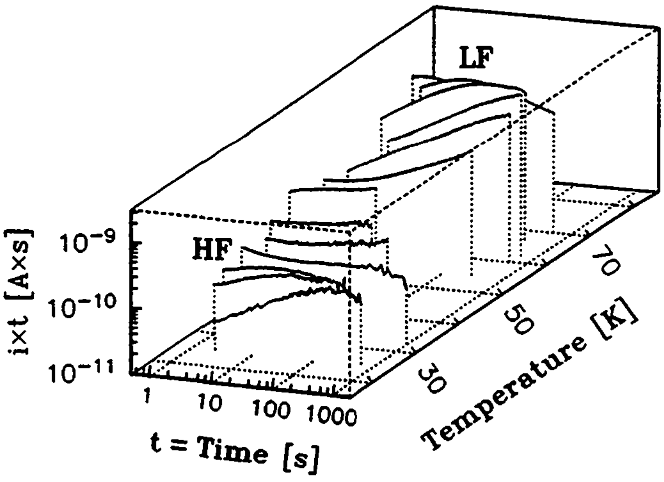

Figure 4.4 Data from Fig. 4.3 for $K_{0.967}Li_{0.033}TaO_3$ plotted in a log(current×time) vs log(time). The two relaxation branches are distinguishable in this representation, and are labelled "LF" and "HF".

To this end, the data are fitted using different empirical relaxation laws. The physical significance of these expressions will be discussed in a later section (4.4).

As pointed out above, a simple exponential time dependence of the depolarization current does not agree with the data. Therefore, the following two generalizations are considered:

1. **The DW(Debye-Wagner) expression,** i.e. a linear superposition of simple exponential (Debye) relaxations [Eq. (4.1)] with a log-Gaussian distribution of relaxation times (as first proposed by Wagner[71] [see Appendix A, Eq. (A.39)]:

$$G(\ln\tau) = \frac{1}{\sqrt{\pi}\Delta}\exp\left\{-\left[\frac{\ln\tau - \ln\tau_o}{\Delta}\right]^2\right\}. \tag{4.2}$$

   This Gaussian is centered at $\ln\tau_o$ and has a standard deviation of $\Delta/2$.

2. **The KWW(Kohlrausch-Williams-Watts) expression,** i.e. a stretched exponential dependence for the decay of polarization, $P(T) \propto \exp\{-(t/\tau_0)^\beta\}$, where τ_o is a characteristic time, and β the stretching variable. This expression was first proposed by Kohlrausch,[72] and became widely used in dielectric spectroscopy after the work of Williams and Watts.[73,74] From Eqs. (A.22) and (A.50), the depolarization current is written

$$i \propto t^{\beta-1}\exp\{-(t/\tau_0)^\beta\}, \qquad 0 < \beta \le 1. \tag{4.3}$$

More details about these expressions, and a discussion of functions not employed here, are given in Appendix A.

The curves in Fig. 4.3 that correspond to the LF relaxation branch (π-flips) have been fitted to both of the above expressions. Results for curves at selected temperatures are shown in Fig. 4.5. HF branch data have not been analyzed in this way for reasons that will become apparent in section 4.3.2.

In order to compare the quality of the fits for each of the above expressions, the quantity χ^2 is defined

$$\chi^2 = \min_{\{a_i\}} \sum_{i=1}^{N} \left(\frac{i_i^{\text{meas}} - i^{\text{calc}}(t_i, \{a_i\})}{i^{\text{calc}}(t_i, \{a_i\})} \right)^2, \tag{4.4}$$

i.e. the "chi-square"[75] for the set of parameters $\{a_i\}$ for which it reaches its minimum value. Here, $i_i^{\text{meas}}(t_i)$ are the experimental data points, and the values $i^{\text{calc}}(t_i, \{a_i\})$ are calculated with the set of parameters $\{a_i\}$.

A smaller value of χ^2 corresponds to a better agreement between data and calculated curve. Figure 4.6 compares these "chi-square" values for the LF data of Fig. 4.3. Results for $\varepsilon(\omega)$ curves presented in section 4.3.2 below are also included (data points for $T > 80$ K). It is seen that at lower temperatures, the data are better described by the KWW expression.

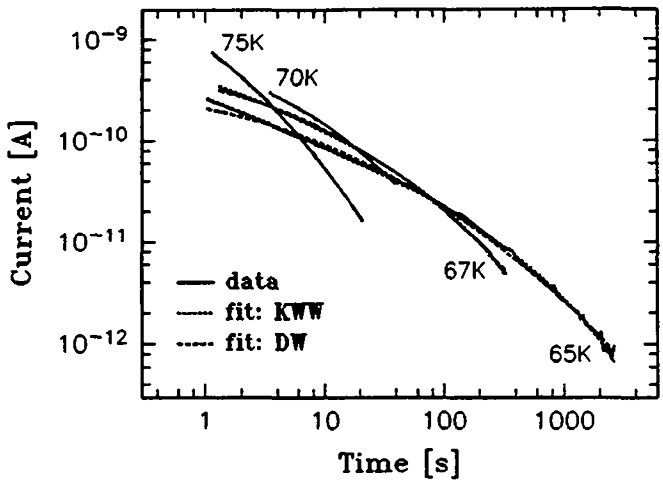

Figure 4.5 Depolarization current measurements (solid curves) for $K_{0.967}Li_{0.033}TaO_3$ (data from Fig. 4.3), and fits to the DW (dashed) and the KWW expression (dotted curve, largely covered by the data). Charging field: 10^4 V/m.

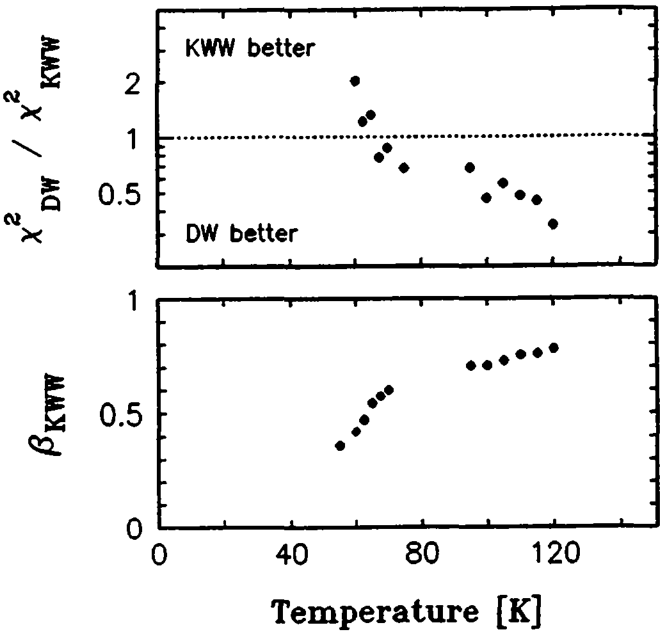

Figure 4.6 Top: Comparison of the "chi-square" values of fits to data of $K_{0.967}Li_{0.033}TaO_3$.
Bottom: KWW fit parameter β for the same sample.

4.3.2 Observations in the frequency domain

a) Test of experimental setup and linearity

Different measurement techniques have been used in the frequency domain (see Chapter 2). In order to show that the respective results agree well with each other, measurements were performed on a $K_{0.967}Li_{0.033}TaO_3$ sample using the GR1616 radio frequency bridge at the IBM Rüschlikon laboratory and the experimental setup of the University of Mainz. The results are compared in Fig. 4.7. The almost perfect overlap shows the precision obtained for the ε'' measurement. In addition, it is seen that the temperature determination agrees to within about 0.5 K for the two experimental setups.

As pointed out above, the system's response must be linear for the equivalence between the $\varepsilon(\omega)$ and the $i(t)$ data to hold. The Kramers-Kronig expression (described in section A.2), relating ε' and ε'', can be used to test this assumption, and to verify that dc conductivity does not perturb the measurements. Experimental results for ε' have thus been numerically transformed into ε'', and are compared to the measured ε'' values. As can be seen in Fig. 4.8, calculated and measured values agree to within experimental error, showing that the above criteria are satisfied.

b) Measurements

Measurements in the frequency range of 10^{-2} Hz $\leq f \leq 1$ GHz have been performed on several samples in the concentration range of $2.5\% \leq x \leq 4\%$. Detailed measurements were restricted to the temperature and frequency range where dielectric relaxation is visible. Measurements at higher frequencies were thus typically performed at higher temperatures. In Fig. 4.9, a three-dimensional plot of the imaginary part of the dielectric permittivity as a function of both temperature and frequency is given. The data shown correspond to the HF relaxation branch. In this representation, the interesting low-temperature behavior of these curves is clearly visible.

In order to show both the HF and the LF branch in one drawing, the temperature-scale is changed in Fig. 4.10. Permittivity data for both relaxation branches are shown. In addition, curves are traced using the DW fit parameters obtained from the depolarization current data in Fig. 4.3.[c] With this, Fig. 4.10 displays in one common representation the data obtained from time-domain ($f < 1$ Hz) and frequency-domain measurements (10^{-2} Hz $\leq f \leq 10^4$ Hz: Chelsea Dielectric Interface; 10 Hz $\leq f \leq 10^5$ Hz: General Radio GR1616 Bridge; 10^5 Hz $\leq f \leq 10^6$ Hz: Boonton 75A Bridge; and 10^6 Hz $\leq f \leq 10^9$ Hz: HP4191A Impedance Analyzer).

---

[c] The DW function has been used rather than the KWW expression, because the temperature-interval over which a fair agreement between fit and data is reached is larger for the DW expression.

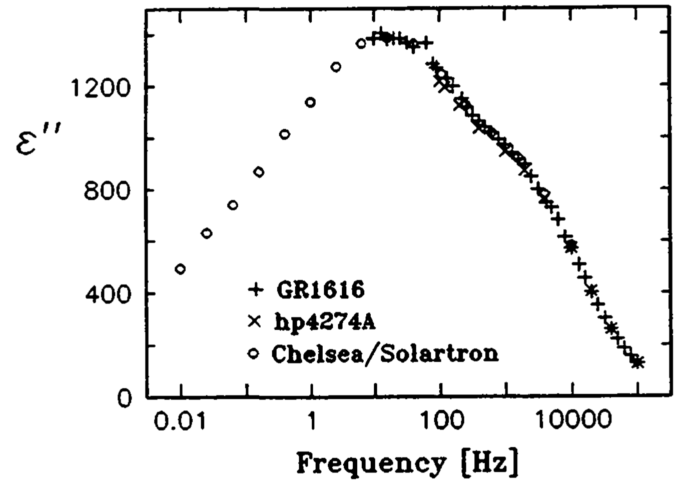

Figure 4.7 Comparison of ε'' data for a $K_{0.967}Li_{0.033}TaO_3$ sample at 50 K, obtained with various experimental techniques at the IBM Rüschlikon laboratory (using the GR1616) and the University of Mainz.

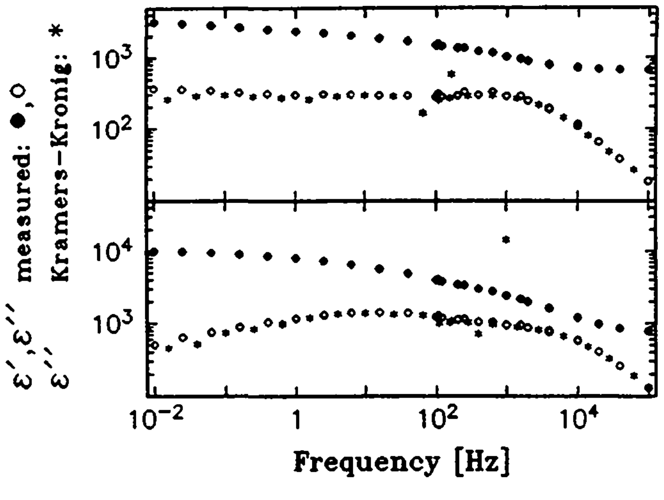

Figure 4.8 Comparison of experimental values for ε'' (open circles) to those calculated (stars) from the experimental ε' data (solid circles) using the Kramers-Kronig relation.

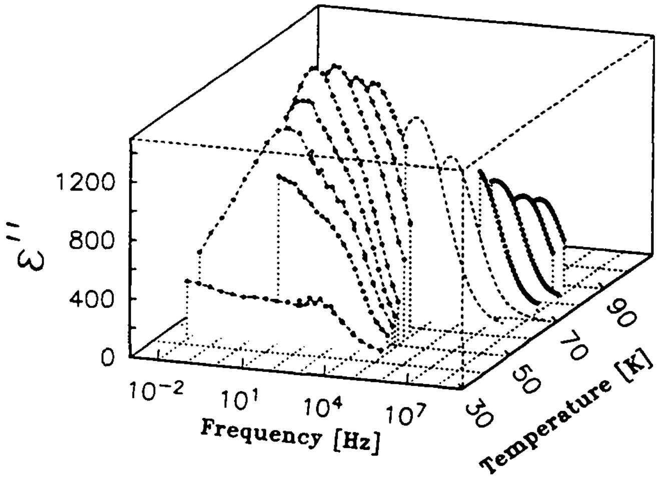

Figure 4.9 Imaginary part of the dielectric permittivity, ε'', as a function of frequency at various temperatures for $K_{0.967}Li_{0.033}TaO_3$. Only data corresponding to the HF branch are shown. Dots are measurements, dashed curves are interpolations to guide the eye.

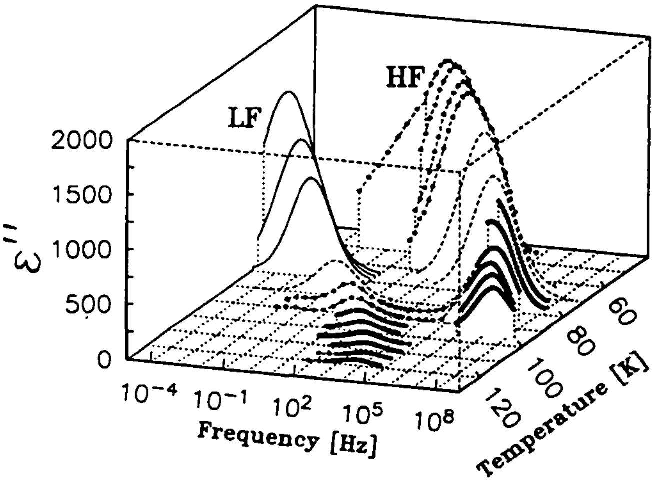

Figure 4.10 Data of Fig. 4.9 in a different representation, together with LF branch results. Solid lines are obtained from the DW fit parameters of the $i(t)$ data taken from Fig. 4.3.

c) Parametrization

The ε'' data of the **LF branch** ($T > 80$ K) show symmetric peaks which can be fitted by the DW expression [Eq. (4.2)]. As was shown in Fig. 4.6, data of the same branch but at lower temperatures ($T \leq 80$ K) are, in contrast, better described by the KWW expression.

For the **HF branch**, however, close inspection shows that the dispersion curves exhibit a more complex structure than those of the LF branch. Fits to the KWW and DW expressions, shown in Fig. 4.11 for the $K_{0.974}Li_{0.026}TaO_3$ sample, are very unsatisfactory. To improve the quality of the fits, a superposition of two Gaussian curves can be used. The characteristic quantities of this distribution are the mean relaxation time τ_o, the width Δ, and the relaxation step $\Delta\varepsilon$. [$\Delta\varepsilon = \varepsilon'(f_-) - \varepsilon'(f_+)$,

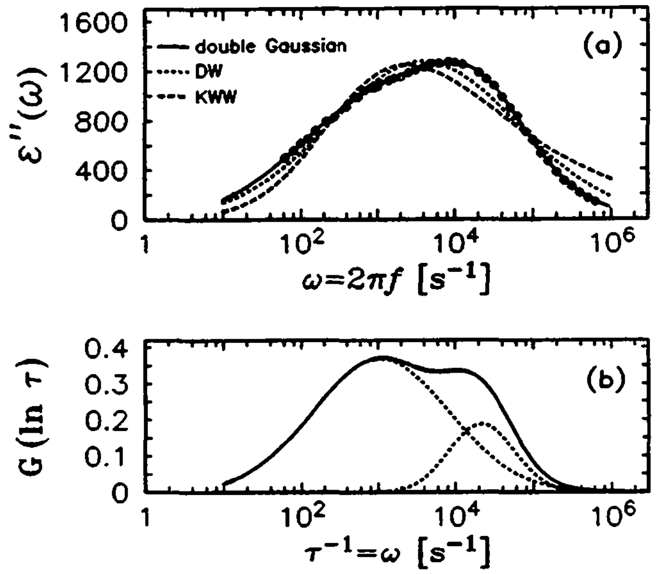

Figure 4.11 (a) Comparison of fits for the HF branch in the sample $K_{0.974}Li_{0.026}TaO_3$ at 50 K. The broken curve is the best fit of the KWW expression and the dotted curve is the fit of the DW function to ε'' data. The full curve is the best fit of a distribution of relaxation times given by a superposition of two log-Gaussian curves. (b) These two Gaussian curves are plotted against $\log(1/\tau)$ (dotted curves), together with the resulting distribution $G(\ln\tau)$ (full curve).

Table 4.1: Fit parameters for $K_{0.975}Li_{0.025}TaO_3$ and $K_{0.967}Li_{0.033}TaO_3$. ν_0 is the attempt frequency, E_b the barrier height (Eq. 4.5). The parameter α describes the temperature dependence of Δ (Eq. 4.6).

Relaxation branch	Parameter	2.5%	3.3%
LF	$\log_{10} \nu_0/\mathrm{s}$	14.4 ± 0.3	14.7 ± 0.1
	E_b [K]	2500 ± 300	2600 ± 100
HF	$\log_{10} \nu_0/\mathrm{s}$	13.5 ± 0.2	14.6 ± 0.2
	E_b [K]	1100 ± 200	1400 ± 200
LF + HF	α	1.7 ± 0.1	1.1 ± 0.2

where f_- (f_+) are defined as frequencies lying well below (above) the interval over which the relative relaxation branch is observed (see also Fig. A.3 of Appendix A for a definition of $\Delta\varepsilon$).] The equations relating τ_o, Δ, and $\Delta\varepsilon$ to the six fit parameters (namely, the mean relaxation times, the widths and the relaxation steps corresponding to each individual Gaussian) are given in Appendix B.

The temperature dependence of these parameters together with the DW fit parameters for the depolarization currents (Fig. 4.3) are shown in Figs. 4.12 and 4.13 for the two samples $K_{0.975}Li_{0.025}TaO_3$ and $K_{0.967}Li_{0.033}TaO_3$.

The values of the mean relaxation time, $\tau_o(T)$, are plotted in Fig. 4.12(a) on a logarithmic scale versus the inverse temperature. In this so-called Arrhenius representation, a straight line corresponds to

$$\tau_o{}^{-1} = \nu_0 \exp(-E_b/T), \tag{4.5}$$

where ν_0 is generally called "attempt frequency," and E_b is an energy (measured in Kelvin). These parameters are shown in Table 4.1.[d]

Figure 4.12(b) shows the width of the distribution of relaxation times as a function of temperature. Surprisingly, the data for the LF and HF branches fall on one curve. This temperature dependence can be approximated by

$$\Delta \propto T^{-\alpha} \qquad \text{with} \quad \alpha > 1. \tag{4.6}$$

---

[d] In a simple double-well-potential model, ν_0 corresponds to the oscillation frequency of a particle in one of the two wells and E_b is the height of the energy barrier separating the two wells. It is noted here that ν_0 takes a value typical of phonon frequencies, and that the values of the energy barriers (100–200 meV) are of the same order of magnitude as the Li-Li interaction energies calculated below, section 4.7.

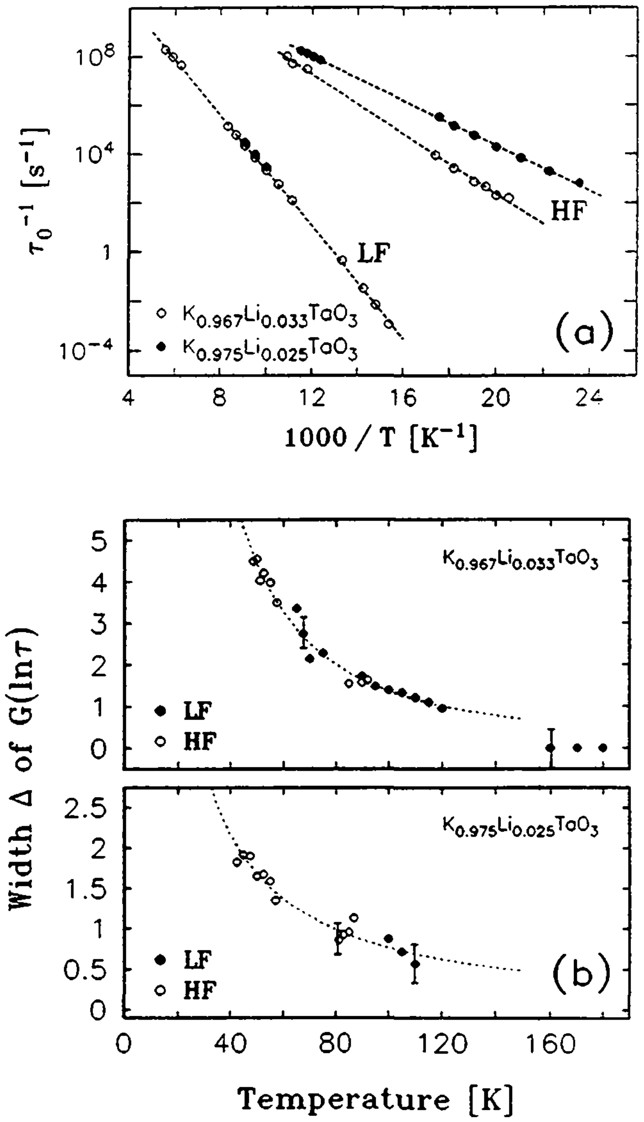

Figure 4.12 (a) Logarithm of the inverse of the mean relaxation time τ_0 as a function of inverse temperature for $K_{0.975}Li_{0.025}TaO_3$ and $K_{0.967}Li_{0.033}TaO_3$. Results for the HF and LF branch are shown. Straight lines are fits to the Arrhenius expression (4.5). (b) Width of the distribution of relaxation times for $K_{0.975}Li_{0.025}TaO_3$ and $K_{0.967}Li_{0.033}TaO_3$ and both relaxation branches. Dotted lines are fits to Eq. (4.6). See Table 4.1.

The values of α are again given in Table 4.1. The temperature dependence of the relaxation step $\Delta\varepsilon$ is shown in Fig. 4.13 for both relaxation branches. The broken and dashed curves drawn in this figure are somewhat speculative guides to the eye. The purpose is to indicate that these data are compatible with the assumption that the qualitative behavior of the samples does not depend on the Li concentration x for these values.

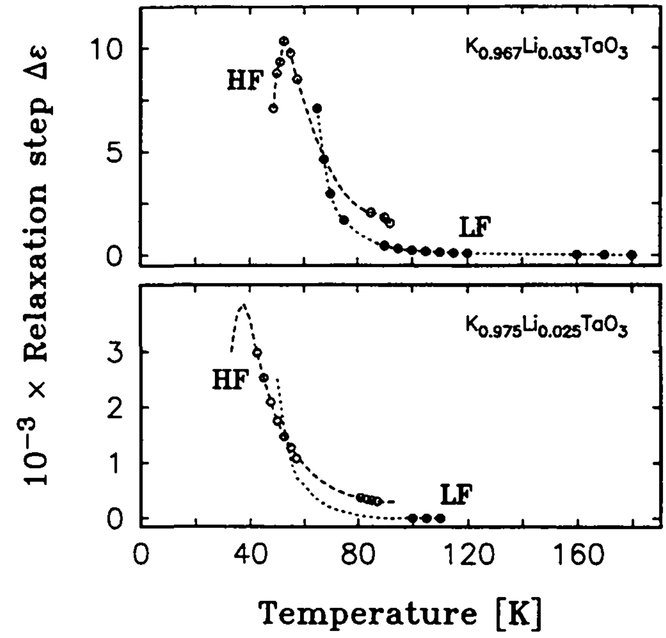

Figure 4.13 Relaxation step $\Delta\varepsilon$ corresponding to the HF and the LF relaxation branches, and for $K_{0.975}Li_{0.025}TaO_3$ and $K_{0.967}Li_{0.033}TaO_3$. Dotted and dashed curves are guides to the eye corresponding to one possible interpretation (see section 4.3.3).

4.3.3 Summary

The characteristic features of dipole dynamics in $K_{1-x}Li_xTaO_3$ are most easily distinguished on the $K_{0.967}Li_{0.033}TaO_3$ sample.[e] For this sample, both relaxation branches

---

[e] For samples with larger concentrations (samples with $x \geq 4\%$, data not shown) the width of the relaxation peaks becomes too wide to be studied quantitatively. Samples with lower concentrations,

have a large strength $\Delta\varepsilon$ at all investigated temperatures, allowing fine details to be observed.

It was shown that the relaxation times relative to both branches follow an **Arrhenius-type temperature dependence** with similar attempt frequencies but different barrier energies, in agreement with previous studies.[52]

A **widening of the loss peaks** is observed. The corresponding spread of relaxation times follows the same temperature dependence for both branches (to within experimental error), indicating that the same mechanism influences the energy barriers involved in both π and $^{\pi}/_{2}$-flips. Upon cooling, the width Δ of the distribution of relaxation times $G(\ln\tau)$ grows as $T^{-\alpha}$, with $\alpha > 1$.

A **double-hill structure** has been found on the HF branch loss peak. This "splitting" of the $\varepsilon''(\omega)$ maxima cannot be observed for the LF peak due to its narrowness. Nevertheless, the data are consistent with the assumption that the same mechanisms influence both branches.

For the LF branch, a **crossover from DW to KWW type relaxation** is found. This behavior can only be observed for the LF branch for reasons described below (page 52), but it is again assumed — in agreement with the data — that the same mechanisms control both π and $^{\pi}/_{2}$-flips.

Upon further lowering of the temperature, a **maximum in the $\Delta\varepsilon(T)$ curve** for the HF($^{\pi}/_{2}$) branch is observed. Strictly speaking, this observation results from an extrapolation of the data to lower frequencies: fitting of the data only "counts" those impurities for which the relaxation time lies within the double Gaussian distribution. If the relaxation time of a small number of moments slows down faster than the majority, a low-frequency tail develops in the loss peak. While the main part of the spectrum is still fitted satisfactorily by the double Gaussian, this tail disappears from the experimental frequency window and thus goes unnoticed.

---

such as $K_{0.975}Li_{0.025}TaO_3$ (for which some results are shown), have a low T_f ($T_f = 535 \cdot x^{2/3}$K). This results in very long relaxation times at temperatures near T_f (e.g. for the $x = 2.5\%$ sample mentioned above, extrapolation using the values of Table 4.1 leads to τ_0 (LF branch) ≈ 3000 s at $T = T_f + 15$ K), and quantitative information can thus not be obtained in the most interesting temperature region.

4.4 Dipole relaxation: models and discussion

The data of the previous section are compared to various types of models. A distribution of relaxation times $G(\ln \tau)$ arises from models describing the system as an ensemble of uncorrelated dipoles, and a double-hill-shaped $G(\ln \tau)$ is related to models taking into consideration nearest-neighbor effects. The observation of KWW-type relaxation at lower temperatures indicates the existence of hierarchical constraints.

4.4.1 Debye model and Arrhenius law

The simplest model for dielectric relaxation for a system containing reorientable moments describes each dipole as a particle in a double potential well. Reorientations of the dipoles correspond to thermally activated jumps of the particles from one local minimum to the other.

If the system, described by a number of such independent particles, is subjected to an external electric field E, the Langevin theory[76] describes the thermodynamic equilibrium of the system, and the approach to equilibrium follows an exponential time dependence. The frequency domain response corresponding to this exponential decay is given by the Debye expression:[77]

$$\frac{\varepsilon(\omega) - \varepsilon_\infty}{\varepsilon_S - \varepsilon_\infty} = \frac{1}{1 + j\omega\tau_O}. \tag{4.7}$$

Here ε_S (ε_∞) stands for the permittivity at frequencies well below (above) the frequency $f = (2\pi\tau_O)^{-1}$ of the maximum of the loss peak.

In a $\log(\varepsilon'')$ versus $\log(\omega)$ representation, the Debye loss peak is symmetric and has a full width at half maximum of 1.144 decades. Such idealized behavior is however rarely observed in real systems.[78]

If, in the above simple picture, each particle oscillates in one of the corresponding wells with an eigenfrequency ν_0, and if for each particle the barrier is described by the same height E_b, then at a temperature T the characteristic relaxation time of the system is given by the Arrhenius law

$${\tau_O}^{-1} = \nu_0 \exp(-E_b/T). \tag{4.8}$$

Such a temperature dependence is in fact observed in the present measurements on $K_{1-x}Li_xTaO_3$ over the entire frequency range spanning 12 decades. This indicates that the dipole reorientations are thermally activated at all temperatures investigated.

However, from the shape and the width of the loss peaks, it follows that $K_{1-x}Li_xTaO_3$ cannot be described by the simple double-well picture.

Therefore, alternative descriptions and more realistic models need to be considered.

4.4.2 Distribution of relaxation times

A conceptually simple generalization of the Debye expressions assumes a distribution of relaxation times, $G(\ln\tau)$. The approach supposes that each relaxation time τ appears with a probability of $G(\ln\tau)d\tau$, implying that each process occurs at a different rate and independently of all others. It is then natural to relate $G(\ln\tau)$ to a distribution of energy barriers, $G(E_b)$. A distribution of relaxation times given by a Gaussian of width Δ [Eq. (4.2)] is equivalent to a distribution of energy barriers corresponding to a Gaussian of width $T\Delta$ if the Arrhenius relation holds with the same attempt frequency ν_0 for all relaxation times.

From a mathematical point of view, it is always possible to parametrize dielectric data in terms of a distribution of relaxation times (see Appendix A). From a physics point of view, the superposition of Debye-like relaxation peaks is justified in the limit of weak interactions or for isolated dipoles. For disordered systems, a spatial distribution of one or more characteristic relaxation parameters, such as the barrier height E_b, can be assumed. However, for strongly interacting moments, the behavior of each individual dipole may no longer be described by the Debye expression.

Various distributions have been proposed (see section A.6.3a), but their relation with physical concepts is not always straight forward. Most frequently used is the above-mentioned Gaussian. Intuitively it can be seen to result from a smearing-out of the value of an energy barrier due to the effects of the local environment. A microscopic model[79] where elastic dipoles are randomly distributed in an elastic continuum leads to such a Gaussian distribution, as shown by Monte Carlo simulations.

The data for the LF relaxation branch in $K_{1-x}Li_xTaO_3$ are seen to exhibit this simple behavior for temperatures $T > 80$ K.

4.4.3 $G(\ln\tau)$ for the HF branch

As shown in Fig. 4.11, the $\varepsilon(\omega)$ data for the HF branch cannot be described by a simple Gaussian distribution of relaxation times. The $\varepsilon''(\omega)$ peaks show a double-hill structure, indicating a more complex behavior. For parametrization, the data have been fitted by a superposition of two Gaussians. Such a dependence was chosen because an analytic expression is required for least-squares fitting. Other functions describing double-hill-shaped loss peaks will probably yield a fit of similar quality.

Before we address the physical origin of this distribution, the question therefore arises whether it is possible to calculate $G(\ln\tau)$ directly from the dielectric data presented above. As described in section A.7.3, appropriate numerical methods are available, but they require knowledge of the ε'' data over a larger frequency window than the present one. In order to perform calculations, the data thus need to be extrapolated towards higher and lower frequencies. As an illustration, the often observed[80] power-law dependence

$$\varepsilon'' \propto \omega^{\alpha} \quad \text{with} \quad \begin{cases} -1 \le \alpha < 0 & \text{at high frequencies} \\ 0 \le \alpha < 1 & \text{at low frequencies} \end{cases} \tag{4.9}$$

was used to calculate the distribution $G_c(\ln\tau)$ of Fig. 4.14(b). This distribution differs from the double Gaussian obtained by fitting, but both expressions lead to an agreement between calculated and measured $\varepsilon''(\omega)$ curves to within experimental error. This indicates that the experimental window is too small for obtaining the exact distribution of relaxation times.

The general feature, however, i.e. the double-peak character of the distribution, is clearly established.

4.4.4 Models resulting in a double-peaked $G(\ln\tau)$

a) Nearest neighbors

Various models are seen to lead to a double-peaked $G(\ln\tau)$. The simplest approach is to assume that each energy barrier is modified by the neighboring impurities. Strain fields resulting from the substitution of potassium by the smaller lithium ions are mentioned as one possible mechanism.

In Appendix C, the probability of finding the nearest neighbor at a given distance is studied as a function of the Li concentration x. For $x = 3.3\%$, the distribution clearly shows two local maxima [Fig. 4.14(c)] due to the large number of sites available at these distances (in a continuous medium, the distribution is smooth).

This crude model gives an intuitive argument for understanding the occurrence of two maxima in the $G(\ln\tau)$ curves. However, it does not explain the physical mechanism relating the distribution of nearest neighbors and the distribution of relaxation times. More sophisticated models have been devised by various groups and are reviewed in the following.

b) The model of Sheng and Chen

Sheng and Chen[81,82] have studied the local field and the effective dielectric properties of a lattice gas of polarizable point particles.

For an applied field $\vec{E}^0 = \vec{e}E^0$, the quantity $E_{\|} = \vec{E}\cdot\vec{e}$ is defined as the parallel component of the local field $\vec{E}$. By generalizing Onsager's reaction-field approach,[76] Sheng and Chen obtain the distribution for the probability of observing the value $E_{\|}$ and its variation with the density. The distribution is found to be double-peaked in general, with the Lorentz value E_L situated between the two peaks.

Figure 4.14(d) shows the probability distribution $P(E_{\|}/E_L)$ for a random system

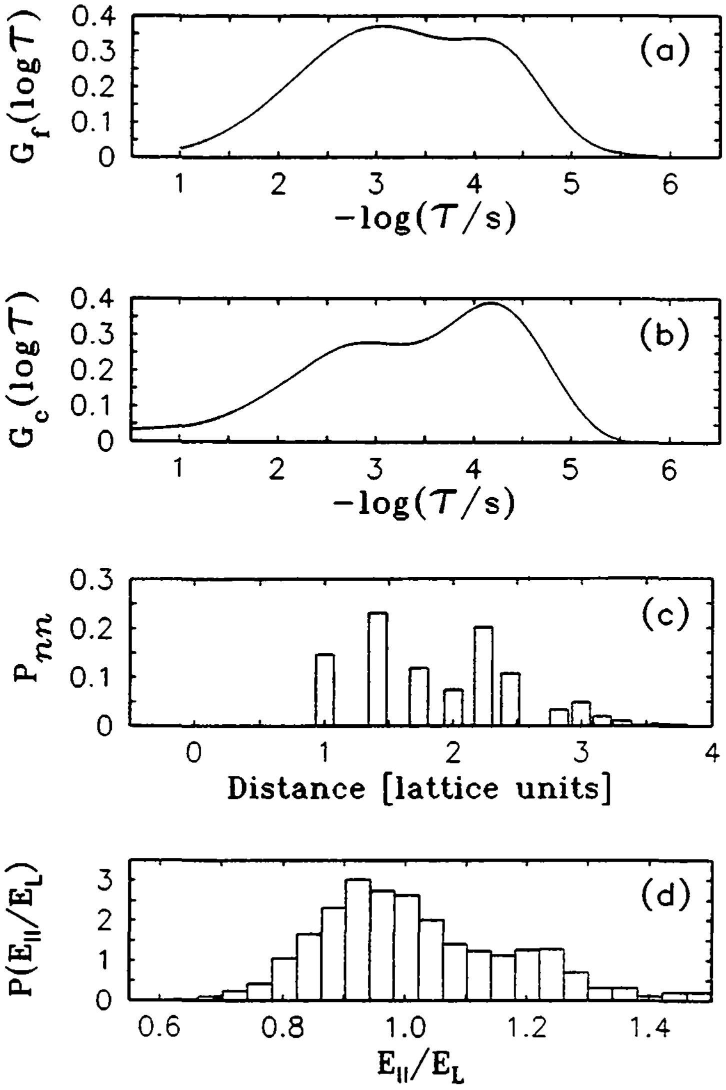

Figure 4.14 (a) Double Gaussian distribution of relaxation times obtained from a least-squares fit for the data in Fig. 4.11. (b) Distribution of relaxation times calculated numerically (as described in section A.7.3) from the same data, using the extrapolations of Eq. (4.9). (c) Probability P_{nn} to find the nearest neighbor at a given distance. (d) Distribution of the local field component $E_{\|}$ parallel to the applied field, normalized by the Lorentz field E_L, in the model of Sheng and Chen.[81]

with density of 0.2,[f] calculated for a system containing 3103 particles on a simple cubic lattice. According to sheng and Chen, the peak above E_L arises from a local environment where the dipole field contributions from the neighbors above and below the site (in the direction of the field) exceed those in the plane of the site, whereas the peak below E_L arises from the reverse situation.

The local field is calculated only on occupied sites, and the polarizable particle has no internal states. Thus, the double-peak character obtained here should be distinguished from a behavior that may originate from the different types of internal states of the dipoles in the vicinity of the test site.

c) Other models

For related systems, similar observations, namely a nonuniform distribution of local fields or dipole-dipole interaction energies due to the local environment, have been made by a number of researchers.

Wang[83] has calculated the local field on lattice sites near a point-charge defect for KCl and for a close-packed fcc lattice, and observed a complicated distance dependence.

Similarly, Van Weperen *et al.*[84] observed more than one local maximum in the probability distribution of dipole-dipole interaction energies calculated for randomly displaced Ce^{3+} ions in SrF_2:Ce^{3+}.

The above observations agree with conclusions from a generalized random field theory, taking pair interactions into more detailed consideration: two maxima are observed in the probability distribution of the local random field.[85,86]

d) Discussion

Various models have been suggested which lead to a double-peaked distribution of local fields or interaction energies. Essentially, in all of the above models this character results from a nonuniform local environment, in particular from the influence of nearest neighbors. It is assumed that this effect also leads to the observed shape of the HF loss peaks in $K_{1-x}Li_xTaO_3$.

The observations made for this relaxation branch are thus dominated by or at least superimposed on the effects of nearest-neighbor interactions. Therefore, it is difficult to extract information about the actual relaxation mechanism and how its properties change as the freezing temperature is approached. As a result, a comparison to predictions of simple models is almost impossible for this branch.

Finally, it is mentioned that similar double-hill-shaped relaxation peaks can also be distinguished in dielectric data for $KTa_{1-x}Nb_xO_3$ as obtained by Fontana *et al.*[70] (their figure 1b), which have however been fitted by a simple Gaussian distribution.

---

[f] This density should not be directly compared to the Li concentration, but to the proportion of the host lattice taken up by the Li-induced polarized clusters.

4.4.5 Description of LF branch data

On page 38, it has been shown that the data for the LF branch (π-flips) are well described by the DW expression at higher temperatures, with the width of this distribution following the same temperature dependence as the width of the HF branch (Fig. 4.12). It is thus assumed that the same mechanism governs the spread of both relaxation branches.

The longer characteristic times of the LF branch renders this relaxation observable at higher temperatures than those at which the HF branch can be studied. At these elevated temperatures, the corresponding width Δ is small. Therefore, if the relaxation time distribution for the LF branch has the same double-peaked shape as the HF branch, it will go unnoticed in our experiments.

As will be shown below, various models predict particular features of the high-frequency limiting behavior of $\varepsilon(\omega)$ as the temperature approaches T_f from above. Thus, it is of great interest to investigate the experimental behavior at frequencies well above the central region of the loss peak, for example at frequencies $f > (2\pi\tau_o)^{-1} \cdot \exp\{\Delta\}$ if the peak is described by a distribution $G(\ln\tau)$ of width Δ. Inspection of Fig. 4.12 shows that with the present experimental setup (10^{-3} Hz $\leq f \leq 10^{9}$ Hz) and for temperatures close to T_f, this is possible for the LF, but not for the HF branch.

For samples with low Li concentrations, the low value of T_f ($T_f = 535 \cdot x^{2/3}$K) implies that the LF relaxation time exceeds the time scale of a typical experiment at temperatures near T_f. Therefore, the limiting high-frequency behavior of this branch can be observed with sufficient precision only on samples in a narrow concentration range (3–4%).

Results of the depolarization current measurements on the $K_{0.967}Li_{0.033}TaO_3$ sample have been presented in section 4.3.1. The curves shown in Fig. 4.5 show clearly that for times much shorter than τ_o, the current can be approximated by $i \propto t^{-\beta}$, contrary to the case of a Gaussian or double Gaussian distribution of relaxation times (as explained in Appendix A, page A-8). The same observation is also made in Fig. 4.6, which shows that the LF relaxation branch — at a temperature well above the freezing temperature T_f — crosses over from a regime where it is best described by the DW expression to one where the KWW function fits the data better.

It should be noted that other relaxation functions, such as the expressions postulated by Jonscher or by Dissado and Hill (see discussion of these models below), or the Fourier transform of the Havriliak-Negami expression (Appendix A, page A-11), would probably fit the data equally well: their high-frequency asymptotic behavior cannot be distinguished from the one of the KWW expression over such a small time interval (three decades). The choice of the KWW decay over any of these other functions is motivated by the models discussed below.

4.4.6 Models leading to stretched exponential decay (KWW)

The KWW function, introduced above in Eq. (4.3), is described in detail in Appendix A, pages A-12ff.

Inspired to some extent by the success of the KWW function in describing relaxation data of polymer systems and spin glasses,[59] a large number of models have been proposed to account for this particular behavior. The model of Palmer, Stein, Abrahams and Anderson[87] (PSAA) has attained considerable popularity due to its conceptual clarity and the fact that the mechanisms involved may be found in a vast class of materials.

In the PSAA model, a "level" (which may be a class of dipoles or clusters) remains locked until the preceding level can release it, and therefore, a hierarchy of degrees of freedom from fast to slow is established. The levels $n = 0$ (fastest), 1, 2,... are represented by N_n pseudospins, and level $n+1$ can change only if μ_n pseudospins at level n attain one particular state. By postulating $\mu_n = \mu_0 n^{-p}$ with $p = 1+\epsilon$, and $N_{n+1} = N_n/\lambda$, $(\lambda < 1)$, one obtains the KWW behavior for $\epsilon \ll 1$ and a stretching variable given by $\beta = (1+\mu_0 \ln 2)^{-1}$. This relates β^{-1} linearly to the number μ_n of pseudospins at level n that need to be in one particular state in order to allow the pseudospins at level $n+1$ to flip, and this number is expected to grow as temperature decreases. The consequence that β is an increasing function of the temperature is well observed in our experiments (Fig. 4.6).

Related models have been proposed following Palmer *et al.*: dynamics in ultrametric spaces[88] and energy transfer by multipolar interactions between binary clusters in a self-similar hierarchical space[89] lead to long-time decay according to the KWW law. Finally, the dynamics in ultrametric and hierarchical spaces has been shown to be equivalent,[90] even if the underlying coupling schemes are different.

Irrespective of the details, which differ in each of these approaches, the main assumption leading to KWW behavior remains the same as for the PSSA model: the dipoles cannot relax independently; much rather, their dynamics is determined by a hierarchy governing the individual relaxing species.[g]

---

[g] A number of other models also result in KWW behavior, but only for a particular choice of the parameters which generally cannot be directly related to the physical properties of a system. Such models include:

-the approach by Stillinger[91] where β and τ_0 are related to gross topographical features of the many-particle potential-energy hypersurface,

-the nonlinear integro-differential equation of Jacobs,[92] where a distribution of relaxation parameters in an inhomogeneous material is assumed,

-the model of de la Fuente *et al.*,[93] describing dipoles with two possible orientations and coupled to a phonon bath.

Further models have been proposed which do not easily relate to the situation in $K_{1-x}Li_xTaO_3$. The models by Kumar and Shenoy[94] (activated hopping over hierarchical barriers), Rajagopal *et al.*[95] (time-dependent entropy contribution to the free energy), and Shlesinger and Montroll[96] (random walk of mobile defects to sites of frozen dipoles) are examples thereof.

The observed crossover from a temperature range where the relaxation is well-described by the DW expression to a range where the KWW function best fits the data is thus interpreted as a crossover from a regime of independent dipole flips to one of hierarchical relaxation.

Monte Carlo simulations of spin-glass type models have also led to results compatible with the KWW function,[h] in one case (Carmesin and Binder[100]) reproducing the temperature dependence of the parameter β of Fig. 4.6 reasonably well. However, this agreement should be interpreted with care. According to Binder,[102] "the statistical inaccuracies of Monte Carlo data inevitably preclude us from making a definitive statement about the precise form of the decay law." In addition, results of a numerical determination of the Li-Li interaction energy (section 4.7) will show that these spin-glass models are based on assumptions that are too crude to take the microscopic properties of $K_{1-x}Li_xTaO_3$ into consideration.

4.4.7 The models of Jonscher and of Dissado and Hill

For the sake of completeness, a short description is given of the following two models, which seem not to correspond to the situation of $K_{1-x}Li_xTaO_3$.

In the approach of **Jonscher**, a loss peak arises from a transition at $t = \omega_p^{-1}$ in the time domain response after a step excitation, from a "primary" relaxation process $f(t) \propto t^{-n}$, $n < 1$, to a "secondary" process with a larger exponent.[80] This secondary process is described by the concept of "screened hopping," i.e. as abrupt transitions of dipoles followed by a gradual adjustment of the surrounding dipoles or charges. This adjustment takes place in a way that satisfies the so-called "energy criterion": the ratio of energy lost per radian to the energy stored per radian is a constant with respect to frequency. Experimentally, this corresponds to the "universal law"

$$\frac{\varepsilon''(\omega)}{\varepsilon'(\omega) - 1} = \cot(n\pi/2) \qquad \text{for } \omega \gg \omega_p.$$

Various attempts have been made to relate this "universal law" to microscopic properties[103,104] but have not attained the popularity of the models listed above for the KWW expression.

The "cluster model" of **Dissado and Hill**[105] shares some similarities with the approach of Jonscher in that the two regimes (at high and low frequencies with respect

---

[h] Monte Carlo simulations of a simple Ising (± 1) spin glass with nearest-neighbor interactions[97] lead to nonexponential decay that is best described by $f(t) \propto (t/\tau)^{-\gamma} \exp\{-(t/\tau)^{\beta}\}$, thus an additional parameter γ is introduced to generalize the KWW law (see also Binder, Ref. 98, for a short introduction to Monte Carlo simulation of glassy systems). It seems, however, that the KWW expression well describes the data of simulations in more refined models, such as the three-state Potts glass[99] if one takes the bonds J_{ij} in the Hamiltonian $\mathcal{H} = -\sum_{(ij)} J_{ij}\delta_{S_i S_j}$ to be a random variable with $P(J_{ij}) \propto \exp\{-J_{ij}^2/2(\Delta J)^2\}$,[100] or such as the isotropic Edwards-Anderson model, where the Hamiltonian is given by $\mathcal{H} = -\sum_{(ij)} J_{ij}[(\sum_{\mu=1}^{3} S_i^{\mu} S_j^{\mu})^2 - \frac{1}{3}]$, again with Gaussian random bonds J_{ij} and where S_i^{μ} are components of a vector in three dimensions.[101]

to the frequency of the relaxation peak) are related to different mechanisms, in the present approach to intra-cluster motion and inter-cluster exchange. In terms of the model, "a microscopic structure is maintained over a cluster containing a number of microscopic units, with an array of clusters described by a steady-state distribution completing the microscopic picture."[105] Dissado and Hill propose a differential equation governing the depolarization,[106] and the solutions for the depolarization current and for the frequency dependence of the permittivity are given in terms of Gaussian hypergeometric functions. It should be noted that the passage from their differential equation containing time-dependent coefficients to the frequency domain response has recently been questioned (see Kliem, Ref. 107, and Appendix A, page A-5).

For both models, it is difficult to relate the parameters to physical quantities. In addition, a change in the shape of the relaxation peaks, such as the variation of the width and of the KWW parameter β as observed in the present experimental study, is obtained only through a temperature variation of the model parameters, which is not described by the model itself.

4.5 Field-induced pyroelectric currents

The previous section has dealt with isothermal measurements. Additional information regarding the properties of the system at temperatures where the relaxation becomes too slow to be studied by dielectric measurements is obtained from temperature-cycling experiments: the release of polarization, frozen in by field-cooling, is studied upon reheating the sample.

The term pyroelectric current[i] is used for the charge flow observed during heating in order to distinguish it from the (isothermal) depolarization currents as studied above (section 4.3.1) and from the "classical" thermally stimulated currents. In the latter approach,[108] the variation of the $i(T)$ curves with the heating rate is studied. If the essential characteristics of the system are known to follow given laws, these measurements are equivalent to low-frequency dielectric spectroscopy. This is certainly not the case for $K_{1-x}Li_xTaO_3$. Therefore, a different approach is followed here: the curves are all recorded for the same heating range, but the value of the electric field applied during cooling is varied. The results shed light on some aspects of the behavior of $K_{1-x}Li_xTaO_3$ which are not observed in dielectric experiments.

4.5.1 Measurements

Measurements were performed on samples with Li concentrations of 3.4% and 7%. Lower concentration samples show very weak currents due to their smaller polarizability, and are thus not considered for these experiments.

Each curve is obtained after field-cooling to $\sim$ 20 K at a controlled rate of 2 ± 0.1 K/s. At this temperature, the bias is removed and the sample short-circuited via the Keithley 642 electrometer. Heating is then started immediately at a rate of 0.02 ± 0.001 K/s.

Figure 4.15 shows results obtained for different fields and both samples. In the chosen representation, a negative value of the current corresponds to a simple depolarization. The occurrence of a change of sign in the curves recorded after field-cooling with $E \lesssim$ 10–20 kV/m indicates that the polarization in the direction of the field applied during cooling increases as the sample is heated. This observation is more easily seen in the polarization vs temperature curves obtained by numerical integration of these $i(T)$ data:

$$P(T) = \int_0^T i(T') \, \frac{\partial T'}{\partial t} dt. \tag{4.10}$$

As observed in Fig. 4.16, only in the case of cooling with a sufficiently strong electric field ($E \gtrsim$ 10–20 kV/m) is the maximum of the polarization reached at the

---

[i] In the "standard" vocabulary of ferroelectrics,[4] the term "pyroelectric effect" is used to denote the occurrence of spontaneous polarization as the sample is cooled below the critical temperature. In the present work, the polarization induced by the field (applied during the cool-down) is studied. Thus, the term "pyroelectric current" is used here as a synonym for "field-induced pyroelectric current."

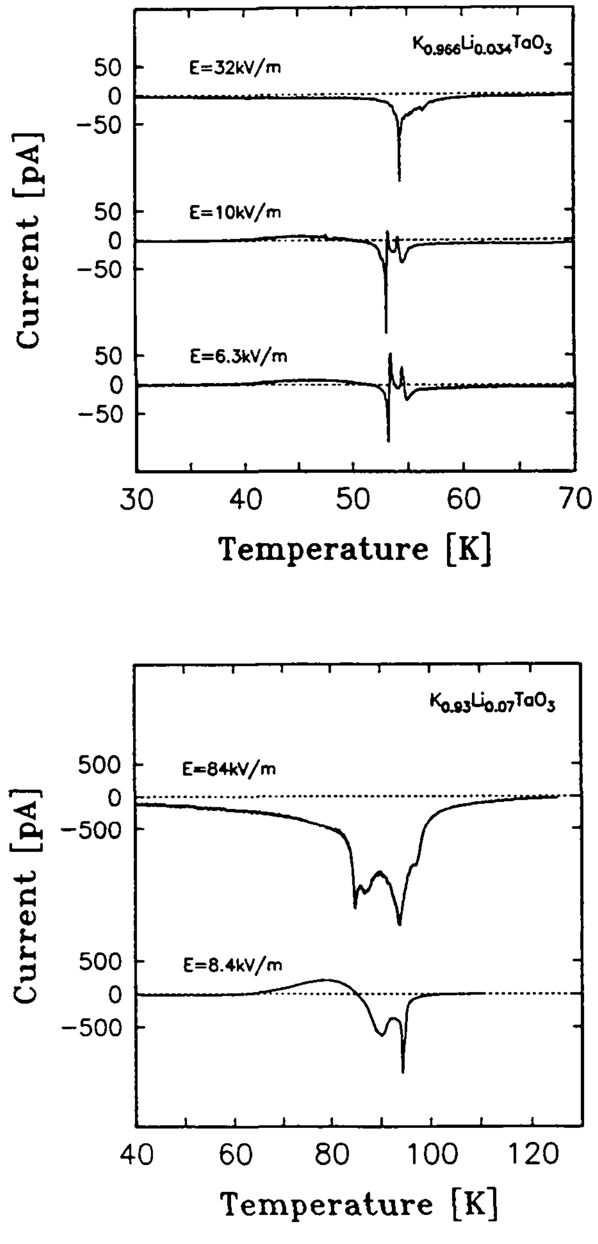

Figure 4.15 Pyroelectric current recorded upon heating (0.02 K/s) after field-cooling (2 K/s) with the field E given as parameter. The current axis is chosen such that polarization and depolarization currents (in the direction of the voltage applied during cooling) correspond to positive and negative values, respectively. Results are shown for $K_{0.966}Li_{0.034}TaO_3$ (top) and $K_{0.93}Li_{0.07}TaO_3$ (bottom).

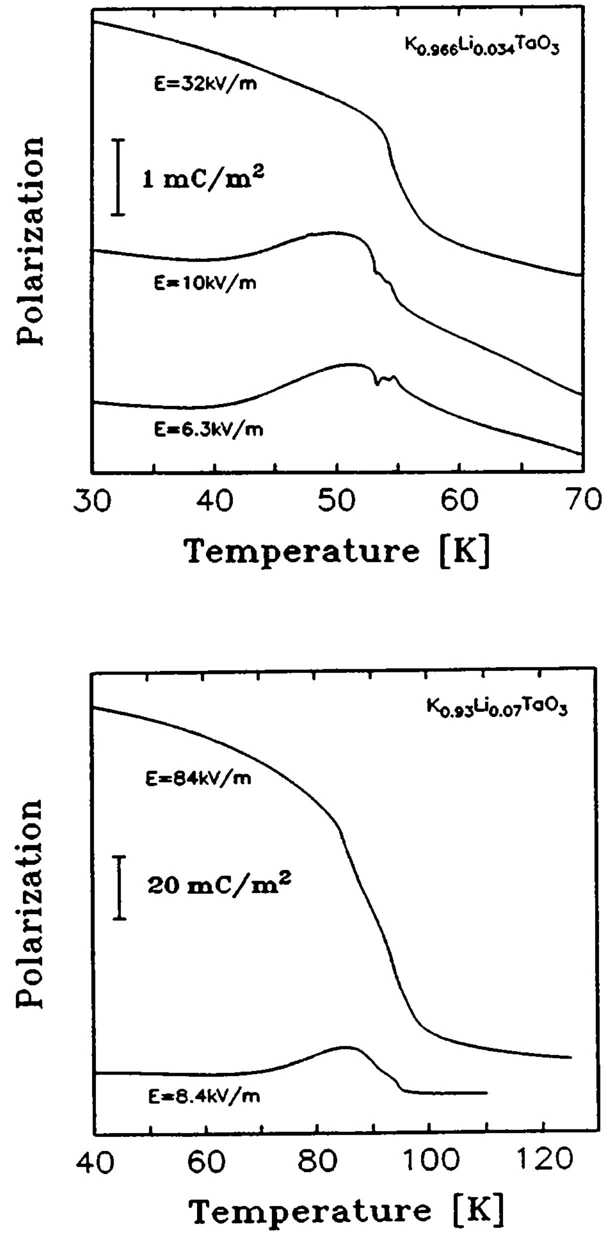

Figure 4.16 Polarization of $K_{0.966}Li_{0.034}TaO_3$ (top) and $K_{0.93}Li_{0.07}TaO_3$ (bottom) as a function of temperature, obtained by numerical integration [Eq. (4.10)] of the data shown in Fig. 4.15.

lowest temperatures. In the other cases, the $P(T)$ curves exhibit a broad maximum at a concentration-dependent temperature a few degrees below T_f. [For $K_{0.966}Li_{0.034}TaO_3$, this maximum occurs at ~52 K (T_f = 56 K), for $K_{0.93}Li_{0.07}TaO_3$ at ~86 K (T_f = 91 K).]

For zero applied field, no spontaneous polarization has been detected in these experiments (the limit of detection lying below 1 nC). In an additional measurement, the $K_{0.966}Li_{0.034}TaO_3$ sample was zero-field-cooled with 0.01 ± 0.01 K/s followed by heating with 0.1 ± 0.1 K/s. This fast heating rate was chosen because it results in larger currents for a given polarization. With this procedure, the limit of detection is lowered to 0.1 nC (20 $\mu C/m^2$ with the present sample geometry), yet no spontaneous polarization was observed.

4.5.2 Interpretation

The behavior of the polarization as a function of temperature and applied electric field can be described as follows: in the absence of an applied electric field, no macroscopic polarization of the sample is observed at any temperature. This result does not exclude the possibility that ordered domains exist: such domains go unnoticed if their spatial extent is smaller than the sample dimensions. Alternatively, the observation is compatible with an interpretation involving dipoles having a strong tendency to develop long-range order but with long relaxation times so that polarization cannot build within on the time scales of the experiment.

The occurrence of a maximum near T_f in the $P(T)$ curves recorded upon reheating a field-cooled sample is interpreted in the following way: in the process of fast field-cooling, the polarization does not have time to build up over all of the sample, due to the long relaxation time of dipole reorientation. While a majority of the impurities aligns with the applied field, a considerable number of dipoles freeze in random orientations. When the sample is then reheated slowly towards the temperature T_f at which the impurities become mobile, the dipoles tend to align with those that were oriented upon field-cooling, resulting in the increase of the polarization. At higher temperatures, the order breaks up due to thermal agitation.

The proportion of the dipoles that can be aligned by field-cooling obviously depends on the strength of the applied field. This explains why the $P(T)$ curves obtained for the larger values of E do not show this peak near T_f.

In this sense, behavior quite similar to that of quenched ferroelectrics is revealed. However, the results show that at temperatures just below T_f, namely where the $P(T)$ curves show a positive slope for small values of E, the dipoles are able to reorient at a sufficiently fast rate to be observable when heating at 0.02 K/s. Nevertheless, zero-field-cooling at this same rate does not lead to a spontaneous polarization (to within ± 20 $\mu C/m^2$), contrary to what would be expected for a ferroelectric with a domain size comparable to or larger than the sample size.

Therefore it is concluded that spontaneous macroscopic polarization does not occur in $K_{1-x}Li_xTaO_3$, irrespective of the cooling rate.

4.6 Comparison with $Sr_{1-x}Ca_xTiO_3$

In the previous section, arguments were made against the occurrence of spontaneous polarization (pyroelectricity) in $K_{1-x}Li_xTaO_3$, irrespective of the cooling rate.

To further illustrate the difference between $K_{1-x}Li_xTaO_3$ and ferroelectrics, a comparison is now made with $Sr_{1-x}Ca_xTiO_3$.

In the doped perovskite $Sr_{1-x}Ca_xTiO_3$, ferroelectricity was inferred[109] above a critical concentration $x_c = 0.0018$ on the basis of $\varepsilon(T)$ measurements. In fact, these curves show a sharp peak at T_c where ε reaches a value which depends on the sample thickness d (Bednorz and Müller[109] observed a value of 1.1×10^5 for $d = 0.3$ mm, while the present measurements with $d = 1$ mm yielded $\varepsilon = 3 \times 10^5$, both for a $\langle 110 \rangle$-oriented sample with $x = 0.0107$). To illustrate the ferroelectric character of $Sr_{1-x}Ca_xTiO_3$, experiments were preformed revealing spontaneous polarization and ferroelectric switching. Spontaneous polarization is observed as a current flow through the leads connecting the two electrodes when the sample is zero-field cooled. Integration of this current yields the polarization vs temperature curve of Fig. 4.17(a).

The $P(E)$ loops measured on the same crystal at different temperatures [Fig. 4.17(b)] show clearly that switching of the ferroelectric polarization occurs at fields as low as 10^4 V/m. $P(E)$ curves of $K_{1-x}Li_xTaO_3$ have a fundamentally different shape. Figure 4.18 shows the sample current recorded during repeated voltage sweeps (saw-tooth shaped with an amplitude of 15 V) and the resulting polarization vs voltage curve. The observed hysteresis is clearly not due to ferroelectric switching, and the shape of the loops changes only insignificantly with temperature.

As pointed out in the discussion of the pyroelectric currents, the long relaxation times are not likely to be the main cause for the absence of spontaneous polarization and ferroelectric switching in $K_{1-x}Li_xTaO_3$. In Chapter 5, $Pb(Mg_{1/3}Nb_{2/3})O_3$ will be given as an example of a material for which the relaxation time also disappears from the experimental window, but for which ferroelectric switching is observed.

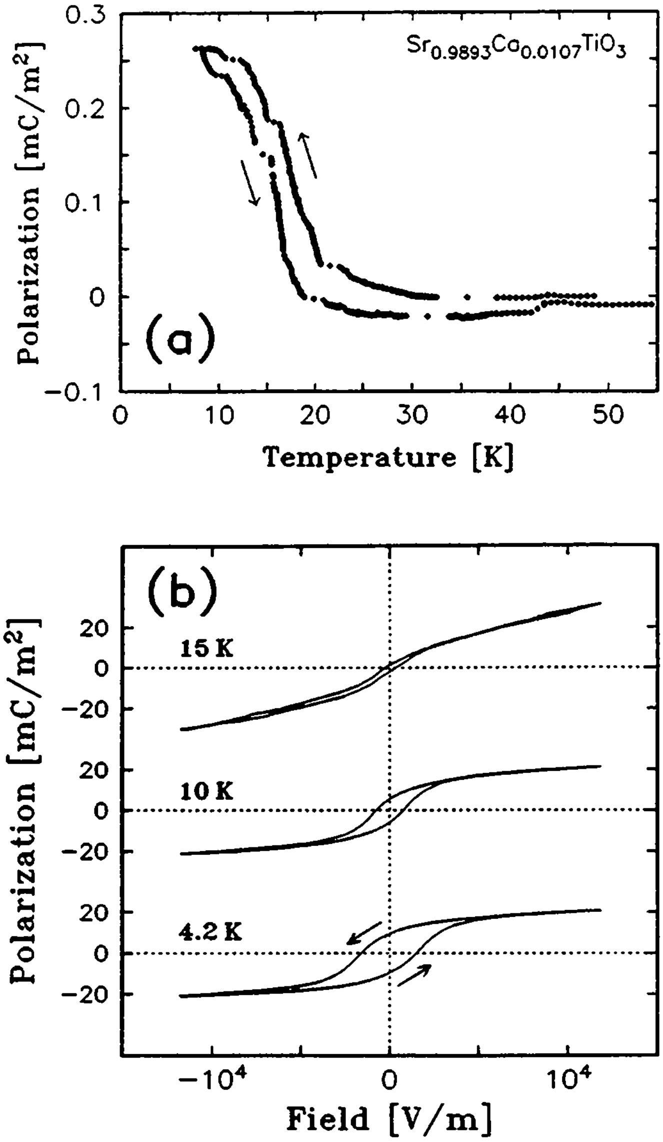

Figure 4.17 Ferroelectric behavior in $Sr_{0.9893}Ca_{0.0107}TiO_3$: (**a**) polarization obtained by numerical integration of the current recorded during zero-field cooling and subsequent reheating, (**b**) polarization vs field hysteresis loops at 1 mHz.

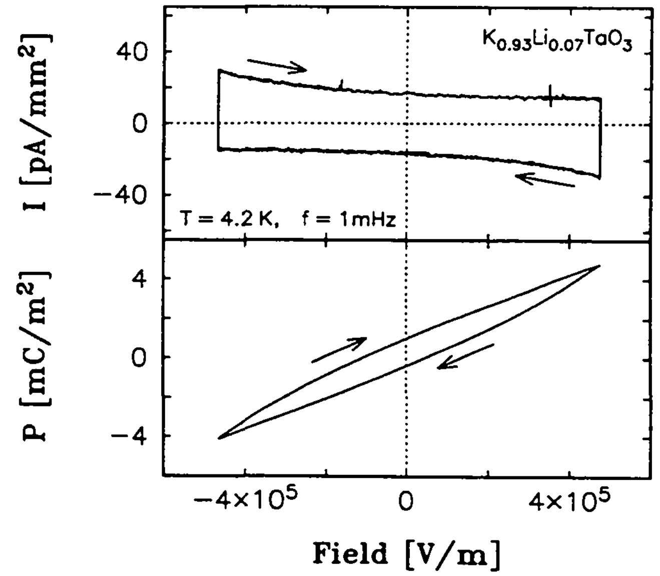

Figure 4.18 $P(E)$ loops for $K_{0.93}Li_{0.07}TaO_3$. The upper frame shows the current I recorded during repeated voltage sweeps (saw-tooth shaped time dependence) and the lower frame displays the polarization obtained by numerical integration thereof.

4.7 Calculation of Li-Li interaction energies

Results of numerical calculations of the Li-Li interaction energy are analyzed and interpreted. Frustration is shown to arise from the complicated dependence of this interaction energy on bond length and bond direction, as well as on the relative dipole orientations. It is concluded that the description of $K_{1-x}Li_xTaO_3$ goes beyond the framework of present spin-glass-type Hamiltonians. The main results of this chapter are found in "Dipole-Dipole Interactions in $K_{1-x}Li_xTaO_3$," M. Stachiotti, R. Migoni, H.-M. Christen, J. Kohanoff, and U. T. Höchli, *J. Phys.: Condens. Matter* (in press).

The preceding sections of this chapter have indicated that $K_{1-x}Li_xTaO_3$ ($2.5\% \leq x \leq 7\%$) exhibits a fundamentally different behavior than that of ordinary ferroelectrics. At the same time, it has become clear from the study of the dynamics of dipole reorientation that for concentrations below $\sim 3\%$, the relaxation times exceed laboratory time scales by several orders of magnitude for temperatures at or below T_f. Therefore, experiments are always performed in a quenched state of the system. The true ground state remains experimentally inaccessible. To explore its properties and to understand the origin of disorder, the interaction energies between two Li impurities in a $KTaO_3$ host lattice are calculated using a microscopic model.

Ricardo Migoni and Marcelo Stachiotti of the University of Rosario, who have both worked at the IBM Rüschlikon Laboratory as visiting scientists for some time during the past three years, and Jorge Kohanoff (now at the University of Lyon) have performed the calculations leading to the results presented below in sections 4.7.1 and 4.7.2. (Details of the method are given in Appendix D.) The analysis in section 4.7.3 arises from the collaboration between U. T. Höchli and myself, and from discussions with R. Migoni, M. Stachiotti, and J. Kohanoff.

4.7.1 Model

The model for the perfect ($KTaO_3$) lattice was originally proposed to explain the ferroelectric behavior in oxidic perovskites.[110] Each ion is described by a core and a polarizable shell. Both the K^+ and Ta^{+5} ions are considered isotropically polarizable. However, an anisotropic core-shell interaction is considered for the O^{-2} ion, since the oxygen polarizability depends strongly on the crystal environment. Interactions consist of long-range Coulomb terms plus short-range forces that couple the oxygen shells to the shells of the nearest K^+, Ta^{+5}, and O^{-2} ions. These interactions are treated in the harmonic approximation, except for an additional fourth-order term $K_{\mathrm{OB-B}}$ coupling the displacement of the oxygen cores to that of their own shells in the direction of the neighboring Ta^{+5} ions. The values of the model parameters were obtained in Ref. 111 from phonon dispersion curves.

The impurities are treated by replacing the K^+-O^{-2} short-range interaction at the Li sites with a Li^+-O^{-2} potential derived from a lattice dynamics study of $LiKSO_4$.[112] For the single-impurity problem, this approach predicts the off-center Li displacement, the enhancement of the polar moment of the Li, and the polarization volume per impurity, in agreement with experimental data.[113,114]

In the present work, two impurities are introduced to evaluate the Li-Li interaction modified by the polarized lattice. Both Li displacements ($\vec{\delta_1}$ and $\vec{\delta_2}$) and the lattice distortion are evaluated self-consistently using a Green's function method extended to the nonlinear polarizable shell model.[113] The set of displacements obtained in this way minimizes the potential energy of the system with two defects.

4.7.2 Results

Results are shown in Fig. 4.19 for all nonequivalent pairs of dipoles at distances of 2, 3, 4, and 6 lattice constants along the $\langle 100 \rangle$ direction.

Contrary to the case of classical dipoles, all interaction energies (irrespective of bond direction) are positive. In addition, the configuration $\uparrow\uparrow$ has a lower energy than $\uparrow\downarrow$, again in contrast to the classical dipolar case. It is also observed that the parallel $\uparrow\uparrow$ and antiparallel $\uparrow\downarrow$ configurations approach each other in energy at short distances, both lying below the three perpendicular ones. On the other hand, the configuration $\rightarrow\rightarrow$ has quite a high energy which grows rapidly with decreasing distance. The energy of the corresponding antiparallel configuration $\rightarrow\leftarrow$, in contrast, decreases rapidly when the impurities approach each other. The energy of the other antiparallel configuration $\leftarrow\rightarrow$ remains between the two previous ones. The large energy difference between these three configurations at short distances must be ascribed to the elastic interaction and higher moments of the electric charge distribution arising from the strong anisotropy of the polarized region around each Li.[113] The fact that this polarized region is smaller in the polar direction than in the opposite one accounts for the difference between the configurations $\leftarrow\rightarrow$ and $\rightarrow\leftarrow$.

Figure 4.20 schematically shows the dipole moments of the Li^+ ions, of the K^+ ions in the chain along the Li^+ ions, and of the ions in the nearest Ta-O chain. For the case of an isolated Li, this chain of ions was shown to yield the most important contribution to the polarization enhancement.[113] The case of an isolated impurity (a) is compared to the pair configurations $\rightarrow\rightarrow$ (b), $\rightarrow\leftarrow$ (c) and $\leftarrow\rightarrow$ (d). In configuration (b), which has the largest potential energy, each Ta^{+5} and O^{-2} ion acquires a larger dipole moment due to cooperative effects of the two Li impurities, and the polarized region becomes larger than in the other cases. On the other hand, competing effects between the two Li atoms are clearly observed in configurations (c) and (d) when compared to the isolated Li case (a). Turning back to Fig. 4.19, we observe that at larger Li-Li distances these configurations have similar energies,

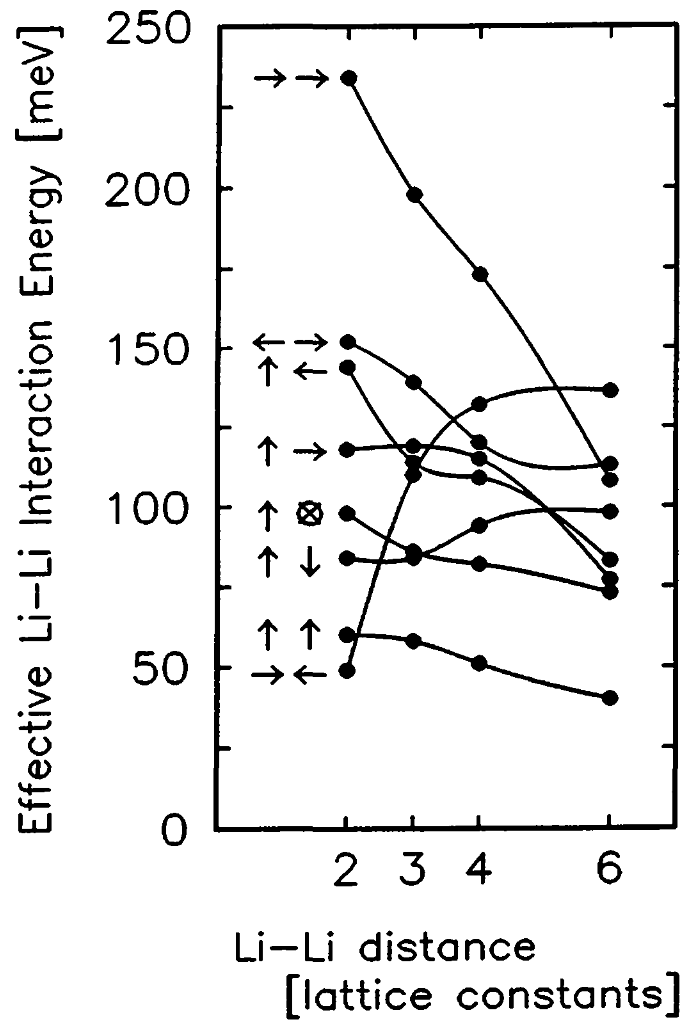

Figure 4.19 Effective Li-Li interaction energies as a function of distance for different relative displacements in the ⟨100⟩ direction. The calculated energies are indicated by solid circles, and the orientation of the Li dipole moments is indicated by arrows to the left of each curve. Solid lines are guides to the eye.

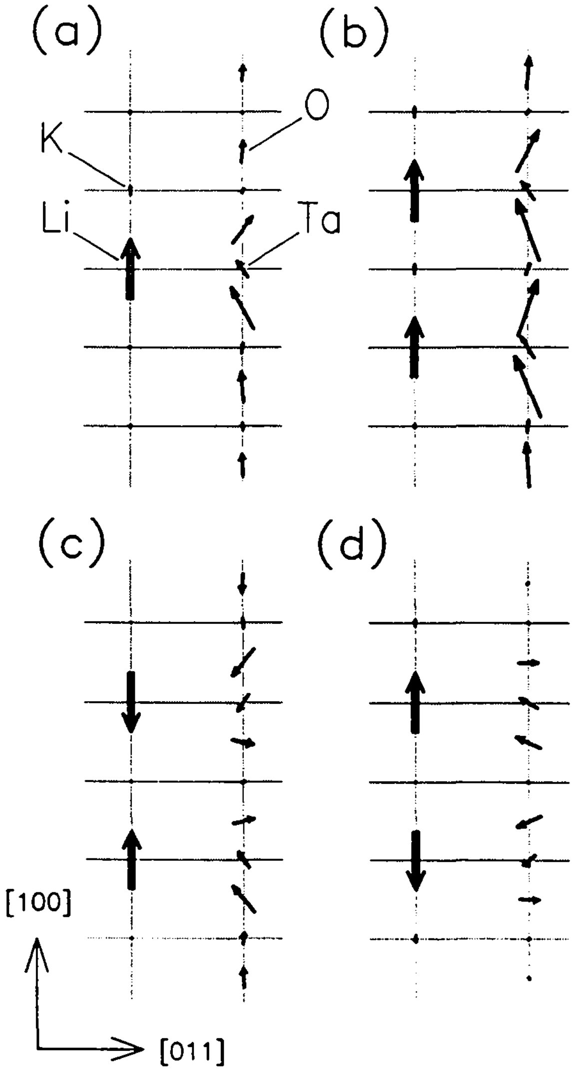

Figure 4.20 Dipole moments resulting from core and shell displacements of the ions on a Li-K chain and its neighboring Ta-O chain, (**a**) for an isolated impurity, (**b**), (**c**), and (**d**) for interacting configurations. The Li^+ dipole moments are drawn as thick arrows on a scale which is reduced by a factor of 100 with respect to that of the K^+, Ta^{+5}, and O^{2-} ions. For the latter ions, the scale has been chosen such that an arrow with length of one lattice constant a represents a polarization of $0.2\ e\ a$ (e = electronic charge).

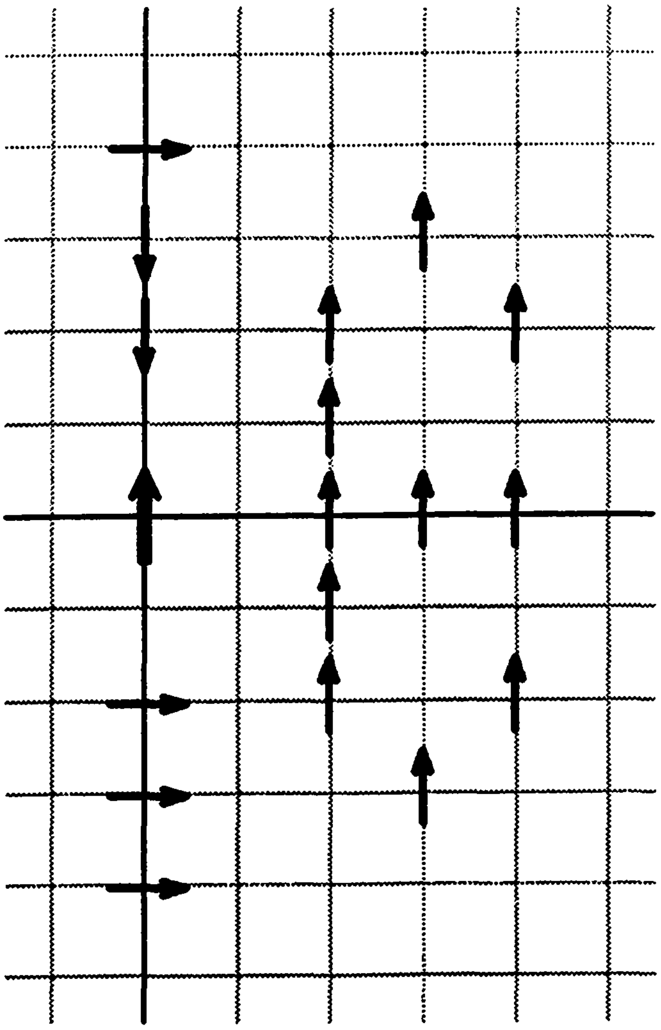

Figure 4.21 Schematic representation of the energetically most favorable dipole orientation of an impurity interacting only with that at the origin, for selected lattice sites in a {100} plane.

and it is to be expected that upon further increasing the separation, the energy of the →→ configuration lies well below all others, because in that limit the impurities should behave like screened point dipoles.

The energies of the configurations ↑↑, ↑↓, ↑←, ↑→ and ↑ ⊗ are less affected by the Li-Li distance than are the cases studied in Fig. 4.20. The reason for this is that the elastic interactions are weaker in the direction perpendicular to the dipole orientation due to the anisotropy of the polarization cloud.

The dependence of the interaction energy on bond direction was studied and again found to be different from that of classical dipoles. In Fig. 4.21, the two-particle interaction energy minima are visualized by drawing for selected sites in a $\{100\}$ plane the direction of the most favorable orientation for an impurity that interacts only with the one at the origin. For cases where the Li-Li direction is not parallel to the polarization of the impurity at the origin, a parallel alignment is favored. The situation changes drastically, however, if the second Li is placed on a site lying in the direction of the first impurity's polarization. In this case, the parallel configuration is the most unfavorable one, and the orientation of the lowest-energy alignment varies from perpendicular to antiparallel, according to the distance between the Li ions. In Table D.1 (page D-4) the values of the interaction energies calculated for the different relative Li-Li positions and orientations are summarized.

4.7.3 Analysis

Earlier theoretical[115] and numerical[83] studies of interacting impurities in polarizable lattices have shown strong deviations from the standard dipolar case. A mean field theory of dipoles coupled via transverse phonons, neglecting elastic interactions, was developed by Vugmeĭster *et al.*[116] This model leads to interaction energies with signs depending on the relative orientation of the two dipoles. However, the distance dependence of the interaction energy is identical for all bond orientations. This marked difference between the results of Vugmeĭster's theoretical study and the present calculation clearly shows the importance of elastic interactions.

The energies computed in the present work exhibit a complex dependence on bond and dipole orientation, strongly suggesting frustration. Generally, frustration arises if minimization of the energy of the entire system does not dictate the orientation for each individual polar moment. The landscape of the energy function in frustrated systems exhibits, in configuration space, a large number of deep valleys (local minima) of identical or almost identical energy, separated by high barriers. The complexity of the interaction energies found in our calculations, together with the random distribution of the impurities, thus indicate further analogies with spin glasses.

Motivated by the great success of spin glass models,[j] an attempt is made to describe the system by a Hamiltonian considering only bilinear couplings (this is equivalent to postulate that two-body interactions yield a satisfactory description). Using the notation of Vollmayr *et al.*,[127] this Hamiltonian reads

$$\mathcal{H} = -\frac{1}{2}\sum_{i,j}\sum_{\mu,\nu} J_{ij}^{\mu\nu} n_i^{\mu} n_j^{\nu} \tag{4.12}$$

where i and j represent Li sites, μ and ν can take six values corresponding to the possible spatial orientations of the Li off-center displacement, and n_i^{μ} is a random variable which takes the value 1 if at site i there is a Li ion and it is displaced with the orientation μ, and zero otherwise. Thus $-J_{ij}^{\mu\nu}$ are the pair interaction energies, many of which have been calculated above.

Obviously, the $6N \times 6N$ matrix $J_{ij}^{\mu\nu}$ (N is the number of Li ions in the system) can be simplified considerably by using the symmetry of the cubic host crystal. According to the present calculations, models that consider only nearest-neighbor couplings are not sufficient. In fact, if d_{NN} is the mean distance to the nearest neighbor of any impurity, then for some configurations (such as $\rightarrow\leftarrow$ and $\uparrow\downarrow$ of Fig. 1), the interaction energy still grows as a function of distance d for $d > d_{\mathrm{NN}}$ [for example,

---

[j] This footnote gives a very brief summary of the most prominent models based on a Hamiltonian of the form

$$\mathcal{H} = -\frac{1}{2}\sum_{i,j} J_{ij} S_i S_j - H\sum_{i} S_i^z \tag{4.11}$$

where the S_i represent the individual spins, and H is an external magnetic field. (See Ref. 59 for a more complete review.) Site disorder can be treated as bond disorder (Edwards-Anderson model[117]): the parameters J_{ij} are random variables with mean value J_O and variance ΔJ, and the probability distribution for J_{ij} can be chosen to be discrete (such as in the $\pm J$ model) or continuous (such as in Gaussian models). Short-range Edwards-Anderson models can be treated either by renormalization-group approaches or by Monte Carlo simulations. Numeric results for asymmetric $\pm J$ and Gaussian spin models[118,119,120] indicate the existence of a low-T glass state for small values of $J_O/\Delta J$, crossing over to a ferromagnetic phase for higher values.

Replacing the spins S_i by three-component quadrupoles leads to a model for orientational glasses. This has been studied extensively for nearest neighbor Gaussian interactions.[101,121,122] However, only the case $J_O = 0$ has been treated, and there is no evidence of a transition to a glass phase at a finite temperature.

For infinite-range interactions, the above Hamiltonian describes the Sherrington-Kirkpatrick[123] model. For Ising spins, the mean-field solution given by Parisi[124] indicates the existence of a spin-glass phase at low T for $J_O/\Delta J < 1$. Such a phase is also found for the case where the S_i are m component vectors in an isotropic m-dimensional space.[59] In the p-state Potts model,[5] where $J_{ij} S_i S_j$ is treated as $J_{ij}\delta(S_i S_j)$, and S_i are p-dimensional vectors, a spin-glass phase can occur depending on the value of $J_O/\Delta J$, but at the lowest temperatures, the system is always ferromagnetic. For the study of $(\mathrm{KBr})_x(\mathrm{KCN})_{1-x}$, Vollmayr, Kree, and Zippelius[125] mapped a model of large lattice anisotropy onto a Potts-glass Hamiltonian (namely, the $m = 2$ case of the uniaxial quadrupolar glass of Ref. 126), coupled to lattice deformations, and more recently proposed a discrete-state model for orientational glasses.[127] The present work, however, shows that the description of $\mathrm{K}_{1-x}\mathrm{Li}_x\mathrm{TaO}_3$ goes beyond the scope of these models, in which the influence of bond orientation is neglected.

Table 4.2: Mean values and variances (in meV) of the pair interaction energies for parallel, antiparallel and perpendicular configurations and for Li-Li distances r of 3, 4, and 6 lattice constants.

r	$-J_0^{\uparrow\uparrow}$ $(\Delta J^{\uparrow\uparrow})$	$-J_0^{\uparrow\downarrow}$ $(\Delta J^{\uparrow\downarrow})$	$-J_0^{\perp}$ $(\Delta J^{\perp})$	$-(J_0^{\uparrow\uparrow} - J_0^{\uparrow\downarrow})$	$-(J_0^{\uparrow\uparrow} - J_0^{\perp})$
3	94 (35)	108 (15)	112 (15)	-14	-18
4	90 (32)	105 (9)	104 (12)	-15	-14
6	75 (25)	87 (13)	83 (6)	-12	-8

$d_{\mathrm{NN}}(1\%) = 3.0a$, $d_{\mathrm{NN}}(4\%) = 1.9a$]. In addition, the strong dependence of $J_{ij}^{\mu\nu}$ on the bond direction (compare, for example, the configurations $\rightarrow\leftarrow$ and $\leftarrow\rightarrow$) excludes the possibility of writing $J_{ij}^{\mu\nu} = J^{\mu\nu}(r_{ij})$, where r_{ij} is the bond length.

Thus it is concluded that $K_{1-x}Li_xTaO_3$ cannot be described by the usual spin-glass type Hamiltonians.

As a crude approximation and in order to gain some qualitative information, the complex dependence on the bond direction can be eliminated by averaging, for a given combination of dipole orientations and for a fixed Li-Li distance r, over all possible bond directions.[k] For symmetry reasons, there are only three independent values to be considered, namely $J_0^{\uparrow\uparrow}(r)$ for parallel orientations, $J_0^{\uparrow\downarrow}(r)$ for antiparallel, and $J_0^{\perp}(r)$ for any perpendicular ones.

The averages and variances of these three quantities are calculated by considering the effective interactions between a given Li ion and a second one on a quasi-spherical shell of mean radius r (containing 26 sites).

Table 4.2 lists the values of these quantities obtained for three different distances. Note that the negative values of the coupling constants are given, as they correspond to the interaction energies.

The quantities $(J_0^{\uparrow\uparrow} - J_0^{\uparrow\downarrow})$ and $(J_0^{\uparrow\uparrow} - J_0^{\perp})$ of Table 4.2 characterize the degree to which — on average — parallel alignment is favored over antiparallel and perpendicular arrangements. Both depend on distance. Considering that small interimpurity spacings are more important at higher Li concentrations, these values indicate that $K_{1-x}Li_xTaO_3$ samples with a higher Li content should have a stronger tendency towards dipolar ordering than samples with a lower impurity concentration, and thus show larger dipolar-ordered and quadrupolar-ordered microdomains, as experimentally observed. However, it has to be kept in mind that these differences are of the

---

[k] Care must be taken when interpreting the results of this strong simplification. New effects and a different type of phase diagram may arise from a bond-orientation dependence of the interaction energy: recently, Vollmayr and Kree[128] have shown that for a triangular (2D) lattice, even uniform couplings can lead to dynamic freezing into a disordered, glass-like state if the coupling constants depend on the bond direction.

same order of magnitude as the variances of $J_0^{\uparrow\uparrow}(r)$, $J_0^{\uparrow\downarrow}(r)$, and $J_0^{\perp}(r)$. Frustration therefore remains dominant, preventing spontaneous ordering of the system.

4.8 Summary and interpretation

The mixed crystal $K_{1-x}Li_xTaO_3$ has been studied for $2.2\% \leq x \leq 4\%$. In this range, the system has previously been described as "disordered ferroelectric" or "domain-state ferroelectric" based on experiments performed on field-cooled samples.

The data presented in this chapter are compatible with results of second-harmonic generation[63] and microwave-induced Brillouin scattering,[64] which revealed dipolar-ordered microdomains with spatial extent of the order of nanometers below T_f.

The question about the nature of these microdomains is answered as follows: clearly they do not behave like ferroelectric domains. In ferroelectrics, by definition (see Chapter 1.2), the polarization can be switched by an applied electric field, contrary to what is observed in $K_{1-x}Li_xTaO_3$ (section 4.6). In addition, the relaxation time τ_O of a ferroelectric diverges at T_c as $\tau_O \propto (T - T_c)^{-1}$, taking small values both above and below T_c. In $K_{1-x}Li_xTaO_3$, $\tau_O(T)$ is described by an Arrhenius law at temperatures above T_f. Below T_f, no fast relaxation has ever been observed, indicating that τ_O continues to increase.

As the temperature is lowered, the spread of relaxation times increases according to $\Delta \propto T^{-\alpha}$, due to a spread of energy barriers. $\alpha > 1$ indicates that the energy barrier distribution itself widens as the temperature is decreased ($\Delta \propto T^{-1}$ would result from a temperature-independent distribution of energy barriers).

This spread results from the randomness of the spatial distribution of the impurities, via the dipole-dipole interactions. Interactions become more important at lower temperatures where the $KTaO_3$ host lattice has a higher polarizability (see Chapter 3).

A crossover from random-barrier behavior to hierarchical relaxation is observed. In the high-temperature random-barrier regime, each particle relaxes independently of its environment, which however influences the value of the energy barrier. At lower temperatures, each dipole can relax only for a given state of the surrounding species.

At even lower temperatures, a maximum occurs in the $\Delta\varepsilon(T)$ curves. This is interpreted consistently with the observed crossover from random-barrier to hierarchical relaxation: as the temperature is lowered, a growing number of dipoles can no longer flip by $\pi/2$ due to the strong associated quadrupolar component. Reorientation by $\pi/2$ is then possible only if the configuration of the neighboring impurities is favorable. This leads to the observed gradual freezing of the HF branch, while for the remaining nonfrozen dipoles, the time constant of these flips still follows the Arrhenius temperature dependence.

Impurities that are frozen due to their quadrupolar interaction can still flip by π. This explains why the LF relaxation branch (corresponding to this latter motion) becomes stronger at low temperatures, its $\Delta\varepsilon$ exceeding the one of the HF branch.

Whether the LF branch eventually freezes out at very low temperatures cannot be determined experimentally, because its relaxation time exceeds experimental time scales.

Results of a numerical study of Li-Li interaction energies show that the state into which the system freezes is disordered, independent of the cooling rate. A concentration-dependent tendency to order, as observed experimentally, can be understood from the properties of the two-particle interaction energy.

$K_{1-x}Li_xTaO_3$ is thus described as a system in which hierarchical constraints lead to KWW-type relaxation and to gradual freezing of dipole motion. In the ground-state of zero-field-cooled samples, uniformly polarized regions form which are not ferroelectric domains: their polarization remains locked (with ferroelectric switching being impossible) and the relaxation time becomes arbitrarily long.

5. Lead magnesium niobate

The stoichiometric complex perovskite $Pb(Mg_{1/3}Nb_{2/3})O_3$ is studied by depolarization current and $\varepsilon(\omega)$ measurements, and dielectric data of Colla *et al.*[129] are carefully reanalyzed. Two relaxation branches, labelled α- and β-type, are observed. No anomalies are detected in the temperature dependence of the parameters describing the loss peaks, supporting the interpretation that zero-field-cooled $Pb(Mg_{1/3}Nb_{2/3})O_3$ is nontransforming.
The article "Small-signal dielectric relaxation in the disordered perovskite $Pb(Mg_{1/3}Nb_{2/3})O_3$," H.-M. Christen, R. Sommer, N. K. Yushin, and J. J. van der Klink, *J. Phys.: Condens. Matter* **6**, 2631 (1994), contains the main results of this chapter.

5.1 Introduction

The stoichiometric mixed perovskites $AB^{(1)}_{p}B^{(2)}_{1\text{-}p}O_3$, where $B^{(1)}$ and $B^{(2)}$ have different nominal charges, and p is a rational fraction (typically $1/2$ or $1/3$), were discovered and studied in the sixties, primarily by Smolenskii's group, following the earlier works of Smolenskii and Isupov on $Ba(Ti_{1-x}Sn_x)O_3$. (For a review see Ref. 130.)

Of these compounds, lead magnesium niobate [$Pb(Mg_{1/3}Nb_{2/3})O_3$], henceforth called "PMN," appears to be one of the most widely studied examples. Owing to its dielectric properties, the material is referred to as a "relaxor" (see Chapter 1.2 for a definition and discussion of this term). PMN has the simple cubic crystal structure shown in Fig. 1.1, where the Mg and the Nb ions are distributed on the B-sites, leading to disorder. A partitioning on the nanometer scale into chemically homogeneous clusters[131,132] has been observed.

The properties of this material are promising for a number of applications. Interest has been focused in particular on the wide temperature maximum of the dielectric constant, $\varepsilon'(T)$, and its electromechanical properties.[133] Lead magnesium niobate is available as ceramic[134,135] or single-crystal[136] samples, and structurally related materials such as $Pb(Zr_{0.5}Ti_{0.5})O_3$ have been grown as polycrystalline thin films.[137] Accordingly, PMN has a high technological potential.

Figure 5.1 depicts the typical temperature dependence of the dielectric constant of PMN. Both the $\varepsilon'(T)$ and $\varepsilon''(T)$ curves show a frequency-dependent maximum.

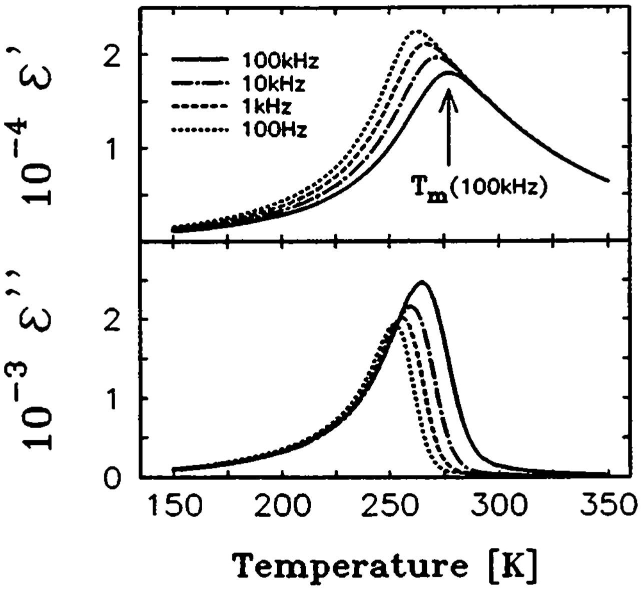

Figure 5.1 Real and imaginary part of the dielectric constant ε of a $\langle 111\rangle$-oriented PMN single crystal, as a function of temperature and for different frequencies. $T_m(f)$ is defined as the temperature at which $\varepsilon'(T)$ is maximum for the frequency f. Data from Sommer.[133]

The temperature of the $\varepsilon'(T)$ maximum is called $T_m(f)$ and is observed near 270 K for frequencies in the Hz–MHz range.

Local polarization exists in zero-field-cooled samples at temperatures well above T_m, but without developing long-range order, and field-cooled samples exhibit anomalies of various properties (such as the expansivity, refractive index, birefringence, permittivity, and thermally stimulated currents) at a temperature of $T_t < T_m$.

At high temperatures, the system is electrostrictive and the $P(E)$ curves show a nonlinear, "slim-loop" behavior. For $T \ll T_m$, PMN is piezoelectric and the $P(E)$ loops become typical of conventional ferroelectrics at temperatures below their transition. However, x-ray studies[138,139] and neutron diffraction data[140] give no evidence of a phase transition in the absence of applied electric fields (not unlike the behavior of $K_{1-x}Li_xTaO_3$).

5.2 Models and open questions

Owing to their dielectric properties, materials such as PMN have been termed "ferroelectrics with diffuse phase transition" in the earliest studies. This interpretation assumes that compositional inhomogeneities lead to ferroelectric "microregions" with different phase transition temperatures. The transition of a macroscopic sample, containing a number of such microregions, then appears to be "smeared out." Quite similarly, Cross[141] described the system in analogy to superparamagnets. However, the mentioned structural studies have shown that this is an incomplete description of the more complex behavior of such materials.

Schmidt and co-workers have described the system as nontransforming (cubically stabilized) with respect to temperature, but that it allows for a phase transition to be induced by an electric field (see Ref. 142 for a review).

The question then arises as to how this stabilization of the lattice against ferroelectric ordering occurs.

Schmidt[142] proposed an analogy with martensitic-type field-induced transitions. In contrast, Viehland and co-workers[3] have compared PMN to spin glasses. However, the latter approach involves some mathematical inconsistencies,[143] and neither of these two models explains the existence of Barkhausen jumps observed during poling.[144]

Sommer, Yushin, and van der Klink[145] have proposed a phase diagram in the (E, T)-plane including ferroelectric as well as nonergodic phases based on dielectric observations. Their approach conciliates some of the above concepts.

5.3 Dielectric data of Colla *et al.*

Colla, Koroleva, Okuneva, and Vakhrushev[129] have performed low-frequency (3×10^{-3} Hz $\leq f \leq 10^2$ Hz) dielectric measurements on a $\langle 100\rangle$-oriented PMN crystal and made their data available to me in tabular form. These results, are presented in Figs. 5.2 and 5.3, are now analyzed in much more detail than in their original article.

To my knowledge, results of measurements at these low frequencies have not been published hitherto. The general shape of the curves agrees with those obtained at higher frequencies (c.f. Fig. 5.1). A temperature T_v ("valley") can be defined (see Fig. 5.3) as the value of T for which the frequency maxima of the $\varepsilon''(\omega)$ curves are minimum with respect to temperature.

If the loss peaks were described by a relaxation function with a temperature-independent shape, the observation of this valley would be interpreted as a temperature minimum of the relaxation step $\Delta\varepsilon$. In the following, it will be shown that a temperature dependence of the parameters describing the relaxation allows this behavior to occur without requiring an extremum in the $\Delta\varepsilon(T)$ curve.

In order to demonstrate the variation of these parameters with temperature, the

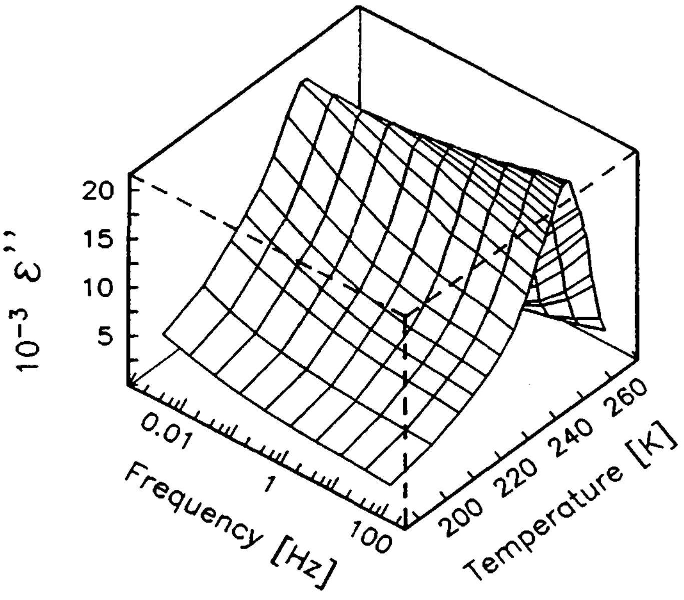

Figure 5.2 Dielectric data by Colla *et al.*[129] The imaginary part of the permittivity, ε'', is shown as a function of temperature (189 K $\leq T \leq$ 267 K) and frequency (0.003 Hz $\leq f \leq$ 100 Hz).

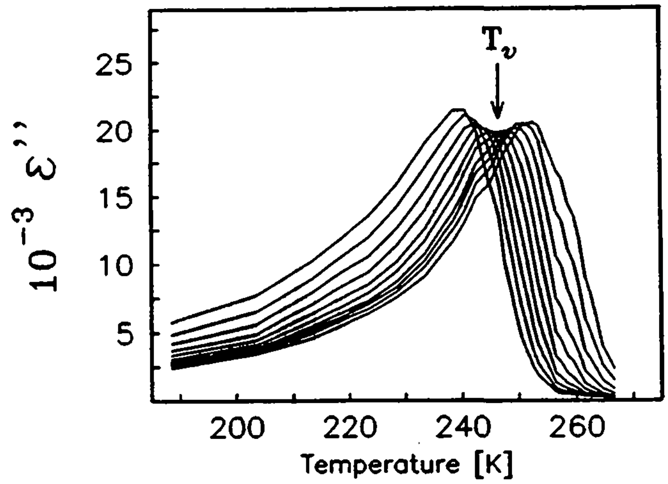

Figure 5.3 The data of Fig. 5.2 presented in a different manner. Two curves are traced per frequency decade and for 0.003 Hz $\leq f \leq$ 100 Hz (frequency increases from left to right).

data can be fit to the Havriliak-Negami expression:

$$\frac{\varepsilon - \varepsilon_\infty}{\varepsilon_S - \varepsilon_\infty} = \{1 + (j\omega\tau_O)^m\}^{\frac{n-1}{m}} . \tag{5.1}$$

The above expression is Eq. (A.45) of Appendix A, where more details regarding its properties can be found. In particular, it is shown there that for very high and very low frequencies, its slopes in a $\log(\varepsilon'')$ vs $\log(\omega)$ representation are given by

$$\omega \gg \frac{1}{\tau_O} \quad : \quad \frac{\partial \log \varepsilon''}{\partial \log \omega} = -(1-n) \tag{5.2}$$

$$\omega \ll \frac{1}{\tau_O} \quad : \quad \frac{\partial \log \varepsilon''}{\partial \log \omega} = m. \tag{5.3}$$

The choice of expression (5.1) is motivated by these experimentally well-observed "power-law limits". Other functions with similar asymptotic behavior (such as the expressions by Dissado and Hill[105] or Jonscher[80]) lead to loss peaks too narrow to fit the data.

A least squares fit to the ε'' data with the four independent parameters τ_O, $\Delta\varepsilon$, m, and n, yields reliable values thereof only if the frequency interval covers most of the loss peak. For temperatures $T > 251$ K, ε_S must therefore be extrapolated from Cole-Cole plots (see section A.5.2) and m is obtained using Eq. (5.3).

The resulting fit functions are shown in Fig. 5.4, and the temperature dependence of the fit parameters is presented in Fig. 5.5 for 245 K $\leq T \leq$ 265 K. No anomalies are observed in this temperature range. Upon cooling, the loss peak widens gradually, as indicated by the decrease of m and the increase of n. This change of shape results in a lowering of the maximum value of $\varepsilon''(\omega)/\Delta\varepsilon$ which, at temperatures above T_v, is stronger than the increase of $\Delta\varepsilon(T)$.

At temperatures below 240 K, the data for $\varepsilon''(\omega)$ are no longer described by any of the usual empirical expressions. In fact, a change of slope near a frequency $\omega^*/2\pi \approx 1$ Hz is observed in the $\log \varepsilon''(\log \omega)$ curves in the temperature range of 190 K $\leq T \leq$ 220 K. Both above and below ω^*, the data can be crudely approximated by

$$\varepsilon''(\omega) \propto \omega^x. \tag{5.4}$$

For a single loss peak, Eq. (5.4) together with the Kramers-Kronig relations (Appendix A) leads to[80]

$$\frac{\varepsilon''(\omega)}{\varepsilon'(\omega) - 1} = \cot(x\pi/2) \qquad \text{for } \omega \gg \omega_p. \tag{5.5}$$

For PMN, this is the case only at frequencies below $\omega^*/2\pi$, where the values of x fall onto the extrapolation of the Havriliak-Negami parameter n. For higher frequencies, Eq. (5.5) is violated, indicating that the measured $\varepsilon''(\omega)$ values result from a superposition of more than one relaxation phenomenon, not described by the same parameters m and n.

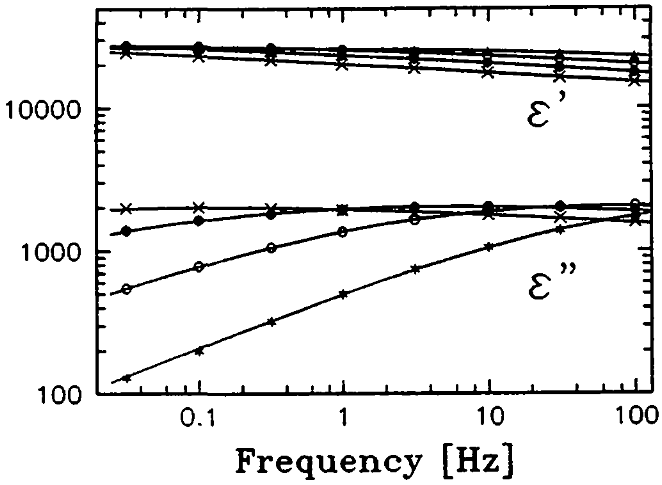

Figure 5.4 Data from Fig. 5.2 for various temperatures (crosses: 244.5 K, solid circles: 248.5 K, open circles: 252.5 K, and stars: 256.6 K), for the real (ε') and imaginary (ε'') parts of the permittivity. Solid lines are best fits to the Havriliak-Negami function.

5.4 Dielectric measurements and the observation of α- and β-type relaxations

To broaden the frequency range covered by the data of Colla *et al.*, depolarization currents were measured for times $1 \text{ s} \leq t \leq 1000 \text{ s}$, thus expanding the frequency interval down to $(2\pi \cdot 1000\text{s})^{-1} = 1.6 \times 10^{-4}$ Hz. Conventional dielectric measurements were performed for $100 \text{ Hz} \leq f \leq 100 \text{ kHz}$.

A $\langle 111 \rangle$-oriented single-crystal PMN sample was cut from a boule grown by A. Titov at the St. Petersburg Optical Institute. Sample dimensions were $2.4 \times 4.6 \times 0.15 \text{ mm}^3$. When comparing the results obtained from this specimen to the ones of Colla *et al.*, quantitative differences are to be expected due to the different sample origin and orientation. They will however turn out to be negligible.

Depolarization currents (measured as described in Chapter 2) were obtained for 11 temperatures between 207 and 250 K with a charging field of 14 kV/m (nonlinear effects were observed for fields in excess of 30 kV/m). As observed in the log-log representation of Fig. 5.6, the slopes of the curves lie close to -1, in agreement with the large widths of the corresponding loss peaks $\varepsilon''(\omega)$. Therefore, the Hamon approximation [Eq. (A.74)] can be used to relate the time-domain and the frequency-domain data and thus to compare the data of Colla *et al.* to the present measurements.

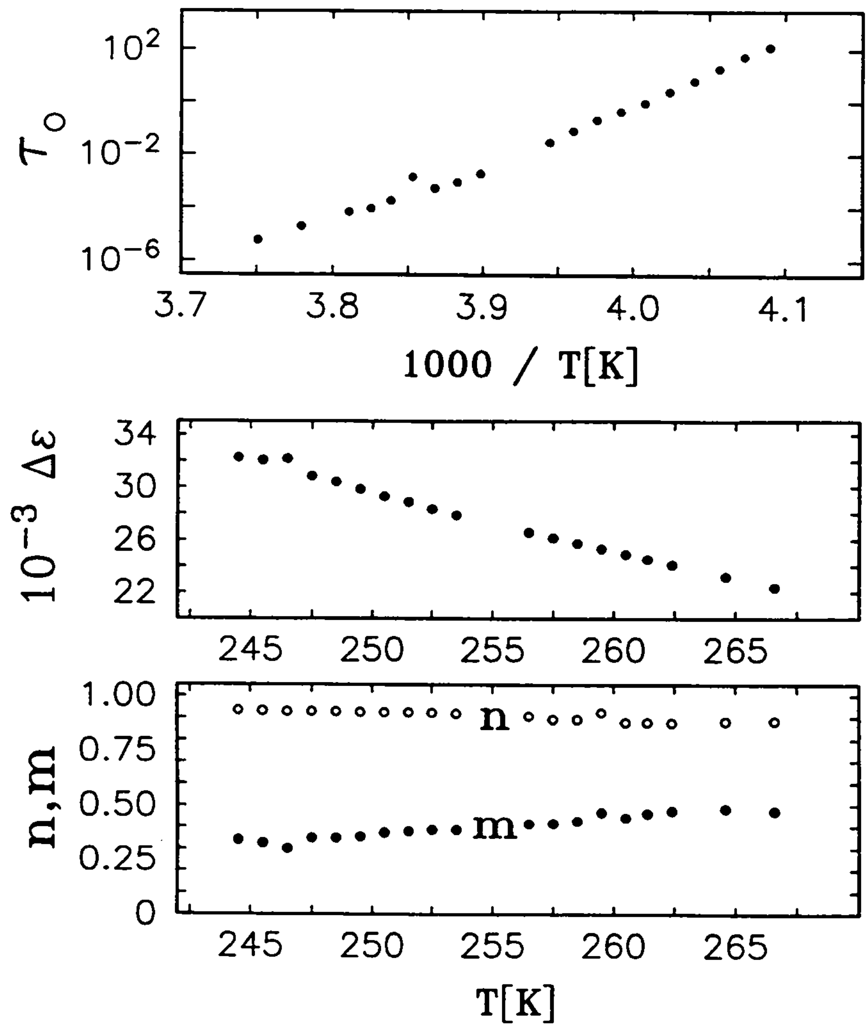

Figure 5.5 Havriliak-Negami parameters τ_0, $\Delta\varepsilon$, n, and m obtained from the fits in Fig. 5.4.

This is done in Fig. 5.7, where the Havriliak-Negami function (calculated with the parameters of Fig. 5.5 and transformed by the Hamon approximation) is compared to the depolarization current measurements shown in Fig. 5.6. The calculated curves have been shifted vertically (by less than one-half of a decade) to account for the quantitative differences between the two samples.

The correspondence between the data sets obtained for the two different samples

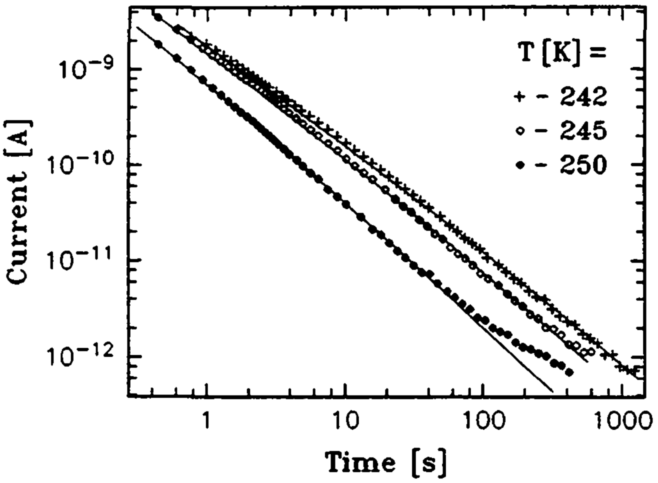

Figure 5.6 Log-log plot of depolarization current for 11 temperatures between 207 and 250 K. The curves have been shifted for clarity: for each curve the position corresponding to a value of 100 pA on the logarithmic vertical scale is indicated on the right-hand axis, and labelled with the temperature.

can also be observed in Fig. 5.8. Here, in addition to the dielectric data of Colla *et al.* and to the depolarization measurements (transformed into the frequency domain by the Hamon approximation), the present dielectric measurements at higher frequencies are also shown.

As seen in this figure, covering eight frequency decades, the slope in the $\log \varepsilon''(\log \omega)$ diminishes continuously with increasing frequency for temperatures below 230 K (clearly visible in the 212 K curve in Fig. 5.8). The behavior of PMN therefore does not conform to Eqs. (5.2) and (5.3), nor am I aware of any empirical expression describing such results. Qualitatively, however, it resembles the behavior of dielectric relaxation in glass formers, where the β-relaxation peak becomes visible in the high-frequency range at or below the freezing temperature.

The terms α- and β-relaxation are used here to describe the behavior of PMN in order to stress the phenomenological analogy with glass formers. However, a common physical origin is not implied.

In this two-branch picture, the increase towards low frequencies seen in the 212 K curve in Fig. 5.8 can be ascribed to remnants of the α-type relaxation, whereas the plateau towards higher frequencies is due to an extremely wide loss peak of the β-type relaxation. As the data show only a plateau rather than a resolved peak, this supposed β-type relaxation unfortunately cannot be quantified. For the sake of argu-

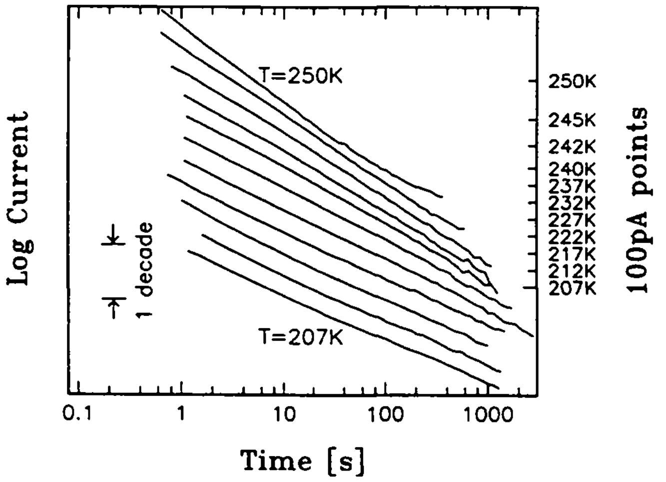

Figure 5.7 Depolarization currents for PMN. Symbols represent measurement data; solid lines are calculated from the Havrililak-Negami function in the Hamon approximation, for which the parameters of Fig. 5.5 were used. The vertical scale has been adjusted (see text).

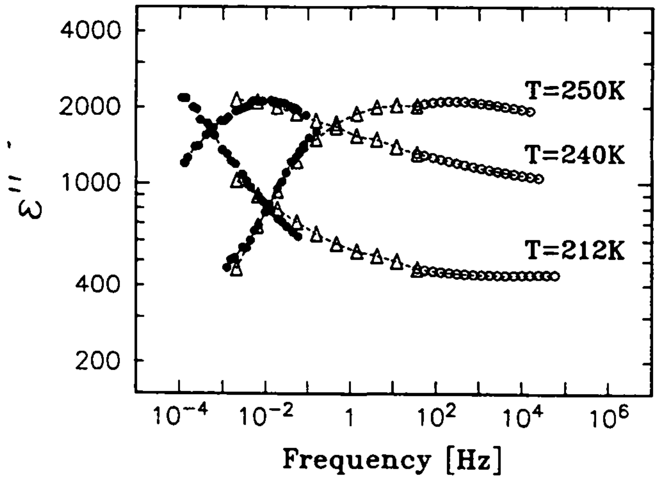

Figure 5.8 The value of $\varepsilon''(\omega)$ in PMN at approximately 212, 240, and 250 K. Triangles are data from Colla *et al.*[129] Points are the depolarization data transformed by the Hamon approximation, and scaled at 10 mHz. Open circles are conventional high-frequency dielectric results scaled at 100 Hz.

ment, suppose it is described by a very large Fröhlich distribution.[146] Then, compared to the α-type relaxation, the average relaxation time $(\tau_{\rm min}\tau_{\rm max})^{1/2}$ is certainly much shorter and the width of the peak much larger. On the basis of the data at hand, however, it is not possible to evaluate the value of the β-relaxation strength or its temperature dependence.

5.5 Comparison to $Pb(Zn_{1/3}Nb_{2/3})O_3$

In order to better appreciate the particularities of the behavior of PMN, published results for the related compound $Pb(Zn_{1/3}Nb_{2/3})O_3$ shall now be summarized. Yokimozo *et al.*[147] have reported $\varepsilon'(\omega, T)$ and $\tan\delta(\omega, T)$ values for single-crystal samples at frequencies $\omega/2\pi = 120$ Hz, 10 kHz, and 1 MHz from room temperature to 500 K. They find that ε' is frequency-dependent only around the peaks that occur at approximately 400 K, while $\tan\delta$ is frequency-dependent for the entire temperature interval. This important qualitative difference with the data for PMN enabled Dissado and Hill[148] to perform a master-plot analysis (see Appendix A, page A-14) over the temperature range 323–498 K. In $Pb(Zn_{1/3}Nb_{2/3})O_3$, the relaxation step $\Delta\varepsilon(T)$ reaches a maximum near 400 K and the characteristic time τ_o a minimum (see Fig. 5.9). This is typical of ferroelectric phase transitions, even if these quantities do not diverge. From x-ray results, Yokimozo *et al.*[147] find a rhombohedral structure at room temperature and a cubic one at 570 K. The masterplot obeys Eqs. (5.2) and (5.3) with $n = 0.88$ and $m = 0.41$ in both phases.

This behavior is significantly different from the one observed above for PMN. In PMN, the parameters n and m change with temperature, but no maximum in the temperature dependence of the relaxation step $\Delta\varepsilon$ is found (although the present data do not rule out the possibility of such a maximum at lower temperatures). The relaxation time in PMN does not reach a maximum at a transition temperature, contrary to the case of ferroelectrics [and in particular of $Pb(Zn_{1/3}Nb_{2/3})O_3$], but disappears completely from the experimental window. In fact, if the behavior of PMN were similar to that of $Pb(Zn_{1/3}Nb_{2/3})O_3$, (i.e. if the relaxation time τ_o again decreased with temperature below some temperature T^*), a second maximum would be visible in the $\varepsilon(T)$ curves (Figs. 5.1 and 5.3).

5.6 Summary and discussion

In the temperature range 189 K $\leq T \leq$ 267 K, the dielectric data of the nontransforming relaxor PMN can be described phenomenologically without having to assume divergences, discontinuities or extrema in the $\Delta\varepsilon(T)$ and $\tau_o(T)$ dependences. This conclusion is based on a careful analysis of the shape of the relaxation spectrum over the frequency interval $(2\pi)^{-1}\times10^{-3}$ Hz $\leq f \leq 10^5$ Hz. The parameters describing the shape of the loss peaks have been found to depend monotonously on temperature.

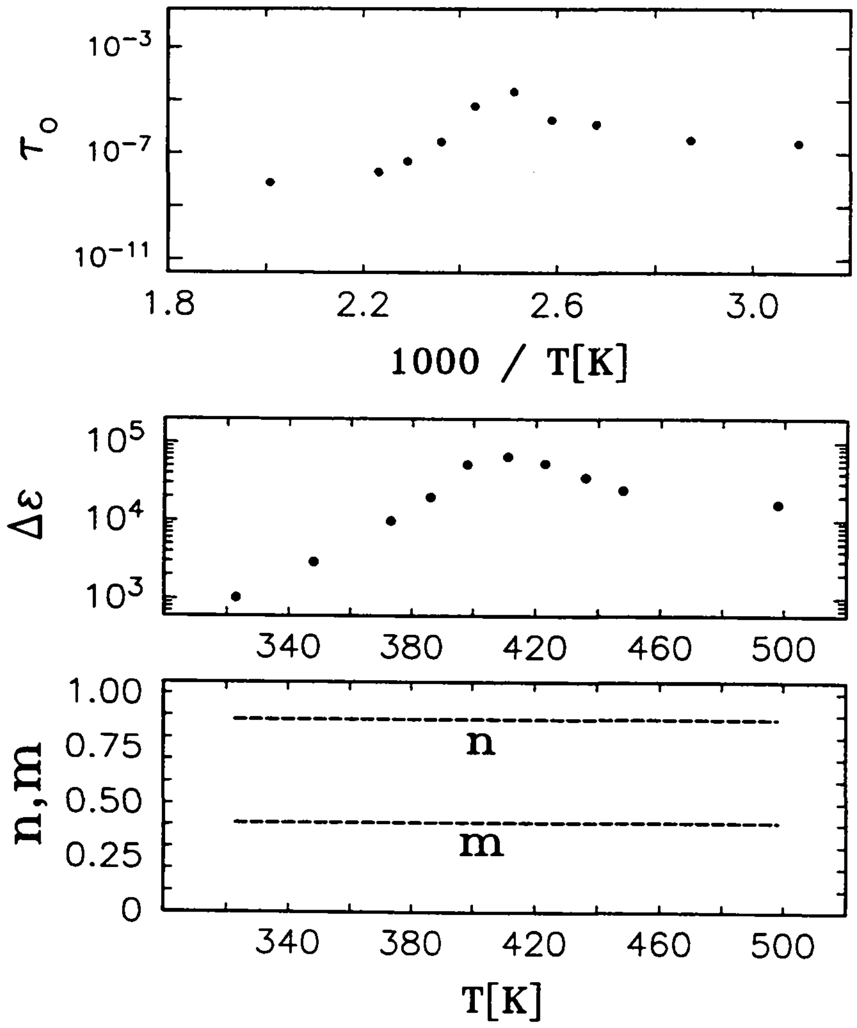

Figure 5.9 Parameters of the master plot by Dissado and Hill[148] of dielectric data for $Pb(Zn_{1/3}Nb_{2/3})O_3$ by Yokimozo *et al.*[147]

From this analysis, the presence of two relaxation branches is concluded, namely

- an α-type relaxation, visible as peak of increasing width with decreasing temperature. At the same time, the corresponding relaxation step $\Delta\varepsilon(T)$ increases continuously and the relaxation time $\tau_o(T)$ grows until it disappears completely from the experimental frequency window. Contrary to the case of ferroelectrics,

τ_0 does not reappear in this frequency window at lower temperatures;

- a β-type relaxation which becomes visible only at the lowest temperatures where the α-type peak begins to disappear from the experimental window. This branch has a shorter average relaxation time and a larger width than the α-peak. Owing to its width and its overlap with the strong α-relaxation, it cannot be described quantitatively.

In this picture, the occurrence of the maxima in the $\varepsilon'(T)$ curves (see Fig. 5.1) is seen as a purely dynamic effect: the maximum occurs at the temperature T_m at which — for the given test signal frequency — the relaxation is strongest. The presented data do not support the occurrence of a phase transition, and thus agree with earlier structural studies (sections 5.1 and 5.2). In addition, the dielectric properties of PMN are clearly distinguished from the behavior of orientational glasses, such as $K_{1-x}Li_xTaO_3$ (Chapter 4).

6. Strontium titanate films

Strontium titanate films in Mg/$SrTiO_3$/$SrTiO_3$:Nb heterostructures are studied between 4.2 and 300 K as an example of an important application of simple perovskites. The results of dielectric measurements are understood in the framework of a simple model based on concepts that will also apply to other types of oxide thin films.
Part of the presented results and analysis will be published in "Dielectric Properties of Sputtered $SrTiO_3$ Films," H.-M. Christen, J. Mannhart, E. J. Williams, and Ch. Gerber, accepted for publication in *Phys. Rev. B.*

6.1 Nb-doped $SrTiO_3$ substrates

Using results from $I(V)$ and $C(V)$ measurements on metal/$SrTiO_3$:Nb diodes, the properties of $SrTiO_3$:Nb crystals, which are relevant to the understanding of the dielectric behavior of $SrTiO_3$ films grown on $SrTiO_3$:Nb substrates, are analyzed. In particular, the free-carrier density near the surface and the surface quality are examined.

Semiconducting niobium-doped strontium titanate, $SrTiO_3$:Nb, has been used by various research groups as a substrate for heterostructures containing high-T_c superconductors (see section 1.3).

The general requirements for a material to be used successfully as a substrate for such applications can be summarized as follows:

- The material remains electrically conductive after exposure to an oxidizing environment at high temperatures (≈ 700 °C) i.e. under the typical conditions for growth of oxide thin films.
- The material does not interact with the film in a way that leads to degraded properties of the film or the formation of an interface layer.

- Crystals are readily available and can be handled with sufficient ease.

The purpose of this section is to explore to what extent $SrTiO_3$:Nb fulfills these requirements.

As mentioned in the introduction (section 1.3), $SrTiO_3$:Nb is an n-type semiconductor. Nb impurities form shallow donor centers,[149] with no carrier freeze-out occurring down to 4.2 K.[150] In recent work by various groups,[15,21,22,23] dopant concentrations in the range of 0.05 to 0.5% have been used. At these concentrations, $SrTiO_3$:Nb can be described as a degenerate semiconductor with a gap of 3.2 ± 0.1 eV.[151,152] Figure 6.1 shows the resistance of a 0.05% (ingot concentration) crystal. The observed decrease of resistivity with decreasing temperature makes this material a very suitable candidate for low-temperature applications. Samples with higher concentrations are more metallic in behavior and thus preferable as electrodes; however, to minimize surface segregation[153] and interdiffusion, samples with 0.05% Nb were chosen for this work. Crystals with an even lower concentration show insulating behavior due to compensating centers such as vacancies, interstitials, dislocations, or impurities.[150]

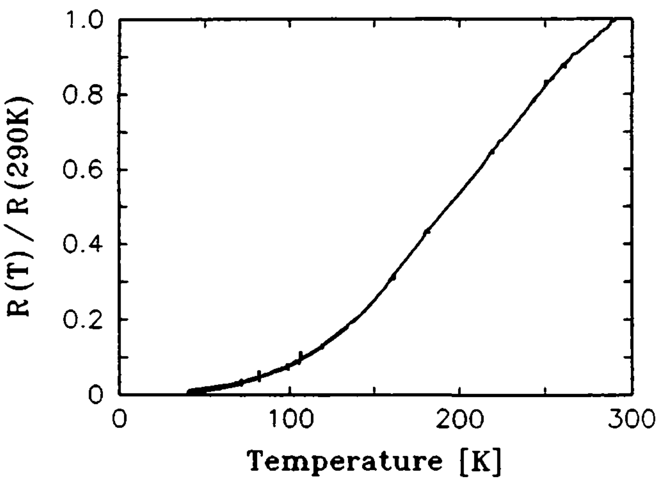

Figure 6.1 Resistance of a $SrTiO_3$:Nb single crystal (Nb-concentration: 0.05%)

Despite the occurrence of surface segregation in ceramics, which implies that the dopant concentration is increased near the surface, it has been observed[154] that an insulating surface layer forms if $SrTiO_3$:Nb is exposed to oxygen at high temperatures ($T > 500$ K). Likewise, the existence of an insulating layer at the interface between $SrTiO_3$:Nb and $SrTiO_3$,[15] Er-Ba-Cu-O,[21] or $Ba_{1-x}K_xBiO_3$[22] was inferred from dielectric and transport properties of such heterostructures.

To predict the behavior of samples involving $SrTiO_3$:Nb surfaces, a better understanding of these properties is crucial. In particular, information on the depth profile of the concentration of ionized donors and on surface layers which contribute to the measured depletion layer capacitance is required. Such information can be gained from $C(V)$ measurements of metal/$SrTiO_3$:Nb contacts, as will be shown below.

6.1.1 Pt/$SrTiO_3$:Nb diode

a) Sample preparation, AFM and TEM analysis

⟨100⟩-oriented surfaces of 0.05% $SrTiO_3$:Nb crystals have been polished using diamond paste and etched in H_3PO_4 as described in Chapter 2.3. The AFM analysis of section 2.3.3 showed the existence of scratches with a typical depth of $\approx$ 10 nm, and the surface roughness was found to be $\approx$ 5.5 nm (rms).

The cross section of the surface region of such a crystal was analyzed by transmission electron microscopy (TEM). Standard techniques for preparing cross sectional specimens[155] were used, and the microscopy was performed at 200 kV in a Jeol 2010. The resulting bright-field image is shown in Fig. 6.2. This micrograph shows a defect layer created during grinding and polishing, which extends about 6 μm below the surface.

To study the surface region's dielectric and transport properties, Pt/$SrTiO_3$:Nb Schottky diodes were fabricated using a process chosen to resemble the one employed to fabricate the heterostructures studied in section 6.2. Thus, the crystals were exposed to the same oxidizing environment (600 °C in 50 mTorr Ar:O_2=2:1) as were the substrates prior to film deposition, and then cooled to room temperature. Subsequently, platinum dots to serve as Schottky contacts were deposited *in situ* by e-beam evaporation.

Several Ag contacts were diffused into the backside of the $SrTiO_3$:Nb crystal, and their Ohmic behavior was verified by measuring the two-point $I(V)$ characteristic between any two of them.

b) Simultaneous $I(V)$ and $C(V)$ measurements

$I(V)$ and $C(V)$ measurements were performed simultaneously on such diodes at 4.2 K. The results are shown in Fig. 6.3. In forward direction (+ on the Pt electrode), the current grows by almost two orders of magnitude when the voltage is increased by 10 mV from V = 746 mV (I = 6 nA/mm^2) to V = 756 mV (I = 204 nA/mm^2), suggesting that the flat-band voltage lies within this interval.

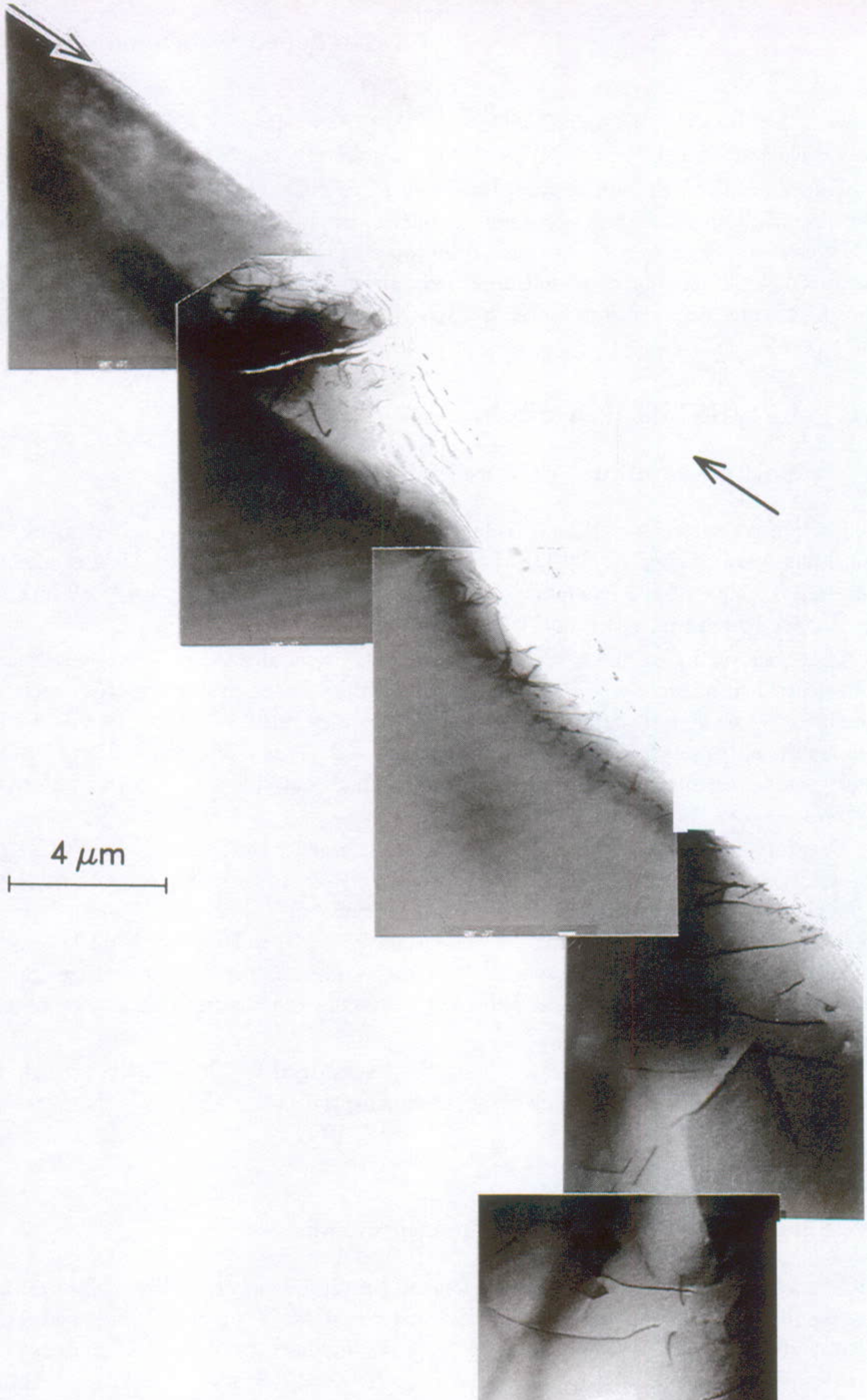

Figure 6.2 TEM bright field image of a $SrTiO_3$:Nb crystal. The arrows indicate the polished surface. Microscopy performed by E. Williams.

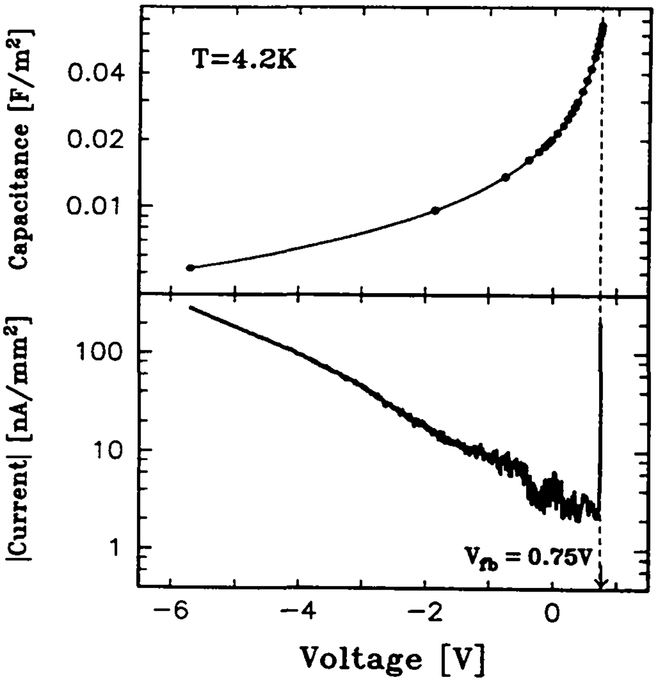

Figure 6.3 Current-voltage (top) and capacitance-voltage (bottom) characteristics of a Pt/SrTiO$_3$:Nb-diode at 4.2 K. Solid lines represent measurements, dots depict the calculated capacitance from the carrier density profile shown in Fig. 6.4.

c) Free-carrier depth profile

To obtain the depth profile of the free-carrier density $n(x)$ (x being the distance from the surface) from the $C(V)$ curve, the nonlinear $P(E)$ relation [Eq. (3.2)] with the parameters $\alpha(T)$ and $\beta(T)$ of Fig. 3.6 is used. As described in Appendix E, the band bending is calculated by integrating the one-dimensional Maxwell equation $\partial D/\partial x = \rho(x)$. For the calculation, an iterative procedure is employed: the $C(V)$ curve resulting from a first choice of $n(x)$ is compared with the measured data, and the difference is used to derive a new approximation of $n(x)$. The iteration is repeated until the agreement between the calculated and the measured $C(V)$ curves is better than the experimental confidence.

Unlike the Schottky model, where the capacitance diverges at the flat-band voltage V_{fb}, the sample in Fig. 6.3 has a capacitance of about 60 nF/mm^2 near $V = V_{fb}$. This disparity is modelled by assuming the existence of a capacitance in series with

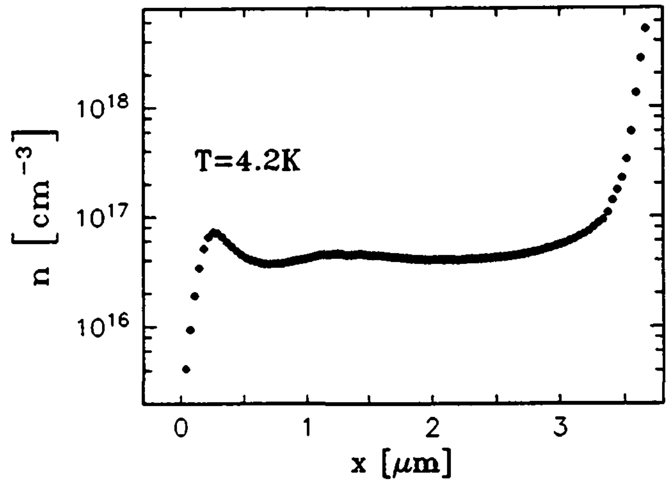

Figure 6.4 Free-carrier density depth profile for a Pt/SrTiO$_3$:Nb diode calculated from the $C(V)$ data in Fig. 6.3.

the depletion layer. (This assumption is consistent, for example, with the presence of an insulating surface layer less than 1 nm thick of a material with ε=5).

The depth profile $n(x)$ obtained from the data of Fig. 6.3 is shown in Fig. 6.4. The corresponding calculated $C(V)$ curve, indicated as dots in Fig. 6.3, agrees with the experimental data. It is pointed out that the values of $n(x)$ for $x < 0.5$ μm are strongly influenced by the exact value of V_{fb} and are thus of tentative nature only. This is also the case for $x > 3$ μm because the value of n is sensitive to C and $\partial C/\partial V$, which are both small at high voltages and thus known with less accuracy. In addition, cumulative errors can also influence $n(x)$ for large x, and therefore it is possible that the strong increase of $n(x)$ observed in Fig. 6.4 near 3 μm is partially a numerical artifact.

These calculations show that in the relevant depth range (less than about 3 μm), the density of ionized Nb donors at 4.2 K lies near 4×10^{16} cm^{-3}, i.e. 200 times lower than the original doping level of 0.05 mol% = 8×10^{18} cm^{-3}, but in agreement with the observed high surface resistivity.

6.1.2 Interpretation of the observed low carrier density

The observed low carrier density can be understood by the following simple considerations. Doping of SrTiO$_3$ with niobium is achieved by substitution of Ti^{4+} ions by niobium. Band conduction occurs if this substitution leads to

(a) $\mathrm{Sr^{2+}\,Nb_x^{4+}\,Ti_{1-x}^{4+}\,O_3^{2-}}$

or

(b) $\mathrm{Sr^{2+}\,Nb_x^{5+}\,Ti_{1-2x}^{4+}\,Ti_x^{3+}\,O_3^{2-}}$.

However, larger ceramic grains result[154] if substitution is accompanied by Sr-vacancies (V_{Sr}), indicating that the system would naturally prefer the following (non-conductive) state:

(c) $\mathrm{Sr^{2+}\,(V_{Sr})_{x/2}\,Nb_x^{5+}\,Ti_{1-x}^{4+}\,O_3^{2-}}$.

It has been observed[150] that a low acceptor doping is always present and that its charge is compensated by oxygen vacancies. Possible acceptors may include Fe, Cr, H,[150] Al,[154] Ni,[156] or broken Ti-O bonds.[157] The present $SrTiO_3$:Nb crystals are insulators for Nb concentrations below ≈ 0.01 mol% $= 1.7 \times 10^{18}$ cm^{-3}. In accordance with Ref. 150, this is interpreted as an indication of a comparably large acceptor doping, leading to charge compensation. It is assumed that the present crystals are described by a combination of Eqs. (a), (b), and (c), and acceptor doping.

Hall measurements performed on $SrTiO_3$:Nb surfaces that have not been exposed to oxygen at high temperatures[23,158] yield values of n very close to the nominal Nb concentration. This suggests that the exposure to oxygen leads to the observed reduction of the carrier density, at least in a region within a few micrometers of the surface. The following mechanisms are listed as possible reasons for the observed behavior:

- Oxidation of the surface region, possibly facilitated by the presence of defects (as observed in Fig. 6.2): filling of oxygen vacancies (which compensated the charge of acceptor states in the sample before oxidation) leads to conduction band electrons being trapped at acceptor states.
- Chemisorption of oxygen (O^- or O^{2-}) at defects leading to the depletion of a surface region, similar to what has been observed in Nb-doped $(Sr,Ca)TiO_{3-x}$.[159]
- Existence of a Sr-rich crystalline phases of the formula $Sr_{n+1}Ti_nO_{3n+1}$ (n = 1,2,3), analogous to what has been observed on $BaTiO_3$ ceramics exposed to oxygen at 500 °C.[160] The formation of such p-type conductive phases requires creation of strontium vacancies in other regions of the sample, possibly leading to the nonconductive case (c).

6.1.3 Summary

The free-carrier density of a $SrTiO_3$:Nb crystal exposed to oxygen at high temperatures ($\approx$600 °C) is strongly reduced in a surface region of at least a few micrometers.

This might be seen as an argument against the use of this material as a substrate for oxide films. However, the following advantages of $SrTiO_3$:Nb for such applications, and in particular for $SrTiO_3$ films, largely outweigh this drawback:

- the (commercial) availability of the material
- the ease with which it can be handled and polished
- the possibility to model its behavior with a constant carrier density in the surface region
- the similarity between the structural properties of the $SrTiO_3$:Nb substrates and the $SrTiO_3$ films.

For these reasons, $SrTiO_3$:Nb substrates will be used in most of this chapter, with other structures considered only for comparison.

6.2 Mg/$SrTiO_3$(sputtered)/$SrTiO_3$:Nb

The preparation and analysis of rf-sputtered epitaxial $SrTiO_3$ films with thicknesses ranging from 50 to 330 nm in Mg/$SrTiO_3$/$SrTiO_3$:Nb heterostructures is described. Results from $\varepsilon(T)$, $C(V)$, and $P(E)$ measurements are presented and compared to predictions from the bulk properties. A later section (section 6.4) will describe a model that qualitatively explains the observations made here.

6.2.1 Sample preparation and analysis

a) Film growth

In the present section, samples of the structure given in Fig. 6.5 are studied. For film growth, the $SrTiO_3$:Nb substrates are mounted onto a furnace/substrate holder with silver paste. In the process of sputtering the $SrTiO_3$ films, the substrate is heated to 600 °C. Therefore the silver diffuses slightly into the $SrTiO_3$:Nb crystal, leading to a good-quality Ohmic back contact (see Appendix F for a characterization of its electrical properties).

The films are rf-sputtered at 600 °C and in a 50 mTorr Ar:O_2 = 2:1 sputter gas. With an rf power of 150 W and a target-substrate distance of 2.5 cm, the growth rate reaches 40 Å/min as determined from cross sectional transmission electron micrographs. Film growth was performed by J. Mannhart.

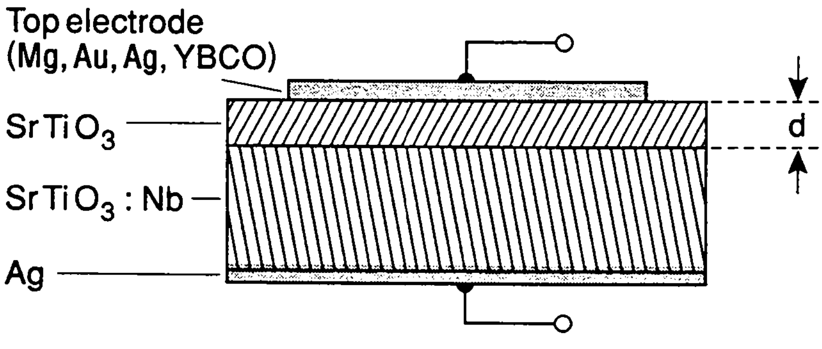

Figure 6.5 Sample structure for the study of $SrTiO_3$ films.

A magnesium top electrode (50–100 nm) is deposited *in situ* by electron beam evaporation at room temperature. Magnesium is chosen because it provides the best Ohmic contacts of all metals tested, including gold, silver, indium and indium-gallium, both on reduced and Nb-doped $SrTiO_3$ (see Appendix F). The Ohmic character of the $Mg/SrTiO_3$:Nb contacts indicates that the transport properties of this junction are not affected by an insulating MgO layer expected to form at the interface.

Using AZ4511 resist and acetic acid, a number of dots with a surface area of approximately 1 mm^2 are produced. Therefore, several contacts are available for each film, allowing different types of measurements to be performed on the same sample.

Samples were also prepared with a 40-nm-thick sputtered epitaxial $YBa_2Cu_3O_{7-x}$ top electrode. The dielectric behavior of these heterostructures could not be distinguished from that of the $Mg/SrTiO_3/SrTiO_3$:Nb samples, indicating the independence of these properties in the top electrode material.

b) TEM analysis

The structure of the $SrTiO_3$ films was analyzed by transmission electron microscopy. Standard techniques were used to prepare cross sectional specimens,[155] and the microscopy was performed at 200 kV in a Jeol 2010.

Figure 6.6 shows a TEM micrograph of a $Au/YBa_2Cu_3O_{7-x}/SrTiO_3/SrTiO_3$:Nb heterostructure. Consistent with the substrate's surface roughness as measured by AFM (section 2.3), the substrate/film and the film/top electrode interfaces are seen to be fairly uneven (the $YBa_2Cu_3O_{7-x}$ upper surface is considerably flatter).

Electron diffraction patterns of the substrate and of the film indicate that the film and the substrate have identical structure and orientation. This conclusion is further supported by the lattice image (Fig. 6.7) of a $SrTiO_3/Pt/SrTiO_3$:Nb structure. This particular type of a specimen, identical to the one in Fig. 6.5 except for the evaporated platinum "droplets" (visible as darker areas on the micrograph), is chosen for reasons that will become apparent in section 6.3. These platinum clusters are seen not to influence the growth of $SrTiO_3$, and similar images were obtained on simple $SrTiO_3/SrTiO_3$:Nb structures.

The homoepitaxial $SrTiO_3$ films are highly defective and are found to contain a larger defect density than the substrate. The substrates, in turn, again exhibit the upper damage layer of $\approx 6\ \mu m$ (see section 2.3) generated during grinding and polishing.

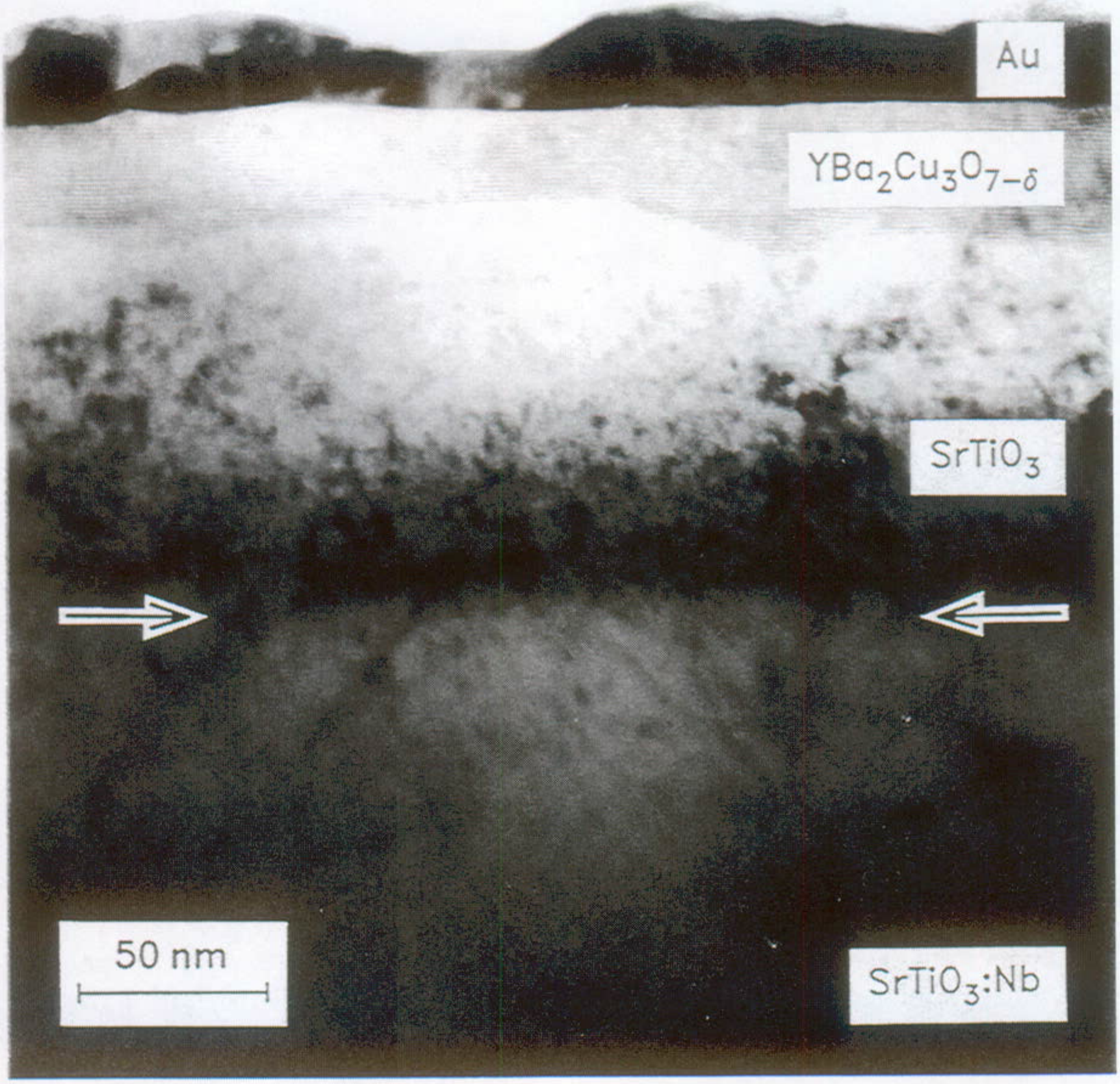

Figure 6.6 TEM micrograph of an Au/YBa$_2$Cu$_3$O$_{7-x}$/SrTiO$_3$/SrTiO$_3$:Nb heterostructure (bright field image). Arrows indicate the SrTiO$_3$/SrTiO$_3$:Nb interface.
Microscopy performed by E. Williams. [Sample number R510]

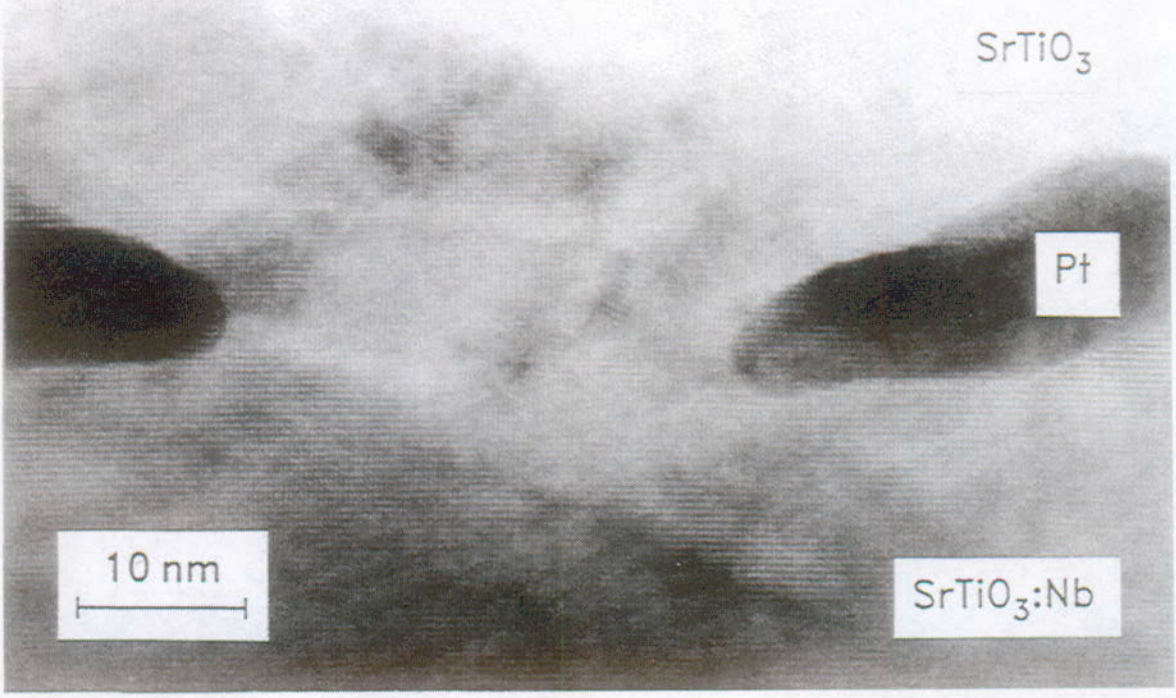

Figure 6.7 TEM lattice image of a $SrTiO_3/Pt/SrTiO_3{:}Nb$ structure (see text).
Microscopy performed by E. Williams. [Sample number R510]

6.2.2 Results of dielectric measurements

Most of the data resulting from capacitance measurements (either as a function of temperature or of an applied static electric field) will be plotted in terms of the **effective dielectric constant**, as introduced in Chapter 1:

$$\varepsilon_{\text{eff}} = \frac{1}{\varepsilon_o} \frac{d}{A} C$$

(d: film thickness, A: electrode surface area, C: capacity). This quantity is introduced because it allows results from samples of various thicknesses to be compared. For a simple parallel-plate capacitor (and neglecting fringe effects),[a] ε_{eff} is equal to the material's dielectric constant. For films grown on a semiconducting substrate, a depletion layer can form in the substrate. The film thickness d is then not equal to the thickness of the insulating layer, and ε_{eff} is smaller than the true dielectric constant.

---

[a] Fringe effects are disregarded because of the large ratio of electrode surface to film thickness.

a) $\varepsilon_{\rm eff}(T)$ and thickness dependence

Insight into the film's behavior is provided by the temperature dependence of $\varepsilon_{\rm eff}$ at zero applied voltage. The results are displayed in Fig. 6.8. Measurements were performed with a test signal amplitude of 50 mV and a frequency of 10 kHz.

Two curves $\varepsilon_{\rm eff}(T)$ are traced in Fig. 6.8 to demonstrate the range over which the samples' characteristics vary. Such changes of up to 20% between nominally identical specimens are attributed to variations of the properties of the substrate surface and film quality.

The occurrence of a maximum of the $\varepsilon_{\rm eff}(T)$ curves at about 30–40 K indicates that the behavior of the insulating $SrTiO_3$ is influenced by an electric field arising from work function differences and interface trapped charges. Comparison to Fig. 3.8 leads to the estimate of a field as large as 0.3–0.5 MV/m.

Figure 6.9 compares the two curves of Fig. 6.8 to the values obtained on films with thicknesses between 50 and 330 nm. No systematic thickness dependence can be observed in the $\varepsilon_{\rm eff}(T)$ behavior for samples with $d \gtrsim 100$ nm; however, 50-nm-thick samples systematically showed a reduced capacitance.

b) $P(V)$ measurements

In order to find the maximum polarization that can be induced in $SrTiO_3$ films, the dependence of the polarization on an applied voltage is studied.

The procedure for obtaining these $P(E)$ curves is illustrated in Fig. 6.10 for a 100-nm-thick film, and consists of the following steps: first, the sample current is recorded while the applied voltage is swept with a saw-tooth-shaped time dependence. The peak values of this ac voltage are then continuously increased until conductivity effects become visible at each polarity [Fig. 6.10(a)]. It is assumed that these voltage values lie just below the breakdown voltage of the sample. Next, the frequency of the ac voltage is increased by a factor of ten, and this in turn increases by a factor of ten only the current due to polarization effects, but not the current due to conductivity. At the same time, the peak values of the voltage are reduced to lie just below the values at which conductivity became visible in Fig. 6.10(a). The result of such sweeps are shown in (b). This current can now be numerically integrated, yielding the dependence of the polarization P on the applied voltage V, as shown in Fig. 6.10(c).

A small hysteresis is observed, possibly due to charge trapping at electrodes and interfaces. The hysteresis increases slightly for higher frequencies. Otherwise, the curves were found to be independent of frequency in the range of 1 mHz to 100 mHz.

Owing to trapped charges and work function differences, the film is polarized at zero applied voltage; however, this polarization cannot be measured with the present methods. Therefore, the quantity $P_{\bar{\imath}}$ is defined as

$$2\,P_{\bar{\imath}} = P(V_{\rm max}) - P(V_{\rm min}) \tag{6.1}$$

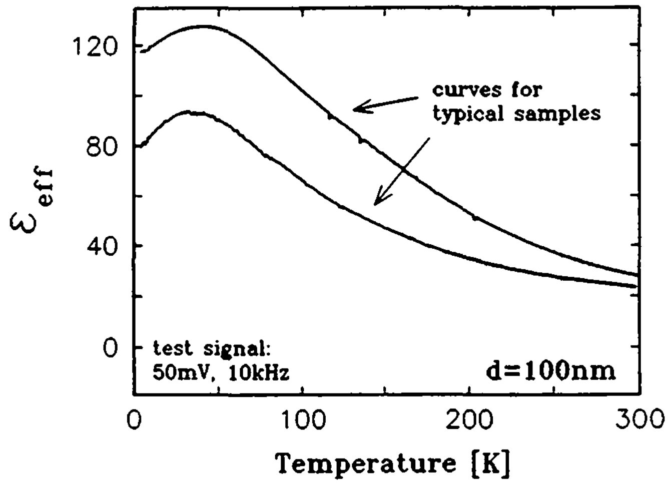

Figure 6.8 Temperature dependence of the effective dielectric constant $\varepsilon_{\mathrm{eff}}(T)$ of 100-nm-thick $SrTiO_3$ films. Two curves are shown to indicate typical variations from one sample to another. Larger values have occasionally been observed.
[Sample number R480 (top) and R468 (bottom)]

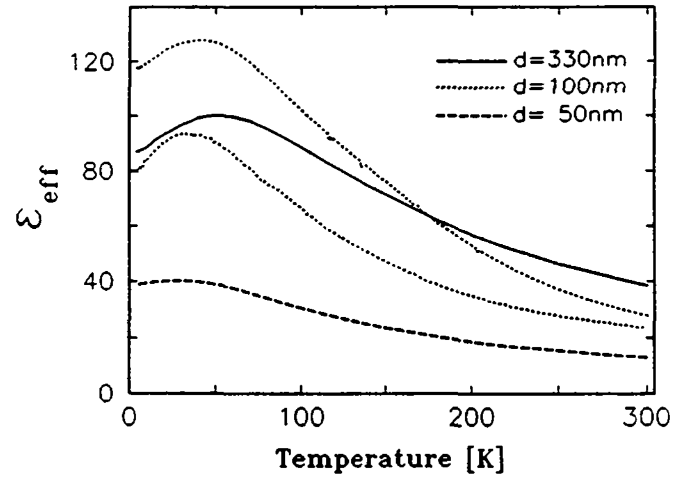

Figure 6.9 Comparison of $\varepsilon_{\mathrm{eff}}(T)$ for samples of different thicknesses. The curves for $d = 100$ nm are taken from Fig. 6.8.
[Sample number R508 (50 nm) and R509 (330 nm)]

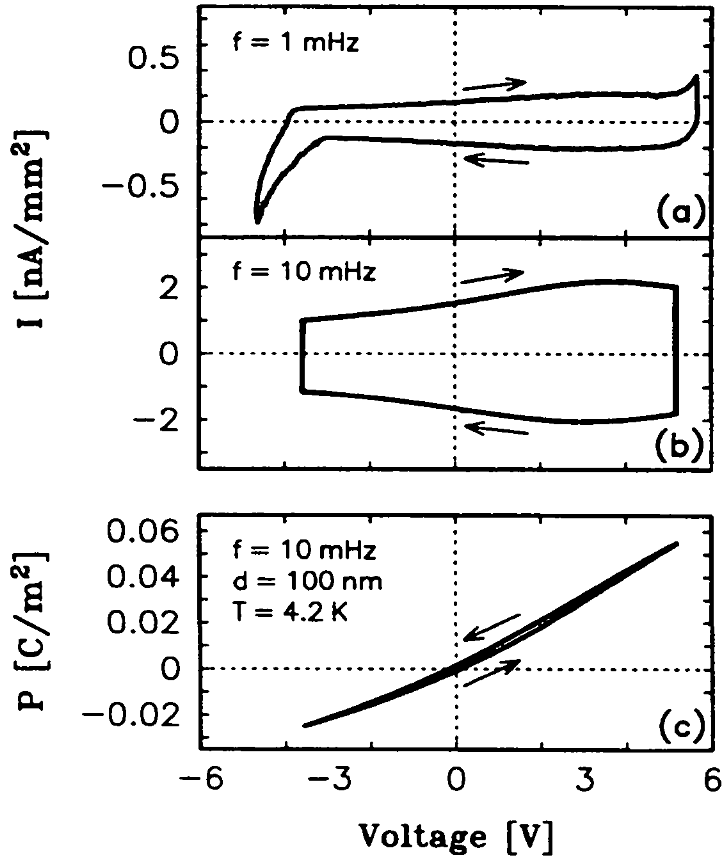

Figure 6.10 Measurement of the $P(V)$ dependence for $SrTiO_3$ films.
(a) and **(b)**: Current measured while the voltage was swept at 1 and 10 mHz, respectively, with the amplitude reduced in (b).
(c): Polarization as obtained from integration of curve (b).
[Sample number R605]

where V_{max} and V_{min} are the extreme values of the voltage that can be applied in an experiment; i.e., they lie just below the breakdown values. Thus, P_l is a measure of the maximum additional polarization that can be induced by a voltage bias. As shown in Fig. 6.11, a value of $P_l \approx 40\ \mathrm{mC/m^2}$ is found, which is approximately a factor of five below the limit extrapolated in section 3.2.2 from the single-crystal properties of $SrTiO_3$ at lower fields. The breakdown strength of the sample in Fig. 6.10 is 5.2 V in forward direction, compared to less than 3.5 V for the opposite polarity. A strong dependence of these values on the sample history is observed. For example, a

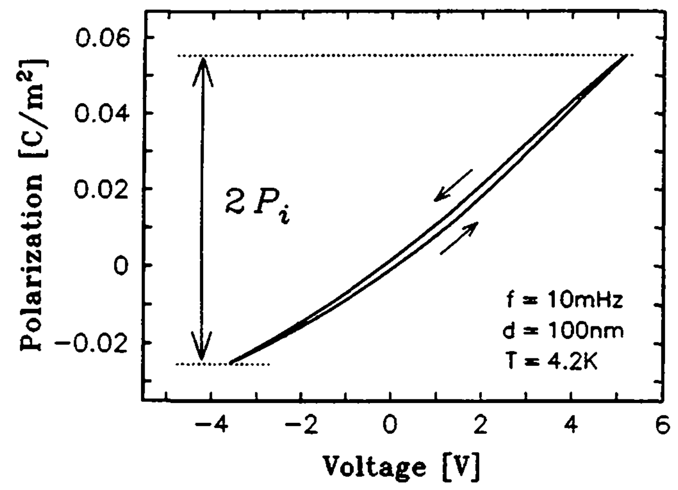

Figure 6.11 Definition of P_i. (Data taken from Fig. 6.10.)

specimen for which the field was first swept to negative and then to positive voltages showed different breakdown characteristics than one undergoing the opposite treatment. Breakdown strengths in excess of 35 V were observed on many samples [see for example Fig. 6.15(b) below], while the values of P_i did not vary much from one film to another.

c) $C(V)$ measurements

With the above method to study the polarization, precise results are obtained only after repeated voltage sweeps; no information is gained concerning the original state of the sample before application of the maximum voltage. Thus, capacitance vs voltage measurements were also performed as they do not exhibit this serious drawback.

Measurements were performed by slowly varying the applied dc bias (at a rate of about 0.5 V/min), while the capacitance was measured with a test signal of amplitude $\lesssim$ 50 mV and frequency 10 kHz. (Measurements with 1 kHz yielded identical results.)

Results from successive voltage sweeps

The $C(V)$ curves obtained on successive voltage sweeps exhibit some rather peculiar characteristics. Figure 6.12 shows a sketch of this behavior, which can be described as follows (numbers in parentheses refer to Fig. 6.12): As the bias is swept from zero (1) to a positive voltage [positive polarity at the top (metal) electrode], the capacitance first reaches a maximum (2), then falls off sharply. Sweeping back towards a negative

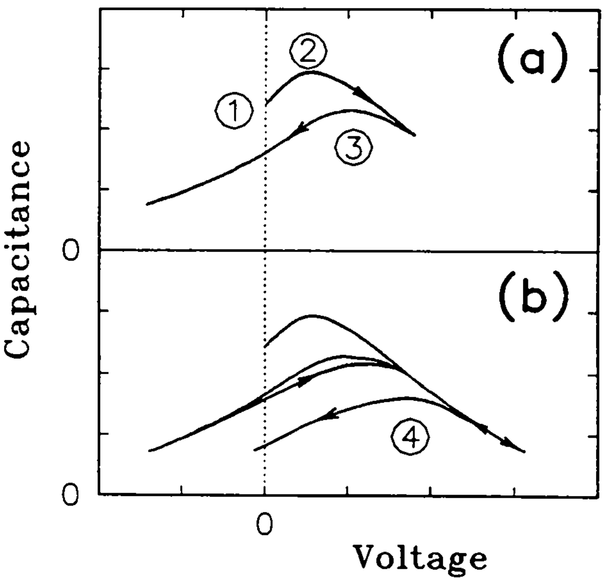

Figure 6.12 Sketch of characteristic features of the $C(V)$ curves. Arrows indicate sweep direction; the curve in (b) represents the continuation of (a) (see text).

bias, the maximum occurs at a higher voltage (3), the value of which depends on the maximum positive bias previously applied. At the same time, the capacitance is strongly reduced. The effect of the negative bias is reversible and relatively small: if the bias is being swept between given voltages, repeated cycling does not modify the shape of the traced hysteretic curve. However, every time the maximum positive field is increased, a change of the $C(V)$ curve's shape is observed (4).

Figure 6.13 displays the results for a 100-nm-thick film. The three simultaneously measured quantities, i.e. the capacity C, the ac conductivity G, and the sample current I, are shown normalized to the electrode surface S. The sample used for this figure had one of the highest values of ε_{eff} observed [ε_{eff}(4 K) > 200]. Figure 6.14 shows $C(V)$ curves for two typical samples with film thicknesses of 100 and 200 nm, respectively. Similar curves were obtained on all samples, with the absolute values varying in the same way as observed above for the temperature dependence $\varepsilon_{\text{eff}}(T)$ (Fig. 6.8).

Influence of the sample current

The properties of a sample change significantly if a current exceeding a fraction of

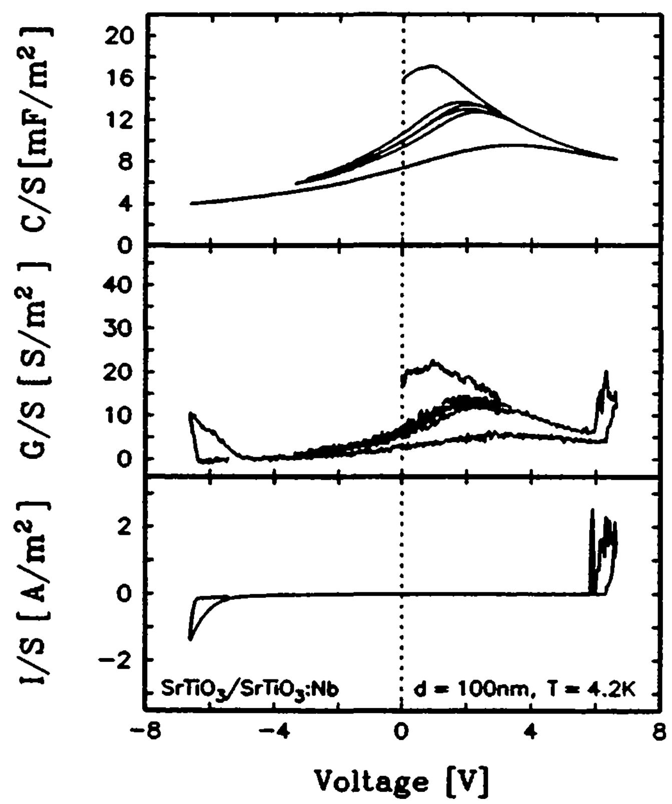

Figure 6.13 Results of a simultaneous measurement of the capacity C, conductivity G, and sample current I, all normalized by the electrode area S, as a function of the applied dc bias V.
[Sample number R605]

1 $\mu A/mm^2$ is forced to pass through the film. This is illustrated in Fig. 6.15. Both capacitance and current are shown for two 100-nm-thick films. The dotted arrows in the lower part of each figure indicate how the voltage is swept. In Fig. 6.15(a), the bias is swept back and forth to successively higher voltages. Additionally, the sweep direction is reversed whenever the sample current exceeds an absolute value of 0.7 $\mu A/mm^2$. Over the first few back-and-forth sweeps, during which no current is observed in forward bias (+ on the Mg electrode), the magnitude of the negative voltage at which the current becomes appreciable increases. However, if a current is forced to pass through the sample in forward direction, the insulation strength in backward direction is reduced by a factor of two.

A similar observation is made in Fig. 6.15(b). Again it is seen that after positive

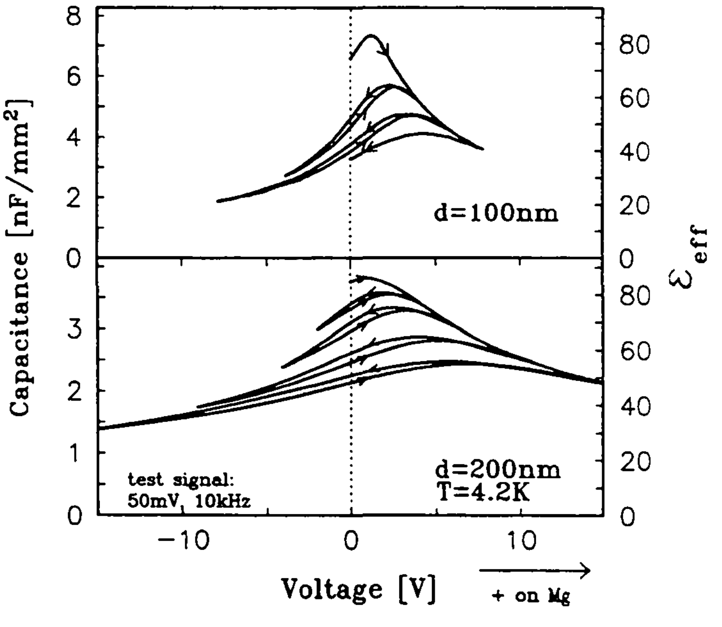

Figure 6.14 Effective dielectric constant ε_{eff} at 4.2 K of two Mg/SrTiO$_3$/-SrTiO$_3$:Nb heterostructures with SrTiO$_3$ film thicknesses of 100 and 200 nm as the bias voltage is swept to successively higher values. [Sample number R468 (top) and R491 (bottom)]

current biasing, the negative breakdown strength decreases from its originally high value of $\gtrsim$ 35 V. Additionally, however, it is also noted that forcing a current in the negative direction *increases* the breakdown strength in positive (forward) bias.

In Fig. 6.15(b), the scale for the positive current was chosen differently from the one for the negative values. The reason for this is as follows: as mentioned above, the criterion for reversing the sweep direction is the detection of a current larger than 0.7 μA/mm^2, after which the voltage is slowly swept back. For the sample in Fig. 6.15(b), conductivity remains high down to voltages considerably lower than the one at which the bias sweep direction was reversed. In fact, the peak in the $I(V)$ curves occurs while sweeping back to zero.

The mechanism leading to these phenomena is not understood in detail. Charge injection into the film or charge trapping at interfaces are possible causes. The conclusion drawn from these experiments is that care must be taken when interpreting results of measurements in which a current has been forced through the sample, showing the importance of the simultaneous measurement of the current and the capacitance. The following analysis is limited to results from experiments in which

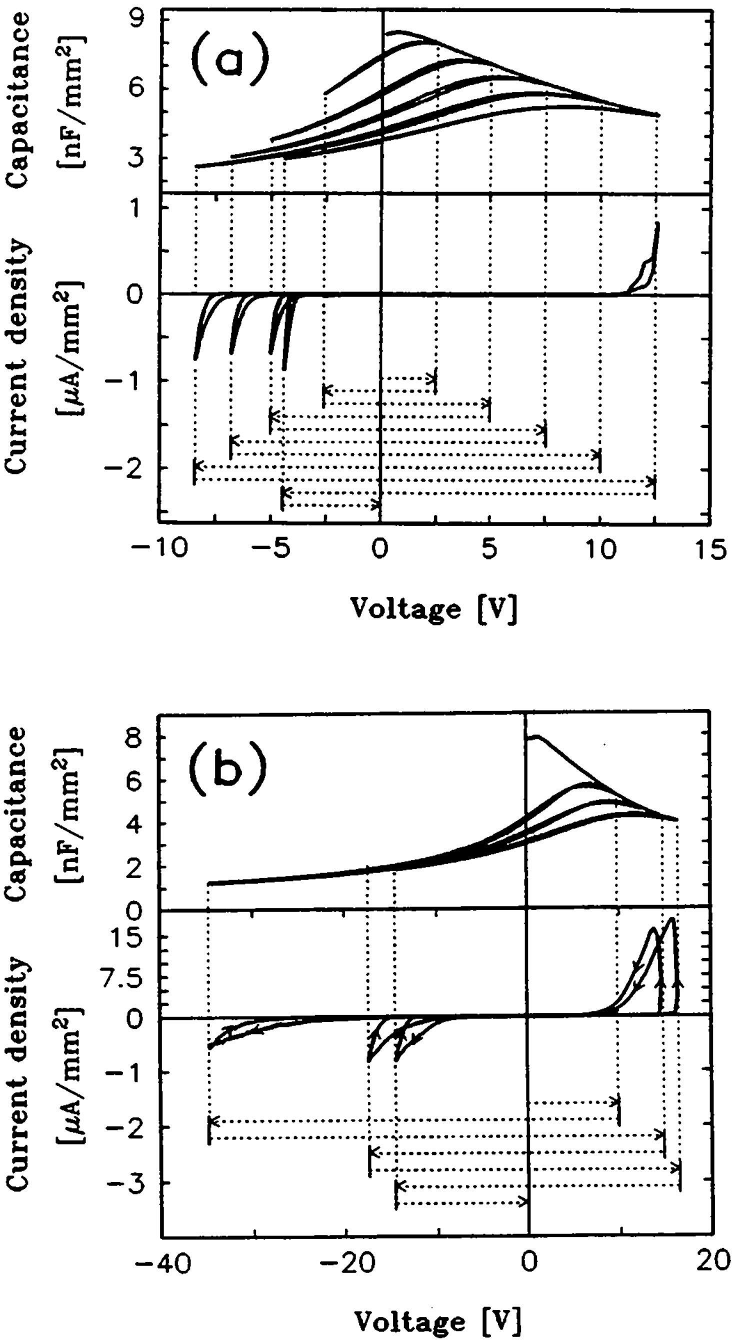

Figure 6.15 Capacitance and current recorded during successive voltage sweeps on two $SrTiO_3$ films (d = 100 nm). The dotted horizontal arrows show the direction in which the voltage is swept (see text). [Sample number R504]

the current flow through the film is negligible. It remains to be noted that the currents observed in the measurement of the $P(E)$ curves (section 6.2.2b), were three orders of magnitude below those relevant here, and well below the detection limit of the setup used for the $C(V)$ measurements.

Comparison to bulk data

It is interesting to compare the effective dielectric constant of the films (measured during the first sweep to positive voltages) to the dielectric constant of bulk $SrTiO_3$. In Fig. 6.16, the data of Figs. 6.13 (thin film) and Fig. 3.5(a) (bulk sample) are thus plotted in one graph. The values of ε_{eff} are traced versus the apparent electric field E^*, defined by

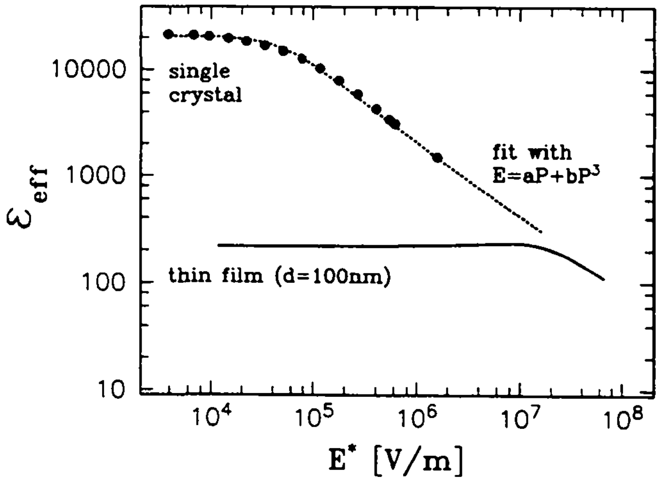

Figure 6.16 Comparison of the dielectric constant of single-crystal $SrTiO_3$ [points are data from Fig. 3.5(a)] and the effective dielectric constant of a $SrTiO_3$ thin film [solid curve, data from Fig. 6.13]. E^* is the apparent electric field defined in Eq. (6.2). Single-crystal data is extrapolated using Eqs. (3.2) and (3.3).

$$E^* = \frac{V}{d}, \tag{6.2}$$

where V is the applied dc voltage, and d is the thickness of the thin film or the bulk sample. Note that for thin film samples, E^* is not necessarily equal to the field across the film because of the voltage drop in the depletion layer in the substrate. This layer may persist to positive voltages (forward bias) due to trapped charges. For the highest positive voltages where the depletion layer is expected to vanish, data for this film and values extrapolated from the bulk correspond exceptionally well. For many samples, however, the agreement is worse, which is attributed to film imperfections, but always remains within a factor of 2–3. However, a strong discrepancy exists between bulk properties and film data for lower fields, as will be explained below (section 6.4).

Causes for the lowering of the capacitance after biasing

After application of a positive bias, the reduced capacitance seems to correspond to a stable state of the sample at these low temperatures, with the original values being recovered only after heating the sample to room temperature. This is illustrated in Fig. 6.17, which shows the curves obtained on a 100-nm-thick film upon cooling and reheating after a typical $C(V)$ experiment. Heating and cooling rates were 1/12 K/s.

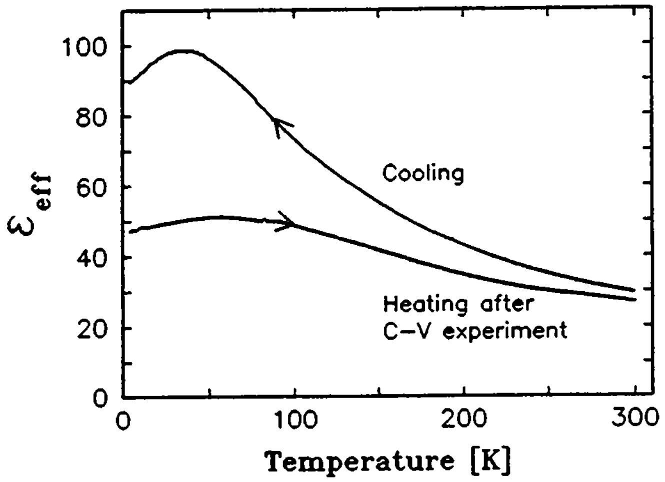

Figure 6.17 Temperature dependence of $\varepsilon_{\mathrm{eff}}$ for a SrTiO3 film (d = 100 nm) before and after a $C(V)$ experiment. [Sample number R444]

To investigate the cause of such a decrease, a constant voltage is applied to an otherwise virgin sample at various temperatures, and the time dependence $C(t)$ of the capacitance is measured after removal of this bias. At very low temperatures, such a study cannot be performed due to the long time scales (largely exceeding 2-3 days). Figure 6.18 displays the results of measurements between 260 and 300 K on a 50-nm-thick film. (This thickness is chosen because thicker films showed less pronounced effects.) The results are shown in terms of the normalized capacitance

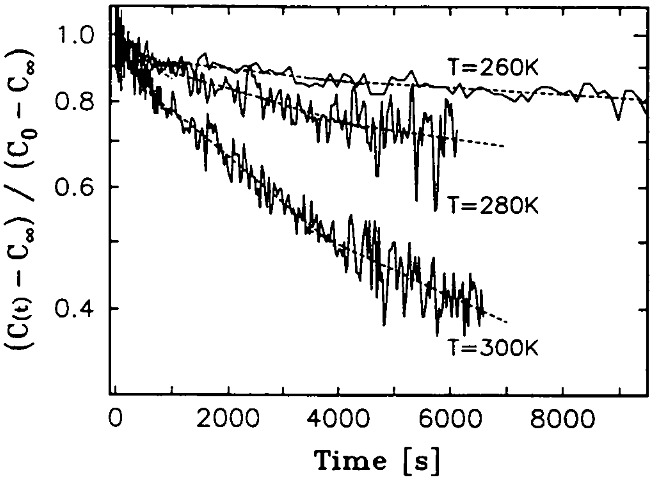

Figure 6.18 Normalized capacitance change of a 50-nm-thick $SrTiO_3$ film after removal of a 5 V bias as a function of time. Fsdjrf curves are fits (see text). [Sample number R508]

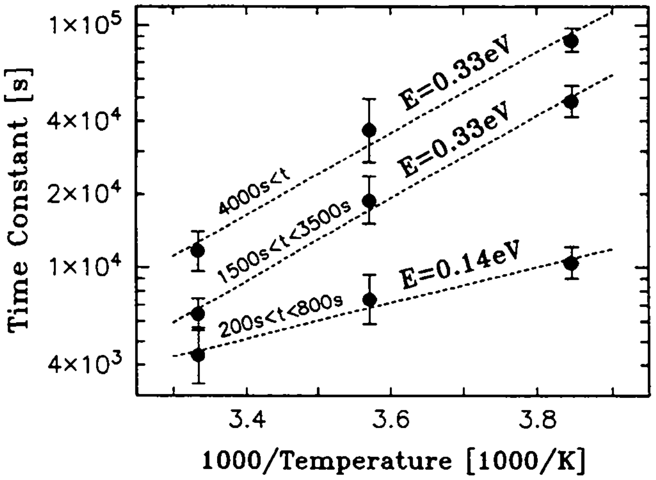

Figure 6.19 Arrhenius representation of the time constants extracted from Fig. 6.18, and fits to Eq. (6.5).

change

$$\Delta C_{\text{norm}} = \frac{C(t) - C_\infty}{C_0 - C_\infty}, \tag{6.3}$$

where $C(t)$ is the capacitance as a function of time measured from the moment the 5 V bias is removed. C_0 is the capacitance with the bias applied, and C_∞ is the capacitance before biasing, which is assumed to be identical to the value of $C(t)$ as $t \to \infty$. Noise on the data in Fig. 6.18 is due to the low ratio between the observed capacitance change (of the order of 50 pF) to the absolute capacitance (typically a few nanofarads).

In a log-lin representation of $\Delta C_{\text{norm}}(t)$, the data in Fig. 6.18 can be approximated by the succession of three linear regimes, leading to an expression of the form

$$\Delta C_{\text{norm}}(t) = \sum_{i=1}^{3} C_i \exp\{-t/\tau_i\}. \tag{6.4}$$

The time constants τ_i were extracted by linear regression of $\log(\Delta C_{\text{norm}})\,(t)$ over the three time intervals $200\,\text{s} < t < 800\,\text{s}$, $1500\,\text{s} < t < 3500\,\text{s}$, and $4000\,\text{s} < t$. The results are shown in Fig. 6.19 in an Arrhenius representation [$\log(\tau)$ vs $1/T$]. It is observed that the temperature dependence of the time constants approximately follows the expression

$$\tau_i = \tau_{i0} \exp \frac{E_i}{k_B T} \tag{6.5}$$

where E_i is an activation energy and k_B is the Boltzmann constant. While the data do not allow a conclusive interpretation to be made, the resulting activation energies, 0.14 and 0.33 eV, are compatible with the assumption made below (section 6.4) that the lowering of the capacitance is due to trapped charges (trap states 0.14 eV and 0.33 eV below the conduction band edge) at the film/substrate interface.

Comparison to $P(V)$ results

In section 6.2.2b, the $P(V)$ dependence of $SrTiO_3$ films was studied. The sample of Figs. 6.10 and 6.11 is used here to measure the capacitance vs voltage dependence over the same voltage interval. Figure 6.20 shows the perfectly overlapping curves obtained for four repeated sweeps. From such curves, the polarization can be obtained as

$$P(V) - P(V_0) = \frac{\varepsilon_0}{d} \int_{V_0}^{V} \{\varepsilon_{\text{eff}}(V') - 1\}\, dV' \tag{6.6}$$

where d is again the film thickness, and V_0 is an arbitrary lower integration bound. The result of this integration is compared in Fig. 6.21 to the data of Fig. 6.11. The agreement (curves differing less than 15%) between the two measurements, one performed at 10 mHz sweep frequency, the other one with a 10 kHz test signal, shows that $C(V)$ measurements probe the same mechanism as the low-frequency polarization vs voltage experiments. Therefore only the capacitance is analyzed further in the following.

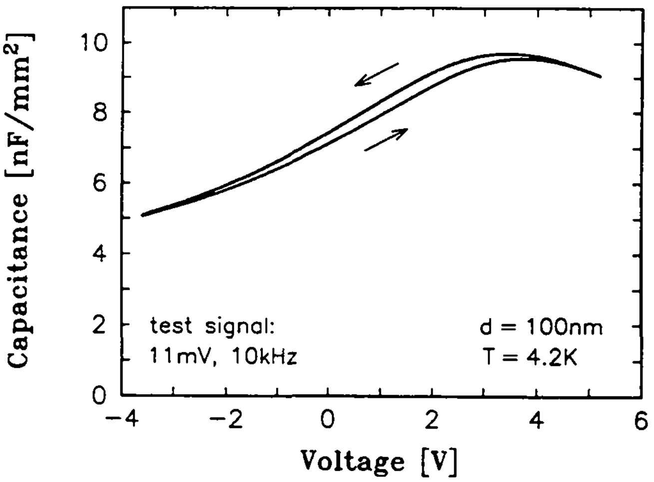

Figure 6.20 Repeated capacitance-voltage sweeps (4 full cycles) for a 100-nm-thick $SrTiO_3$ film. Arrows indicate sweep direction.

[Sample number R605]

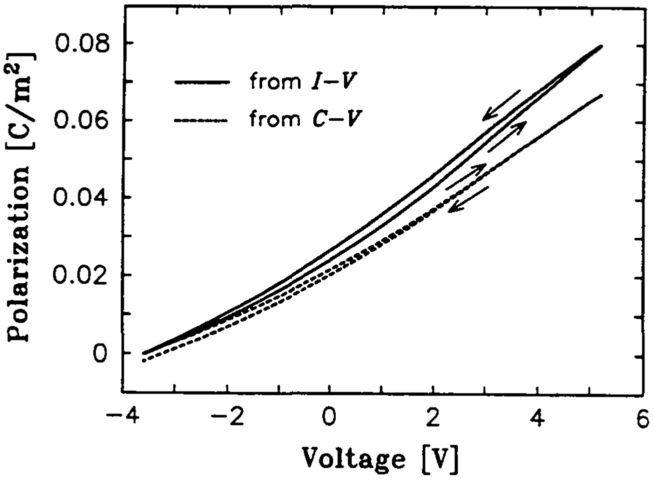

Figure 6.21 Comparison of the polarization vs voltage curves obtained by integration of the sample current (solid line) and of the capacitance (dashed line). Arrows indicate sweep direction.

[Sample number R605]

Before turning to a discussion of these results in terms of a simple model, alternative sample structures are considered in the following section, showing that similar phenomena are observed in modified structures.

6.3 Alternative sample structures

Experimental results are given for films grown by laser ablation, and for films sputtered onto Pt-covered $SrTiO_3$:Nb substrates or onto $SrRuO_3$ layers. No complete description of these structures' dielectric behavior is attempted; the results given suffice to justify the assumptions made in section 6.4 (modelling of the Mg/$SrTiO_3$/$SrTiO_3$:Nb heterostructures).

6.3.1 Laser-ablated films

Samples were prepared with the same structure as studied above (depicted in Fig. 6.5), but with $SrTiO_3$ films grown by pulsed laser ablation rather than rf sputtering. The substrate was kept at 710 °C during deposition in an oxygen pressure of 200 mTorr. These samples were studied by the dielectric methods described section 6.2.2 [see Fig. 6.22 for a $C(V)$ curve of a laser-ablated film]. No clear distinction can be made between the dielectric properties of the samples grown by the two different methods. However, the laser-ablated films showed slightly lower breakdown strengths and dielectric constants, possibly due to imperfections.

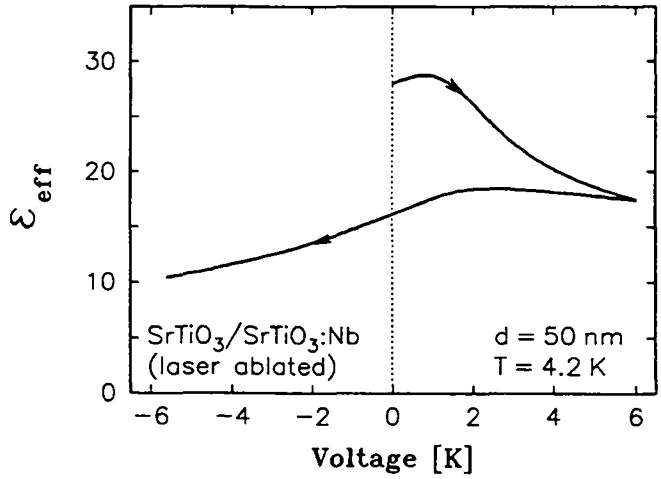

Figure 6.22 Capacitance-voltage curve for a 50-nm-thick $SrTiO_3$ film grown by pulsed laser ablation. [Sample number R565]

6.3.2 Pt layer

Platinum is a promising material to be used as a substrate for $SrTiO_3$ films. Its lattice constant is 3.92 Å, compared to the 3.91 Å of $SrTiO_3$, and $SrTiO_3$ films have recently been grown on Pt layers by various groups (for example in $Pt/SrTiO_3/Pt/SiO_2/Si$[10] and $Ni/SrTiO_3/Pt/MgO$ [Ref. 161] heterostructures).

A stronger modulation of the superconducting properties was obtained in Ref. 19 by applying a voltage to $Au/YBa_2Cu_3O_{7-x}/SrTiO_3/Pt/SrTiO_3$:Nb samples than to specimens without platinum. This further motivates the study of $Mg/SrTiO_3/Pt/$-$SrTiO_3$:Nb heterostructures. For these samples, the $SrTiO_3$ films are grown by rf sputtering onto a Pt layer which is deposited by e-beam evaporation onto the $SrTiO_3$:Nb substrate. A substrate temperature of 600 °C is used for the growth of both the Pt and the $SrTiO_3$ layers.

As seen in TEM micrographs (Appendix G), the platinum does not grow in a single layer under the present growth conditions. Instead, crystalline "droplets" of $\sim$ 20–50 nm diameter form. The $SrTiO_3$ films in these structures exhibit an increased low-field polarizability but a lower breakdown strength compared to the $SrTiO_3/SrTiO_3$:Nb samples. This results in a smaller maximum polarization. More details about these samples are given in Appendix G.

6.3.3 $SrTiO_3$ films grown on a $SrRuO_3$ layer

$SrRuO_3$ is a perovskite with metallic conductivity.[162] Its growth conditions are compatible with those of $SrTiO_3$ films, and it is thus possible to grow $SrTiO_3/SrRuO_3/SrTiO_3$:Nb heterostructures. A sketch of the cross section of this type of samples is shown in Fig. 6.23.

The 40–50-nm-thick $SrRuO_3$ layer is grown by pulsed laser ablation, and a metal mask is used to shield half the substrate during deposition. The resulting structure has the advantage that the effect of the $SrRuO_3$ layer can be studied without having to compare films obtained from different growth runs. This eliminates the complications due to the large differences in the dielectric properties of nominally identical films (see Fig. 6.8). Figure 6.24 shows the effective dielectric constant, ac conductance, and sample current recorded during repeated voltage sweeps on structures with and without a $SrRuO_3$ layer. The sweep parameters were identical for the experiments on both types of structures. The $SrRuO_3$ layer lowers the effective dielectric constant, and increases the ac conductance and the dc current considerably, implying a lower breakdown voltage. Additionally, it is seen that the film's properties do not change upon field cycling. At the beginning of the experiment this sample was thus already in the state that would be reached in $SrTiO_3/SrTiO_3$:Nb structures only after strong positive biasing.

The following section describes a model in which the lowering of the capacitance after positive biasing is ascribed to the trapping of charges at the film/substrate interface. In this interpretation, the data of Fig. 6.24 are seen as an indication of

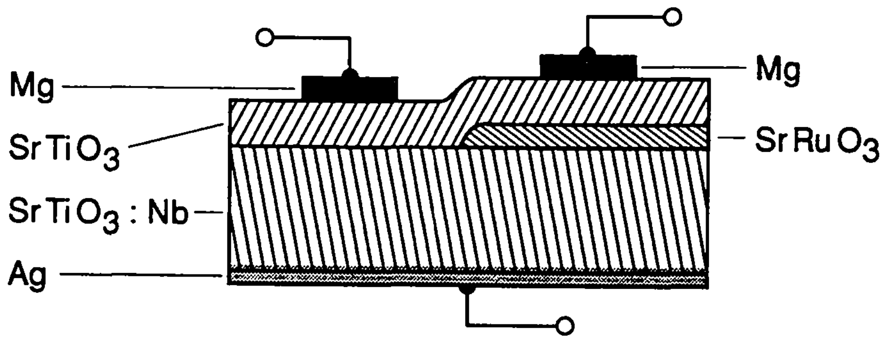

Figure 6.23 Sample structure allowing films grown on $SrRuO_3$ and $SrTiO_3$:Nb to be compared. Thickness of the $SrRuO_3$ layer: 40–50 nm.

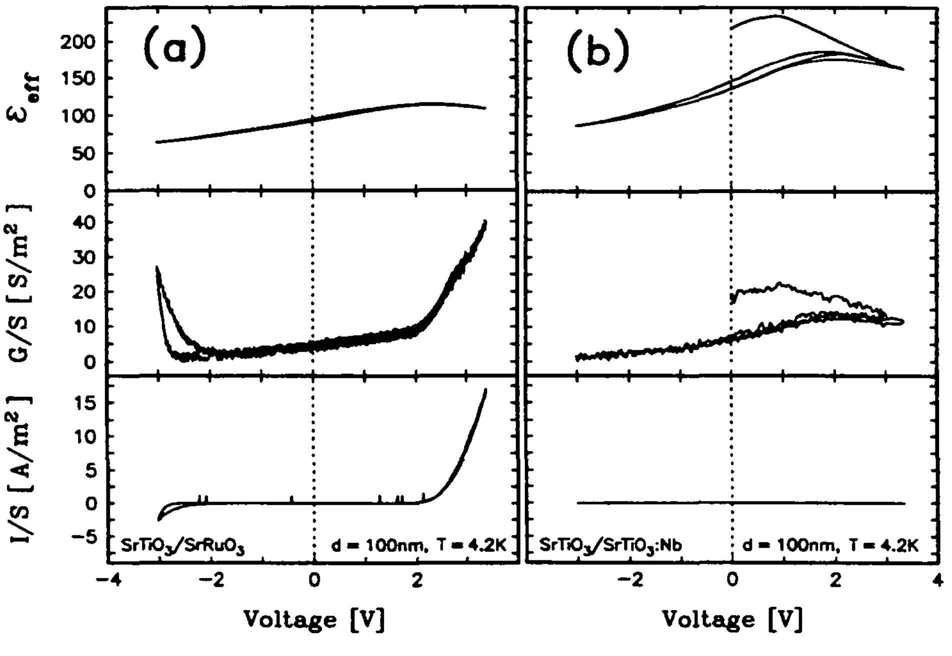

Figure 6.24 Effective dielectric constant, ac conductance and sample current for repeated voltage sweeps, measured (**a**) on a $SrTiO_3$ film deposited on a $SrRuO_3$ layer, and (**b**) on a $SrTiO_3$/$SrTiO_3$:Nb heterostructure for comparison. [Sample number R605]

strong charge trapping at the $SrRuO_3/SrTiO_3$:Nb or the $SrTiO_3/SrRuO_3$ interface. Interdiffusion between $SrTiO_3$ and $SrRuO_3$, and possibly a larger surface roughness, are probable reasons for the reduction of the breakdown strength.

6.4 Model

A simple model based on the nonlinear $P(E)$ relation, taking into consideration the low carrier density of the substrate and assuming charge trapping at the film/substrate interface, is shown to describe well the qualitative behavior of Mg/SrTiO$_3$/SrTiO$_3$:Nb heterostructures.

6.4.1 Assumptions and equations

The data presented in section 6.2 show strong qualitative and quantitative deviations from the single-crystal properties discussed in Chapter 3. Nevertheless, considering the results obtained for SrTiO$_3$ and SrTiO$_3$:Nb, a simple model is constructed in order to explain most of the characteristics of the presented thin film data, such as:

- the occurrence of a maximum near 30 K in the $C(T)$ curves,
- the relatively small value of the capacitance of the sample even at zero external bias,
- the occurrence of a maximum of the $C(V)$ curves at a positive voltage,
- the shift of this maximum to higher voltages after application of a positive bias,
- and the lowering of the capacitance after positive biasing.

The model is based on the following assumptions:

- the relation $E = \alpha P + \beta P^3$ holds for both the film and the substrate,
- the depletion approximation is valid in the substrate, i.e. it is assumed that the charge carrier density is constant within the depletion layer and given by the value obtained from measurements on Pt/SrTiO$_3$:Nb diodes (section 6.1),
- charge trapping occurs at the film/substrate interface when the semiconducting substrate is biased into accumulation, i.e. a proportion q of the charge accumulated at the film/substrate interface in positive bias (+ on the Mg electrode) remains trapped after the bias is removed,
- and some charge Q_{it} is already trapped at this interface at the beginning of the experiment.

The charge Q_{it} which is trapped in the film/substrate interface in the beginning of an experiment, and the proportion of the accumulated charge q which remains trapped after biasing, are the only free parameters of this model. They will be chosen such that the best qualitative agreement between model calculations and the experimental $C(V)$ and $\varepsilon_{\text{eff}}(T)$ curves is attained.

Figure 6.25 shows the band diagram and the charge density at weak forward bias (+ on the metal electrode). At this small positive voltage, the substrate is in depletion due to the interface trapped charge Q_{it}. The charge density as a function of distance measured from the substrate/film interface is given by

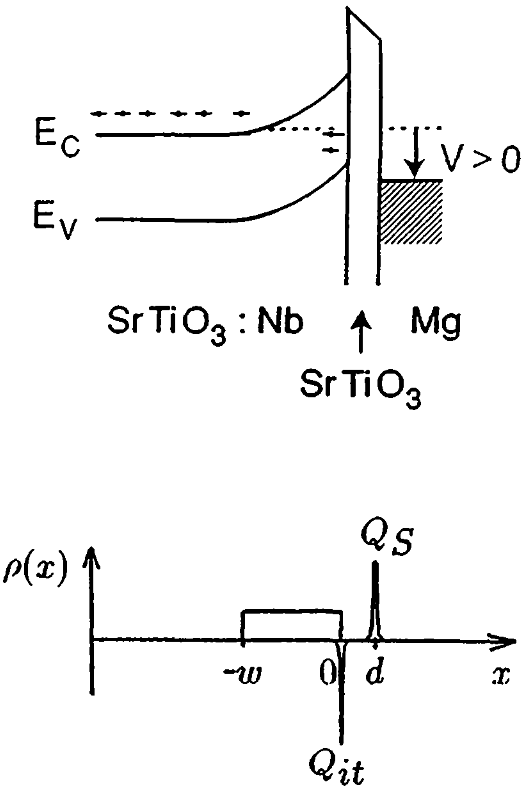

Figure 6.25 Band diagram (top) and space charge distribution (bottom) of a metal/$SrTiO_3$/$SrTiO_3$:Nb heterostructure under small forward bias.

$$\rho(x) = \rho_d(x) + Q_{\text{it}} \cdot \delta(x) + Q_s \cdot \delta(x - d) \tag{6.7}$$

with

$$\rho_d = \begin{cases} 4\times10^{16}\, e\,\text{m}^{-3} & -w < x < 0 \quad \text{(depletion)} \\ 0 & \text{elsewhere.} \end{cases} \tag{6.8}$$

Here, d is again the film thickness, e the electronic charge, and $Q_{\rm it} < 0$. The sign of $Q_{\rm s}$ is positive (negative) if the voltage difference across the film is positive (negative) [measured in the direction of the x-axis].

The band diagram is calculated numerically by integration of the one-dimensional Maxwell equation

$$\frac{\partial}{\partial x} \cdot D(x) = \rho(x) \tag{6.9}$$

with the boundary condition

$$D(x = d) = Q_{\rm s}. \tag{6.10}$$

Integration of Eq. (6.9) yields $D(x)$ for all values of x.

Using $D(E) = P(E) + \varepsilon_0 E$ [with the $P(E)$ relation as described in Chapter 3, Eq. (3.2)], $E(x)$ is obtained from $D(x)$ for any given $Q_{\rm s}$. The voltage across the sample is then determined by integrating

$$V = \int_{-w}^{d} E(x)\, dx \tag{6.11}$$

and is thus also given as a function of the surface charge, i.e. $V = V(Q_{\rm s})$. Numerical inversion yields $Q_{\rm s}(V)$, and the capacitance is found as

$$C(V) = \frac{\partial Q_{\rm s}(V)}{\partial V}. \tag{6.12}$$

More details about this calculation are given in Appendix E.

6.4.2 Calculation of $\varepsilon_{\rm eff}(T)$

Using the method described above with the values $\alpha(T)$ and $\beta(T)$ taken from Fig. 3.6, and of ρ determined in section 6.1,[b] the temperature dependence of the effective dielectric constant $\varepsilon_{\rm eff}$ is calculated.

In order to obtain the best qualitative agreement with the experimental data, the parameter $Q_{\rm it}$ has been chosen as

$$Q_{\rm it} = 143\,{\rm mC/m^2} = 8.9 \times 10^{13}\, e\,{\rm cm}^{-2} = 0.14\, e\, a^{-2}, \tag{6.13}$$

where a the lattice constant. It is noted that this value lies below those observed on clean Si surfaces (see Ref. 41, page 380).

In Fig. 6.26, the numerical results for $\varepsilon_{\rm eff}(T)$ are compared to the typical experimental values of Fig. 6.8, showing satisfactory agreement.

---

[b] The value of $\rho(T)$ for $T = 4.2$ K is chosen, assuming in agreement with the findings of other groups[23,158] that the temperature dependence can be neglected.

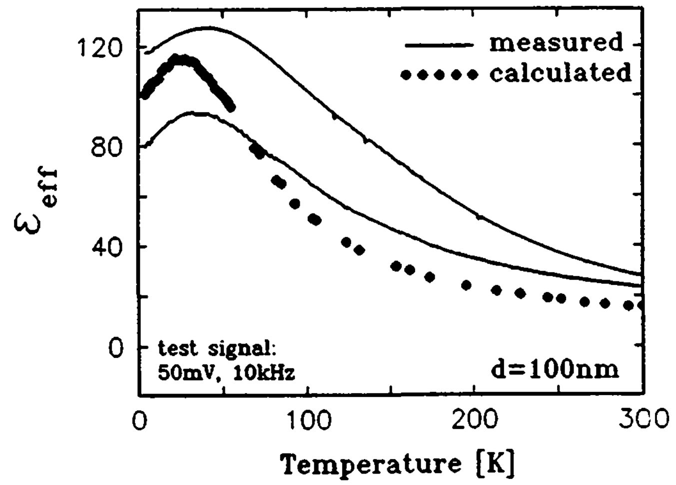

Figure 6.26 Comparison of the effective dielectric constant ε_{eff} as predicted by the model (dots) to the measurements. Both curves in Fig. 6.8 are shown again to indicate the typical spread of experimental data.

6.4.3 Calculation of $C(V)$

a) Procedure

With Eqs. (6.7)–(6.13), the capacitance of the heterostructure is readily calculated for any given voltage if the charge density profile $\rho(x)$ is known. In the sample's initial state, $\rho(x)$ is given by Eq. (6.7), as shown in Fig. 6.25. This charge profile correctly describes the sample for a nonvanishing depletion layer in the substrate. Reducing the voltage (applying a smaller positive or a negative voltage to the top electrode) leads to a larger depletion layer width, whereas increasing the voltage results in a smaller one. This latter case is shown in Figs. 6.27(1)–(3). Raising the voltage first increases the capacitance, because the depletion layer width (and thus the thickness of the insulating region of the sample) decreases [Fig. 6.27(2)]. At the same time, the field across the $SrTiO_3$ film increases, leading, due to the nonlinear $P(E)$ relation [Eq. (3.2)], to reduced polarizability. As the voltage is now further increased, sample capacitance is reduced [case (3)].

Let V^* be the voltage for which the depletion layer vanishes. In other words, V^* is defined as the voltage at which the substrate passes from depletion to accumulation,

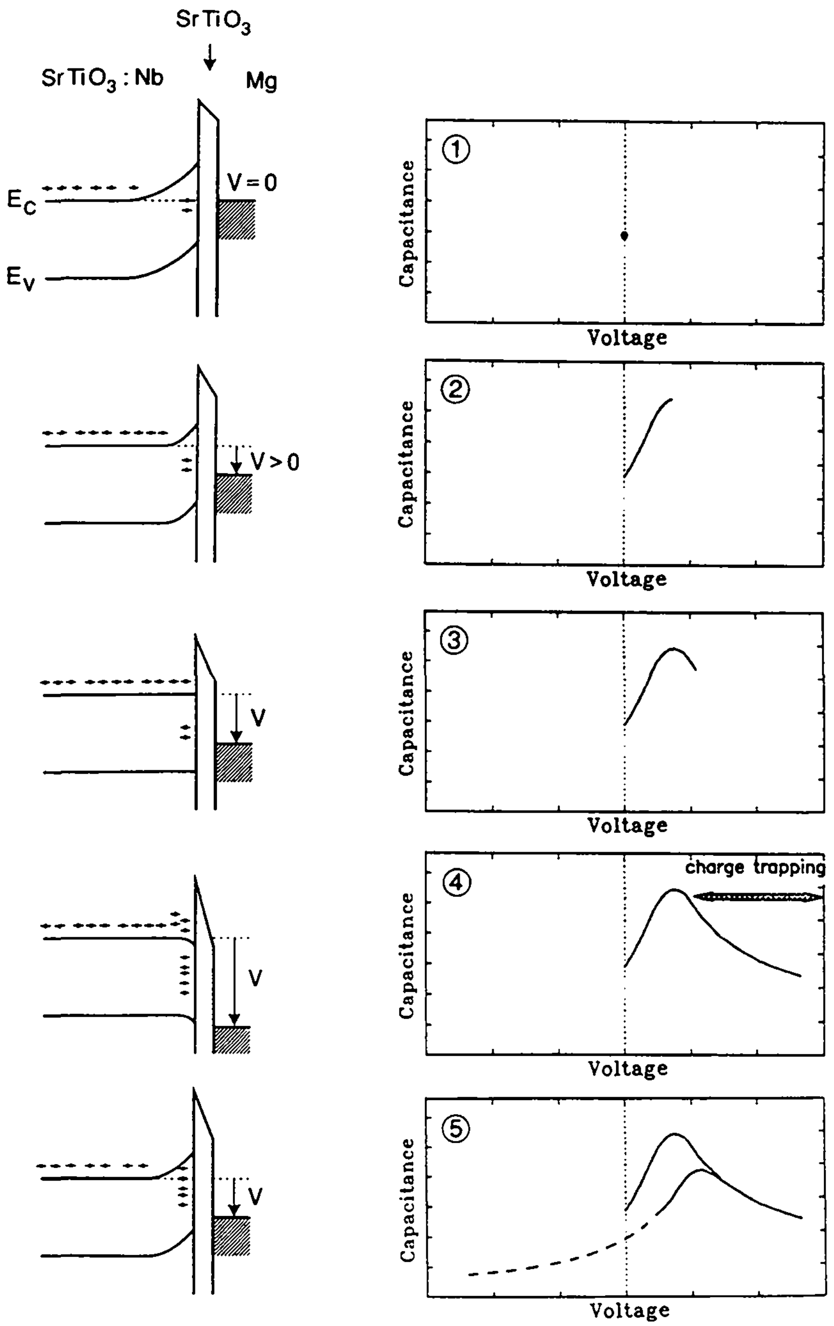

Figure 6.27 Band diagram and resulting $C(V)$ curves for different biases (see text).

or vice versa:

$$\begin{cases} V < V^* : & \text{depletion} \\ V > V^* : & \text{accumulation.} \end{cases} \tag{6.14}$$

As will be explained below, V^* depends on the sample history, due to the assumption that charges can be trapped at the film/substrate interface. Therefore, the quantity V_0^* is defined as the value of V^* for the first sweep towards positive bias. The situation for $V = V_0^*$ is shown in Fig. 6.27(3).

For larger positive voltages, case (4), the charge profile is no longer described by Eq. (6.7). Instead, the charge at $x = 0$ is now given by

$$\rho(x = 0) = Q_{\text{it}} + Q_{\text{acc}} , \tag{6.15}$$

where Q_{acc} is the additional accumulated charge [see Fig. 6.27(4)].

It is assumed that a proportion q of charge Q_{acc} becomes trapped at the interface. Whether an electronic charge is accumulated in the substrate's conduction band (near the film/substrate interface) or trapped at an interface state does not influence the sample's capacitance. However, if the sweep direction of the bias voltage is now reversed, it must be considered that only $(1 - q)$ of the accumulated charge can be removed from the interface. For numerical calculation, this is implemented by the following two replacements:

$$Q_{\text{it}} \leftarrow Q_{\text{it}} + qQ_{\text{acc}} \tag{6.16}$$

$$Q_{\text{acc}} \leftarrow (1 - q)Q_{\text{acc}} . \tag{6.17}$$

Therefore, as the bias is being swept back towards zero, the voltage V^*, determined by $Q_{\text{acc}} = 0$, now occurs at a higher value than was the case while sweeping up:

$$V^* > V_0^* . \tag{6.18}$$

In other words, the depletion case is reached at a higher bias, and thus the curve seems to be shifted towards more positive voltages. The amount of this shift is determined by the value of q. In order to have qualitative agreement with the experimental results, this value was chosen as

$$q = 0.9. \tag{6.19}$$

The value of C at the maximum of the capacitance-voltage curve is reduced because of the stronger field across the film resulting from the larger interface charge [Fig. 6.27(5)].

b) Results

Using the above procedure, the capacitance can be calculated for successive voltage sweeps.

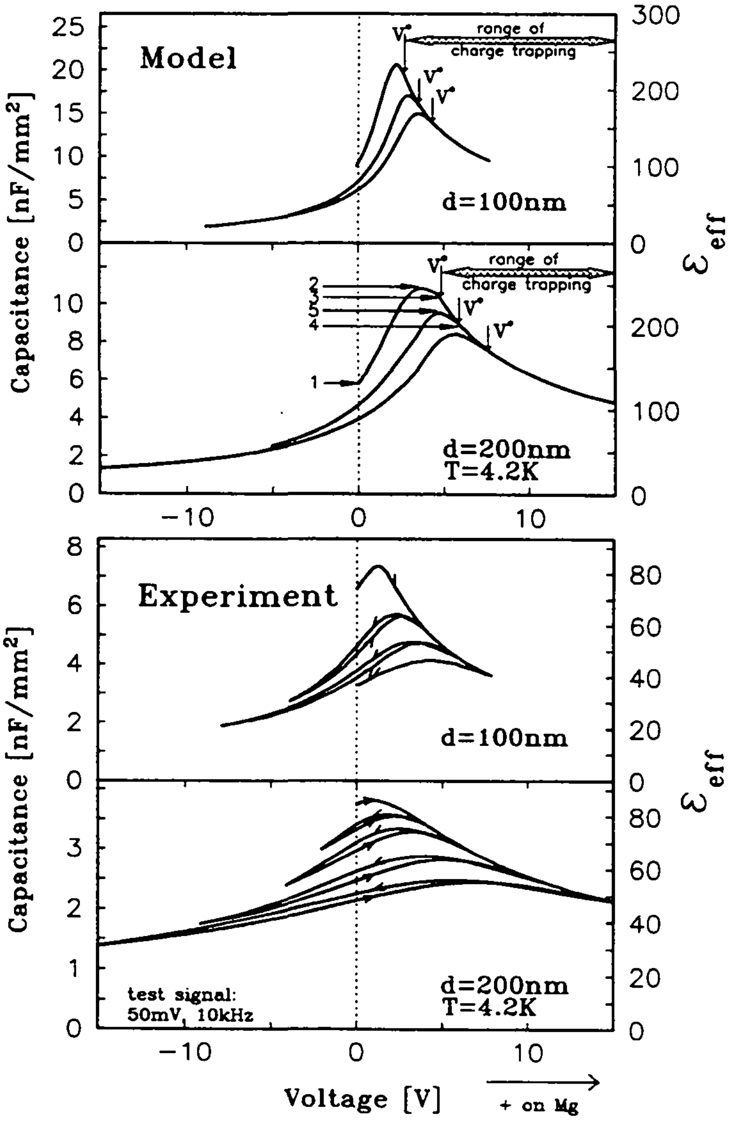

Figure 6.28 Top: Results of successive voltage sweeps calculated for $d = 100$ nm and $d = 200$ nm. V^* indicates the voltage at which the depletion layer vanishes.

Bottom: Experimental results from Fig. 6.14 for comparison.

The results for several sweeps at 4.2 K with repeatedly increased amplitude are shown in Fig. 6.28(a) and compared to the data of section 6.2.2. The general qualitative features of the calculated $C(V)$ curves agree with the experimental results. However, the calculated values are systematically lower than the measurements, except for the special case $V = 0$.

Choosing a different value for the model parameters does not improve agreement. In fact, during the first sweep towards a positive bias, Q_{it} is the only free parameter and is thus directly related to the capacitance measured at zero bias. From the $\varepsilon_{\text{eff}}(T)$ curves (Fig. 6.26), it is concluded that the parameter had been reasonably well chosen (although it is clearly seen that no unique value of Q_{it} is prescribed by the $\varepsilon_{\text{eff}}(T)$ curves: varying Q_{it} by a few percent does not result in significantly different values for the zero-bias capacitance).

Quite generally, the model predicts the maximum capacitance to be approximately double the zero-voltage value [see Fig. 6.28(a)]. In contrast, the experimental data never reach such a high peak, but remain close to the values obtained at $V = 0$.

The second free parameter, q, determines how much the maxima of the $C(V)$ curves are shifted after biasing to positive voltages. Choosing any value between 0.8 and 0.95 leads to very similar curves.

The differences between the measured and the calculated curves are discussed in the next section.

6.5 Comparison model–experiment

The roughness of the film/substrate interface and of the film's upper surface, as observed by TEM and AFM, as well as the high defect density are expected to influence the sample's dielectric behavior considerably. Interface roughness and defects will both result in mechanical stress, which lowers the dielectric constant.[1] Additionally, the surface roughness creates areas with larger and with smaller actual film thickness. In the present calculations, however, a single value d has been assumed. For large electrodes (in comparison to the characteristic length scales of the roughness and the film thickness), the effect of the thickness variation is expected to average out, and to have only a minor influence on the final result. However, the sharp maximum in the $C(V)$ curves predicted by the model will be slightly smeared out by this thickness variation.

Field inhomogeneities also result from defects and surface roughness. Therefore, parts of the sample are subject to a larger electric field and thus have a lower dielectric constant.

The model is limited by the assumption that the following two parameters are constant over the entire sample surface: the initial amount of charge Q_{it} trapped at the film/substrate interface and the proportion q of the accumulated charge that remains trapped at the interface when the bias is removed. A more realistic model would consider distributed values of these two parameters, and it is expected that the experimental $C(V)$ curves, which are considerably more smeared out than the calculated ones, would be better reproduced.

Studying the maximum polarization that can be induced on the film, a strong difference between the calculated ($P_{\mathrm{max}} = 200$ mC/m^2) and experimental ($P_i = 40$ mC/m^2) values is also observed. The two quantities are however not defined in the same way. For bulk samples, the breakdown voltage is defined by a precise value: applying a field above this threshold fractures the sample, indicative of an avalanche process.[40] For the films here, a different phenomena is observed: as the voltage is raised, the current increases in a manner that can be roughly approximated by an exponential dependence, and a small sample current does not destroy the film. Charge transport due to defects is a possible explanation for this conductivity, which occurs at fields below the bulk breakdown voltage.

The present interpretation implies that the Mg/SrTiO$_3$/SrTiO$_3$:Nb heterostructures withstand the high voltages (exceeding 35 V for a 100-nm-thick film) not because of a large breakdown strength, but because of a wide depletion layer. In this picture, the variations between different samples are mainly due to changes in the surface properties of the substrates, in particular to the density of trapped charge at the film/substrate interface.

6.6 Summary and discussion

A detailed study of the dielectric behavior of rf-sputtered $SrTiO_3$ thin films in $Mg/SrTiO_3/SrTiO_3$:Nb heterostructures has been presented (section 6.2) and complemented by results obtained for films grown by pulsed laser ablation and experiments on $Mg/SrTiO_3/Pt/SrTiO_3$:Nb and $Mg/SrTiO_3/SrRuO_3/SrTiO_3$:Nb samples (section 6.3).

A formalism has been introduced in section 6.4 which allows the capacitance of metal/$SrTiO_3/SrTiO_3$:Nb structures to be calculated. Using the nonlinear polarization vs voltage dependence (as studied in Chapter 3), taking into consideration the low carrier density near the surface of the $SrTiO_3$:Nb substrates (section 6.1) and assuming charge trapping to occur at the film/substrate interface, model calculations yield qualitatively correct results for the $\varepsilon_{\text{eff}}(T)$ and $C(V)$ dependences. The reproduced features include

- the maximum of the $\varepsilon_{\text{eff}}(T)$ curves,
- the generally low values of the capacitance at zero voltage bias,
- the occurrence of a maximum in the $C(V)$ curves for $V > 0$,
- the shift of this maximum induced by positive biasing,
- and the lowering of the capacitance after positive biasing.

Experimental values for the effective dielectric constant in excess of 200 (corresponding to a capacitance of 18 nF/mm^2) are obtained for the best samples, and an induced polarization as large as 40 mC/m^2 is routinely observed.

The differences between calculated and measured values for the capacitance are attributed to the surface roughness of the substrate and the imperfection of the film's crystallinity. In addition, the simple model assumes that the two free parameters, i.e. the interface trapped charge Q_{it} and the proportion q of the accumulated charge being trapped, are constant over the entire sample surface. For a more detailed model, a spatial distribution of these two quantities would have to be considered.

The maximum polarization that has been induced in these samples lies approximately a factor of five below the value P_{max} extrapolated from the bulk properties of $SrTiO_3$ at lower fields. It is assumed that in addition to being caused by defects and surface roughness, much of this difference arises due to electronic transport at voltages below the breakdown field.

7. Conclusion

Fundamental properties of systems containing dipoles interacting via a highly polarizable host lattice have been investigated in the mixed crystal $K_{1-x}Li_xTaO_3$. Here, the dipoles induced by the off-center positions of the Li impurities can reorient through π or $\pi/2$-flips. The π-flips correspond to head-to-tail reorientations, such as changes from a displacement along [100] to a displacement along [$\bar{1}$00]. All other reorientations involve a rotation of the associated moment by 90° and are thus called $\pi/2$-flips. In this study, results are presented for $2.5\% \leq x \leq 4\%$, i.e. for concentrations where the two relaxation branches (associated with π- and $\pi/2$-flips) are observable, and slightly above the range in which a dipole glass state was previously observed. It is concluded that modelling the system at these concentrations goes beyond the scope of current orientational glass Hamiltonians, in which the dependence of the coupling constants on the bond direction is usually neglected. The previously observed clusters of nonvanishing polarization develop to minimize the Li-Li interaction energy, but without leading to ferroelectric properties. The polarization of these clusters cannot be switched by an applied electric field, and the relaxation time neither diverges as in ideal ferroelectrics, nor peaks as in diffuse phase transitions materials. Instead, motion slows down with an Arrhenius-type temperature dependence of the leading relaxation time, indicating that single-particle hopping remains the dominant mechanism at all investigated temperatures. However, relaxation is controlled by hierarchical constraints. Upon cooling, the quadrupole moments of a growing number of impurities are "locked" into a particular state. This leads to a gradual freeze-out of the relaxation branch associated with $\pi/2$-flips, while head-to-tail motion of the moments, which is not accompanied by a change of the quadrupolar component, remains possible. Therefore, a crossover of the dynamics from a faster to a slower relaxation branch is observed at a temperature T_f.

The present work shows the existence of two relaxation branches in the prototype "relaxor" $Pb(Mg_{1/3}Nb_{2/3})O_3$. The microscopic origin of this behavior is unclear at present, but it closely resembles the properties of glass-forming polymers: at high temperatures, relaxation is dominated by a branch which is labelled α-type; upon cooling, this branch disappears from the experimental frequency window and a β-type relaxation takes over. At T_m, defined as the frequency-dependent maximum of the $\varepsilon'(T)$ curves, neither the relaxation step, nor the relaxation time, nor the parameters describing the shape of the $\varepsilon(\omega)$ dependence, show any anomalies. The peaks in the $\varepsilon'(T)$ curves are of purely dynamic origin, rather than being related to a structural phase transition.

As an application of highly polarizable perovskites, epitaxial $SrTiO_3$ films deposited on semiconducting $SrTiO_3$:Nb substrates have been studied.

A formalism has been developed to calculate the capacitance of metal/insulator/semiconductor heterostructures for insulators and semiconductors with a polarizability given by the Devonshire theory, $E = \alpha(T)\,P + \beta(T)\,P^3$, and for strong charge trapping at the insulator/semiconductor interface.

For $SrTiO_3$, the $\alpha(T)$- and $\beta(T)$-values were obtained from single-crystal samples, allowing the $C(T)$ curves of Mg/$SrTiO_3$/$SrTiO_3$:Nb heterostructures to be calculated. The difference between the measured and the calculated values of $C(T)$ is comparable to the observed variations from one sample to another. For the capacitance-voltage curves, the disagreement remains within a factor of three and is attributed to film imperfections.

On typical samples, polarization changes of 80 mC/m^2 can be induced at 4.2 K by applying voltages as small as ± 5 V. To date, equally high charge densities induced by comparably small voltages have been reported only for devices based on ferroelectric films. Extrapolation from $SrTiO_3$ single crystal data (Chapter 3) shows that values up to 400 mC/m^2 are expected for more perfect films of this paraelectric.

Appendix A

Phenomenology of dielectric relaxation

The purpose of this appendix is to summarize the basic concepts of dielectric relaxation required for the understanding of this work. It does not contain new results, but justifies the choices made for data representation and parameterization.
The present study is restricted to small excitations, and thus to a linear response. Section A.1 defines the fundamental quantities amd establishes consistent notation. The Kramers-Kronig theorem is introduced in section A.2, and the importance of time-domain measurements and their relation to the frequency-domain observations are discussed in section A.3. The connections between these fundamental concepts and observable quantities are treated in section A.4, and the various possibilities for representation of dielectric data are compared in section A.5. Several frequently-used empirical decay functions are discussed in section A.6, and different methods of data parameterization are explained in section A.7.

A.1 Susceptibility and response function

For simplicity of notations we assume a sample shaped as a thin plate with two identical faces of surface S and with thickness d, as shown in Fig. A.1. For this configuration, the general tensor equation relating polarization and electric field reduces to a scalar expression, and for sufficiently low fields can be written as

$$P = \varepsilon_o \chi_S E \tag{A.1}$$

where $\varepsilon_o = 8.85$ pF/m is the permittivity of free space. Equation (A.1) defines the **static, linear (dielectric) susceptibility** χ_S.

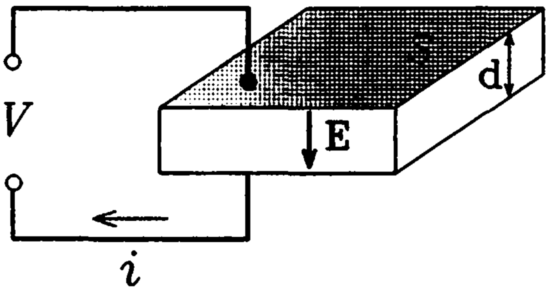

Figure A.1 Simplified sample geometry: The application of a voltage V to the surfaces S creates an electric field E across the plate with thickness d. A current i will flow either if the voltage is time-dependent or if the sample is conducting.

In the general case of a time-varying electric field $E(t)$, the behavior of the dielectric polarization $P(t)$ can be described by the **response function** $f(t)$ defined by

$$P(t) = \varepsilon_o \chi_s \int_0^\infty f(\tau)\, E(t-\tau)\, d\tau \quad \text{with} \quad \int_0^\infty f(t)\, dt = 1. \tag{A.2}$$

Here it is assumed that the response of the system is independent of its polarization (**superposition principle**), which is a consequence of the linear $P(E)$ relation [Eq. (A.1)]. Taking 0 rather than $-\infty$ as the lower integration bound is equivalent to defining $f(t) = 0$ for $t < 0$, thus satisfying the principle of **causality**. The energy conservation is expressed as $\int_0^\infty f(t)\, dt < \infty$.

If we choose a **step excitation** $E(t) = E_0(1 - \theta(t))$, where $\theta(t)$ is the Heavyside function, and hence

$$E(t) = \begin{cases} E_0 & t < 0 \\ 0 & t > 0 \end{cases} \tag{A.3}$$

then (A.2) reduces to

$$P(t) = \varepsilon_o E_0 \chi_S F(t). \tag{A.4}$$

The function $F(t)$ introduced in (A.4) is called the **decay function** and is defined

$$F(t) \equiv 1 - \int_0^t f(\tau)\, d\tau. \tag{A.5}$$

It is a dimensionless quantity and takes the value 1 at time zero and vanishes for $t = \infty$.

For a **sinusoidal excitation** $E(t) = E_0 \sin \omega t$, (A.2) becomes

$$\begin{aligned} P(t) &= \varepsilon_o \chi_S E_0 \int_0^\infty f(\tau)\, \sin(\omega(t-\tau))\, d\tau \\ &= (\varepsilon_o E_0 \sin \omega t \int_0^\infty \chi_S f(\tau) \cos \omega\tau\, d\tau \\ &\quad -\varepsilon_o E_0 \cos \omega t \int_0^\infty \chi_S f(\tau) \sin \omega\tau\, d\tau). \end{aligned} \tag{A.6}$$

Introducing the frequency-dependent quantities

$$\chi'(\omega) = \int_0^\infty f(\tau)\, \cos \omega\tau\, d\tau \tag{A.7}$$

$$\chi''(\omega) = \int_0^\infty f(\tau)\, \sin \omega\tau\, d\tau \tag{A.8}$$

we can simply rewrite (A.6) as

$$P(t) = \chi'(\omega)\, E(t) - \chi''(\omega)\, E(t + \frac{1}{\omega} \cdot \frac{\pi}{2}) \tag{A.9}$$

where $\chi'(\omega)$ describes the in-phase behavior of $P(t)$ and $\chi''(\omega)$ the quadrature component.

Using the complex notations $E(t) = E_0^* \exp[j\omega t]$, and $P(t) = P_0^* \exp[j\omega t]$, where E_0^* and P_0^* are complex numbers, we have

$$P_0^* = \chi(\omega) \cdot E_0^* \tag{A.10}$$

with

$$\chi(\omega) = \chi'(\omega) - j\chi''(\omega). \tag{A.11}$$

It is now obvious that the relation between $f(t)$ and $\chi(\omega)$ can be expressed in terms of one-sided Fourier (i.e. imaginary Laplace) transforms

$$\chi(\omega) = \int_0^\infty \chi_S f(t)\, e^{-j\omega t}\, dt \tag{A.12}$$

$$f(t) = \frac{1}{2\pi\chi_S} \int_0^\infty \chi(\omega)\, e^{j\omega t}\, d\omega, \tag{A.13}$$

i.e.

$$\chi(\omega) = \{\mathcal{F}[P(t)](\omega)\} \cdot \{\mathcal{F}[E(t)](\omega)\}^{-1} \tag{A.14}$$

where $\mathcal{F}$ denotes the Fourier transform in the usual sense. The relations between $\chi(\omega)$ and $F(t)$ are given by

$$\chi(\omega) = \chi_S\{1 - \int_0^\infty F(t) j\omega\, e^{-j\omega t}\, dt\} \tag{A.15}$$

$$F(t) = 1 - \frac{1}{2\pi\chi_S} \int_0^\infty \frac{\chi(\omega)}{j\omega}\, e^{j\omega t}\, d\omega. \tag{A.16}$$

A.2 Kramers-Kronig theorem and dc conductivity

Linearity, causality, and energy conservation lead to Eq. (A.2) relating $P(t)$ and $E(t)$. The same assumptions, together with the homogeneity of time, result in the following equations, known as the **Kramers-Kronig equations**, which relates the real and imaginary parts or the susceptibility:[163]

$$\chi'(\omega) = \frac{2}{\pi}\mathcal{P}\int_0^\infty \frac{x \cdot \chi''(x)}{x^2-\omega^2}\,dx \tag{A.17}$$

$$\chi''(\omega) = -\frac{2\omega}{\pi}\mathcal{P}\int_0^\infty \frac{\chi'(x)}{x^2-\omega^2}\,dx \tag{A.18}$$

where $\mathcal{P}$ denotes the principal value in Cauchy's sense. For very wide relaxation peaks, the previous equations can be approximated by[164]

$$\chi''(\omega) \sim \frac{\partial\chi'(\omega)}{\partial \ln\omega}. \tag{A.19}$$

Equations (A.17) and (A.18) show that either $\chi''(\omega)$ or $\chi'(\omega)$ is sufficient to characterize a system without loss of information if the system satisfies the above conditions. However, if **dc conductivity** σ_0 is present in the system under investigation, then an additive term σ_0/ω appears in the imaginary part of the experimentally determined susceptibility.[78] Knowledge of the complete complex susceptibility together with a numerical calculation of (A.17) allows the σ_0 term to be determined.

Finally, it follows from (A.17) that

$$\chi'(0) = \frac{2}{\pi}\int_{-\infty}^{\infty} \chi''(\omega) d\ln\omega. \tag{A.20}$$

This relates the area under the loss curve in a log-linear representation to the total polarizability and also shows that $\chi' \neq 0$ necessarily implies the presence of a frequency interval for which $\chi'' \neq 0$.

A.3 Time-domain and frequency-domain observations

It is tempting to use the first-order differential equation

$$\frac{dP}{dt} = \frac{h(t)}{\tau}[c_0E(t) - P(t)]. \tag{A.21}$$

as a model for dielectric relaxation. By allowing, for example, $h(t) = a \cdot t^{-b}$, $b \neq 1$, one finds[165,166] the "Kohlrausch" decay [see page A-12] $P(t) \sim \exp\{-(\alpha t)^\beta\}$ as a response to a step excitation (A.3). However, it should be noted that the Fourier relations (A.12) and (A.13) are not applicable to systems governed by an equation of the type (A.21), as was pointed out recently by Kliem.[107] In fact, only functions that originate from linear time-invariant systems may be Fourier transformed in order to yield the material properties in the frequency range.[167] A differential equation with time-dependent coefficients can result in a nonsinusoidal time dependence of the polarization even if the system is sinusoidally excited, and it would be impossible to define a time-independent susceptibility.

In other words, it is always possible to determine a decay function experimentally if Eq. (A.4) [$P(t) \propto F(t)$ after a step excitation] is taken as a definition [which is not the case: it is a consequence of (A.2)]. With the knowledge of such a possibly ill-defined "decay function", we **cannot** always proceed to define a susceptibility by use of the Fourier transforms (A.12). The latter equation is only valid if we suppose a dependence of P on E as described by Eq. (A.2) .

Based on these considerations it is clear that time-domain measurements are an essential part of dielectric studies.

A.4 Observable quantities

The **depolarization current** $i(t)$ is the measurable response of a system to a step variation (A.3) of the external electric field. From the proportionality of the polarization to the decay function, it follows that

$$\begin{aligned} i(t) = -\frac{\partial D}{\partial t} &= -\frac{\partial}{\partial t}(\varepsilon_o E(t) + P(t)) \\ &= \varepsilon_o E_0 \{\delta(t) + \chi_s f(t)\}. \end{aligned} \tag{A.22}$$

As $f(t)$ is a normalized function [Eq. (A.2)], a measurement of $i(t)$ yields both χ_s and $f(t)$. The experimental requirement for approximating the Heavyside time dependence of the charging field by a finite pulse consists of choosing the charging time to be nearly one order of magnitude larger than the largest time for which $f(t)$ is to be determined. Figure A.2 shows the effect of shorter charging times for a typical measurement on a $Pb(Mg_{1/3}Nb_{2/3})O_3$ single crystal.

Most often, the dielectric properties of a sample are determined from its capacitance C and conductance G. If we define the **dielectric permittivity**

$$\varepsilon(\omega) = 1 + \chi(\omega) \tag{A.23}$$

and write $\varepsilon = \varepsilon'(\omega) - j\varepsilon''(\omega)$, then it follows from simple considerations that

$$\varepsilon' = \frac{C}{C_o} \quad \text{and} \quad \varepsilon'' = \frac{G}{\omega C_o} \tag{A.24}$$

where $C_o = \varepsilon_o(S/d)$.

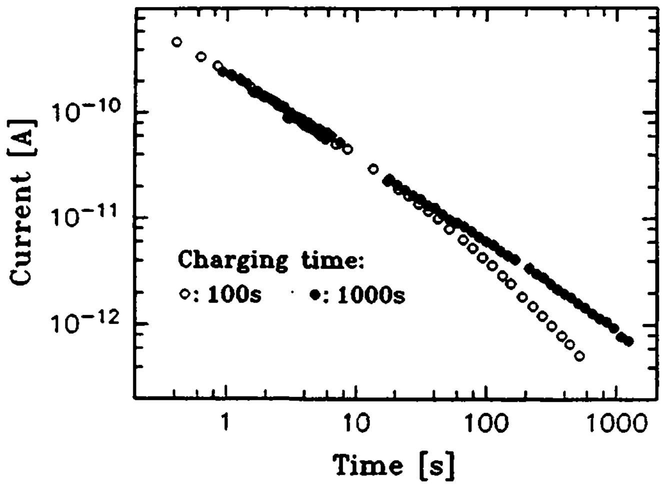

Figure A.2 Effect of charging time on the measured decay current: Open circles represent a measurement after a 100 s, solid circles after a 1000 s charging pulse. The sample is a $Pb(Mg_{1/3}Nb_{2/3})O_3$ single crystal.

The permittivity thus arises as a more natural quantity in experiments, and all results in this thesis are given in terms of ε. Figure A.3 shows a typical dielectric spectrum. Different regions of dielectric loss, and, correspondingly, different relaxation steps

$$\Delta\varepsilon^i = \int_{\ln\omega_-^i}^{\ln\omega_+^i} \varepsilon''(\ln\omega)d\ln\omega \tag{A.25}$$

can usually be distinguished, where the definition of $\omega_\pm^i$ is obvious from Fig. A.3. If the dielectric loss becomes negligibly small for ω approaching $\omega_\pm^i$, then the Kramers-Kronig relations [Eqs. (A.17) and (A.18)] hold for each such interval $[\omega_-^i, \omega_+^i]$ if ε' is extrapolated up to $\omega = \pm\infty$ by the value $\varepsilon'(\omega_\pm^i)$.

When studying a specified loss region, the notations

$$\begin{aligned} \varepsilon_\infty &= \varepsilon(\omega_+^i) \text{ and} \\ \varepsilon_S &= \varepsilon(\omega_-^i) \end{aligned}$$

are used.

The decay current corresponding to the spectrum of Fig. A.3 is shown in fig. A.4. It also exhibits the characteristics of the different loss regions, and can be written as a superposition

$$i(t) \propto f(t) = \frac{1}{\sum\Delta\varepsilon^i}\sum\Delta\varepsilon^i \cdot f^i(t). \tag{A.26}$$

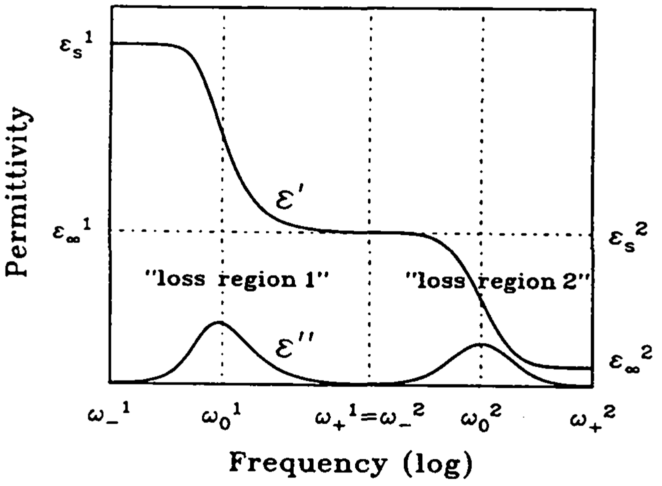

Figure A.3 Typical dielectric spectrum, where two relaxation phenomena can be distinguished. See text for explanations of the symbols used.

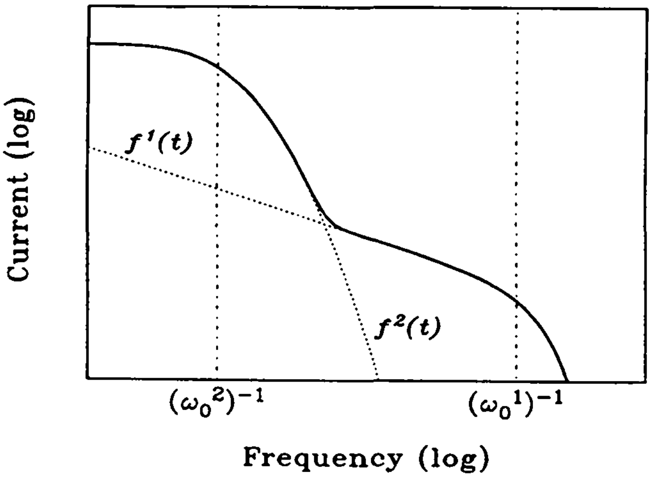

Figure A.4 Decay current corresponding to the dielectric spectrum in Fig. A.3. The two different relaxation phenomena are clearly distinguished and their response functions can be extrapolated.

Note that $\sum \Delta\varepsilon^i = 1 + \chi_S$. If the loss phenomena are sufficiently separated from each other in time (and frequency), then the $f^i(t)$ can be distinguished.

A.5 Data representation

A.5.1 Time-domain data

Decay currents usually vary over several orders of magnitude, with a very fast decrease during a short time interval. A log(i) versus log(t) plot is therefore the preferred representation.

A.5.2 Frequency-domain data

Frequency-domain data are represented on a logarithmic frequency scale throughout this thesis. There is, however, some discussion on whether the chosen ordinate should be linear or logarithmic. The choice between the two finally determines how much importance – with respect to the largest values – will be given to the very small values far from a relaxation peak. Some models are easily distinguished using the asymptotic behavior at very high and very low frequencies, i.e. in the frequency range where the loss is weak. A logarithmic representation is favorable from this point of view. However, this does not take into account that lower values are obtained with less experimental accuracy and that interpretation should be based on the most precise data. In addition, an (additive) contribution to ε' is present wherever there are other relaxation phenomena at higher frequencies. In a log-log, unlike a lin-log, representation, this changes the shape of the curves. Both types of representations are used here depending on the information to be extracted from the data.

Cole-Cole[168] (or Argand) diagrams consisting of a plot of $\varepsilon''(\omega)$ vs $\varepsilon'(\omega)$ have been mentioned in Chapter 5. This representation eliminates the frequency dependence from the data, thus resulting in a loss of information, but quantities such as ε_S and ε_∞ are more easily extrapolated as axis intercepts.

A.6 Empirical relaxation functions

A.6.1 General considerations: the shape of loss peaks

In Chapters 4 and 5, the shape of loss peaks is carefully analyzed to give insight to the underlying physical processes. Much attention has been given to the so-called asymptotic behavior of both permittivity and decay currents. In order to discuss some aspects of these considerations, we define the following quantities:

$$\lim \varepsilon \;=\; [a;b] \qquad \text{(A.27)}$$

$$\text{where} \quad a = \lim_{\omega \to 0} \frac{\partial \log \varepsilon''}{\partial \log \omega}$$
$$b = \lim_{\omega \to \infty} \frac{\partial \log \varepsilon''}{\partial \log \omega}$$

and

$$\begin{aligned} \lim i &= [x; y] \qquad (A.28) \\ \text{where} \quad x &= \lim_{t \to 0} \frac{\partial \log i}{\partial \log t} \\ y &= \lim_{t \to \infty} \frac{\partial \log i}{\partial \log t}. \end{aligned}$$

Note that if these limits exist (i.e. if both $\varepsilon(\omega)$ and $f(t)$ can be approximated by power laws at extreme values of ω and t, respectively), $\lim \varepsilon$ is related to $\lim i$ by the Fourier transforms (A.12) and (A.13). If we adopt the notation that has become common for the description of such functions, we have

$$\begin{aligned} \lim \varepsilon &= [m; n-1] \\ \lim i &= [-n; -1-m]. \qquad (A.29) \end{aligned}$$

The values n and m are related to the angles of intersection of a Cole-Cole plot with the real axis. The low-frequency angle is $m\pi/2$, the high-frequency angle is $(1-n)\pi/2$.

A.6.2 Exponential relaxation and the Debye expression

For an exponential decay of the dielectric polarization, we can write

$$F(t) = e^{-t/\tau_o} \qquad (A.30)$$
$$f(t) = \frac{1}{\tau_o} e^{-t/\tau_o}. \qquad (A.31)$$

The corresponding permittivity has become known as the **Debye** expression:[77]

$$\tilde{\varepsilon}_D = \frac{1}{1 + j\omega\tau_o}. \qquad (A.32)$$

Here we have introduced the notation

$$\tilde{\varepsilon} \equiv \frac{\varepsilon - \varepsilon_\infty}{\varepsilon_S - \varepsilon_\infty} = \frac{\varepsilon - \varepsilon_\infty}{\Delta \varepsilon}. \qquad (A.33)$$

In a $\log(\varepsilon'')$ versus $\log(\omega)$ representation, the Debye peak is symmetric and has a full width at half maximum of 1.144 decades.

A.6.3 Generalizations of Debye permittivity

As experimental data often have asymmetric, broader peaks, numerous **generalizations** of the simple Debye-response have been introduced. Thet can be classified into the three following categories:

1) distributions of relaxation times
2) empirical expressions that have $\tilde{\varepsilon}_D$ as a special case, and
3) response or decay functions with the exponential as a special case.

a) Distribution of relaxation times

The use of a distribution of relaxation times for parameterization of data is well-established. The approach consists of writing

$$F(t) = \int_0^\infty g(\tau)e^{(-t/\tau)}d\tau = \int_{-\infty}^\infty G(\ln\tau)e^{(-t/\tau)}d\ln\tau \tag{A.34}$$

or

$$\tilde{\varepsilon}(\omega) = \int_0^\infty \frac{g(\tau)}{1+j\omega\tau}d\tau = \int_{-\infty}^\infty \frac{G(\ln\tau)}{1+j\omega\tau}d\ln\tau \tag{A.35}$$

with

$$G(\ln\tau) = \tau g(\tau) \tag{A.36}$$

and

$$\int_0^\infty g(\tau)d\tau = \int_{-\infty}^\infty G(\ln\tau)d\ln\tau = 1. \tag{A.37}$$

Obviously it follows from (A.34) and (A.5) that

$$f(t) = \int_{-\infty}^\infty G(\ln\tau)\frac{e^{(-t/\tau)}}{\tau}d\ln\tau = \int_{-\infty}^\infty g(\tau)e^{(-t/\tau)}d\ln\tau. \tag{A.38}$$

Various simple distributions have been introduced. The most frequently used was first proposed by Wagner in 1913,[71] leading to what is referred to as "Debye-Wagner" (DW) relaxation. The name Hill-Ichiki-distribution is also used.[169,170] $G(\ln\tau)$ is chosen to be a **Gaussian** centered at $\ln\tau_o$:

$$G(\ln\tau) = \frac{1}{\sqrt{\pi}\Delta}\exp\left\{-\left[\frac{\ln\tau-\ln\tau_o}{\Delta}\right]^2\right\}. \tag{A.39}$$

The corresponding permittivity and decay current can only be given as the integrals (A.35) and (A.38) which must be calculated numerically. As an illustration, the "loss region 2" in Fig. A.3 and correspondingly the response function $f^2(t)$ in Fig. A.4 are calculated with $\Delta = 2$. It is of particular interest to note that we have

$$\begin{aligned} \lim\varepsilon &= [1;-1] \qquad \text{and} & \text{(A.40)}\\ \lim i &= [0;-\infty]. & \text{(A.41)} \end{aligned}$$

The latter follows from the fact that we can write the development of $i(t)$ around $t = 0$:

$$i(t) = \varepsilon_o E_0 \Delta\varepsilon \sum_{n=0}^{\infty} \frac{1}{\tau_o} \exp\left\{\frac{\Delta^2}{4}(n+1)^2\right\} \frac{(-t/\tau_0)^n}{n!} \tag{A.42}$$

and use the properties $i(0) \neq 0$ and $\partial i/\partial t < \infty$.

Fröhlich[171] has proposed the simple distribution

$$g(\tau) = \begin{cases} \frac{1}{\tau}(\ln\frac{\tau_1}{\tau_2}) & \text{if } \tau_1 > \tau > \tau_2 \\ 0 & \text{otherwise,} \end{cases} \tag{A.43}$$

for which the permittivity and the response function expression for $\tilde{\varepsilon}$ is symmetric, as is the one resulting from a Gaussian distribution.

Other distributions have been proposed by Fuoss-Kirkwook,[172] Pareto,[173] Macdonald,[174,175] Kliem and Arlt[176] and others. None of them are very widely applied because either they do not correspond to an established physical model, or they lead to permittivities and response functions that are not obtained by analytical means, or both.

It must be noted that a distribution of relaxation times corresponding to any analytical expression of the permittivity can always be found by using the Stieltjes transform (see page 523 of Ref. 146):

$$G(\ln\tau) \propto \lim_{\omega\to 0}\left[\varepsilon''\left(\frac{i}{\tau} - \omega\right) - \varepsilon''\left(\frac{i}{\tau} + \omega\right)\right]. \tag{A.44}$$

Mathematically speaking, ε'' data are thus equivalent to $G(\ln\tau)$ graphs. In reality, problems may occur because the resulting $G(\ln\tau)$ may have unphysical properties (for example, it may not be integrable). Methods for calculating $G(\ln\tau)$ from experimental data are presented in section A.7.3.

b) Empirical frequency-domain expressions

Havriliak and Negami[177] have proposed a generalized expression of the form

$$\tilde{\varepsilon} = \left\{1 + (j\omega\tau_o)^{1-\alpha}\right\}^{-\gamma} \qquad \begin{matrix} 0 \leq \alpha < 1 \\ 0 < \gamma \leq 1 \end{matrix} \tag{A.45}$$

which is a combination of the previously proposed **Cole-Cole**[178] ($\gamma = 1$) and **Davidson-Cole**[179] ($\alpha = 0$) expressions.[a] It is easy to see that

$$\lim\varepsilon = [1-\alpha; -\gamma(1-\alpha)] \tag{A.47}$$

---

[a] Equation (A.45) is often written in terms of the logarithmic slopes m and $n-1$ defined by $\lim\varepsilon = [m; n-1]$:

$$\tilde{\varepsilon} = \left\{1 + (j\omega\tau_O)^m\right\}^{\frac{n-1}{m}} \qquad \begin{matrix} 0 < m \leq 1 \\ 0 < 1-n \leq m. \end{matrix} \tag{A.46}$$

and obviously $|1-\alpha| > -|\gamma(1-\alpha)|$, so that only one "direction" of asymmetry can be represented. Böttcher and Bordevijk[146] have introduced what is called the **reverse Havriliak-Negami** function

$$\tilde{\varepsilon} = 1 - \left\{ \frac{(j\omega\tau_o)^{1-\alpha}}{1+(j\omega\tau_o)^{1-\alpha}} \right\}^{\gamma} \tag{A.48}$$

which has just the opposite limiting behavior

$$\lim \varepsilon = [\gamma(1-\alpha); -(1-\alpha)]. \tag{A.49}$$

With the Fourier relations (A.13) relating $f(t)$ to $\varepsilon(\omega)$ and the Stieltjes transform relating $\varepsilon(\omega)$ to $G(\ln\tau)$, the response and distribution functions can in principle be calculated. For the Cole-Cole expression, $g(\tau)$ is found analytically, and $f(t)$ can be given as a series approximation.[168] Tor the Davidson-Cole function, analytical expressions for both $f(t)$ and $g(\tau)$ are available.[180] An analytic expression for $g(\tau)$ can also be found for the **Havriliak-Negami** function (both the ordinary and the reverse), and was published by Havriliak and Negami in 1967.[181]

Other purely empirical functions have been proposed by Fuoss and Kirkwood,[172] Jonscher,[182] and Hill,[183] but they have not obtained the popularity of the above expressions.

c) Empirical time-domain expressions

Attempts to generalize the exponential function have been less numerous, and we will be mainly concerned with the Kohlrausch-Williams-Watts expression and only summarize some aspects of other more general functions.

The Kohlrausch-Williams-Watts expression

In 1947, R. Kohlrausch[72] described elastic creep with a **stretched exponential** of the form

$$F(t) = e^{-(t/\tau_o)^{\beta}}. \tag{A.50}$$

A few years later, he used the same function to parameterize data of electric relaxation in the Leyden jars.[184] The function received widespread recognition after Williams and Watts calculated the corresponding frequency response, in 1970 for the special case $\beta = 1/2$ (Ref. 73)

$$\tilde{\varepsilon} = \sqrt{\frac{\pi}{4j\omega\tau_o}} \exp\left(\frac{1}{4j\omega\tau_o}\right) \operatorname{erfc}\frac{1}{4j\omega\tau_o} \tag{A.51}$$

and a year later as a series expansion[74] for the general case[b]

$$\tilde{\varepsilon} \cong \sum_{n=1}^{\infty} (-1)^{n-1} \frac{1}{(\omega\tau_o)^{n\beta}} \frac{\Gamma(n\beta+1)}{\Gamma(n+1)} \left[\cos\frac{n\beta\pi}{2} - j\sin\frac{n\beta\pi}{2}\right]. \tag{A.52}$$

The permittivity corresponding to the stretched exponential is usually referred to as the **KWW function**.

Numerical calculation of the sum (A.52) is not trivial. According to the original publication, it converges only in the following range:

$$\begin{array}{ccccccccc} 0 & < & \beta & < & 0.25 & \text{and} & -4 & \le & \log\omega\tau_o & \le & 4 \\ 0.25 & < & \beta & < & 1 & \text{and} & -1 & \le & \log\omega\tau_o & \le & 4. \end{array} \tag{A.53}$$

Efforts to find approximate expressions have been numerous, even more so because the so-called **"stable" probability density** or Lévy[186] distribution function[c]

$$Q_\beta(z) \equiv \frac{1}{\pi}\int_0^\infty e^{-u^\beta}\cos(zu)\,du\ , \tag{A.54}$$

which plays an important role in the theory of probability and fractals, is related to this permittivity by[187]

$$\varepsilon''(\omega) = \pi\omega\tau Q_\beta(\omega\tau). \tag{A.55}$$

Various approximations have been proposed by Montroll and Bendler (1980)[187] and Macdonald and Hurt (1986)[188]. Page A-15 describes how the KWW function is calculated in this thesis.

Special note should be taken of

$$\lim i = [-\beta; -\infty]. \tag{A.56}$$

This clearly distinguishes the KWW function from the case of a Gaussian distribution of logarithmic relaxation times, where we had $\lim i = [0; -\infty]$ [Eq. (A.41)].

As an illustration, the response function $f^1(t)$ in Fig. A.4 was taken from the Kohlrausch type, with $\beta = 0.6$. The permittivity can be seen on Fig. A.3, where the "loss region 1" corresponds to this decay.

Lindsey and Patterson[189] have calculated the distribution of logarithmic relaxation times. It is given analytically for $\beta = 0.5$ and as a series expansion for the general case.[d]

---

[b] It is noted that this calculation essentially consists of re-deriving the results by Wintner,[185] which had been published thirty years earlier, and using the recursion relation $\Gamma(1+n) = n\Gamma(n)$ in the final result.

[c] The distribution is defined for $0 < \beta \le 2$. For $\beta = 2$ one finds the normal (Gaussian) distribution, and for $\beta = 1$ the Cauchy distribution $Q_1(z) = (1/\pi)(1+z^2)^{-1}$.

[d] This expansion had been published by H. Pollard[190] long before Lindsey and Patterson.

Other expressions

Various computer simulations of complex systems have led to results incompatible with the simple exponential. Power-law decay can sometimes be observed not only in simulations, but also in experiments over a relatively short time period. Other expressions involve logarithms of time and also lead to slower-than-exponential decay. Finally, a generalization of the Kohlrausch expression was proposed by Ogielski[97]

$$F(t) \sim t^{-x} \exp[-(t/\tau_o)^{\beta}], \tag{A.57}$$

a special case of which (namely, $\beta = 1$) corresponds to the Davidson-Cole relaxation.

d) Relations between several empirical expressions

The large number of empirical functions used to describe dielectric data complicates the comparison of the parameters presented in different publications. Approximate relations giving the parameters of one expression as a function of the parameters of another expression which would describe the same data in the best possible way have been proposed. Such relations for the Havriliak-Negami and the Kohlrausch-Williams-Watts functions were given by Böhmer (1989)[191] and Alvarez *et al.* (1991).[192] For the Kohlrausch-Williams-Watts and the Davidson-Cole functions, they were first published by Lindsey and Patterson (1980).[189]

A.7 Data Parameterization and Comparison

A.7.1 Master plots

A particular presentation of data is obtained by shifting several curves in a log-log representation until all data points are lying on one curve, the so-called master curve.[78] This is possible if each set of data, which we shall call $y^{(i)}(x^{(i)})$, scales according to

$$y^{(i)} = a^{(i)} \cdot f(s^{(i)} \cdot x^{(i)}), \tag{A.58}$$

where f is a function describing the shape of the curve.

In the case of dielectric measurements, the $y^{(i)}(x^{(i)})$ can be $\log \varepsilon''(\log \omega)$ or $\log i(\log t)$ data obtained at different temperatures. Suppose, for example, that we obtain such a plot for $\log i(\log t)$. This means that we can write

$$i(t) = \varepsilon_0 E_0 \Delta\varepsilon(T) \cdot f\left(\frac{t}{\tau_0(T)}\right), \tag{A.59}$$

where f is a temperature-independent response function, $\Delta\varepsilon(T)$ describes the temperature dependence of the relaxation step and $\tau_0(T)$ the temperature dependence of some central (or average) relaxation time.

Given a set of curves $i(t)$, the parameters $\Delta\varepsilon(T)$ and $\tau_0(T)$ can of course not be obtained directly, because the response function f is not yet known. The procedure for their determination is the following: starting with one curve, $\log i_{T_1}(\log t)$, a second curve $\log i_{T_2}(\log t)$ is shifted vertically by $a(T_1;T_2)$ and horizontally by $s(T_1;T_2)$ (on the logarithmic plot) to obtain the most perfect overlap. Then,

$$\Delta\varepsilon(T_1) = \frac{a(T_1;T_2)}{s(T_1;T_2)}\Delta\varepsilon(T_2) \tag{A.60}$$

and

$$\tau_0(T_1) = \frac{1}{s(T_1;T_2)}\tau_0(T_2)\,. \tag{A.61}$$

If at one temperature, $\Delta\varepsilon$ can be obtained from integrating numerically the $i(t)$ curve (possibly requiring an extrapolation of the data), then $\Delta\varepsilon(T)$ can be deduced from (A.60). The same is true for $\tau_0(T)$: it is sufficient to determine at one temperature a characteristic time such as defined by $\partial \ln i/\partial \ln t = -1$ (see section A.7.4).

Not all data can be represented in this fashion, because $f(t)$ is temperature-dependent in most cases. If this temperature dependence is weak, it may go unnoticed in a master-plot approach. In this case, however, the analysis is not valid and the resulting parameters lack physical significance.

A.7.2 Least-squares fitting

Least-squares fitting is performed using a Marquardt[75] algorithm. The sum of the squares of the absolute errors is minimized for permittivity data, and that of the relative errors for the decay currents.

Fitting to the Havriliak-Negami function and the KWW depolarization current is simple and straightforward. However, the following two cases involved some more complicated computations:

- For the calculation of the depolarization currents corresponding to a Gaussian distribution of relaxation times, the computer program written for this purpose first finds - as a function of the parameters of $g(\tau)$ - the integration interval from which the most important contribution arises.

- In the case of the Kohlrausch (stretched exponential) response, the susceptibility can be calculated according to the series expansion (A.52) or by numerical integration, depending on the values of the parameters [see expression (A.53)]. For a given value of β, there are certain values of ω for which one or the other method is preferable. The algorithm we have used here decides at each point ω between the two methods according to an empirical criterion established by S. Hutton.[193] Figure A.3 shows that the results of the two methods overlap perfectly. In fact, the ε''-curve of the loss region 1 has been numerically integrated in the lower fourth of the interval $(\ln\omega_-^1, \ln\omega_+^1)$, and the series expansion was used otherwise.

A.7.3 Calculations of relaxation time distributions

A distribution of relaxation times provides a description of the system's response that is mathematically equivalent to the susceptibility and the decay current. In this sense, it is a very useful tool for comparing data obtained by either method.

In some cases, it is possible to approximate $G(\ln\tau)$ without the need for complicated mathematics: for very wide distributions (and thus for very wide relaxation peaks or very slowly varying decay currents), $G(\ln\tau)$ is proportional to $\varepsilon''(1/\tau)$ and to $t\cdot i(t)$.[194] However, in most instances, the numerical calculations discussed below are necessary.

a) Calculation of the distribution from frequency-domain data

The previously introduced Stieltjes transform [Eq. (A.44)] is of little to for the experimentalist since it requires knowledge of the susceptibility in the complex frequency plane. The following description of one possible method for calculating the distribution follows the ideas proposed by Franklin and de Bruin (1983).[195] In order to be able to use common numerical techniques, we first rewrite Eq. (A.35), which reads

$$\hat{\varepsilon}(\omega)=\int_0^\infty \frac{g(\tau)}{1+j\omega\tau}d\tau,$$

with the notation

$$\begin{aligned} z(x) &= \varepsilon''(\omega_0\exp x) \\ x &= \ln\frac{\omega}{\omega_0} \\ y &= \ln\omega\tau \end{aligned}$$

yielding

$$z(x)=\frac{\Delta\varepsilon}{2}\int_{-\infty}^{\infty}\mathrm{sech}\,y\,G(y-x)\,dy \qquad \text{(A.62)}$$

This ordinary convolution integral can then be solved using numerical Fourier transforms. To apply the usual Fast-Fourier-Transform algorithms, it is of interest to have data defined on logarithmically equally spaced intervals. For this purpose, the interval $(\omega_{\min},\omega_{\max})$ is divided into N (where N is even) sections of length

$$T=\frac{\ln\frac{\omega_{\max}}{\omega_{\min}}}{N-1} \qquad \text{(A.63)}$$

and write

$$\tau_k=\frac{1}{\omega_0}\exp\left((k-\frac{1}{2})T\right) \qquad k=-\frac{N}{2}+1,\ldots,\frac{N}{2}. \qquad \text{(A.64)}$$

Extracting G from Eq. (A.62) by Fourier transforms yields

$$g(\tau_k) = \omega_0 \exp\left((\frac{1}{2} - k)T\right)\ G\left((k - \frac{1}{2})T\right). \tag{A.65}$$

This method was used in section 4.4.2. Alternatively, Colonomos and Gordon (1979)[196] have proposed a method to calculate the cumulative distribution, and to estimate the errors thereof. Imanishi *et al.*[197] used a histogram method quite similar to the algorithm that will be described for the case of time-domain data.

b) Calculation of the distribution from time-domain data

The method proposed here is essentially the one introduced by Kliem *et al.* (1988).[198] We start with Eq. (A.38), which we rewrite as

$$i(t) = \int_0^\infty \exp[-xt]\ f(x)dx, \tag{A.66}$$

with the notation

$$x = \frac{1}{\tau} \qquad f(x) = \frac{1}{x} \cdot g\left(\frac{1}{x}\right). \tag{A.67}$$

The method for numerically inverting this Laplace transform starts with a first assumption

$$f^{(0)}(x) = \begin{cases} f_0 & \text{if } x_1 > x > x_2 \\ 0 & \text{otherwise,} \end{cases} \tag{A.68}$$

where it is supposed that i is known on N points t_j, which are equidistant on a logarithmic scale, and f is to be calculated in the points $x_{N-j+1} = 1/t_j$. The distribution f is now found iteratively:

1. Obtain $i^{(k)}(t_j)$ from $f^{(k)}(x_n)$:

$$i^{(k)}(t_j) = \sum_{l=1}^{N} f^{(k)}(x_l) \exp[-t_j x_l] \Delta x_l \qquad \text{with} \quad \Delta x_l = \sqrt{x_l x_{l+1}} - \sqrt{x_l x_{l-1}}. \tag{A.69}$$

2. Calculate the next higher order iteration as

$$f^{(k+1)}(x_{N-j}) = f^{(k)}(x_{N-j}) \cdot \frac{i(t_j)}{i^{(k)}(t_j)}. \tag{A.70}$$

Repeating these two steps and introducing a smoothing of $f^{(k)}$ for odd values of k leads to the desired spectrum. Unfortunately, the data presented in this thesis cover only three decades in time, and were found not to yield reliable information about the distribution.

c) Approximations

For many purposes, it is sufficient and appropriate to consider approximate relations between the experimentally accessible quantities and the distribution of relaxation times. The corresponding relations are[146,199]

$$G\left(\ln\left\{\tau=\frac{1}{\omega}\right\}\right) = \frac{\omega}{\chi_S}\left(-\frac{\partial\chi'}{\partial\omega}+\frac{1}{4}\omega^2\frac{\partial^3\chi'}{\partial\omega^3}+\ldots\right) \tag{A.71}$$

$$G\left(\ln\left\{\tau=\frac{1}{\omega}\right\}\right) = \frac{2}{\pi\chi_S}\left(\chi''-\omega^2\frac{\partial^2\chi''}{\partial\omega^2}+\ldots\right) \tag{A.72}$$

$$G\left(\ln\left\{\tau=\frac{1}{\omega}\right\}\right) = t\cdot f(t)-\ldots \quad \propto t\cdot i(t)\,. \tag{A.73}$$

More elaborate approximations have been proposed,[200] but are rarely used.

A.7.4 Conversion between time domain and frequency domain

There have been a considerable efforts[201,202,203] to develop methods to convert time-domain into frequency-domain representations. These methods are somewhat similar to the ones outlined above for the calculation of $G(\ln\tau)$, and the idea is again to have a common representation of both types of data.

For very smoothly varying $i(t)$ and $\varepsilon(\omega)$ curves, the **Hamon approximation**[78,204] can be used for the rapid appraisal of loss data from the depolarization currents, or vice versa. The basic assumption of this approximation is that the loss curve $\chi''(\omega)$ can be approximated locally by a power law, for which the Fourier transform is known analytically. In this case,

$$i\left(\frac{1}{2\pi f}\right) = C_0V_0\pi f\frac{\chi''(f)}{a(f)} \tag{A.74}$$

where $a(f) = \Gamma(1-s)\cos(s\pi/2)$ with $s = 1-\partial\log\chi''/\partial\log f$. For data satisfying $-1 < \partial\log\chi''/\partial\log f \leq 0.5$, as observed in many experiments, the parameter a changes only by a little over a factor of two. From this it is seen that most characteristics of decay currents to be compared to susceptibility data may be obtained by plotting $t\cdot i(t)$ logarithmically against t (as done in Fig. 4.4). In addition, it is observed from Eq. (A.74) that for such smoothly varying curves, the loss peak ($\partial\log\chi''/\partial\log f = 0$) occurs at the frequency $\omega = 1/t_1$, where t_1 is the time at which the logarithmic slope goes through the value $\partial\log i/\partial\log t = -1$, and thus where the $t\cdot i(t)$ curves are maximum.

Appendix B

Properties of the double-Gaussian distribution

In the study of dielectric relaxation of $K_{1-x}Li_xTaO_3$, the data were interpreted in terms of a double-Gaussian distribution of relaxation times. This appendix gives the equations relating the characteristic quantities (the relaxation step $\Delta\varepsilon$, the mean relaxation time τ_O, and the width Δ of the distribution) to those of the constituent simple Gaussian distributions.

In order to relate the characteristic quantities describing the double-Gaussian distribution to those of the two constituent simple Gaussians, namely the relaxation steps $\Delta\varepsilon_i$, $(i = 1, 2)$, the mean relaxation times $\tau_{O,i}$, and the widths Δ_i, which are obtained from least-squares fitting, we use the notation

$$\begin{aligned} x &= \ln \tau \\ x_O &= \ln \tau_O. \end{aligned}$$

A simple Gaussian distribution can be written

$$G\{\Delta_i, x_{O,i}\}(x) = \frac{1}{\Delta_i\sqrt{\pi}} \exp\left\{-\left(\frac{x - x_{O,i}}{\Delta_i}\right)^2\right\} \tag{B.1}$$

and the resulting permittivity

$$\varepsilon(\omega) - \varepsilon_\infty = \Delta\varepsilon_i \int_{-\infty}^{\infty} \frac{G\{\Delta_i, x_{O,i}\}(x)}{1 + j\omega \exp(x)}\, dx. \tag{B.2}$$

The mean value of the relaxation time corresponding to $G\{\Delta_i, x_{O,i}\}(x)$ is given as

$$\int_{-\infty}^{\infty} x G\{\Delta_i, x_{O,i}\}(x)\, dx = x_{O,i}, \tag{B.3}$$

and the standard deviation becomes

$$\left(\int_{-\infty}^{\infty}(x - x_{o,i})^2 G\{\Delta_i, x_{o,i}\}(x)\, dx\right)^{1/2} = \left(\frac{\Delta_i}{2}\right). \tag{B.4}$$

If we define the double Gaussian as

$$\begin{aligned} G\{\Delta_1, \Delta_2, x_{o,1}, x_{o,2}\} &= a_1 G\{\Delta_1, x_{o,1}\} + a_2 G\{\Delta_2, x_{o,2}\} && \text{(B.5)} \\ \text{where} \qquad a_i &= \frac{\Delta\varepsilon_i}{\Delta\varepsilon_1 + \Delta\varepsilon_2}, && \text{(B.6)} \end{aligned}$$

then integration analogous to Eqs. (B.3) and (B.4) yields for the mean relaxation time τ_o

$$\ln \tau_o = x_o = \frac{1}{\Delta\varepsilon_1 + \Delta\varepsilon_2}(\Delta\varepsilon_1 x_{o,1} + \Delta\varepsilon_2 x_{o,2}), \tag{B.7}$$

and for the standard deviation $\Delta/2$

$$\left(\frac{\Delta}{2}\right)^2 = \sum_{i=1}^{2} \frac{\Delta\varepsilon_i}{\Delta\varepsilon_1 + \Delta\varepsilon_2}\left[\Delta_i^2 + (x_{o,i} - x_o)^2\right]. \tag{B.8}$$

The relaxation step $\Delta\varepsilon$ is given by

$$\Delta\varepsilon = \Delta\varepsilon_1 + \Delta\varepsilon_2. \tag{B.9}$$

Appendix C

Distribution of nearest neighbors

> In Chapter 4, the probability of one Li impurity to see its nearest neighbor impurity at a distance r was considered for the interpretation of dielectric data. This appendix presents the calculations which lead to the data shown in Fig. 4.14(c).

The impurities are assumed to occupy random sites on a simple cubic lattice, and their concentration is given by x. Let $n(r)$ be the number of lattice sites (occupied or not) found at a distance $d = r$ from the test site, and $N(r)$ the number of sites at distances $d \leq r$.

If $P(\textit{none nearer than } r)$ denotes the probability of finding no neighbor at distances smaller than r, and $P(\textit{at least one at } r)$ the probability of finding at least one neighbor at a distance r, then the probability $P_{nn}(r)$ of finding the nearest neighbor at $d = r$ is given by the product

$$P_{nn}(r) = P(\textit{none nearer than } r) \cdot P(\textit{at least one at } r) \tag{C.1}$$

with
$$\begin{aligned} P(\textit{none nearer than } r) &= (1-x)^{N(r)} && \text{(C.2)} \\ P(\textit{at least one at } r) &= \sum_{m=1}^{n(r)} \binom{n(r)}{m} x^m (1-x)^{n(r)-m} \\ &= 1-(1-x)^{n(r)}. && \text{(C.3)} \end{aligned}$$

Therefore
$$P_{nn}(r) = (1-x)^{N(r)} \left[1-(1-x)^{n(r)}\right]. \tag{C.4}$$

Figure C.1 shows $P_{nn}(r)$ for different concentrations.

The probability of finding the nearest neighbor at a given distance depends strongly on the number of sites available at that distance. In order to visualize this influence, the above results are now compared to the case of a continuous medium,

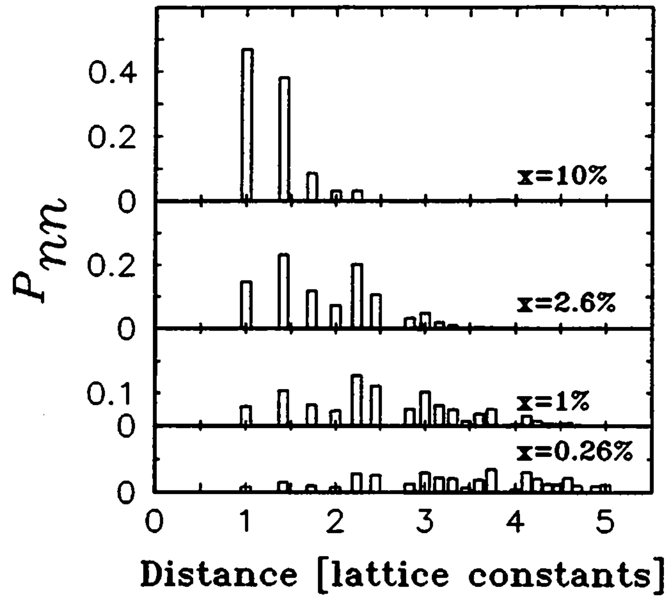

Figure C.1 Probability of finding the nearest neighbor impurity at a given distance, on a simple cubic lattice, and for impurity concentrations x = 0.26%, 1%, 2.6%, and 10%.

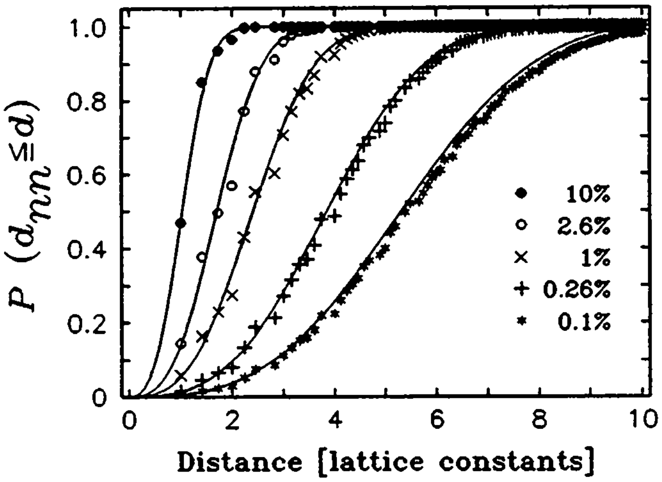

Figure C.2 Probability of finding the nearest neighbor at a distance less than or equal to d, for various impurity concentrations x. Symbols correspond to impurities placed on a cubic lattice, solid lines to a continuous medium.

where the placement of the impurities is not restricted to lattice sites. Here x denotes the concentration defined as number of impurities per volume element a^3. For comparison with the discrete case, a is chosen equal to the lattice constant. The probability of finding no neighbor nearer than r becomes

$$P(\textit{none nearer than } r) = (1-x)^{\frac{4\pi}{3}\frac{r^3}{a^3}} \tag{C.5}$$

and the probability of finding at least one neighbor between $d = r$ and $d = r + \mathrm{d}r$ is

$$P(\textit{at least one for } r \leq d \leq r + \mathrm{d}r) = \left[1 - (1-x)^{\frac{4\pi}{3}\frac{r^2}{a^2}}\right] \frac{\mathrm{d}r}{a}. \tag{C.6}$$

If we define

$$F(r) = \left[(1-x)^{\frac{4\pi}{3}\frac{r^3}{a^3}}\right] \left[1 - (1-x)^{\frac{4\pi}{3}\frac{r^2}{a^2}}\right], \tag{C.7}$$

then

$$P_{nn}(r)\,\mathrm{d}r = \frac{F(r)\frac{\mathrm{d}r}{a}}{\displaystyle\int_0^\infty F(r')\frac{\mathrm{d}r'}{a}}. \tag{C.8}$$

The cumulative probability $P(d_{nn} \leq d) = \int_0^\infty P_{nn}(r)\mathrm{d}r$ of finding the nearest neighbor at a distance less than or equal to d is compared in Fig. C.2 for the continuous and the discrete cases. Differences between the two expressions are seen most clearly for concentrations in the percentage range.

Appendix D

Calculation of the Li – Li interaction energy

Computational aspects regarding the calculation of the Li-Li interaction energy, which have not been included in Chapter 4, are discussed here. The presented method has been developed by Ricardo Migoni and Marcelo Stachiotti at the University of Rosario, Argentina, and most of the numerical calculations were performed by Jorge Kohanoff at the IBM Rüschlikon laboratory. The results will be published in "Dipole-Dipole Interactions in $K_{1-x}Li_xTaO_3$," M. Stachiotti, R. Migoni, H.-M. Christen, J. Kohanoff, and U. T. Höchli, submitted to *J. Phys.: Condens. Matter.*

The Li-Li interaction energy to be minimized consists of the perfect lattice energy plus an effective potential (V_2^{eff}) defined by

$$V_2^{\mathrm{eff}} = \phi(\vec{u},\vec{v}) + V(\vec{u},\vec{v}). \tag{D.1}$$

Here $\phi(\vec{u},\vec{v})$ is the shell model potential for pure $KTaO_3$, and $V(\vec{u},\vec{v})$ is the defect potential. The first term can be written as

$$\begin{aligned}\phi(\vec{u},\vec{v}) &= \frac{1}{2}\vec{u}^{\dagger}(\mathcal{S}+\mathcal{C}^{zz})\vec{u} + \frac{1}{2}(\vec{v}-\vec{u})^{\dagger}(\mathcal{S}+\mathcal{K}+\mathcal{C}^{yy})(\vec{v}-\vec{u}) \\ &\quad + \vec{u}^{\dagger}(\mathcal{S}+\mathcal{C}^{zy})(\vec{v}-\vec{u}) + \frac{1}{4!}K_{\mathrm{OB-B}}\mathcal{L}(\vec{v}-\vec{u})^4 \end{aligned} \tag{D.2}$$

where $\vec{u}$ and $\vec{v}$ denote core and shell displacements, respectively. $\mathcal{S}$ is the short-range force matrix and $\mathcal{C}^{ij}$ represent the Coulomb force matrices between ions ($\mathcal{C}^{zz}$), between shells ($\mathcal{C}^{yy}$), and between ions and shells ($\mathcal{C}^{zy}$), where z denotes ionic charge and y shell charge. $\mathcal{K}$ is a diagonal matrix which contains the core-shell coupling constants and the matrix $\mathcal{L}$ selects the appropriate components for the nonlinear interaction at the O^{-2} ions. $K_{\mathrm{OB-B}}$ represents the fourth-order term in the coupling of the oxygen cores to their shells in the direction of the neighboring Ta_{+5} ion.

The second contribution to V_2^{eff}, i.e. the defect potential $V(\vec{u},\vec{v})$ (where the term "defect" stands for a Li^+ ion at the off-center position plus the K^+ vacancy) can be written as the sum of a defect-lattice contribution V_{DL} plus a defect-defect interaction V_{DD}:

$$V(\vec{u},\vec{v}) = V_{\mathrm{DL}} + V_{\mathrm{DD}} \tag{D.3}$$

with

$$V_{\mathrm{DL}} = \sum_{l\kappa}\sum_{n=1}^{2} V(\mathrm{Li}_n^+, l\kappa) - V(\mathrm{K}_n^+, l\kappa) \tag{D.4}$$

$$V_{\mathrm{DD}} = V(\mathrm{Li}_1^+, \mathrm{Li}_2^+) - V(\mathrm{K}_1^+, \mathrm{K}_2^+). \tag{D.5}$$

$V(\mathrm{Li}_n^+, l\kappa)$ includes short-range and Coulomb interactions between the Li^+ ion at site n and a host lattice ion of type κ (κ=K^+, Li^+, Ta^{+5}, O^{-2}) in the cell l. $V(\mathrm{K}_n^+, l\kappa)$ cancels the same type of interaction that would arise from the K^+ ion, now replaced by the Li^+. $V(\mathrm{Li}_1^+, \mathrm{Li}_2^+)$ is the Coulomb Li-Li interaction while $V(\mathrm{K}_1^+, \mathrm{K}_2^+)$ cancels the missing K-K interaction.

The equilibrium condition (V_2^{eff}= minimum) implies that

$$f_\alpha^c(l,\kappa) \equiv -\frac{\partial V}{\partial u_\alpha(l,\kappa)} = \frac{\partial \phi}{\partial u_\alpha(l,\kappa)} \tag{D.6}$$

$$f_\alpha^s(l,\kappa) \equiv -\frac{\partial V}{\partial v_\alpha(l,\kappa)} = \frac{\partial \phi}{\partial v_\alpha(l,\kappa)}. \tag{D.7}$$

For the following it is convenient to work with the relative shell-core displacements $\vec{w} = \vec{v} - \vec{u}$, rather than with the absolute shell coordinates. From (D.6) and (D.7), together with (D.2), we obtain

$$\vec{f}^t \equiv \vec{f}^c + \vec{f}^s = (\mathcal{S} + \mathcal{C}^{zz})\vec{u} + (\mathcal{S} + \mathcal{C}^{zy})\vec{w} \tag{D.8}$$

$$\vec{f}^s = (\mathcal{S} + \mathcal{C}^{yz})\vec{u} + (\mathcal{S} + \mathcal{K} + \mathcal{C}^{yy})\vec{w} + \frac{1}{3!}K_{\mathrm{OB-B}}\mathcal{L}(\vec{w})^3 \tag{D.9}$$

The right-hand sides of the above equations are linear in $\vec{u}$ and $\vec{w}$ except for the term arising from the nonlinear interaction at the oxygen ions. Therefore, to solve the system (D.8) and (D.9), we define

$$\vec{f}' \equiv \vec{f}^s - \frac{1}{3!}K_{\mathrm{OB-B}}\mathcal{L}(\vec{w})^3, \tag{D.10}$$

which leads to the following system of nonlinear coupled equations:

$$\vec{u} = \mathcal{G}\vec{f}^t - \mathcal{A}\vec{f}' \tag{D.11}$$

$$\vec{w} = \mathcal{B}\vec{f}' - \mathcal{C}\vec{u}. \tag{D.12}$$

The matrices $\mathcal{G}$, $\mathcal{A}$, $\mathcal{B}$ and $\mathcal{C}$ are obtained as Fourier transformations of the following matrices in reciprocal space :

$$\begin{aligned}
\mathcal{G} &= \mathcal{D}^{-1} \\
\mathcal{A} &= \mathcal{D}^{-1}(\mathcal{S}+\mathcal{C}^{yz})(\mathcal{S}+\mathcal{K}+\mathcal{C}^{yy})^{-1} \\
\mathcal{B} &= (\mathcal{S}+\mathcal{K}+\mathcal{C}^{yy})^{-1} \\
\mathcal{C} &= (\mathcal{S}+\mathcal{K}+\mathcal{C}^{yy})^{-1}(\mathcal{S}+\mathcal{C}^{yz})
\end{aligned}$$

where $\mathcal{D} = (\mathcal{S}+\mathcal{C}^{zz}) - (\mathcal{S}+\mathcal{C}^{zy})(\mathcal{S}+\mathcal{K}+\mathcal{C}^{yy})^{-1}(\mathcal{S}+\mathcal{C}^{zy})^{\dagger}$ is the dynamic matrix of the shell model. In the limiting case where the ions are nonpolarizable, i.e. $\mathcal{K} \rightarrow \infty$, the matrices $\mathcal{A}$, $\mathcal{B}$ and $\mathcal{C}$ vanish to yield the familiar expression $\vec{u} = \mathcal{G}\vec{f}^{t}$. In this case, $\mathcal{G}$ becomes the static Green's function of the rigid ion model.

The forces $\vec{f}^{t}$ and $\vec{f}^{s}$ are evaluated in the distorted lattice, hence they are functions of $\vec{u}$, $\vec{w}$, $\vec{\delta}_1$ and $\vec{\delta}_2$. Therefore, Eqs. (D.11) and (D.12) must be solved self-consistently together with the equilibrium condition for the Li^+ impurities (namely that the total force on each Li^+ ion is equal to zero).

To perform the calculation, the defect-lattice Coulomb forces must be restricted to a finite region. As was shown for a single defect, there is an enhancement of the bare Li dipole moment due to the polarization of a neighboring ellipsoidal region with a length of about five lattice constants (a) in the polar direction [113,114]. Hence, to avoid boundary effects, a spherical lattice region large enough to include the polarized ellipsoids associated with both impurities is considered. This sphere has a diameter of 11.6 a and contains 799 K^+ ions, 840 Ta^{+5} ions and 2520 O^{-2} ions. It should be noted that the only approximation imposed by a finite radius is a truncation of the defect-lattice Coulomb forces at this radius. The interactions within the host lattice, as well as the infinite lattice relaxation, are not affected by the truncation, since the Green's function method ensures the inclusion of all infinite-range terms. We have verified that a further increase of the diameter of this sphere does not modify the final result.

The equilibrium solution for $\vec{u}$, $\vec{w}$, $\vec{\delta}_1$ and $\vec{\delta}_2$ is obtained iteratively by a steepest descent procedure. The initial ionic positions are chosen to be those of the perfect lattice ($\vec{u} = \vec{w} = 0$), except for the Li^+, which are arbitrarily displaced. Once the final configuration is obtained, the potential energy V_2^{eff} is computed according to Eq. (D.1), where the lattice relaxation energy $\phi(\vec{u},\vec{v})$ is obtained from Eqs. (D.11) and (D.12):

$$\phi = \frac{1}{2}\vec{f}^{t\,\dagger}\mathcal{G}\vec{f}^{t} + \frac{1}{2}\vec{f}^{s\dagger}(\mathcal{C}\mathcal{A}+\mathcal{B})\vec{f}^{s} - \vec{f}^{t\,\dagger}\mathcal{A}\vec{f}^{s} \tag{D.13}$$

Finally, the effective Li-Li interaction energy is defined as :

$$V_{\mathrm{int}}^{\mathrm{eff}} = V_2^{\mathrm{eff}} - 2V_1^{\mathrm{eff}} \tag{D.14}$$

where V_1^{eff} is the energy of an isolated defect in the infinite lattice.

Results of this calculation are given in Table D.1 and discussed in Chapter 4.

Table D.1 : Interaction energies (in meV) for selected relative Li positions $\vec{r}_{Li-Li}$ and all nonequivalent pairs of Li orientations (the first column corresponds to the impurity at the origin). Data are grouped for $\vec{r}_{Li-Li} \| (100)$ (top frame), $\vec{r}_{Li-Li} \| (101)$ (middle frame), and for out-of-plane directions of $\vec{r}_{Li-Li}$ (bottom frame).

Li orientations		effective interaction energy [meV]			
		$\vec{r}_{Li-Li}$:	(3,0,0)	(4,0,0)	(6,0,0)
$+z$	$+z$		58	51	40
$+z$	$-z$		84	94	98
$+z$	$+x$		119	115	77
$+z$	$-x$		114	109	83
$+z$	$-y$		86	82	73
$+x$	$+x$		198	173	108
$+x$	$-x$		110	132	136
$-x$	$+x$		139	117	113
		$\vec{r}_{Li-Li}$:	(2,0,2)	(3,0,3)	(4,0,4)
$+z$	$+z$		92	92	76
$+z$	$-z$		108	99	81
$+z$	$+x$		124	114	81
$+z$	$-x$		124	113	83
$+z$	$+y$		96	90	83
$-z$	$+z$		105	98	83
$-z$	$+x$		125	115	82
$-z$	$+y$		95	93	80
$+y$	$+y$		57	55	41
$+y$	$-y$		93	103	77
		$\vec{r}_{Li-Li}$:	(2,1,2)	(2,3,2)	(3,4,3)
$+y$	$+y$		107	106	95
$+y$	$-y$		125	114	91
$+y$	$+x$		128	117	93
$+y$	$-x$		127	115	89
$-y$	$+y$		125	112	94
$-y$	$+x$		130	114	93
$-y$	$-x$		128	113	88

Appendix E

The nonlinear $P(E)$ relation, and band diagrams

> Experimental evidence of a nonlinear $P(E)$ relation in $SrTiO_3$ and $KTaO_3$ was presented in Chapter 3, and energy-band diagrams for $Mg/SrTiO_3/SrTiO_3$:Nb heterostructures, taking into account this nonlinearity, were discussed in Chapter 6. In this appendix, mathematical details are presented which have been omitted from those chapters for clarity.

Neglecting fifth and higher order terms, the $E(P)$ relation as given by the Devonshire theory becomes

$$E = \alpha P + \beta P^3. \tag{E.1}$$

This cubic polynomial can be inversed[205] analytically:

$$\begin{aligned} P(E) &= (r+s)^{1/3} + (r-s)^{1/3} && \text{(E.2)} \\ \text{where} \quad r &= E(2\beta)^{-1} \\ s &= \sqrt{\frac{\alpha^3}{27\beta^3} + r^2}. \end{aligned}$$

The derivative of P with respect to E yields the dielectric constant ε,

$$\begin{aligned} \frac{\partial P}{\partial E} = \varepsilon(E) - 1 &= \frac{2^{2/3}}{6\varepsilon_o \beta^{1/3}} \frac{E^{-2/3}}{R(E)} \left\{ [1 + R(E)]^{1/3} - [1 - R(E)]^{1/3} \right\} && \text{(E.3)} \\ \text{with} \qquad R(E) &= \sqrt{1 - \frac{1}{E^2} \frac{4\alpha^3}{27\beta^3}}\,. \end{aligned}$$

Observing that

$$\lim_{E\to\infty} R(E) = 1$$

and

$$R(E) \gg 1 \qquad \text{for} \quad E \ll \frac{4\alpha^3}{27\beta},$$

the approximations introduced in Eq. (3.4) are found directly.

In calculating the band diagram for metal/SrTiO$_3$/SrTiO$_3$:Nb structures, the one-dimensional Maxwell equation

$$\vec{\nabla}\cdot\vec{D} = \frac{\partial}{\partial x}D(x) = \rho(x) \tag{E.4}$$

is solved. In accumulation, the problem is trivial, thus only the depletion case is treated here.

With the notations inof Fig. 6.25, the film/substrate interface lies at $x=0$, the substrate itself is located at negative values of x, and the trapped surface charge at $x=0$ is given by Q_{it}.

For the depletion layer, we have from Eq. (E.4)

$$\int_{-x}^{0} \rho(x')\mathrm{d}x' = D(0) - D(-x). \tag{E.5}$$

The width w of the depletion layer is defined by

$$D(-w) = 0. \tag{E.6}$$

In the depletion approximation (assuming a constant carrier density $\rho(x) = \rho_d$ within the depletion layer, and zero outside),

$$\int_{-x}^{0} \rho(x')\mathrm{d}x' = x\cdot\rho_d. \tag{E.7}$$

Inserting $D = P - \varepsilon_0 E = (1+\varepsilon_0\alpha)P + \varepsilon_0\beta P^3$ into Eq. (E.5) and comparing to Eq. (E.7), we find

$$\varepsilon_0\beta P^3(x) + (1+\varepsilon_0\alpha)P(x) - \left[x\cdot\rho_d\varepsilon_0\beta P^3(0) + (1+\varepsilon_0\alpha)P(0)\right] = 0, \tag{E.8}$$

which can again be solved to find the polarization $P_{P(0)}(-x)$ at $-x$ for a given value of $P(0)$ at $x=0$.

The electric field is thus given for any point in the depletion layer using Eq. (E.1): $E_{P(0)}(-x) = E\{P_{P(0)}(-x)\}$. The voltage drop across the depletion layer becomes

$$V_d = \int_{-w}^{0} E_{P(0)}(x)\mathrm{d}x. \tag{E.9}$$

Inside the insulating $SrTiO_3$ film, D is constant: $D(x) = D_i$. Its value is determined by the sum of the value in the depletion layer at $x=0$ $[D_d(x=0) = D(P(0))]$, and the interface trapped charge Q_{it}:

$$D_i = D_d(x=0) + Q_{\text{it}}. \tag{E.10}$$

In the metal electrode, $D(x) = 0$, and thus

$$Q_s = -D_i. \tag{E.11}$$

The total voltage drop across the structure is given as

$$V = V_d + E(D_i) \cdot d, \tag{E.12}$$

where d is the thickness of the film.

With these equations, calculation of the voltage for a given charge Q_s is straightforward. For the calculation of the $C(V)$ curves, the relation $V(Q_s)$ is inversed numerically, and the capacitance of the structure is calculated by numerical derivation as

$$C = \left(\frac{\partial V(Q_s)}{\partial Q_s}\right)^{-1}. \tag{E.13}$$

All programs were written in APL2, using the AGSS graphical/statistical library.

Appendix F

Contact characterization

This appendix describes the electrical properties of the metal electrodes in Mg/$SrTiO_3$/$SrTiO_3$:Nb/Ag heterostructures.

To measure the film capacitance, Ohmic back electrodes (metal/$SrTiO_3$:Nb) are required: if these contacts behaved like Schottky diodes, the resulting series capacitance would disturb the measurements.

The Ag/$SrTiO_3$:Nb contacts were obtained by applying silver paste to the crystal surfaces before film growth, in the process of which the sample was heated to 600 °C. The as-prepared junctions were blocking. Figure F.1 shows an $I(V)$ curve recorded on a Ag/$SrTiO_3$:Nb/Ag structure at 300 K. As the voltage was swept up, no appreciable current ($I < 10^{-8}$ A) was recorded for $V \lesssim 4$ V, but then increased rapidly (steeper than $I \propto V^7$). To obtain good Ohmic properties, the electrodes were "burnt-in" by forcing a current of ~10 mA through the contacts (electrode surface ~1 mm^2). As seen in Fig. F.1, this results in linear $C(V)$ curves recorded in subsequent voltage sweeps at all temperatures between 4.2 and 300 K.

Contacts to the films are less critical than those to the substrates if the films are known to be insulating. However, semiconducting properties are observed in reduced $SrTiO_3$, such as might be obtained here under unfavorable growth conditions. In this case, a metal electrode may again act as a Schottky contact, and the true conductivity across the film would not be observed.

Whether a metal leads to Ohmic contacts can only be tested on a conducting material. Characterization of the top electrodes was thus performed on reduced $SrTiO_3$ films (obtained by heating of the film to 700 °C in vacuum). Figure F.2 shows the current-voltage dependence measured across two Mg electrodes evaporated at 300 K onto such a reduced $SrTiO_3$ film. Contrary to other tested metals, including Au, Ag, In, and In-Ga, the present electrodes exhibited excellent linearity of the current-voltage curves, requiring no burn-in. It is assumed that the surface region of the $SrTiO_{3-x}$ film is additionally reduced by the formation of a small amount of MgO. However, the present data show that no insulating oxide layer forms.

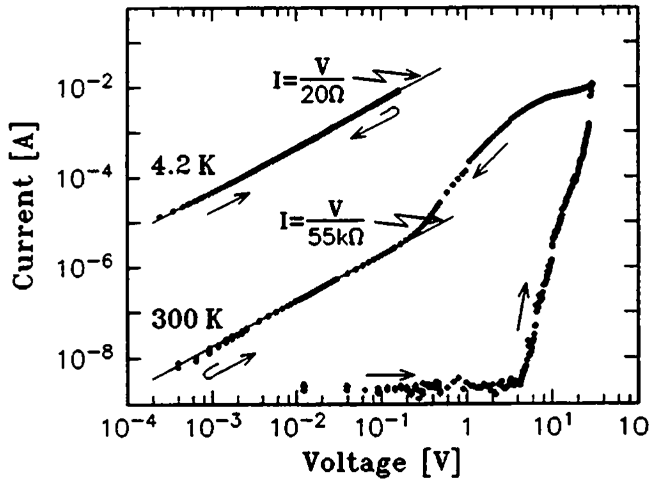

Figure F.1 Current-voltage characteristics measured across two Ag contacts on a $SrTiO_3$:Nb crystal. The 300 K curve shows the current recorded during burn-in; the 4.2 K curve demonstrates the resulting linearity of the current-voltage dependence. Arrows indicate the sweep direction.

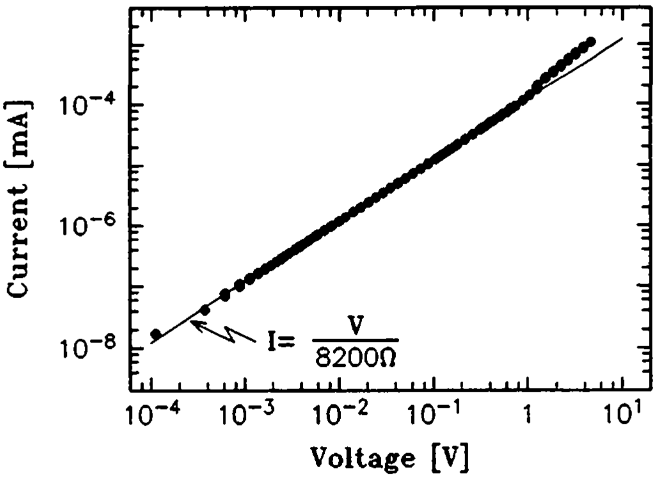

Figure F.2 Current-voltage characteristics measured across two Mg contacts evaporated at 300 K onto a reduced $SrTiO_3$ film. Linearity is observed over five decades, down to 10^{-4} V. Unlike the Ag contacts of Fig. F.1, no burn-in is required.

Appendix G

Mg/SrTiO$_3$/Pt/SrTiO$_3$:Nb structures

> SrTiO$_3$ films grown on a platinum layer have been mentioned in Chapter 6 as alternative sample structures to the investigated Mg/SrTiO$_3$/SrTiO$_3$:Nb specimens. In this appendix, such Mg/-SrTiO$_3$/Pt/SrTiO$_3$:Nb heterostructures are studied.

For the growth of Mg/SrTiO$_3$/Pt/SrTiO$_3$:Nb heterostructures, the SrTiO$_3$:Nb substrates were prepared as for the SrTiO$_3$/SrTiO$_3$:Nb samples, and a platinum layer of nominally 20–50 Å thickness was deposited by electron beam evaporation at 600 °C. Half of the substrate was shielded by a metal mask during evaporation, so that only part of the surface was Pt-covered. A SrTiO$_3$ layer was then sputtered onto the whole substrate *in situ*. Magnesium electrodes were again evaporated at room temperature. This structure, shown in Fig. G.1, has the advantage that the effect of the platinum layer can be studied without having to compare films obtained from different growth runs. This reduces the complications due to the large differences in the dielectric properties of nominally identical films (see Fig. 6.8).

A bright-field TEM image of a SrTiO$_3$/Pt/SrTiO$_3$:Nb structure is presented in Fig. G.2. It is seen that the platinum does not grow as a film of uniform thickness. Instead, it is deposited in a "lump-like" fashion without completely covering the surface. These "droplets," however, are crystalline, as seen on the lattice image in Fig. 6.7.

As was previously reported,[19] the low-field dielectric properties of such samples are improved in comparison to those with films grown on bare SrTiO$_3$:Nb substrates. Figure G.3 shows the $\varepsilon_{\text{eff}}(T)$ dependence for the films grown on the bare and the Pt-covered portion of the SrTiO$_3$:Nb substrates and for film thicknesses of 100 nm [Fig. G.3(a)] and 50 nm (b). It is clearly seen that the effect of the Pt layer is stronger on the thinner film, and in both cases is visible primarily at the lower temperatures.

The results of 1-mHz $P(V)$ loops are shown in Fig. G.4 for a 100-nm-thick films.

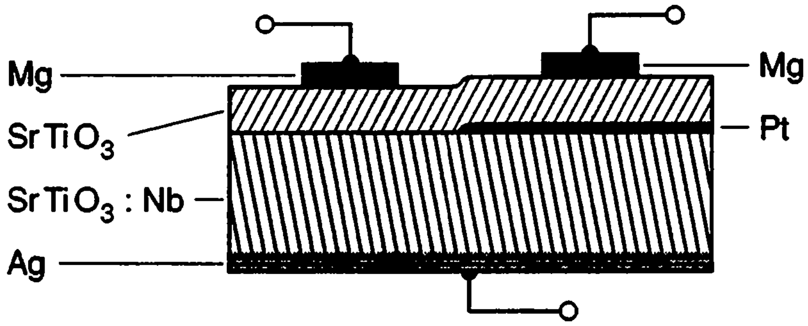

Figure G.1 Sample structure in which part of the $SrTiO_3$ film is grown directly onto the bare substrate, and the other part onto a 20–50-Å-thick platinum layer.

In agreement with the $\varepsilon_{\text{eff}}(T)$ curves in Fig. G.3, the $P(V)$ curve for the portion grown on platinum has a steeper slope corresponding to the higher dielectric constant. However, its breakdown strength is also considerably reduced, so that the maximum attainable polarization P_l is smaller. Similar observations can be made on Fig. G.5. The film grown on a Pt layer clearly shows a larger effective dielectric constant at the lowest voltages, but the ε_{eff} values of the two films seem to approach each other for larger values of the bias. Again, the breakdown strength of the film grown on Pt is strongly reduced (in this sample by more than a factor of two).

From these observations it is concluded that the present type of Pt "layers," which only partially covers the surface, does not lead to an overall improvement of the dielectric properties of the $SrTiO_3$ films. It seems to result in a decrease of the substrate's depletion layer width at zero bias, thus to a higher ε_{eff} at zero applied voltage, but also to large field inhomogeneities in the film and thus to a reduced breakdown voltage. The main characteristics of the samples, such as the reduction of the capacitance after positive biasing, are not modified.

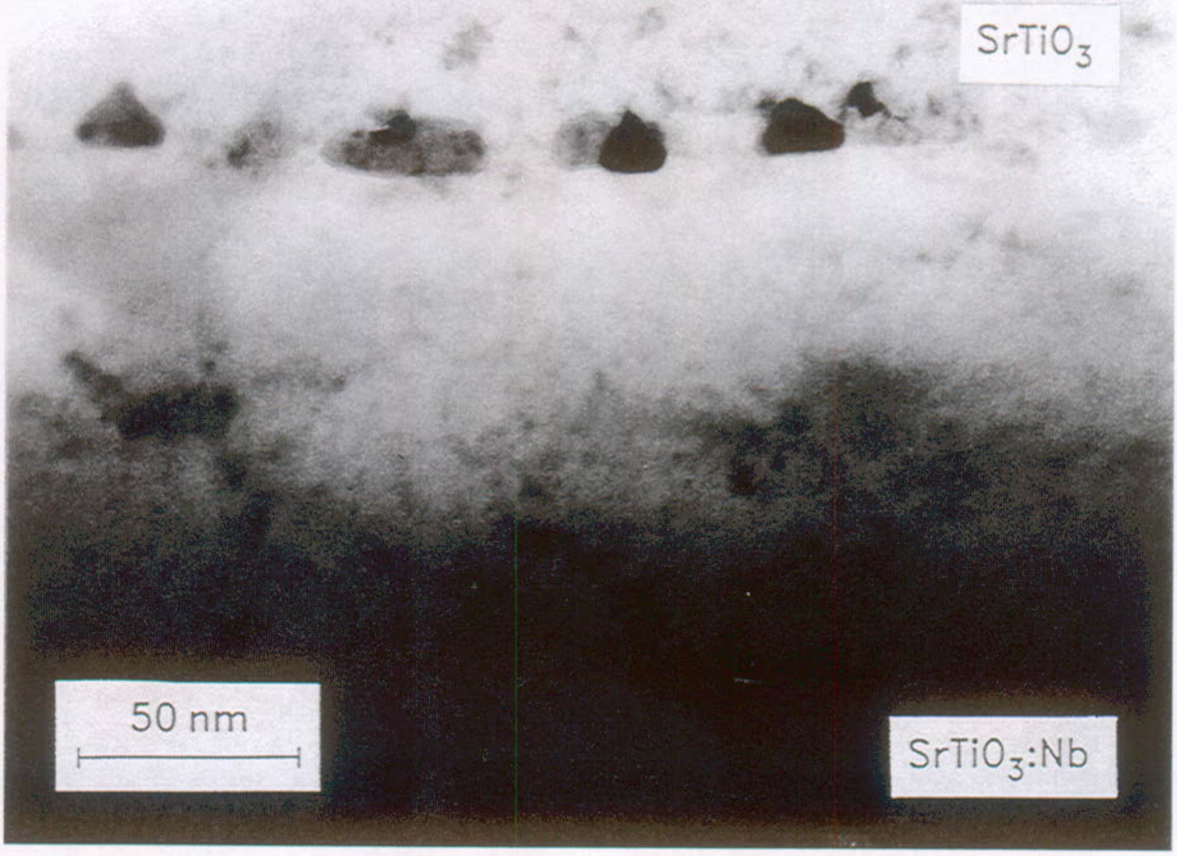

Figure G.2 TEM micrograph of a Au/$YBa_2Cu_3O_{7-x}$/$SrTiO_3$/Pt/$SrTiO_3$:Nb heterostructure (bright field image). The platinum (darker areas) does not grow as an even layer, but as "lumps" of 20–50 nm diameter.
Microscopy performed by E. Williams. [Sample number R510]

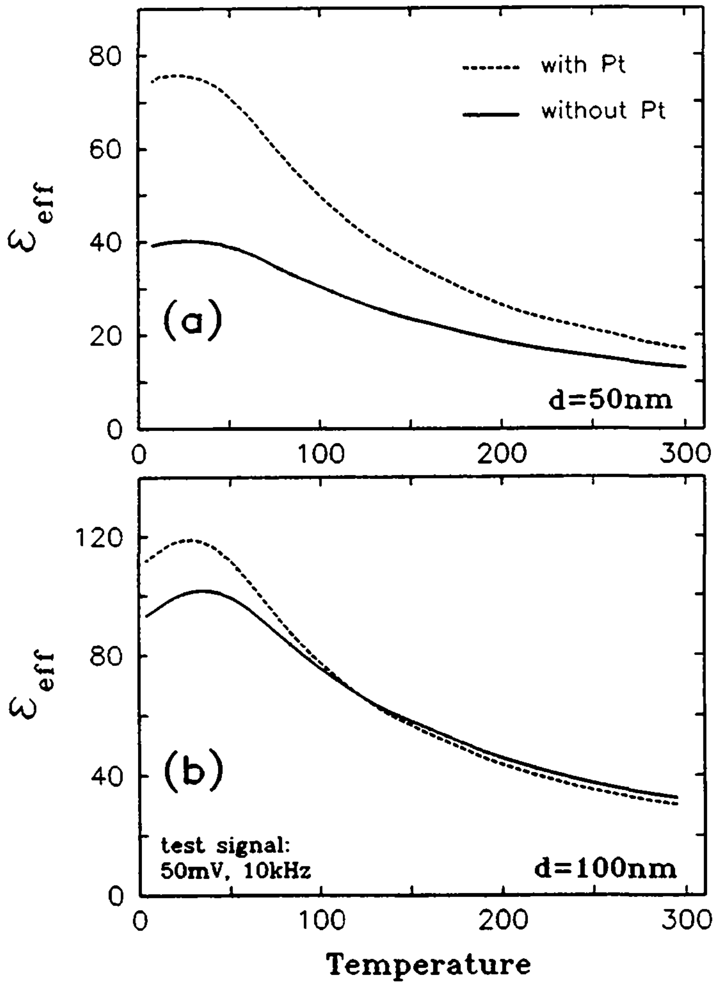

Figure G.3 Temperature dependence of the effective dielectric constant, (**a**) for 50 nm, and (**b**) for 100-nm-thick films, grown on bare (solid lines) and Pt-covered (dashed lines) $SrTiO_3$:Nb substrates.
[Sample number R508 (top) and R504 (bottom)]

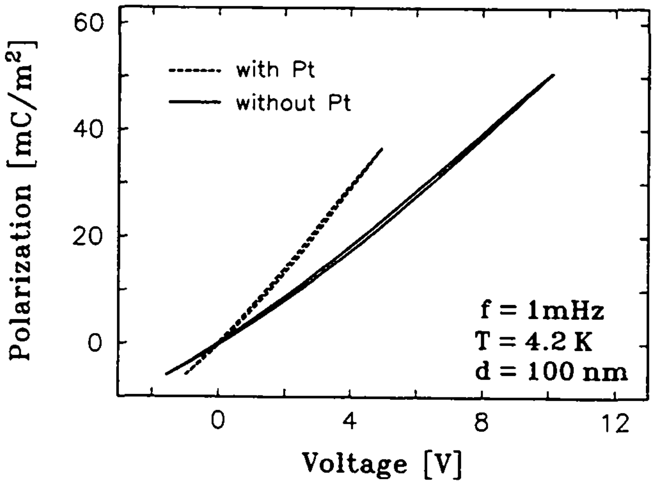

Figure G.4 Polarization vs voltage curves for 100-nm-thick films grown on a bare (solid line) and Pt-covered (dashed line) $SrTiO_3$:Nb substrate. [Sample number R504]

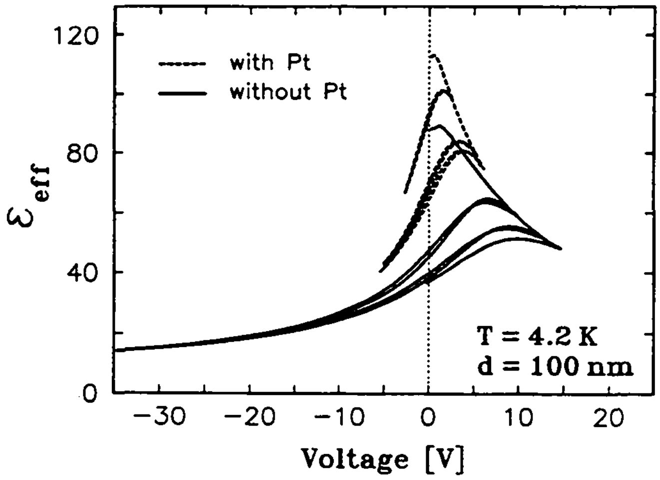

Figure G.5 Effective dielectric constant of a 100-nm-thick $SrTiO_3$ film deposited onto a bare (solid curve) and a Pt-covered (dashed curve) $SrTiO_3$:Nb substrate as a function of bias voltage for repeated sweeps. [Sample number R504]

References

1 K. A. Müller and H. Burkard, "$SrTiO_3$: an intrinsic quantum paraelectric below 4K," *Phys. Rev. B*, **19**, 3593 (1979).

2 U. T. Höchli, H. E. Weibel, and L. A. Boatner, "Quantum limit of ferroelectric phase transitions in $KTa_{1-x}Nb_xO_3$," *Phys. Rev. Lett.*, **39**, 1158 (1977).

3 D. Viehland, J. F. Li, S. J. Jang, L. E. Cross, and M. Wuttig, "Dipolar-glass model for lead magnesium niobate," *Phys. Rev. B*, **43**, 8316 (1991).

4 M. E. Lines and A. M. Glass. *Principles and Applications of Ferroelectrics and Related Materials.* Clarendon Press, Oxford, 1977.

5 K. Binder and J. D. Reger, "Theory of orientational glasses. models, concepts, simulations," *Adv. Phys.*, **41**, 547 (1992).

6 U. T. Höchli, H. E. Weibel, and L. A. Boatner, "Stabilization of polarised clusters in $KTaO_3$ by Li defects: formation of a polar glass," *J. Phys. C: Solid State Phys.*, **12**, L563 (1979).

7 Jack C. Burfoot and George W. Taylor. *Polar Dielectrics and their Applications.* MacMillan Press, London, 1979.

8 U. T. Höchli, K. Knorr, and A. Loidl, "Orientational glasses," *Adv. Phys.*, **39**, 405 (1990).

9 S. L. Swartz and V. E. Wood, "Ferroelectric thin films," *Condensed Matter News*, **1**, 5 (1992).

10 T. Kuroiwa, T. Honda, H. Watarai, and K. Sato, "Electric properties of $SrTiO_3$ thin films prepared by RF sputtering," *Jpn. J. Appl. Phys.*, **31**, 3025 (1992).

11 D. Roy, C. J. Peng, and S. B. Krupanidhi, "Excimer laser ablated strontium titanate thin films for dynamic random access memory applications," *Appl. Phys. Lett.*, **60**, 2478 (1992).

12 P. C. Joshi and S. B. Krupanidhi, "Structural and electrical characteristics of $SrTiO_3$ thin films for dynamic random access memory applications," *Appl. Phys. Lett.*, **61**, 1525 (1992).

13 R. B. Laibowitz, J. Z. Sun, V. Foglietti, W. J. Gallagher, and R. H. Koch, "High-T_c, multilevel edge junction superconducting quantum interference devices with $SrTiO_3$ barriers operating at 77 K," *Appl. Phys. Lett.*, **64**, 247 (1994).

14 N. Newman and W. G. Lyons, "High-temperature superconducting microwave devices: Fundamental issues in materials, physics, and engineering," *J. Supercond.*, **6**, 119 (1993).

15 J. Mannhart, D. G. Schlom, J. G. Bednorz, and K. A. Müller, "Electric field effect on superconducting $YBa_2Cu_3O_{7-x}$ films," *Z. Phys. B*, **83**, 307 (1991).

16 A. Walkenhorst, C. Doughty, X. X. Xi, S. N. Mao, Q. Li, T. Venkatesan, and R. Ramesh, "Dielectric properties of $SrTiO_3$ thin films used in high-T_c superconducting field-effect devices," *Appl. Phys. Lett.*, **64**, 1744 (1992).

17 T. Hirano, M. Ueda, K. Matsui, T. Fujii, K. Sakuta, and T. Kobayashi, "Dielectric properties of $SrTiO_3$ epitaxial film and their application to measurement of work function of $YBa_2Cu_3O_{7-x}$ epitaxial film," *Jpn. J. Appl. Phys.*, **31**, L1345 (1992).

18 K. Sakuta, T. Awaji, K. Matsui, T. Hirano, T. Fujii, and T. Kobayashi, "Electric field effect in Al/$SrTiO_3$/$YBa_2Cu_3O_{7-x}$ structure in the normal state," *Jpn. J. Appl. Phys.*, **31**, L1411 (1992).

19 J. Mannhart, D. G. Schlom, J. G. Bednorz, and K. A. Müller, "Influence of electric fieds on pinning in $YBa_2Cu_3O_{7-x}$ films," *Phys. Rev. Lett.*, **67**, 2099 (1991).

20 A. Yoshida, H. Tamura, K. Gotoh, H. Takauchi, and S. Hasuo, "Electrical properties of Au/ and $YBa_2Cu_3O_{7-x}$/-$SrTi_{1-y}Nb_yO_3$ diodes," *J. Appl. Phys.*, **70**, 4976 (1991).

21 H. Hasegawa, T. Fukazawa, and T. Aida, "Contact between high-T_c superconductor and semiconducting niobium-doped $SrTiO_3$," *Jpn. J. Appl. Phys.*, **28**, L2210 (1989).

22 H. Suzuki, T. Yamamoto, S. Suzuki, M. Iyori, K. Takahashi, T. Usuki, Y. Yoshisato, and S. Nakano, "Preparation and characteristics of a superconducting base transistor with an Au/$Ba_{1-x}K_xBiO_3$/niobium-doped $SrTiO_3$ structure," *Jpn. J. Appl. Phys.*, **32**, 783 (1993).

23 H. Takauchi, A. Yoshida, H. Tamura, and S. Hasuo, "Rectifying current-voltage characteristics in $YBa_2Cu_3O_{7-x}$/$NdGaO_3$/n-$SrTiO_3$ diodes," *Appl. Phys. Lett.*, **61**, 1462 (1992).

24 M. Maglione. *Métastabilité dans les verres dipolaires.* PhD thesis, École Polytechnique Fédérale de Lausanne, Lausanne, Switzerland, 1987.

25 H. J. Scheel, J. G. Bednorz, and P. Dill, "Crystal growth of strontium titanate $SrTiO_3$," *Ferroelectrics*, **13**, 507 (1976).

26 D. Rytz and H. J. Scheel, "Crystal growth of $KTa_{1-x}Nb_xO_3$ ($0 < x \leq 0.04$) solid solutions by a slow-cooling method," *J. Cryst. Growth*, **59**, 468 (1982).

27 J. J. van der Klink and D. Rytz, "Growth of $K_{1-x}Li_xTaO_3$ crystals by a slow-cooling method," *J. Cryst. Growth*, **56**, 673 (1982).

28 H. M. Christen, U. T. Höchli, A. Châtelain, and S. Ziolkievicz, "Random-barrier and hierarchical relaxation in $K_{1-x}Li_xTaO_3$," *J. Phys.: Condens. Matter*, **3**, 8387 (1991).

29 Q. Bick, "a, *b*, and *c* are equal, but *c* in particular," *J. Irrelev. Res.* (1994).

30 K. A. Müller and W. Berlinger, *Phys. Rev. Lett.*, **26**, 13 (1971).

31 R. C. Neville, B. Hoeneisen, and C. A. Maed, "Permittivity of strontium titanate," *J. Appl. Phys.*, **43**, 2124 (1972).

32 Y. Fujii and T. Sakudo, "Dielectric and optical properties of $KTaO_3$," *J. Phys. Soc. Jpn.*, **41**, 888 (1976).

33 J. H. Barrett, "Dielectric constant in perovskite type crystals," *Phys. Rev.*, **86**, 118 (1952).

34 M. A. Saifi and L. E. Cross, "Dielectric properties of strontium titanate at low temperature," *Phys. Rev. B*, **2**, 677 (1970).

35 U. T. Höchli and L. A. Boatner, "Electromechanical properties and electron tunneling in $KTaO_3$," *J. Phys. C: Solid State Phys.*, **10**, 4319 (1977).

36 J. P. Ansermet, D. Rytz, A. Châtelain, U. T. Höchli, and H. E. Weibel, "Surface layer in ferroelectric $KTa_{1-x}Nb_xO_3$," *J. Phys. C: Solid State Phys.*, **14**, 4541 (1981).

37 E. Hegenbarth, "Die Feldstärkeabhängigkeit der Dielektrizitätskonstanten von $SrTiO_3$-Einkristallen im Temperaturbereich von 15 bis 80°K," *Phys. Status Solidi*, **6**, 333 (1964).

38 D. Itschner. *Dielektrische Eigenschaften von Strontiumtitanat bei tiefen Temperaturen, Prom. Nr. 3576.* PhD thesis, Eidgenössische Technische Hochschule, Zürich, Switzerland, 1965.

39 A. F. Devonshire, *Phil. Mag. Suppl.*, **3**, 85 (1954).

40 H. H. Barrett, "Dielectric breakdown of single-crystal strontium titanate," *J. Appl. Phys.*, **35**, 1420 (1964).

41 S. M. Sze. *Physics of Semiconductor Devices.* John Wiley & Sons, New York, second edition, 1981.

42 G. S. Oehrlein, F. M. d'Heurle, and A. Reisman, "Some properties of crystallized tantalum pentoxide thin films on silicon," *J. Appl. Phys.*, **55**, 3715 (1992).

43 S. C. Abrahams and E. T. Keve, "Structural basis of ferroelectricity and ferroelasticity," *Ferroelectrics*, **2**, 129 (1971).

44 A. V. Postnikov, T. Neumann, and G. Borstel, "Ferroelectric structure of $KNbO_3$ and $KTaO_3$ from first-principles calculations," *Phys. Rev. B* (submitted).

45 H. Uwe, K. B. Lyons, H. L. Carter, and P. A. Fleury, "Ferroelectric microregions and Raman scattering in $KTaO_3$," *Phys. Rev. B*, **33**, 6436 (1986).

46 W. B. Pearson. *Crystal Chemistry and Physics of Metals and Alloys*. Wiley, New York, 1972.

47 J. J. van der Klink and S. N. Khanna, "Off-center lithium ions in $KTaO_3$," *Phys. Rev. B*, **29**, 2415 (1984).

48 Y. Yacoby, "Defect induced fluctuations in Li:$KTaO_3$," *Z. Phys. B*, **41**, 269 (1981).

49 G. A. Smolensky, E. G. Nadolinskaya, N. K. Yushin, and A. V. Shilnikov, "Dielectric properties of $K_{1-x}Li_xTaO_3$ at frequencies 10^{-2} – 10^3Hz," *Ferroelectrics*, **69**, 275 (1986).

50 H. Schremmer, W. Kleemann, and D. Rytz, "Field-induced sharp ferroelectric phase transition in $K_{0.937}Li_{0.063}TaO_3$," *Phys. Rev. Lett.*, **62**, 1896 (1989).

51 U. T. Höchli and D. Baeriswyl, "Coexisting polar configurations in potassium lithium tantalate," *J. Phys. C: Solid State Phys.*, **17**, 311 (1984).

52 U. T. Höchli and M. Maglione, "Dielectric relaxation spectroscopy and the ground state of $K_{1-x}Li_xTaO_3$," *J. Phys.: Condens. Matter*, **1**, 2241 (1989).

53 J. J. van der Klink and F. Borsa, "NMR study of the quasi-reorientational dynamics of Li ions in $KTaO_3$:Li," *Phys. Rev. B*, **30**, 52 (1984).

54 S. Rod, F. Borsa, and J. J. van der Klink, "Order and disorder in pure and doped $KTaO_3$: a ^{181}Ta NMR study," *Phys. Rev. B*, **38**, 2267 (1988).

55 P. Doussineau, C. Frènois, A. Levelut, and S. Ziolkievicz, "Ultrasonic dispersion and quadrupolar moments in $K_{0.95}Li_{0.05}TaO_3$," *J. Phys.: Condens. Matter*, **3**, 8369 (1991).

56 U. T. Höchli, J. Hessinger, and K. Knorr, "Low-frequency elastic shear constant and low-temperature configuration of $K_{1-x}Li_xTaO_3$," *J. Phys.: Condens. Matter*, **3**, 8377 (1991).

57 J. J. van der Klink, D. Rytz, F. Borsa, and U. T. Höchli, "Collective effects in a random-site electric dipole system: $KTaO_3$:Li," *Phys. Rev. B*, **27**, 89 (1983).

58 U. T. Höchli, P. Kofel, and M. Maglione, "Dipolar relaxation and limit of ergodicity in $K_{1-x}Li_xTaO_3$," *Phys. Rev. B*, **32**, 4546 (1985).

59 K. Binder and A. P. Young, "Spin glasses: experimental facts, theoretical concepts, and open questions," *Rev. Mod. Phys.*, **58**, 801 (1986).

60 E. Courtens, "Birefringence measurements on $KTaO_3$:Li," *J. Phys. C: Solid State Phys.*, **14**, L37 (1981).

61 R. L. Prater, L. L. Chase, and L. A. Boatner, "Raman scattering studies of the impurity-induced ferroelectric phase transition in $KTaO_3$:Li," *Phys. Rev. B*, **23**, 5904 (1981).

62 M. Maglione, U. T. Höchli, J. Joffrin, and K. Knorr, "Strain distributions in the dipolar glass $KTaO_3$:Li," *J. Phys.: Condens. Matter*, **1**, 1527 (1989).

63 G. A. Azzini, G. P. Banfi, E. Giulotto, and U. T. Höchli, "Second harmonic generation and origin of polar configuration in $KTaO_3$:Li," *Phys. Rev. B*, **43**, 7473 (1991).

64 D. Sommer, W. Kleemann, M. Lehndorff, and K. Dransfeld, "Microwave-induced Brillouin scattering in $K_{1-x}Li_xTaO_3$ with glassy and ferroelectric domain state phases," *Solid St. Comm.*, **72**, 731 (1989).

65 W. Kleemann, S. Kütz, and D. Rytz, "Cluster glass and domain state properties of $KTaO_3$:Li," *Europhys. Lett.*, **4**, 239 (1987).

66 P. Doussineau, Y. Farssi, C. Frénois, A. Levelut, K. McEnaney, J. Toulouse, and S. Ziolkiewicz, "Dielectric study of the pase transition in $K_{1-x}Li_xTaO_3$," *Europhys. Lett.* (submitted).

67 P. Doussineau, C. Frénois, A. Levelut, and S. Ziolkiewicz, "Effect of the electric field on the elastic and and dielectric properties of a lithium-potassium tantalate crystal," *Phys. Rev. B* (submitted).

68 P. Voigt and S. Kapphan, "Variations of the second harmonic intensity at the low temperature phase transition in $K_{1-x}Li_xTaO_3$ under electric field," *Ferroelectrics*, **124**, 243 (1991).

69 W. A. Kamitakahara, C.-K. Loong, G. E. Ostrowski,
and L. A. Boatner, "Time-dependent phase transformation in $KTaO_3$:Li," *Phys. Rev. B*, **35**, 223 (1987).

70 M. D. Fontana, M. Maglione, and U. T. Höchli, "Glassy and ferroelectric aspects of potassium tantalate niobate," *J. Phys.: Condens. Matter*, **5**, 1895 (1993).

71 K. W. Wagner, "Zur Theorie der unvollkommenen Dielektrika," *Ann. Phys., Lpz.*, **40**, 817 (1913).

72 R. Kohlrausch, *Ann. Phys., Lpz.*, **12**, 393 (1847).

73 G. Williams and D. Watts, "Non-symmetrical dielectric relaxation behaviour arising from a simple empirical decay function," *Trans. Faraday Soc.*, **66**, 80 (1970).

74 G. Williams, D. C. Watts, S. B. Dev, and A. M. North, "Further considerations of non symmetrical dielectric relaxation behaviour arising from a simple empirical decay function," *Trans. Faraday Soc.*, **67**, 1323 (1971).

75 W. H. Press, B. P. Flannery, S. A. Teukolsky, and W. T. Vetterling. *Numerical Recipes: The Art of Scientific Computing*. Cambridge University Pres, Cambridge, 1986.

76 R. Coelho. *Physics of Dielectrics for the Engineer*. Volume 1 of *Fundamental Studies in Engineering*, Elsevier, Amsterdam, 1979.

77 P. Debye, *Z. Phys.*, **13**, 97 (1912).

78 A. K. Jonscher. *Dielectric Relaxation in Solids*. Chelsea Dielectric Press, London, 1983.

79 E. R. Grannan, M. Randeira, and J. P. Sethna, "Low-temperature properties of a model glass. I. Elastic dipole model. II. Specific heat and thermal transport," *Phys. Rev. B*, **41**, 7784 and 7799 (1990).

80 A. K. Jonscher, "The 'universal' dielectric response," *Nature*, **267**, 673 (1977).

81 P. Sheng and Z. Chen, "Local-field distribution in random dielectric media," *Phys. Rev. Lett.*, **60**, 227 (1988).

82 Z. Chen and P. Sheng, "Local fields in random dielectrics: distribution characteristics and the effects of microstructure," *Phys. Rev. B*, **43**, 5735 (1991).

83 J. Wang, "Local fields near a point-charge defect in cubic ionic crystals," *Phys. Rev. B*, **22**, 2725 (1980).

84 W. van Weperen, B. P. M. Lenting, E. J. Bijvank, and H. W. den Hartog, "Effect of the Ce^{3+} concentration on the reorientation of dipoles in SrF_2:Ce^{3+}," *Phys. Rev. B*, **16**, 2953 (1977).

85 B. E. Vugmeĭster and V. A. Stephanovich, *Solid St. Comm.*, **66**, 673 (1988).

86 B. E. Vugmeĭster and M. D. Glinchuck, "Dipole glass and ferroelectricity in random-site electric dipole systems," *Rev. Mod. Phys.*, **62**, 993 (1990).

87 R. G. Palmer, D. L. Stein, E. Abrahams, and P. W. Anderson, "Models of hierarchically constrained dynamics for glassy relaxation," *Phys. Rev. Lett.*, **53**, 958 (1984).

88 A. T. Ogielski and D. L. Stein, "Dynamics in ultrametric spaces," *Phys. Rev. Lett.*, **55**, 1634 (1985).

89 E. W. Knapp, "Relaxation in self-similar hierarchical spaces," *Phys. Rev. B*, **38**, 2264 (1988).

90 E. W. Knapp, "Equivalence of dynamics in ultrametric and hierarchical spaces," *Phys. Rev. B*, **38**, 2664 (1988).

91 F. H. Stillinger, "Relaxation behavior in atomic and molecular glasses," *Phys. Rev. B*, **41**, 2409 (1990).

92 R. L. Jacobs, "Relaxation processes in glass-forming materials," *J. Phys. C: Solid State Phys.*, **19**, L119 (1986).

93 M. R. de la Fuente, M. A. Pérez Jubindo, and M. J. Tello, "Two-level model for the nonexponential Williams-Watts dielectric relaxation," *Phys. Rev. B*, **37**, 2094 (1988).

94 D. Kumar and S. R. Shenoy, "Hierarchical energy barriers, hierarchical constraints, and non-exponential decay in glasses," *Solid St. Comm.*, **57**, 927 (1986).

95 A. K. Rajagopal, S. Teitler, and K. L. Ngai, "Low-frequency relaxation in condensed matter and the evolution of entropy," *J. Phys. C: Solid State Phys.*, **17**, 6611 (1984).

96 M. F. Shlesinger and E. W. Montroll, "On the Williams-Watts function of dielectric relaxation," *Proc. Natl. Acad. Sci. USA*, **81**, 1280 (1984).

97 A. T. Ogielski, "Dynamics of three-dimensional Ising spin glasses in thermal equilibrium," *Phys. Rev. B*, **32**, 7384 (1985).

98 K. Binder, "Monte carlo methods and glassy systems," *Ferroelectrics*, **104**, 3 (1990).

99 F. Y. Wu, *Rev. Mod. Phys.*, **54**, 235 (1982).

100 H.-O. Carmesin and K. Binder, "Monte-Carlo study of the Potts glass with nearest-neighbour random Gaussian interactions," *J. Phys. A: Math. Gen.*, **21**, 4053 (1988).

101 H.-O. Carmesin and K. Binder, "Isotropic Edwards-Anderson models for quadrupolar glasses: a Monte-Carlo simulation," *Europhys. Lett.*, **4**, 269 (1987).

102 K. Binder, "Computer simulation of models for orientational glasses," *J. Non-Cryst. Solids*, **131-133**, 262 (1991).

103 K. Weron, "How to obtain the universal response law in the Jonscher screened hopping model for dielectric relaxation," *J. Phys.: Condens. Matter*, **3**, 221 (1991).

104 H.-J. Queisser, "Logarithmic hierarchy of universal dielectric response," *Appl. Phys. A*, **52**, 261 (1988).

105 L. A. Dissado and R. M. Hill, "A cluster approach to the structure of imperfect materials and their relaxation spectroscopy," *Proc. R. Soc. Lond.*, **A 390**, 131 (1983).

106 L. A. Dissado and R. M. Hill, "Small-signal ac frequency response functions," *Solid State Ionics*, **22**, 331 (1987).

107 H. Kliem, "A comment on dielectric theory: differential equations and permittivity," *J. Appl. Phys.*, **70**, 1861 (1991).

108 J. Vanderschueren and J. Gasiot, "Field-induced thermally stimulated currents," *Topics in Appl. Phys.*, **37**, 135 (1979).

109 J. B. Bednorz and K. A. Müller, "$Sr_{1-x}Ca_xTiO_3$: an XY quantum ferroelectric with transition to randomness," *Phys. Rev. Lett.*, **52**, 2289 (1984).

110 R. Migoni, H. Bilz, and D. Bäuerle, "Origin of raman scattering and ferroelectricity in oxyde perovskites," *Phys. Rev. Lett.*, **37**, 1155 (1976).

111 C. Perry, R. Currat, H. Buhay, R. Migoni, W. Stirling, and J. Axe, "Phonon dispersion and lattice dynamics of $KTaO_3$ from 4K to 1220K," *Phys. Rev. B*, **39**, 8666 (1989).

112 S. Chaplot and K. Rao, "Computer simulation of translational and rotational dynamics in $LiKSO_4$," *Phys. Rev. B*, **35**, 9771 (1987).

113 M. G. Stachiotti and R. L. Migoni, "Lattice polarisation around off-centre Li in $K_{1-x}Li_xTaO_3$," *J. Phys.: Condens. Matter*, **2**, 4341 (1990).

114 M. G. Stachiotti, R. L. Migoni, and U. T. Höchli, "Validity of nonlinear shell model for localized dipole moments in $K_{1-x}Li_xTaO_3$," *J. Phys.: Condens. Matter*, **3**, 3689 (1991).

115 B. E. Vugmeĭster and M. D. Glinchuk, "Some features of the cooperative behaviour of paraelectric defects in strongly polarizable crystals," *Soviet Phys. JETP*, **52**, 3 (1980).

116 B. E. Vugmeĭster and M. D. Glinchuck, "Dipole glass and ferroelectricity in random-site electric dipole systems," *Rev. Mod. Phys.*, **62**, 993 (1990). and references therein.

117 S. F. Edwards and P. W. Anderson, "Theory of spin glasses," *J. Phys. F*, **5**, 965 (1975).

118 M. Sakata, F. Matsubara nad Y. Abe, and S. Katsura, "Computer experiments for the glass-like phase of two-dimensional spin systems," *J. Phys. C: Solid State Phys.*, **10**, 2887 (1977).

119 D. C. Rapaport, "Susceptibilites of spin glass models: a monte carlo study," *J. Phys. C: Solid State Phys.*, **11**, L111 (1978).

120 W. Kinzel. *Static Critical Phenomena in Inhomogeneous Systems*, page 113. Volume 206 of *Lecture Notes in Physics*, Springer, Berlin, 1984.

121 D. Hammes, H. Carmesin, and K. Binder, "Two-dimensional isotropic orientational glass: a computer simulation study," *Z. Phys. B*, **76**, 115 (1989).

122 H.-O. Carmesin, "Stabilisation of the orientational glass phase by cubic anisotropy," *J. Phys. A: Math. Gen.*, **22**, 297 (1989).

123 D. Sherrington and S. Kirkpatrick, "Solvable model of a spin-glass," *Phys. Rev. Lett.*, **35**, 1792 (1975).

124 G. Parisi, "The order parameter for spin glasses: a function on the interval 0–1," *J. Phys. A: Math. Gen.*, **13**, 1101 (1980).

125 H. Vollmayr, R. Kree, and Z. Zippelius, "Phase diagram and elastic properties of disordered mixed crystals," *Europhys. Lett.*, **12**, 235 (1990).

126 P. M. Goldbart and D. Sherrington, "Replica theory of the uniaxial quadrupolar glass," *J. Phys. C: Solid State Phys.*, **18**, 1923 (1985).

127 H. Vollmayr, R. Kree, and A. Zippelius, "Discrete-state models of orientational glasses," *Phys. Rev. B*, **44**, 12238 (1991).

128 H. Vollmayr and R. Kree, "Disordered states in a generalized potts model with uniform nonfrustrated couplings," *Phys. Rev. B*, **47**, 14177 (1993).

129 E. V. Colla, E. Yu Koroleva, N. M. Okuneva, and S. B. Vakhrushev, "Low-frequency dielectric response of $Pb(Mg_{1/3}Nb_{2/3})O_3$," *J. Phys.: Condens. Matter*, **4**, 3671 (1992).

130 G. A. Smolensky, "Ferroelectrics with diffuse phase transitions," *Ferroelectrics*, **53**, 129 (1984).

131 J. Chen, H. Chan, and M. Harmer, *J. Am. Ceram. Soc.*, **79**, 593 (1989).

132 C. Randall and A. Bhalla, *J. Materials Sci.*, **29**, 5 (1990).

133 Roland Sommer. *Propriétés diélectriques, pyroélectriques et electromécaniques du* $Pb(Mg_{1/3}Nb_{2/3})O_3$*: Existence d'une transition de phase structurale.* PhD thesis, Ecole Polytechnique Fédérale Lausanne, Lausanne, Switzerland, 1992.

134 G. A. Smolensky and A. I. Agranovskaya, *Zh. tech. Fiz.*, **28**, 1491 (1958).

135 G. A. Smolenskii and A. I. Agranovskaya, "New ferroelectrics of complex composition of the type $A_2^{2+}(B_I^{3+}B_{II}^{5+})O_6$," *Soviet Phys. Solid State*, **1**, 1429 (1959).

136 G. A. Smolenskii, "Diffuse phase transitions," *J. Phys. Soc. Jpn.*, **28**, 26 (1970).

137 O. Auciello, L. Mantese, J. Duarte, X. Chen, S. H. Rou, A. I. Kingon, A. F. Schreier, and A. R. Krauss, "Synthesis and characterization of $Pb(Zr_xTi_{1-x})O_3$ thin films produced by an automated laser ablation deposition technique," *J. Appl. Phys.*, **73**, 5197 (1993).

138 H. Arndt, R. Sauerbier, G. Schmidt, and L. A. Shebanov, "Field induced phase transition in PMN single crystals," *Ferroelectrics*, **145**, 145 (1988).

139 E. Prouzet, E. Husson, N. de Mathan, and A. Morell, "A low-temperature extended x-ray absorption study of the local order in simple and complex perovskites: II. PMN ($\mathrm{Pb(Mg_{1/3}Nb_{2/3})O_3}$)," *J. Phys.: Condens. Matter*, **5**, 4889 (1993).

140 N. de Mathan, E. Husson, G. Calvarin, J. R. Gavarri, A. W. Hewat, and A. Morell, "A structural model for the relaxor $\mathrm{Pb(Mg_{1/3}Nb_{2/3})O_3}$ at 5 K," *J. Phys.: Condens. Matter*, **3**, 8159 (1991).

141 L. E. Cross, "Relaxor ferroelectrics," *Ferroelectrics*, **76**, 241 (1987).

142 G. Schmidt, "Diffuse ferroelectric phase transitions in cubically stabilized perovskites," *Phase Transitions*, **20**, 127 (1990).

143 H.-M. Christen, R. Sommer, N. K. Yushin, and J. J. van der Klink, "Small-signal dielectric relaxation in the disordered perovskite $\mathrm{Pb(Mg_{1/3}Nb_{2/3})O_3}$," *J. Phys.: Condens. Matter*, **6**, 2631 (1994).

144 V. Westphal, W. Kleemann, and M. D. Glinchuk, "Diffuse phase transition and random-field-induced domain states of the "relaxor" ferroelectric $\mathrm{Pb(Mg_{1/3}Nb_{2/3})O_3}$," *Phys. Rev. Lett.*, **68**, 847 (1992).

145 R. Sommer, N. K. Yushin, and J. J. van der Klink, "Polar metastability and an electric-field induced phase transition in the disordered perovskite $\mathrm{Pb(Mg_{1/3}Nb_{2/3})O_3}$," *Phys. Rev. B*, **48**, 13230 (1993).

146 C. J. F. Böttcher and P. Bordewijk. *Theory of electric polarization*. Volume II, Elsevier, Amsterdam, 1978.

147 Y. Yokimozo, K. Takahashi, and S. Nomura, *J. Phys. Soc. Jpn.*, **28**, 1278 (1970).

148 L. A. Dissado and R. M. Hill, *J. Phys. C: Solid State Phys.*, **16**, 4023 (1983).

149 O. N. Tufte and P. W. Chapman, "Electron mobility in semiconducting strontium titanate," *Phys. Rev.*, **155**, 796 (1967).

150 H. P. R. Frederikse, W. R. Thurber, and W. R. Hosler, "Electronic transport in strontium titanate," *Phys. Rev.*, **134**, A442 (1964).

151 H. W. Gandy, *Phys. Rev.*, **113**, 795 (1959).

152 G. Campet, S. Z. Wen, C. Puprichitkun, J. P. Manaud, and J. Claverie, "Physical properties of $\mathrm{(n^+)SrTiO_3}$ films," *Phys. Stat. Sol. (a)*, **103**, 175 (1987).

153 S. B. Desu and D. A. Payne, "Interfacial segregation in perovskites: II, experimental evidence," *J. Am. Ceram. Soc.*, **73**, 3398 (1990).

154 I. Burn and S. Neirman, "Dielectric properties of donor-doped polycrystalline $\mathrm{SrTiO_3}$," *J. Materials Sci.*, **17**, 3510 (1982).

155 S. B. Newcomb, C. B. Boothroyd, and W. M. Stobbs, *J. Microsc. (Oxford)*, **140**, 195 (1985).

156 J. Blanc and D. L. Staebler, "Electrocoloration in $\mathrm{SrTiO_3}$: vacancy drift and oxidation-reduction of transition metals," *Phys. Rev. B*, **4**, 3548 (1971).

157 G. Campet, M. Carrere, C. Puprichitkun, S. Z. Wen, J. Salardenne, and J. Claverie, "N-type $\mathrm{SrTiO_3}$ thin films: electronic precesses and photoelectrochemical behavior," *J. Sol. State Chem.*, **69**, 267 (1987).

158 H. Suzuki, M. Iyori, T. Yamamoto, S. Suzuki, K. Takahashi, T. Usuki, and Y. Yoshisato, "Junction characteristics of an $\mathrm{Au/Ba_{1-x}K_xBiO_3}$/niobium-doped $\mathrm{SrTiO_3}$ structure," *Jpn. J. Appl. Phys.*, **31**, 2716 (1992).

159 Y. Nakano, M. Watanabe, and T. Takahashi, "Investigation of interface states in $\mathrm{(Sr,Ca)TiO_{3-x}}$-based ceramics," *J. Appl. Phys.*, **70**, 1539 (1991).

160 K. Szot, C. Freiburg, and M. Pawelczyk, "Layer structures BaO-$\mathrm{SrTiO_3}$ in the region of p-type conductivity on the surface of $\mathrm{BaTiO_3}$," *Appl. Phys. A*, **53**, 563 (1991).

161 K. Abe and S. Komatsu, "Measurement and thermodynamic analyses of the dielectric constant of epitaxially grown $\mathrm{SrTiO_3}$ films," *Jpn. J. Appl. Phys.*, **32**, L1157 (1993).

162 R. J. Bouchard and J. L. Gillson, *Mat. Res. Bull.*, **7**, 873 (1972).

163 C. D. Landau and E. F. Lifshitz. *Electrodynamics of Continuous Media*. Addison-Wesley, Reading, Mass., 1960.

164 L. Lundgren, P. Svedlindh, and O. Beckmen, *J. Magn. Mater.*, **25**, 33 (1981).

165 G. A. Niklasson, "Comparison of dielectric response functions for conducting materials," *J. Appl. Phys.*, **66**, 4350 (1989).

166 J. Jäckle, "Models of the glass transition," *Rep. Prog. Phys.*, **49**, 171 (1986).

167 A. Papoulis. *The Fourier Integral and its Applications*. McGraw-Hill, New York, 1962.

168 K. S. Cole and R. H. Cole, *J. Chem. Phys.*, **10**, 98 (1942).

169 Ion Bunget and Mihai Popescu. *Physics of Solid Dielectrics*. Elsevier, Amsterdam, 1984.

170 R. M. Hill and S. K. Ichiki, "Polarization in tryglycine sulfate above the Curie temperature," *Phys. Rev. Lett.*, **128**, 1140 (1962).

171 H. Fröhlich. *Theory of Dielectrics*. Oxford University Press, London, U.K., 1958.

172 R. M. Fuoss and J. G. Kirkwood, *J. Am. Ceram. Soc.*, **63**, 385 (1941).

173 N. L. Johnson and S. Kotz. *Continuous Universal Distributions*. Volume 1, Houghton Mifflin, Boston, 1970.

174 J. R. Macdonald, "Frequency response of unified dielectric and conductive systems involving an exponential distribution of activation energies," *J. Appl. Phys.*, **58**, 1955 (1985).

175 J. R. Macdonald, "Relaxation in systems with exponential or Gaussian distribution of activation energies," *J. Appl. Phys.*, **61**, 700 (1987).

176 H. Kliem and G. Arlt, "The temperature-dependence of dielectric response in relation to distribution functions," *Phys. Stat. Sol. (b)*, **155**, 309 (1989).

177 D. W. Havriliak and S. Negami, *J. Polymer Sci.*, **C14**, 99 (1966).

178 K. S. Cole and R. H. Cole, "Dispersion and absorption in dielectrics," *J. Chem. Phys.*, **9**, 341 (1941).

179 D. W. Davidson and R. H. Cole, *J. Chem. Phys.*, **19**, 1417 (1951).

180 D. W. Davidson, *Can. J. Chem.*, **39**, 571 and 579 (1961).

181 S. Havriliak and S. Negami, "A complex plane representation of dielectric and mechanical relaxation processes in some polymers," *Polymer*, **8**, 161 (1967).

182 A. K. Jonscher, *Colloid Polym. Sci.*, **253**, 231 (1975).

183 R. M. Hill, *Nature*, **275**, 96 (1987).

184 R. Kohlrausch, "Theorie des elektrischen Rückstandes in der Leidener Flasche," *Poggendorf Annalen der Physik*, **91**, 56 and 179 (1857).

185 A. Wintner, *Duke Math. J.*, **8**, 678 (1941).

186 P. Lévy. *Théorie de l'addition des variables aléatoires*. Gauthier-Villars, Paris, 1937.

187 E. W. Montroll and J. T. Bendler, "On Lévi (or stable) distributions and the Williams-Watts model of dielectric relaxation," *J. Stat. Phys.*, **34**, 129 (1984).

188 J. R. Macdonald and L. Hurt, "Analysis of dielectric or conductive system frequency response data using the Williams-Watts function," *J. Chem. Phys.*, **84**, 496 (1986).

189 C. P. Lindsey and G. D. Patterson, "Detailed comparison of the Williams-Watts and Cole-Davidson functions," *J. Chem. Phys.*, **73**, 3348 (1980).

190 H. Pollard, *Bull. Am. Math. Soc.*, **52**, 908 (1946).

191 Roland Böhmer. *Dielektrische Relaxation in multipolar ungeordneten kondensierten Gasmischungen*. PhD thesis, Johannes Gutenberg-Universität, Mainz, F.R.G., August 1989.

192 F. Alvarez, À. Algería, and J. Colmenero, "Relationship between the time-domain Kohlrausch-Williams-Watts and frequency-domain Havriliak-Negami relaxation functions," *Phys. Rev. B*, **44**, 7306 (1991).

193 S. Hutton. Private communication, 1991.

194 E. Schlosser and A. Schönhals, "Recent development in dielectric relaxation spectroscopy of polymers," *Colloid Polym. Sci.*, **267**, 963 (1989).

195 A. D. Franklin and H. J. de Bruin, "The Fourier analysis of impedance sprectra for electroded solid electrolytes," *Phys. Stat. Sol. (a)*, **75**, 647 (1983).

196 P. Colonomos and R. G. Gordon, "Bounded error analysis of experimental distribution of relaxation times," *J. Chem. Phys.*, **71**, 1159 (1979).

197 Y. Imanishi, K. Adachi, and T. Kotaka, "Dielectric relaxation spectra for the bulk and concentrated solutions of *cis*-polyisoprene," *J. Chem. Phys.*, **89**, 7593 (1988).

198 H. Kliem, P. Fuhrmann, and G. Arlt, "A numerical method for the determination of first-order kinetics relaxation time spectrum," *IEEE Trans. Electr. Insul.*, **23**, 919 (1988).

199 F. Schwarzl and A. J. Staverman, "Higher approximation methods for the relaxation spectrum from static and dynamic measurements of visco-elastic materials," *Appl. sci. Res.*, **4**, A127 (1953).

200 N. W. Tschoegl, *Rheol. Acta*, **10**, 582 (1971).

201 D. Hayard, M. Gawayne, M. Mahboubian-Jones, and R. A. Pethrick, "Low-frequency dielectric measurements (10^{-4} to $6 \cdot 10^{4}$ hz): a new computer-controlled method," *J. Phys. E: Sci. Instrum.*, **17**, 683 (1984).

202 J. Ühlken, R. Waser, and H. Wiese, "A Fourier transform impedance spectromenter using logarithmically spaced time samples," *Ber. Bunsenges. Phys. Chem.*, **92**, 735 (1988).

203 S. Takeishi and S. Mashimo, "Dielectric relaxation measurements in the ultralow frequency region," *Rev. Sci. Instrum.*, **53**, 1155 (1982).

204 B. V. Hamon, *Proc. IEE*, **94**, 151 (1952).

205 M. Abramowitz and I. A. Stegun. *Handbook of Mathematical Functions.* Dover Publications, New York, 1970.

Acknowledgments

It is my pleasure to acknowledge the fruitful collaboration with U. T. Höchli and J. Mannhart, who have guided me here at the IBM Research Laboratory, and with A. Châtelain, whose support throughout this work has been invaluable. I greatly appreciate their help and encouragement in both technical and personal matters.

S. Rod and M. Fazan (EPF Lausanne) produced a number of $K_{1-x}Li_xTaO_3$ samples and helped me with crystal growth. S. Ziolkievicz (University of Paris VI) is acknowledged for supplying additional $K_{1-x}Li_xTaO_3$ specimens, and A. Titov (St. Petersburg Optical Institute) for providing the $Pb(Mg_{1/3}Nb_{2/3})O_3$ crystal.

I wish to thank J. G. Bednorz for providing pure and doped $SrTiO_3$ crystals, and J. Mannhart, together with T. Frey, D. G. Schlom, and J. Ströbel, for growing the $SrTiO_3$ films.

Ch. Gerber is gratefully acknowledged for the AFM analysis of the $SrTiO_3$:Nb substrates, and E. Williams for the TEM investigation of the heterostructures and for support in many different ways.

I also wish to express my gratitude for the close and fruitful collaboration with J. J. van der Klink and R. Sommer (EPF Lausanne), A. Loidl, R. Böhmer, P. Lunkenheimer, and K. Liedermann (University of Mainz), R. Migoni, M. Stachiotti (University of Rosario), J. Kohanoff (University of Lyon), E. V. Colla, E. Yu. Koroleva, S. B. Vakhrushev, and N. Yushin (A. F. Ioffe Institute, St. Petersburg), and S. Hutton (Montana State University).

Enlightening discussions with numerous people have contributed significantly to this thesis. In particular I wish to acknowledge P. Doussineau and A. Levelut (University of Paris VI), M. D. Fontana, G. E. Kugel, and R. Klein (Supélec and University of Metz), M. Maglione (University of Dijon), and E. Marchal (Institut Charles Sadron, Strasbourg). I am also indebted to D. Boese, E. Courtens, M. Daglish, L. Dissado, W. Kleemann, and K. A. Müller for helpful remarks.

My colleagues N. Blanc, O. Martin, H. Rothuizen and A. Stalder have contributed to this work through their friendship and their assistance in the lab and with solving computer problems.

The members of the IBM workshop, in particular H. Nievergelt, H. P. Ott, and K. Wasser, the publications department, in particular L. Pavka, and the librarians, D. Reichlin and S. Thaly, are acknowledged for their excellent work.

Many other co-workers at the IBM Laboratory, in particular all the members of the superconductivity group, have contributed to this work in various ways for which I am most thankful.

Finally, I am very much indebted to the support and encouragement of my wife Kris, who has managed to brighten even my most difficult days.

On Monday, when the sun is hot
I wonder to myself a lot:
"Now is it true, or is it not,
"That what is which and which is what?"

On Tuesday when it hails and snows
The feeling on me grows and grows
That hardly anybody knows
If those are these or these are those.

LINES WRITTEN BY A BEAR
OF VERY LITTLE BRAIN

Curriculum Vitae

Hans-Martin CHRISTEN

Alte Landstrasse 131
CH-8804 Au, Switzerland

Date of birth: 17 August 1966
Nationality: Swiss

EDUCATION

1991 - 1994	Ph.D. student at Swiss Federal Institute of Technology (EPFL), Lausanne, Switzerland Thesis Advisor: Prof. A. Châtelain, Experimental Physics
1986 - 1991	Swiss Federal Institute of Technology (EPFL) Lausanne, Switzerland Degree in Physics Engineering
1985	Maturität (A-Level), Solothurn, Switzerland
1983 - 1984	High School Diploma, Iowa, USA (foreign exchange student)

PRACTICAL EXPERIENCE

1991 - 1994	Pre-doctorate position at IBM Research Laboratory Rüschlikon (Zurich), Switzerland
1989	IAESTE Internship (duration of 9 weeks) Siemens AG, Research and Development Munich, Germany: – study of temperature evolution of semiconductor substrates during Reactive Ion Beam Etching
1985 - 1986	Teaching Assistant German Department, Central University of Iowa, USA